

**BIOMASS GASIFICATION USING A HORIZONTAL  
ENTRAINED-FLOW GASIFIER AND CATALYTIC  
PROCESSING OF THE PRODUCT GAS**

**By**

**Isack Amos Legonda**

B.Sc (Mech), M.Sc (Energy)

**A Thesis Submitted to Cardiff University for the Degree of Doctor of  
Philosophy in Mechanical Engineering**

**Cardiff Institute of Energy  
Cardiff University, Wales, United Kingdom**

**October, 2012**

## Abstract

A novel study on biomass-air gasification using a horizontal entrained-flow gasifier and catalytic processing of the product gas has been conducted. The study was designed to investigate the effect of catalyst loading on the product gas. The use of a horizontal entrained-flow gasifier reactor was used to assess the effect of the gasifier reactor orientation on the gasification process. Both experimental and computational fluid dynamics (CFD) approaches were employed. The gasification tests were conducted at 800 °C and equivalence ratio of 0.23 while the product gas was catalysed at 350-400 °C and a gas hourly space velocity (GHSV) of 8000 h<sup>-1</sup>. Preparation and characterisation of wood powder and catalysts were performed using classical methods. Moreover, the syngas and tar composition were analysed using a gas chromatograph (GC) and GC-mass spectrometer (GC-MS) respectively.

The research findings showed that maximum fuel conversion and cold gas efficiency using a horizontal entrained-flow gasifier were 99 % and 70 % respectively. The gasifier length can also be reduced from the common 1000-2000 mm to 500 mm. The catalysis study showed that pumice and kaolin have limited catalytic effect on the product gas. However, doping with CeO<sub>2</sub>, ZrO<sub>2</sub>, CuO and NiO improved the syngas heating value, coking resistance and tar conversion. A notable increase in syngas LHV was achieved using ceria doped pumice (8.97 MJ/Nm<sup>3</sup>) and copper doped pumice (8.66 MJ/Nm<sup>3</sup>) compared to 6.67 MJ/Nm<sup>3</sup> of non-catalytic test. For the tested catalysts, CeO<sub>2</sub> doped pumice exhibited highest coking resistance. Furthermore, catalytic tar conversion was mainly through cracking and partial oxidation reactions. The lowest tar yield was found to be 3.55 g/Nm<sup>3</sup> using kaolin-ceria-zirconia catalyst compared to 14.92 g/Nm<sup>3</sup> of non-catalytic gasification. Tar reduction using untreated pumice was through adsorption and ranged 4-6 g/Nm<sup>3</sup>.

In general, the results of this study suggest that there exist a sensitivity to the gasifier orientation on the overall gasification process. It has also shown that metal oxides have both beneficial and detrimental effects of syngas composition. Although syngas heating value increased with increasing catalyst loading, H<sub>2</sub> showed a decreasing trend highlighting that further catalyst modification is required. Furthermore, pumice and kaolin can be utilised as catalyst support in the gasification technology. However, further experimental investigation on doping various catalytic metals and testing at different operating conditions are hereby proposed.

## **Dedication**

To my wife Esther and our sons Amos and Daniel

## **Acknowledgement**

I would like to express my thanks to the University of Dar es Salaam Tanzania through World Bank Project for their financial support to undertake this study. Also thanks to the Cardiff University for the 125 Award which encouraged and supported my research activities.

Thanks to Prof. Tony Griffiths and Dr. Richard Marsh my supervisors for their guidance on research skills and scientific inputs. To Dr. Karen Wilson for her inputs on catalysis investigations.

Thanks to Malcolm Seaborn and other technical staff for their technical support during experimentation. To my colleagues that have encouraged me with this investigation. Specifically, Hosanna choir CCT-UDSM and St. Teilo of Cathays for their prayers.

## Table of Contents

<b>Declaration and Copyright</b> .....	i
<b>Abstract</b> .....	ii
<b>Dedication</b> .....	iii
<b>Acknowledgement</b> .....	iv
<b>List of Figures</b> .....	x
<b>List of Tables</b> .....	xiv
<b>List of Abbreviations</b> .....	xvi
<b>Nomenclature</b> .....	xvii
<b>1 INTRODUCTION</b> .....	1
1.1 Background .....	1
1.2 Energy Situation in Tanzania .....	3
1.3 Biomass as Energy Resource .....	4
1.4 Aims of the Research .....	5
1.5 Research Hypothesis .....	5
1.6 Thesis Structure.....	6
<b>2 LITERATURE REVIEW</b> .....	8
2.1 Biomass Gasification .....	8
2.1.1 Gasification Process .....	8
2.1.2 Factors affecting gasification process .....	11
2.1.3 Entrained-flow gasifiers .....	18
2.2 Catalytic Processing of Gasification Product Gas .....	21
2.2.1 Catalysis overview .....	21
2.2.2 Steps in heterogeneous catalytic reactions .....	21
2.2.3 Factors affecting catalyst performance .....	22
2.2.4 Catalytic oxidation of hydrocarbon compounds .....	23
2.2.5 Catalyst supports .....	24
2.2.6 Preparation and characterisation of supported metal catalysts .....	26
2.2.7 Catalyst screening .....	27
2.3 Modeling in Gasification and Catalysis .....	29
2.3.1 Background .....	29

2.3.2 Partially Premixed Combustion Model.....	29
2.3.3 Discrete Phase Model.....	30
2.3.4 Species Transport Model.....	31
2.4 Summary .....	33
<b>3 MATERIALS AND METHODS OF CHARACTERISATION STUDIES</b>	<b>34</b>
3.1 Introduction .....	34
3.2 Characterisation of Sawdust.....	34
3.2.1 Sample preparation.....	34
3.2.2 Proximate analysis .....	35
3.2.3 Calorific value .....	37
3.2.4 Ultimate analysis .....	38
3.2.5 Thermo gravimetric analysis (TGA).....	39
3.2.6 Particle shape and size distribution .....	39
3.3 Characterisation of Pumice .....	40
3.3.1 Major and trace elements analysis .....	40
3.3.2 Thermogravimetric analysis.....	42
3.3.3 Porosity of the packed bed and surface area of pumice .....	43
3.3.4 Loss on ignition (LOI) .....	44
3.4 Preparation of Ceria (CeO <sub>2</sub> ) doped pumice .....	45
3.4.1 Experimental rig set-up .....	45
3.4.2 Impregnation process .....	45
3.5 Preparation of nickel doped pumice.....	46
3.6 Preparation of copper doped pumice.....	46
3.7 Preparation of kaolin catalysts .....	47
3.7.1 Extraction of kaolin.....	47
3.7.2 Kaolin-Ceria (KL/CeO <sub>2</sub> ) .....	48
3.7.3 Kaolin-Ceria-Zirconia (KL/CeO <sub>2</sub> /ZrO <sub>2</sub> ) .....	49
3.8 Characterisation of Catalysts .....	49
3.9 Summary .....	49

<b>4</b>	<b>GASIFICATION TRIALS AND MEASUREMENTS</b> .....	51
4.1	Introduction .....	51
4.2	Testing Parameters .....	51
4.2.1	Performance of the horizontal entrained-flow gasifier .....	51
4.2.2	The effect of catalysts on gasification products .....	52
4.3	Equipment .....	53
4.3.1	The experimental rig .....	53
4.3.2	The fuel feeder .....	53
4.3.3	The furnace.....	54
4.3.4	The gasifier.....	56
4.3.5	Catalytic reactor and the heating system.....	56
4.3.6	Tar sampling system .....	59
4.3.7	Vacuum pump .....	59
4.3.8	Sundry equipment .....	60
4.4	Gasification Process Procedures .....	60
4.4.1	Gasification operating procedures.....	60
4.4.2	Preparation procedures.....	60
4.4.3	Operation procedures .....	61
4.5	Experimental Data Measurements .....	63
4.5.1	Temperatures.....	63
4.5.2	Syngas analysis .....	63
4.5.3	Tar Analyses.....	64
4.5.4	Pressure drop across the catalyst reactor.....	66
4.5.5	Fuel conversion and cold gas efficiency .....	68
4.5.6	Catalyst activity and selectivity .....	68
4.5.7	Feed rate settings.....	69
4.6	Summary .....	72
<b>5</b>	<b>MODEL DEVELOPMENT</b> .....	73
5.1	Introduction .....	73
5.2	Gasification Predictions .....	74
5.2.1	The model geometry .....	74

5.2.2	The computational domain and grid quality .....	74
5.2.3	Gasification models.....	78
5.2.4	Boundary conditions .....	79
5.3	Modeling of the Catalytic Processing of Gasification Products .....	81
5.3.1	The model geometry .....	81
5.3.2	The computational domain.....	81
5.3.3	Modeling approach.....	82
5.3.4	Boundary conditions .....	83
5.4	Solution Algorithms and Accuracy .....	84
5.5	Summary .....	86
<b>6</b>	<b>EXPERIMENTAL RESULTS</b> .....	<b>87</b>
6.1	Introduction .....	87
6.2	Material Characterisation .....	87
6.2.1	Characterisation of the feedstock .....	87
6.2.2	Thermogravimetric analysis.....	88
6.2.3	Particle size distribution.....	88
6.3	Characterisation of Pumice and Kaolin.....	90
6.3.1	Major and trace elements .....	90
6.3.2	Thermogravimetric analysis.....	92
6.3.3	Characterisation of catalysts .....	92
6.4	Pressure Drop in the Catalytic Bed .....	97
6.5	Gasification Conditions.....	99
6.6	Performance of the Horizontal Entrained-flow Gasifier Reactor .....	101
6.6.1	Fuel conversion .....	101
6.6.2	Cold Gas Efficiency (CGE) .....	101
6.6.3	Syngas composition .....	101
6.6.4	Tar composition .....	102
6.7	Catalytic Gasification Results.....	105
6.7.1	Effect of Catalyst Support on the Gasification Product Gas.....	105
6.7.2	Ceria (CeO <sub>2</sub> ) Doped Pumice .....	108

6.7.3 CuO doped pumice.....	113
6.7.4 Nickel doped pumice.....	119
6.7.5 Kaolin-Ceria (KL/CeO <sub>2</sub> ) .....	124
6.7.6 Kaolin-Ceria-Zirconia (KL/CeO <sub>2</sub> /ZrO <sub>2</sub> ) .....	130
6.8 Catalyst Screening.....	133
6.9 Material and Energy Balances .....	139
6.10 Summary .....	144
<b>7 MODELLING RESULTS .....</b>	<b>145</b>
7.1 Introduction.....	145
7.2 Gasification Predictions .....	145
7.3 Predictions for Catalytic Processing of the Product Gas .....	151
7.4 Gasifier Reactor Orientation .....	156
7.5 Summary .....	158
<b>8 COMPARISON OF EXPERIMENTAL AND MODEL RESULTS.....</b>	<b>159</b>
8.1 Introduction.....	159
8.2 Gasification Model Results.....	159
8.3 Catalytic Processing of the Syngas .....	160
8.4 Interaction of Gasification Product Gas with Redox Catalysts.....	162
8.5 Summary .....	164
<b>9 CONCLUSIONS AND RECOMMENDATIONS.....</b>	<b>165</b>
9.1 Conclusions.....	165
9.2 Recommendations for Future Work.....	167
<b>REFERENCES .....</b>	<b>168</b>
<b>APPENDICES .....</b>	<b>179</b>
Appendix B. Biomass Gasification Modeling.....	184
Appendix C. Catalytic Gasification Modeling .....	188
Appendix D: Material and energy balances for all experimental tests .....	191

## List of Figures

Figure 1.1 A typical effect of tar on processing surfaces.....	2
Figure 1.2 Pumice and kaolin samples.....	3
Figure 1.3 Share of total primary energy supply in Tanzania [17]. ....	4
Figure 2.1 Reaction sequence for gasification of coal and biomass [4].....	9
Figure 2.2 Schematic diagrams of (a) Downdraft gasification, and (b) Updraft gasification [26] .....	12
Figure 2.3 Moving bed gasifier reactor (Lurgi) [4].....	12
Figure 2.4 Schematic diagrams of a common circulating fluid-bed gasifier [4] .....	13
Figure 2.5 The schematic diagram of cyclone air gasification [28].....	14
Figure 2.6 The schematic diagram of the innovated cyclone gasifier [27].....	14
Figure 2.7 Schematic diagrams for typical entrained flow gasifiers.....	20
Figure 2.8 Map of Tanzania showing locations of pumice and kaolin deposits [82]	25
Figure 3.1 Feedstock samples .....	34
Figure 3.2 Bomb calorimeter (Parr 6100) .....	38
Figure 3.3 Thermogravimetric analyser (STA-780 series) .....	39
Figure 3.4 ICP-OES analyser (PerkinElmer Optima 4300 DV) .....	41
Figure 3.5 XRF analyser (InnovXsystem X-50) .....	42
Figure 3.6 Experimental layout for determining the porosity of pumice.....	44
Figure 3.7 Experimental set-up for preparation of ceria doped pumice .....	45
Figure 3.8 Extraction of kaolin from raw sample .....	48
Figure 4.1 Schematic layout of the gasification trials set-up.....	54
Figure 4.2 Experimental test rig used for gasification and catalysis studies .....	55
Figure 4.3 Schematic diagram for the gasifier reactor and the fuel feed mechanism	57
Figure 4.4 Catalytic reactor and the heating system .....	58
Figure 4.5 Schematic diagram of the tar sampling system .....	59
Figure 4.6 GC-MS spectra for naphthalene (C <sub>10</sub> H <sub>8</sub> ) .....	66
Figure 4.7 Schematic layout for the pressure drop experiments.....	67
Figure 4.8 Pumice sample for 2-4 mm size.....	67
Figure 4.9 Carbon-Sulphur analyser (Leco SC-144DR).....	68
Figure 5.1 The Model geometry representing the experimental rig.....	74
Figure 5.2 Types of 3D mesh cells.....	76

Figure 5.3 The meshed computational domain .....	77
Figure 5.4 PDF curve for biomass combustion.....	80
Figure 5.5 Model geometry of the catalytic reactor .....	81
Figure 5.6 Computational domain of the catalytic reactor.....	82
Figure 5.7 Pressure-Based Segregated Algorithm .....	85
Figure 6.1 Thermogravimetric behavior of pinewood sawdust .....	88
Figure 6.2 Particle size distribution of the wood powder .....	89
Figure 6.3 Particle size and shape of wood powder.....	89
Figure 6.4 XRD pattern for the calcined (a) Pumice from Arusha, Tanzania (b) Pumice from Mbeya, Tanzania and (c) Pumice from Mexico and (d) Kaolin from Pugu Hills , Tanzania .....	90
Figure 6.5 Mass loss analysis of the dried pumice.....	92
Figure 6.6 XRD analysis of the pumice and the derived ceria doped pumice catalysts .....	94
Figure 6.7 XRD analysis of the pumice and the derived copper doped pumice catalysts .....	94
Figure 6.8 XRD analysis of the pumice and the derived ceria doped kaolin catalysts .....	95
Figure 6.9 XRD analysis of the pumice and the derived ceria and zirconia doped kaolin catalysts .....	96
Figure 6.10 XRD analysis of the nickel doped pumice catalysts.....	97
Figure 6.11 Pressure drop profile in the catalyst reactor .....	99
Figure 6.12 Temperature pattern of the experimental set-up.....	100
Figure 6.13 The effect of CeO <sub>2</sub> loading on (a) syngas composition, (b) Selectivity to gaseous products and (c) Cold gas efficiency (CGE) and gas ratios .....	109
Figure 6.14 Carbon deposition profile in the catalytic reactor with fresh pumice (FP) and ceria treated pumice .....	113
Figure 6.15 Syngas composition at different CuO loading.....	114
Figure 6.16 Catalyst selectivity on gaseous product at different CuO loading.....	114
Figure 6.17 The effect of CuO loading on cold gas efficiency .....	115
Figure 6.18 The effect of CuO loading on tar yield.....	118
Figure 6.19 The effect of CuO loading on light tar yield.....	118
Figure 6.20 Syngas composition at different NiO loading .....	120
Figure 6.21 Catalyst selectivity at different NiO loading .....	120

Figure 6.22 The effect of NiO loading on cold gas efficiency and gas ratios.....	121
Figure 6.23 The effect of NiO loading on tar yield.....	123
Figure 6.24 The effect of NiO loading on light tar yield .....	123
Figure 6.25 Syngas composition at different CeO <sub>2</sub> loading in the Kaolin-ceria mix catalysts .....	126
Figure 6.26 Catalyst selectivity at different CeO <sub>2</sub> loading in the kaolin-ceria mix catalysts .....	126
Figure 6.27 The effect of CeO <sub>2</sub> loading on cold gas efficiency in the kaolin-ceria mix .....	127
Figure 6.28 The effect of CeO <sub>2</sub> loading on tar yield using kaolin-ceria mix catalysts .....	129
Figure 6.29 The effect of CeO <sub>2</sub> loading on light tar yield using kaolin-ceria mix catalysts .....	129
Figure 6.30 The effect of adding ZrO <sub>2</sub> in the CeO <sub>2</sub> doped kaolin on tar yield, (KL=kaolin) .....	133
Figure 6.31 Comparison on the selectivity of catalysts to gaseous products.....	135
Figure 6.32 Activity of different catalysts based on coking resistance.....	137
Figure 6.33 A comparison on the maximum cold gas efficiency achieved by different catalysts .....	137
Figure 6.34 Distribution of the material flow in the gasification system .....	139
Figure 6.35 Relationship between material and energy balance in a gasification system.....	143
Figure 7.1 Predicted temperature profile in the gasifier reactor .....	145
Figure 7.2 Contours of mole fraction of CO .....	147
Figure 7.3 Contours of mole fraction of CO <sub>2</sub> .....	147
Figure 7.4 Contours of mole fraction of H <sub>2</sub> .....	148
Figure 7.5 Contours of mole fraction of CH <sub>4</sub> .....	148
Figure 7.6 Contours of mole fraction of O <sub>2</sub> .....	149
Figure 7.7 Contours of mole fraction of C(s).....	149
Figure 7.8 Particle traces colored by particle residence time (s) .....	150
Figure 7.9 Particle traces colored by particle volatile fraction .....	150
Figure 7.10 Vector plot of the axial velocity along the catalytic reactor.....	153
Figure 7.11 Contour plots for CO and CO <sub>2</sub> concentration.....	154
Figure 7.12 Contour plots for H <sub>2</sub> and CH <sub>4</sub> concentration .....	154

Figure 7.13 Contour plots for tar conversion and temperature profile .....	155
Figure 7.14 Contours of surface coverage of catalysts .....	155
Figure 7.15 Comparison between a horizontal and vertical gasifier configurations on the gasification process .....	157
Figure 8.1 Comparison between model and experimental data on catalytic processing of gasification product gas .....	161
Figure 8.2 The conceptual model for the interaction of biomass gasification product gas over pumice and kaolin treated with redox catalysts.....	163

## List of Tables

Table 2.1 Principle reactions in coal or biomass gasification process [4].	9
Table 2.2 Tar classification adapted from Li and Suzuki [3].	10
Table 2.3 Tar cracking kinetic equations adapted from [25]	11
Table 2.4 Typical analysis of biomass composition [6, 29-31]	15
Table 2.5 Typical geometrical parameters of the entrained-flow gasifier reactors.	19
Table 2.6 Properties and characterisation methods of heterogeneous catalysts [84, 85]	27
Table 3.1 Mixing ratios for the preparation of copper doped pumice	47
Table 3.2 Mixing proportions of kaolin and ceria	48
Table 4.1 Parameter settings for testing of the gasifier performance	52
Table 4.2 Study matrix for catalytic processing of gasification product gas	52
Table 4.3 Reference standards for identifying tar compounds	65
Table 4.4 Air-Fuel ratio for gasification process at ER=0.23	71
Table 5.1 Particle properties of pine sawdust [116].	79
Table 5.2 Parameters setting for boundary conditions.	80
Table 5.3 Boundary conditions for catalysis trials as measured experimentally	84
Table 6.1 Proximate and ultimate analysis of sawdust	87
Table 6.2 Elemental analyses of the pumice from Mexico (MEX), Arusha (ARU), Mbeya (MBY) and Kaolin (KL) from Pugu Hills	91
Table 6.3 Prepared catalysts and their composition as determined by ICP-OES	93
Table 6.4 Syngas composition and yields from biomass gasification using a horizontal entrained-flow gasifier reactor	102
Table 6.5 Tar yield from biomass gasification using a horizontal entrained-flow gasifier reactor.	104
Table 6.6 Comparison of syngas composition from different catalyst supports.	106
Table 6.7 Comparison of tar yield from different catalyst supports	107
Table 6.8 Tar yield at different ceria loading (FP, CeO <sub>2</sub> =0 g; CeO <sub>2</sub> -1=0.65 g; CeO <sub>2</sub> -2=1.44 g; CeO <sub>2</sub> -3=1.73 g).	111
Table 6.9 Tar yield at different copper loading (FP=0 g CuO, CuO-1=0.74 g, CuO-2=1.79 g, CuO-3=2.81 g)	117
Table 6.10 Tar yield at different NiO loading (FP, NiO=0 g; NiO-1=1.07 g; NiO-2=2.04 g)	122

Table 6.11 Tar yield at different copper loading (Kaloïn-1, CeO <sub>2</sub> =0 g; Kaolin-2, CeO <sub>2</sub> =9.2 g; Kaolin-3, CeO <sub>2</sub> =14 g; Kaolin-4, CeO <sub>2</sub> =21 g).....	128
Table 6.12 The effect of doping zirconia in the kaolin-ceria mix catalyst on the biomass gasification product gas .....	130
Table 6.13 Tar yield at different copper loading (KL/CeO <sub>2</sub> , CeO <sub>2</sub> =14 g; KL/CeO <sub>2</sub> /ZrO <sub>2</sub> , CeO <sub>2</sub> =14 g, ZrO <sub>2</sub> =14 g).....	132
Table 6.14 Summary of results from all experimental tests.....	138
Table 6.15 LHV and density of gases typically found in gasification process [160]. .....	141
Table 6.16 Material and energy balances for non-catalytic test.....	142
Table 6.17 Material and energy balances for all experimental tests .....	143
Table 8.1 Comparison between model and experimental data .....	159

## **List of Abbreviations**

BET	Brunauer Emmett Teller
BWGS	Biological Water Gas Shift
CCT	Christian Council of Tanzania
CFD	Computational Fluid Dynamics
CHNSO	Carbon Hydrogen Nitrogen Sulphur Oxygen
DPM	Discrete Phase Model
EDX	Energy-Dispersive X-ray
EFG	Entrained-Flow Gasifier
EHT	Electron High Tension
ESP	Electrostatic Precipitation
FP	Fresh Pumice
GC	Gas Chromatography
GC-MS	Gas Chromatography-Mass Spectrometer
ICG	Inverted Cyclone Gasifier
ICP-OES	Inductive Coupled Plasma-Optical Emission Spectroscopy
IR	Infra Red
KL	Kaolin
NEP	National Energy Policy
OSC	Oxygen Storage Capacity
PAH	Polycyclic Aromatic Hydrocarbon
PDF	Probability Density Function
PVC	Polyvinyl Chloride
RDF	Refuse Derived Fuel
SEM	Scan Electron Microscopy
SVOC	Semi Volatile Organic Compound
TGA	Thermogravimetric Analysis
TPR	Temperature Programmed Reduction
UDSM	University of Dar es Salaam
VOC	Volatile Organic Compound
XPS	X-ray Photoelectron Spectroscopy
XRD	X-ray Diffraction
XRF	X-ray Fluorescence

## Nomenclature

<b>Symbol</b>	<b>Definition</b>	<b>Unit</b>
AC	Ash content	% wt
$C_i$	Concentration	ppm by mass
$C_p$	Specific heat capacity	J/kg K
D, d	Diameter	mm
e	Offset distance	mm
ER	Equivalence ratio	-
f	Mixture fraction	-
FC	Fixed Carbon	% wt
ID	Inside Diameter	mm
L	Length of the gasifier reactor	mm
LHV	Low Heating Value	J/kg, J/Nm <sup>3</sup>
LOI	Loss on Ignition	% wt
m	Mass	g
MC	Moisture content	% wt
q	Calorific value	J/kg
Q	Volume flow rate	l/min
r	Air-fuel ratio	-
R	Universal gas constant	J/mol K
Re	Reynolds number	-
S	Selectivity	%
STY	Space Time Yield	mol L <sup>-1</sup> h <sup>-1</sup>
SV	Space Velocity	m <sup>3</sup> /kg s]
T	Temperature	°C, K
U	Velocity	m/s
VM	Volatile matter	% wt
X	Conversion	mol/mol or %]
Z	Surface coverage	-

## Greek Symbols

$\mu$	Dynamic viscosity	kg/m/s
$\varepsilon$	Void fraction	-
$\eta$	Efficiency	%
$\theta$	Angle	Degrees
$\rho$	Density	kg/m <sup>3</sup>
$\tau$	Residence time	s

# 1 INTRODUCTION

## 1.1 Background

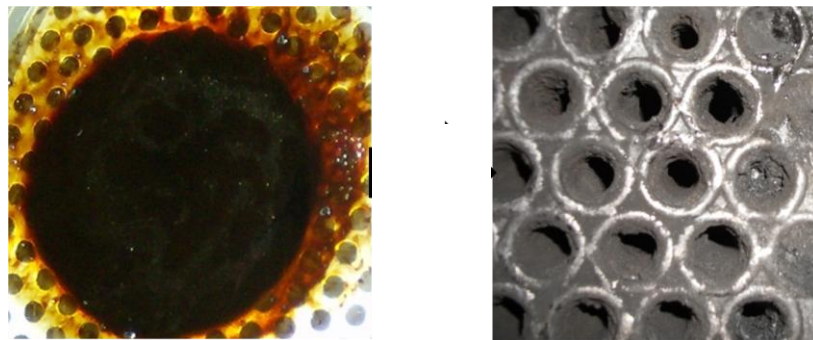
There is an increasing awareness of the energy conservation and the concern over climate change. Nowadays, fossil fuels such as coal, oil and natural gas are being consumed at an accelerating rate which threatens their availability in the near future. For instance according to BP statistics [1], natural gas and oil reserves are estimated to be  $185 \times 10^9 \text{ m}^3$  and  $172 \times 10^9$  tonnes which will be depleted in 60 and 42 years respectively. Coal could substitute for oil and gas but its reserves world wide are estimated as  $826 \times 10^9$  tonnes which will last 120 years at the current consumption rate. As well as the loss of energy reserves, global warming due to increased carbon dioxide ( $\text{CO}_2$ ) concentration in the atmosphere will lead to climate change threatening our society. Carbon dioxide molecules resonate with the infrared from the sun by transforming into heat which is then released into the space. The major source of  $\text{CO}_2$  emissions is from combustion of high carbonaceous fuels such as coal and oil.

The need to supply energy sufficiently without causing serious environmental pollution is obvious. According to the recent environmental conference held at Copenhagen, Denmark [2], climate change is one of the greatest challenges of our time and deep cuts in global emission are necessary. There are various proposed alternative sources of energy which can mitigate  $\text{CO}_2$  emission. These sources include biomass, solar, wind, geothermal and tidal. With the exception of biomass, the viability of other energy sources is limited by capital investment. Owing to low additional  $\text{CO}_2$  emissions compared to coal and oil, biomass has been believed to be an alternative source of fuel. Biomass can be converted into compatible alternative fuels such as bio-oil through pyrolysis and synthetic gas (syngas) using gasification technology. However, the former process yields char which need further conversion to useful energy in form of gas.

Gasification involves the thermal conversion of carbonaceous fuel into syngas in a controlled supply of a medium such as air, oxygen, steam or  $\text{CO}_2$ . The produced syngas is mainly composed of  $\text{H}_2$ ,  $\text{CO}$ ,  $\text{CO}_2$ ,  $\text{CH}_4$  and heavy hydrocarbons referred as "tar". Tars are hydrocarbons with molecular weight higher than that of benzene ( $\text{C}_6\text{H}_6$ ) [3]. These compounds are generally derived from volatiles released from the biomass during heating and contains significant amount of chemical energy [4].

Biomass gasification has found many applications including internal combustion engines, gas turbines, boilers and cooking stoves. Syngas can also be used as feedstock for the production of liquid biofuels [5]. Biomass gasification plants can be installed in remote areas for power generation and water pumping systems. Feedstock from agricultural and municipal wastes can be utilised effectively, thus, reducing environmental pollution [6].

However, the presence of tar in the syngas hinders the technology development. In most cases, tar forming compounds condense on critical surfaces such as processing surfaces, potentially causing blockages as revealed in Figure 1.1. Various techniques have been applied to reduce tar in the syngas stream to meet recommended concentration limits. Tar removal from syngas has been achieved through filtration using water scrubbers and porous materials [7]. These approaches result in the loss of output energy in the tar. Other tar treatment methods are thermal cracking and the use of catalysts. While the former require intensive heating ( $>1200$  °C), the latter, can be achieved at lower temperatures (approx. 350 °C) [8, 9].



(a) Tar from biomass gasification      (b) Blocked heat exchanger

Figure 1.1 A typical effect of tar on processing surfaces

Catalysts have been successfully used in biomass gasification plants for tar conversion into useful gases such as  $H_2$ ,  $CO$  and  $CH_4$ . Tar conversion is possible through cracking, reforming or reduction and oxidation reactions (redox). These methods use catalysts composed of metal oxides such as those of copper, nickel, cerium or zirconium. In many cases, supported catalysts (heterogeneous) are used as they can resist higher temperatures more than liquid (homogeneous) ones [10, 11]. Catalyst supports such as monolith, activated alumina, activated carbon, kaolin and

pumice have been employed in catalytic processing of gasification product gas. Despite the low cost of pumice and kaolin compared to others, their application in biomass gasification is limited. A typical pumice and kaolin are shown in Figure 1.2.



(a) Pumice sample



(b) Raw kaolin sample

Figure 1.2 Pumice and kaolin samples

Since the Tanzania government was the main sponsor of this research, the research focuses on improving biomass gasification technology utilising natural resources such as pumice and kaolin which are readily available in Tanzania. This research provides a contribution to the energy supply, specifically, to the remote areas in Tanzania.

## 1.2 Energy Situation in Tanzania

Electricity generation in Tanzania is mainly from hydropower sources which has not been reliable nowadays due to hydrological uncertainties. According to Tanzania national policy [12], electricity generation is 863 MW of which 559 MW is from hydro-based and the balance is from thermal sources. This power supplies only 10 % of the population (34.6 millions) in Tanzania. A number of strategies to increase power generation to meet a target of 6546 MW by 2033 have been initiated by the country. These include effective exploitation of natural resources such as natural gas, coal and biomass derivatives. Moreover, availability of uranium deposits has shown a possibility of developing nuclear power generation, however the programme is still at the consideration stage [13]. Therefore, the goal is to build capacity of energy production in Tanzania to support the national energy strategies.

### 1.3 Biomass as Energy Resource

While the use of fossil fuels is debatable, the biomass shares about 10-15 % ( $45 \times 10^{18}$  J) of total annual fuel use in the world [14]. According to World Energy Report [15], the global wood biomass was estimated to be  $1.665 \times 10^{21}$  J (390 Gtoe) which will deplete in 75 years (assuming zero growth rate). However, to avoid deforestation, the total sustainable worldwide biomass energy potential is estimated at  $100 \times 10^{18}$  J/a (2.38 Gtoe) with a woody biomass share of 40% [16].

In Tanzania, the scenario for energy share is that about 90 % of total primary energy ( $19.616 \times 10^6$  toe) supply is from biomass resources and the balance is oil, natural gas, hydro and coal as shown in Figure 1.3 [17]. In most cases, biomass in the form of wood or charcoal is used domestically for heating and food processing. Biomass resources are estimated to be 4.39 billion  $\text{m}^3$  ( $31.4 \times 10^{18}$  J) as a growing stock with a mean annual increment of 140 million  $\text{m}^3$  ( $1.0 \times 10^{18}$  J) [15]. However, the consumption is approximately 24% of annual increment thus contributing to deforestation at an estimated rate of 91,276 ha/yr. The major cause of high consumption is due to the inefficient (typically 11-25%) biomass conversion methods such as simple pyrolysis for charcoal production [18, 19]. Another cause is due to the ineffective use of biomass waste such as sawdust and agricultural residues. It has been reported that 6920 tonnes/year of sawdust (dry basis) are produced as waste at Sao Hill Mill company [20]. Furthermore, agricultural residues generated from coffee, sisal, sugar, and cereal are estimated to be 468,100 tonnes/year [21]. Therefore, utilising such bio-wastes using gasification can reduce deforestation and sustain biomass and other energy resources such as natural gas and coal.

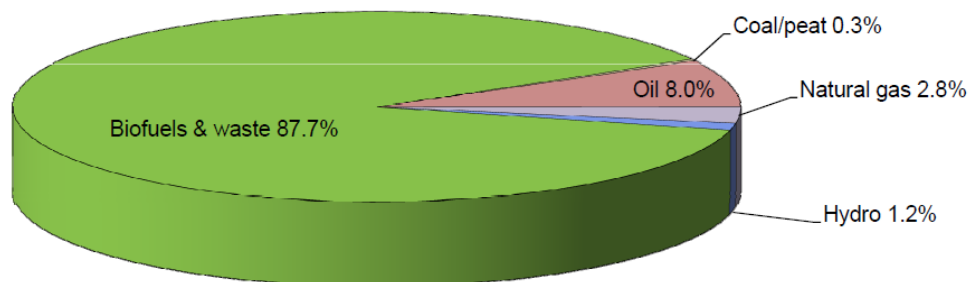


Figure 1.3 Share of total primary energy supply in Tanzania [17].

#### **1.4 Aims of the Research**

This study has two primary aims: The first aim was to investigate the effect of catalyst loading on the biomass gasification product gas. Both syngas and tar composition were measured for each catalyst loading test. The overall goal was to improve the heating value of the product gas.

The second aim was to assess the performance of a lab-scale entrained-flow gasifier. The study focused on the effect of gasifier reactor orientation and geometrical sizing. The gasifier was configured horizontally to increase the particles residence time as opposed to a vertical entrained-flow system, where gravity forces results in lower residence time. Additionally, the enhanced particle to metal surface contact promotes heat transfer to the particle, thus increasing fuel conversion. As the design requires high flow rates to cause efficient premixing of the fuel and the oxidizing agent, particle separation can be achieved using a common cyclone separator (not considered in this study).

A 3 kW (based on fuel mass flow rate) biomass gasifier reactor was used for the experimental study. In addition, computational fluid dynamics (CFD) employing FLUENT 12.1 software was used to study the non-isothermal characteristics relative to the gasifier reactor geometry. Moreover, a 200 ml catalytic reactor was employed for catalysis study of the gasification product gas. Furthermore, comparison between the experimental and modeling data was also carried out.

#### **1.5 Research Hypothesis**

The uncertainty of energy security and the increasing risks from global climate change highlight the need to develop efficient energy conversion systems. Although a number of researches have been conducted on biomass gasification, syngas quality in terms of tar content and heating value still need further improvement. This study aimed to address the following research hypotheses:

- (i) Whether the horizontal configuration of the entrained flow gasifier has significant effect on the gasifier reactor performance. This configuration could result in different product gas yield compared to the well known vertical designs.
- (ii) Whether catalyst loading has a significant effect on the syngas and tar composition. Tar cracking is possible through further oxidation in an

enhanced environment. This approach can be achieved using catalysts with redox properties which could have additional impact on tar cracking, carbon conversion and product gas composition.

- (iii) Whether pumice has a chemical effect on the biomass gasification product gas and is a potential catalyst support.
- (iv) Whether catalytic activity of pumice and kaolin can be improved by doping metal oxides.

## **1.6 Thesis Structure**

Chapter 1 highlights the general overview on the energy conservation and climate change. Energy resources are discussed and alternative approaches to reducing sources contributing to the climate change are presented. The aims of the current research and hypotheses are also described.

Chapter 2 provides overview on the biomass gasification and catalytic processing of the product gas. Factors affecting gasification process and syngas quality are discussed in detail. The development of the entrained-flow gasifier reactor from coal feedstock to biomass is highlighted. The use of catalysts for processing the syngas is also discussed.

Chapter 3 describes the materials and methods of characterisation that were performed on the wood powder and catalysts used in this study. Experimental procedures are described in detail for reproducibility of the research. In addition, equipments and reagents used in this study are also presented.

Chapter 4 details the experimental layout and describes procedures that were used during the gasification and catalysis studies of this work. Study parameters of interest and operating conditions for all experimental tests are explained in detail.

Chapter 5 describes the theory and modeling procedures used in predicting gasifier performance as well as the effect of catalysts loading on the product gas. Partially Premixed Combustion and Species Transport models were chosen and their background theory is highlighted.

Chapter 6 presents and discusses experimental results obtained from this study. Product gas and tar composition under different experimental tests are discussed. Moreover, the effect of catalysts loading on the product gas is also discussed. Furthermore, catalyst screening is presented to compare the performance of the catalysts employed.

Chapter 7 presents and discusses the CFD modeling results for both non-catalytic and catalytic studies. The comparison between the horizontal and vertical design is provided to study the effect of gasifier orientation on the overall gasification process. Results for catalytic processing of product gas are also presented.

Chapter 8 compares the model results with those measured experimentally. The general interaction between the gasification product gas and the catalysts is also highlighted.

Chapter 9 concludes the findings from experimental and numerical modeling undertaken in this study. The recommendations for future work in the field of gasification to improve syngas heating value are highlighted. Further improvement on the catalytic activity of pumice and kaolin is also proposed.

## **2 LITERATURE REVIEW**

### **2.1 Biomass Gasification**

#### **2.1.1 Gasification Process**

The gasification process involves thermal conversion of carbonaceous fuel to gaseous products in a controlled environment. The feedstock undergoes drying where moisture content is driven off before being pyrolysed to evolve volatiles to produce char. Both char and volatiles are then partially oxidised with oxygen, air and/or steam to produce mainly carbon monoxide (CO), hydrogen (H<sub>2</sub>) and carbon dioxide (CO<sub>2</sub>). The latter reduces to CO when it comes in contact with hot carbon. Feedstock in the form of solid, liquid or gases such as coal, biomass, residue oils, natural gas and municipal waste can be employed within the gasification process.

With regard to environmental pollution from energy conversion systems, gasification has been proven to be a green technology for synthetic gas production. However, the lower limit of low heating value (LHV) for the feedstock material is suggested to be 7-8 MJ/kg [4]. This limitation dictates pretreatment of feedstock such as drying, pelleting and briquetting to qualify for use in the gasification process.

There are various thermal processes taking place during gasification including pyrolysis, combustion, cracking and reforming as illustrated in Figure 2.1. The quality of the product gas depends on the rate of pyrolysis and partial combustion processes in the reactor. Pyrolysis releases volatiles (>350 °C) which are mainly heavy hydrocarbons (tar), while partial combustion produces combustible gases and also generate heat to sustain the overall process. In order to attain clean product gas, these major conversion processes need to occur simultaneously. This can be achieved by increasing the rate of heating the fuel particles. Higher heating rates can be achieved by particle size reduction and minimisation of temperature gradient within the gasifier reactor.

During the gasification process various chemical reactions occur which are mainly dependent on operating conditions. These reactions take place in the reactor and some may occur in the gas downstream depending on the level of activation energy. Typical reactions for coal or biomass gasification are presented in Table 2.1.

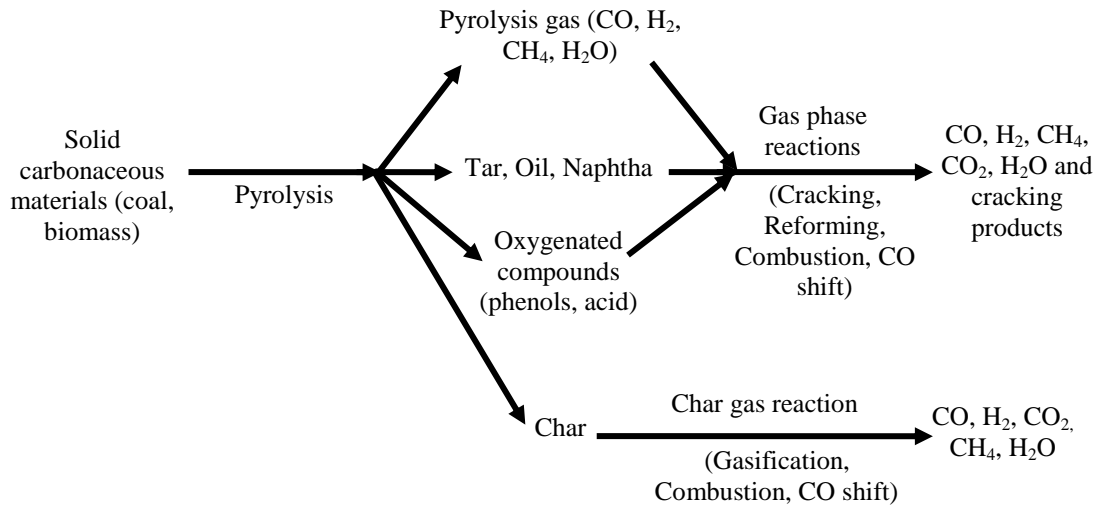


Figure 2.1 Reaction sequence for gasification of coal and biomass [4]

Table 2.1 Principle reactions in coal or biomass gasification process [4].

Reaction	Chemical Equation
Combustion	$C + \frac{1}{2}O_2 \rightarrow CO - 111 \text{ MJ/kmol}$ $CO + \frac{1}{2}O_2 \rightarrow CO_2 - 283 \text{ MJ/kmol}$ $H_2 + \frac{1}{2}O_2 \rightarrow H_2O - 252 \text{ MJ/kmol}$
Boudouard	$C + CO_2 \rightarrow CO + 172 \text{ MJ/kmol}$
Carbon gasification	$C + H_2O \leftrightarrow CO + H_2 + 131 \text{ MJ/kmol}$
Methanation	$C + 2H_2 \leftrightarrow CH_4 - 75 \text{ MJ/kmol}$
Water gas shift	$CO + H_2O \leftrightarrow CO_2 + H_2 - 41 \text{ MJ/kmol}$
Steam methane reforming	$CH_4 + H_2O \leftrightarrow CO_2 + 3H_2 + 206 \text{ MJ/kmol}$
Hydrogenation	$H_2 + COS \leftrightarrow H_2S + CO + 7 \text{ MJ/kmol}$
Hydrolysis	$COS + H_2O \leftrightarrow H_2S + CO_2 - 34 \text{ MJ/kmol}$

The chemistry of tar formation is complex. In an overview paper by Li and Suzuki [3] they reported that tar maturation occurs at increments of 100 °C starting from 400 °C. These stages in order of occurrence produce oxygenates, phenolic ethers, alkyl phenolics, heterocyclic ethers, polycyclic aromatic hydrocarbon (PAH), and larger PAH. The formed compounds are classified according to their property as shown in Table 2.2.

Table 2.2 Tar classification adapted from Li and Suzuki [3]

Class	Class name	Property	Representative compound
1	GC-undetectable	Very heavy tars that can not be detected by GC	Determined by removing the GC-detectable tar fraction from the total gravimetric tar
2	Heterocyclic aromatics	Tars containing hetero atoms; highly water soluble compounds	Pyridine, phenol, cresols, quinoline, isoquinoline, dibenzophenol
3	Light aromatic (one ring)	Single ring compounds: No problem regarding condensability and solubility	Toluene, ethylbenzene, xylenes, styrene
4	Light PAH compounds	2 and 3 rings compounds: Condenses at low temperature even at very low concentration	Indene, naphthalene, methylnaphthalene, biphenyl, acenaphthalene, fluorene, phenanthrene, anthracene
5	Heavy PAH compounds	Larger than 3-ring: Condenses at high-temperatures at low concentrations	Fluoranthene, pyrene, chrysene, perylene, coronene

Moreover, tar represented as  $C_nH_x$  decomposes to light hydrocarbons ( $C_mH_y$ ) through thermal cracking, as well as steam reforming, and dry reforming yielding CO and  $H_2$  as illustrated in Table 2.3. Tar reduction through thermal cracking require temperatures above 1100 °C [8]. These temperatures can be attained at the expense of preheating the gasifying agent [22] or burning part of the product gas.

Plasma gasification has been reported to generate gasification temperatures as high as 9,927 °C. Heat is generated between electrodes where high voltage is supplied. With this technology, tar in syngas was reported to be less than 4 % by volume, whilst gas yield is about 25 % more than conversional pyrolysis. However, the overall efficiency of the plasma gasification is as low as 6 % as a result of thermal and circuit losses amounting to about 30 % each [23].

Han and Kim [24] reviewed the development of gasification technologies for tar control and reduction. The review showed that tar can be extracted from the product gas by different combination methods of water scrubbing, cyclone, electrostatic precipitation (ESP) and rotational particle separator. However, the

technologies concentrate on either capturing or removal of tar from syngas, thus wasting inherent energy and substantially increasing the cost of the process.

Table 2.3 Tar cracking kinetic equations adapted from [25]

Process	Reaction
Thermal cracking	$pC_nH_x \rightarrow qC_mH_y + rH_2$
Steam reforming	$C_nH_x + nH_2O \rightarrow \left(n + \frac{x}{2}\right)H_2 + nCO$
Dry reforming	$C_nH_x + nCO_2 \rightarrow \frac{x}{2}H_2 + 2nCO$
Carbon formation	$C_nH_x \rightarrow nC + \frac{x}{2}H_2$

## 2.1.2 Factors affecting gasification process

### 2.1.2.1 Gasifier design

The design of the gasifier reactor affects the resulting gas quality in various ways including flow configuration and geometrical parameters. Gasification reactors can be grouped into six categories: downdraft, updraft, moving bed gasifiers, fluid-bed, entrained flow and swirl flow gasifiers. Although these gasifiers employ similar principals for fuel conversion, their performance and operations are different.

Downdraft and updraft gasifiers have a different principle of operation as illustrated in Figure 2.2. In updraft reactors, the product gas flows through the feedstock material for preheating purposes. Usually the product gas temperatures are low as a result tar concentration in the product gas is relatively high. Unlike the updraft reactors, the gas flow in the downdraft gasifier reactors ensures less tar in the gasification product gas. The product gas is drawn through the hottest part of the reactor, thus promoting tar cracking. In the moving bed gasifier as shown in Figure 2.3, the feedstock moves slowly under gravity as it is gasified. The operating temperature ranges from 425 to 650 °C usually at atmospheric pressure. With these low temperatures, the biomass is not used as feedstock due to the high tar yield which increases the cost of gas cleaning. The feed material size is between 6 and 50 mm, typically using coal as feedstock [4].

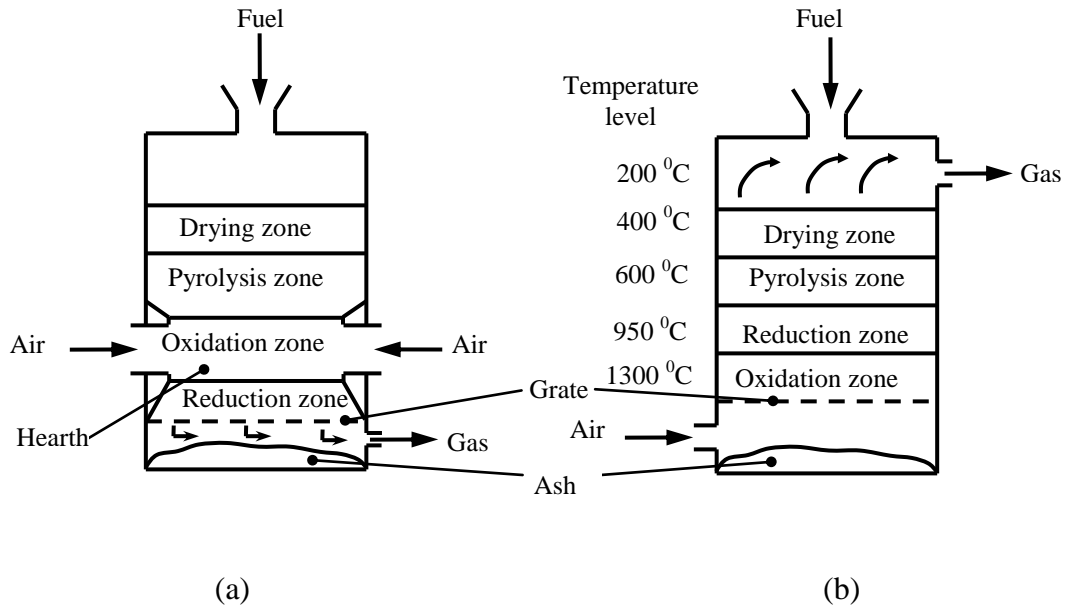


Figure 2.2 Schematic diagrams of (a) Downdraft gasification, and (b) Updraft gasification [26]

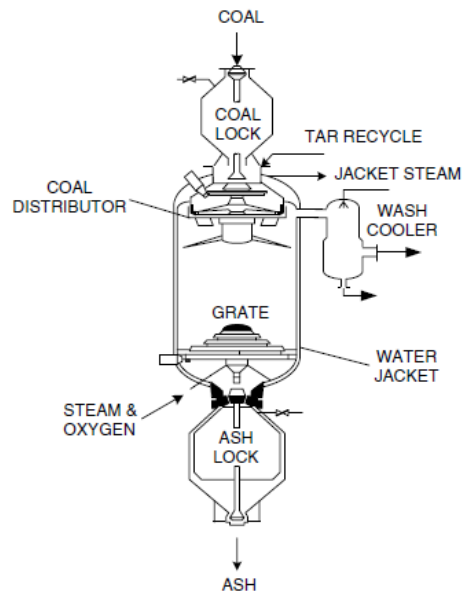


Figure 2.3 Moving bed gasifier reactor (Lurgi) [4]

The fluid-bed gasifiers suspend the materials providing good mixing with the gasifying agent as illustrated in Figure 2.4. It employs feed particles at a maximum size of 25 - 50 mm for biomass application with temperatures limited to 950-1100 °C for coal and 800-950 °C for biomass. At the low temperatures high tar content in the syngas is produced. This problem has been reduced by employing high slip velocity (5-8 m/s) to ensure good mixing of gas and feedstock hence promoting excellent heat

and mass transfer. The carbon conversion is 97 % compared to 99 % of a moving bed system [4]. However, as the residues such as unburnt carbon can be re-circulated, the control of the oxidising agent requires great attention.

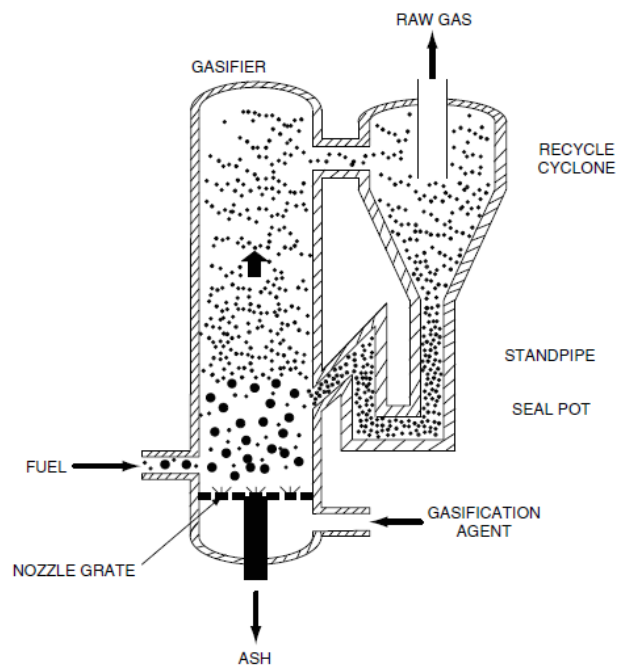


Figure 2.4 Schematic diagrams of a common circulating fluid-bed gasifier [4]

In the swirl flow (cyclone) gasifier, as in a circulating fluid-bed gasifier, the feed and gasifying agents are fed tangentially thus inducing vortex flow. Swirl flow enhances excellent mixing of the reactants, thus promoting excellent heat and mass transfer. The operating velocities range between 3 and 30 m/s with feedstock ranging from 5  $\mu\text{m}$  to 2 mm. Development of cyclone gasification has gone far to invert a principal flow and integrate a vortex collector pockets to improve particulate removal in the product gas. This new design is termed as an inverted cyclone gasifier (ICG). Although this innovation improved separation of alkalis metal such as Na and K by 50 % and burnout by 99 %, further work is required to reduce particle carry-over in the product gas [27]. A typical cyclone gasifier is shown in Figure 2.5 while the inverted cyclone gasifier Figure 2.6.

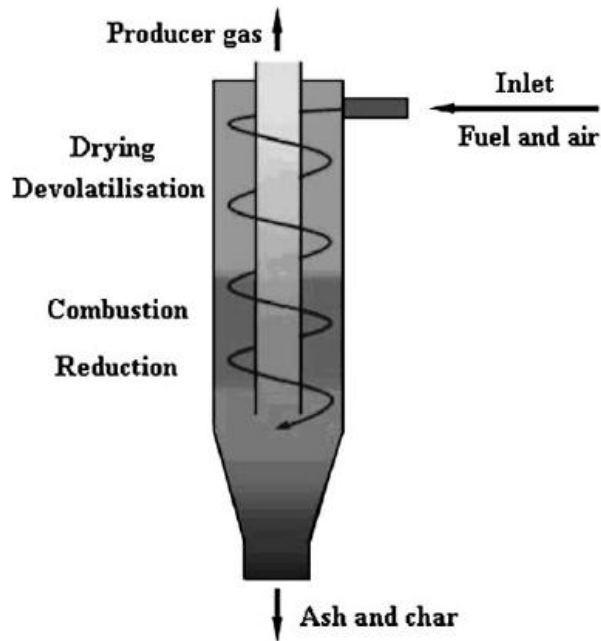


Figure 2.5 The schematic diagram of cyclone air gasification [28]

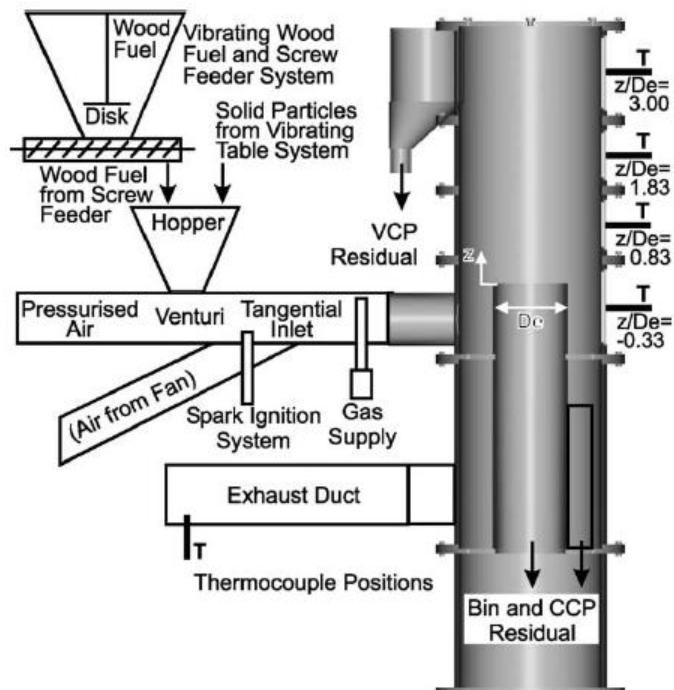


Figure 2.6 The schematic diagram of the innovated cyclone gasifier [27].

Gasification process can also be achieved using entrained flow gasifiers. These reactors have been shown to be more efficient, producing less tar in the gas stream with ash being trapped as inert slag. However, this performance depends on the working temperatures employed. As this reactor is of interest in this study, more details are provided in Section 2.1.3.

### 2.1.2.2 Feedstock

The chemical properties of biomass as a feedstock are important in establishing gasification operating conditions. This characterisation involves proximate analysis where moisture content, ash, volatiles and fixed carbon as well as heating value are determined. Further analysis takes account of inherent elements such as C, H, O, S, N and other trace elements. A typical analysis of biomass is provided in Table 2.4. It can be concluded that biomass is composed of heterogeneous constituents. Moreover agricultural biomass contains more trace elements than forestry biomass. However, in the comparison made, a significant difference in element contents was observed which imply that biomass composition could be different from one site to another.

Table 2.4 Typical analysis of biomass composition [6, 29-31]

Proximate Analysis		Trace Elements (ppm)			
Moisture content (wt %)	6-10	As	0-5	Ti	10-214
Ash (wt % db)	1-15	Ba	0-125	V	0-9
Volatile matter (wt %)	61-76	Cd	0-1	Zn	11-162
Fixed carbon (wt %)	13-21	Co	0-9	Al	19-5001
Calorific value (MJ/kg)	16-20	Cr	2-23	Si	1-46000
		Cu	1-128	Ca	650-23301
Ultimate Analysis (wt %)		Mn	17-1052	Mg	160-7613
C	38-58	Mo	0-7	Fe	26-4867
H	5-8	Ni	0-60	K	400-25000
O	32-47	Pb	1-86		
S	<0.4	P	75-2900		
N	0-2	Na	24-3497		

Furthermore, the presence of chlorine in feedstock results in the consumption of H<sub>2</sub> generated as it reacts to form HCl. High nitrogen content leads to the formation of ammonium chloride which causes corrosion to plant equipments. Additionally, chlorine can foul the heat exchanger within gasification temperature range [32, 33].

Many researchers have studied the influence of the feedstock particle size on the gasification process. Marsh *et al*, [6] conducted an experimental study on compressive strength of wood, paper and refuse derived fuels (RDF) pellets 50 mm diameter. The pellets were exposed to a temperature of 800 °C and different residence time prior to cooling. The results showed that the compression strength of the pellets decreased significantly as a result of devolatilization, thus disqualifying the size for gasification process.

Another study by Tinaut *et al*, [34] revealed that particle diameter decrease by approximately 30 % during oxidation and diminishes more slowly during gasification of char. Further observation deduced that the particle size was inversely proportional to the rate of gasification and had no influence on the maximum temperature. However, this study was limited to biomass feedstock with a diameter of 4 mm, 9 mm and 15 mm. Moreover, the advantages gained over the smaller particle size are high gas quality, yield as well as gasification efficiency [35, 36]. This finding was based on biomass particle sizes ranging between 0.10 mm and 1.20 mm.

### **2.1.2.3 Gasifying agent**

A gasifying agent is the fluid used to oxidise the biomass during the gasification process. These oxidants include pure oxygen, air and steam which can be employed individually or in a combination. While the oxygen or air oxidants offers more CO, steam reforming favours H<sub>2</sub> production during gasification process. In pneumatic fuel feed system, higher flow rates are required to enhance particle transport. These operating conditions can be achieved easily with air compared to pure oxygen due to high mass per mole.

### **2.1.2.4 Equivalence ratio**

Equivalence ratio (ER) is a dimensionless parameter describing the proportion of the actual air-fuel ratio to the stoichiometric condition and gives an indication of the type of thermal conversion taking place. Depending on the combustion environment, the products are highly influenced by equivalence ratio. Findings from the previous researches show that an optimal ER range between 0.2 and 0.25 for biomass gasification [37-39].

### 2.1.2.5 Temperature

Many researchers have investigated the effect of temperature on gasification product gas. Zang *et al* [8] conducted an experimental study on tar destruction and coke formation during rapid pyrolysis and gasification of biomass in a drop tube furnace in the temperature range of 600 to 1400 °C. The results showed that tar concentration decreased with increasing temperature from 900 to 1200 °C. However, benzene and toluene derivatives were detected in significant amounts. A similar finding was reported by Phuphuakrat *et al* [40] in the gasification of dried sewage sludge. Another study by Gang *et al* [22] revealed that increasing gasification temperature increases the heating value of syngas as a result of increasing H<sub>2</sub> and CO. This correlation was a maximum at the temperature range of 1200 to 1300 °C.

Although higher temperatures improves gasification product gas, achieving these temperatures require additional heat through either preheating the gasifying agent or increasing the equivalence ratio. While the latter results in the consumption of combustible gases, the former requires additional component for preheating. Another possible approach to improving syngas quality is through catalytic processing. With catalysts, tar conversion to useful gases such as CO, H<sub>2</sub> and CH<sub>4</sub> can be achieved at temperatures as low as 350 °C [41, 42].

### 2.1.2.6 Pressure

A central problem in operating at higher pressure during gasification is the energy required to reach the required value. On one hand, Higman and Burgt [4] reported that increasing pressure to 100 bar in the gasifier increases energy content of the syngas as a result of CH<sub>4</sub> increase. On the other hand, CO and H<sub>2</sub> decrease as a result of increase in oxygen which oxidises H<sub>2</sub> and CO to form H<sub>2</sub>O and CO<sub>2</sub> respectively, thus causing low gas yield. While at pressures above 30 bar carbonyl is formed, CO reacts with water to form formic acid hence increasing cost of gas cleaning up. Moreover, higher operating pressures require complex equipments such as valves, fluidising systems and compression of fluidising gases. Furthermore, as the resulting product gas is toxic, it makes such system difficult to commercialise in especially rural areas where safety awareness issues are limited.

### 2.1.2.7 Residence time

In the gasification process, the residence time is the time required for the fuel particle to completely convert into combustible gases. There are several factors affecting the time including temperature, particle size and reactor design [43, 44]. While the residence time decreases with increasing operating temperatures, decreasing particle size enhances fuel conversion, thus reducing gasification time. The correlation between devolatilisation time and particle size of a wood fuel can be expressed using Equation 2.1 [45].

$$\tau = 2.673d_p^n \quad (2.1)$$

Where  $n = 1.02e^{233/T}$ ,  $d_p$  and  $T$  are diameter (mm) of particle and temperature (K) respectively.

Reactor design affects the particle residence time in the gasifier reactor depending on the flow configuration [43]. It is well known that particle transport is associated with several forces including gravity. Therefore, down-flow could result in short residence times compared to the horizontal and up-flow types. Although residence time can be increased by decreasing feed flowrate, the overall gas output is also reduced accordingly. Thus, combinations of these factors are important in generating syngas with high energy content.

### 2.1.3 Entrained-flow gasifiers

Biomass gasification has been achieved through different reactor designs including entrained-flow types. Entrained-flow gasifiers (EFG) have been used successfully for coal gasification since 1950. The majority of these gasifiers are of a slagging type and operate at higher pressures. Typical operating pressure range from 20-70 bar and temperatures are above 1400 °C. Although the elevated conditions ensure high fuel conversion and destruction of tar, the conditions are achieved at the expense of high oxygen consumption, as well as needing an efficient heat recovery system. On the other hand, gasification at atmospheric pressure is also possible. For atmospheric gasification conditions, the feed mechanisms are of the premix type and

operate at high velocity to avoid flash back. High velocities lead to increased syngas yield.

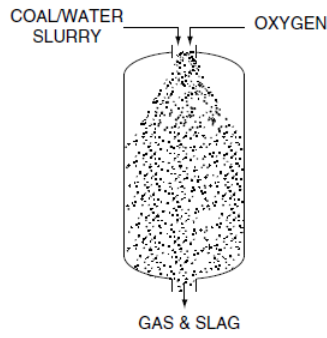
There are various criteria for classifying entrained flow gasifiers including the flow configuration. The common designs are down-flow and up-flow reactors. In both designs, the fuel feedstock and oxidising agents (usually oxygen and steam) are introduced into a reactor in co-current flow as shown in Figure 2.7. The down-flow configuration is intended to improve slag separation and makes gravity fuel feed possible [46, 47]. However, owing to the short space residence time of the fuel particles, the length of the gasifier is crucial in attaining efficient fuel conversion. While a shorter reactor may result in poor fuel conversion, a longer reactor is associated with increased energy production cost.

On the other hand, the up-flow reactor is mainly characterised by large recirculation resulting from temperature differences, thus increasing particle residence time. This increase results in improved fuel burn-out and syngas quality. However, with excessive recirculation zones, caution must be applied, as the reverse flow may cause flash back.

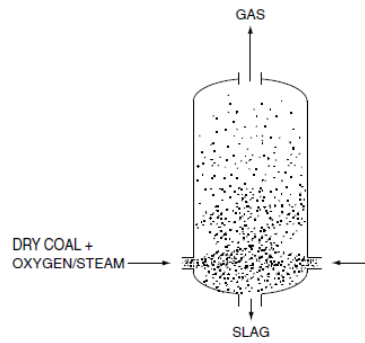
Recent developments in the field of entrained-flow gasification have led to an interest in using biomass as the fuel feedstock. This arises from its higher reactivity compared to that of coal. A number of research studies have been carried out on entrained flow air gasification at non-slagging temperatures (~700-1100 °C) [38, 43, 48]. In most cases, the gasifier reactor has been configured vertically employing a down flow regime as highlighted in Table 2.5. Although this configuration improves particulate separation from the product gas, more heat and manufacturing materials are required due to long gasifier reactors (1200 – 2000 mm). Moreover, the heating value of the product gas has been reported to be below 6.0 MJ/Nm<sup>3</sup>.

Table 2.5 Typical geometrical parameters of the entrained-flow gasifier reactors

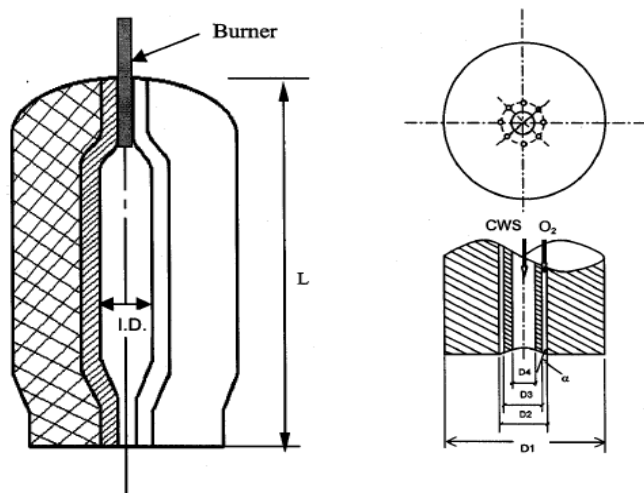
Reference	Configuration	Length (mm)	Diameter (mm)	Temperature (°C)
[44]	Top-down	1200	75	750-1250
[49]	Top-down	2000	255	1200
[50]	Top-down	2000	80	1000-1350
[38, 43, 48].	Top-down	1200	60	1050
[38, 43, 48].	Top-down	1900	100	700-1000



(a) Down-flow EFG [4]



(b) Up-flow EFG [4]



Gasifier (mm)		Burner (mm)			
I.D	Length	D <sub>1</sub>	D <sub>2</sub>	D <sub>3</sub>	D <sub>4</sub>
200	1000	60	13.28	12	3

(c) Typical geometrical parameters of EFG [51]

Figure 2.7 Schematic diagrams for typical entrained flow gasifiers

## **2.2 Catalytic Processing of Gasification Product Gas**

### **2.2.1 Catalysis overview**

Catalysis is the study of catalytic reactions. These reactions occur in cyclic processes where the reactants are bound to one form of the catalyst and the products are released from another after the reaction. Most industrial catalysts are either liquid (homogeneous) or solid (heterogeneous). Catalytic reactions are widely employed in industrial processes such as purification of crude oil, production of chemicals, emissions control and of particular interest, biomass gasification.

In gasification processes, heterogeneous catalysts are widely employed due to their ability to resist higher operating temperatures. The use of catalysts is aimed at enhancing syngas quality in terms of heating value and to reduce impurities. The major impurities in this perspective are heavy hydrocarbons (tar), unwanted side products and trace elements. The former is more critical in biomass gasification compared to the others. Cracking of hydrocarbons depend on several factors which can be explained from the individual steps of catalytic reactions [52]. Various catalysts have been tested in gasification processes as reviewed in Section 2.2.4.

### **2.2.2 Steps in heterogeneous catalytic reactions**

Catalytic reactions in heterogeneous catalysts involve individual steps which are purely physical and chemical. The chemical reactions take place when the reactants are in contact with the active sites. The transport of reactants to the active sites is promoted by physical processes namely: diffusion, adsorption and desorption. Typical steps for heterogeneous catalysts are [53]:

- (i) Diffusion of the feed materials to the surface of the catalyst.
- (ii) Diffusion of the feed materials into the support pores.
- (iii) Adsorption of the reactants on the inner surface of the pores.
- (iv) Chemical reaction on the catalyst surface.
- (v) Desorption of the products from the catalyst surface.
- (vi) Diffusion of the products out of the pores.
- (vii) Diffusion of the products from the catalyst surface.

Of particular importance, is the enhancement of the chemical reactions occurring on the catalyst surface. This process depends on the adsorption of the reactants and desorption of the products. The rate of adsorption increases with

increasing reactor temperature. Therefore the catalytic reactor's temperature needs careful control to protect the reproducibility of the experiment.

### **2.2.3 Factors affecting catalyst performance**

Most heterogeneous catalysts lose activity during the catalytic process. The common causes of loss of catalytic activity are fouling, poisoning, sintering, attrition and loss due to vaporisation of active sites.

Fouling and poisoning cause similar effects on catalyst performance. Fouling refers to a physical coverage of active sites by either trace materials in the feed or the feed materials. These foreign materials can undergo chemical adsorption (chemisorptions) to form a strong adsorptive bond with the catalyst surface, thus covering the active sites. This chemical effect is referred to as catalyst poisoning. In biomass gasification, catalyst poisoning is caused by the deposition of carbon (coking). Carbon deposits on catalysts originates from hydrocarbons contained in the producer gas and the by-products formed during the catalytic reaction. Coking of catalyst depends on the oxygen storage capacity (OSC). OSC is the ability of the catalyst to absorb and release oxygen at elevated temperatures [54]. Increasing OSC in a catalyst can reduce the coking problems through oxidation process. Moreover, a deactivated catalyst can be regenerated by a controlled combustion of the carbon layer.

Sintering is a result of a change of crystallite size of the active sites due to the fusion of particles at higher temperatures. Atoms of any material become mobile and coalesce when heated above the Tamman temperature (defined as half of the material melting point, in Kelvin) [55, 56]. Increased sintering results in the loss of active surface area, thus, decreasing the catalyst activity. Therefore, the use of catalyst supports with high thermal stability is recommended.

Attrition is a breakup of the catalyst into fine sizes as a result of particle to particle or particle to wall collisions in the fluid-bed reactors. The generated fines can be carried-over with the gas stream or cause blockages. Although supported catalysts in fixed beds are stationary, high abrasion resistance is required to avoid loss of active sites due to attrition.

Another factor that affects the performance of a catalyst is the loss due to evaporation of active sites. This loss is mainly caused by higher operating temperatures of a catalytic reactor. One might be tempted to go for lower

temperatures, but, lower temperatures can lead to formation of toxic compounds. For instance, at temperatures below 150 °C, nickel catalysts deactivate by forming a highly toxic nickel tetracarbonyl in the methanation of synthesis gas [53]. This implies that, apart from losing the required chemical reaction, poor control of the process temperature may yield unwanted products.

#### **2.2.4 Catalytic oxidation of hydrocarbon compounds**

Catalytic oxidation of hydrocarbons involves addition of an oxygen atom to cause selective oxidation or complete combustion. While the complete combustion results in water and carbon dioxide, selective oxidation produce several by-products such as syngas, alcohols, aldehydes and ketones [57, 58]. Further oxidation of alcohols can lead to formation of carbonyl compounds while aldehydes and ketones form acids. These reactions are mainly controlled by free-radical co-oxidation [59].

On the other hand, major aromatic compounds such as benzene, toluene and naphthalene found in biomass gasification tar can be oxidised at lower temperatures using catalysts with reduction oxidation (redox) characteristics. For instance, benzene-air and toluene-air mixtures can be oxidised to CO<sub>2</sub> and H<sub>2</sub>O over redox catalyst (Ce<sub>0.5</sub>Zr<sub>0.5</sub>O<sub>2</sub>/Al<sub>2</sub>O<sub>3</sub>, CeO<sub>2</sub>/Al<sub>2</sub>O<sub>3</sub>) at 350 °C and gas hourly space velocity (GHSV) of 40,000 h<sup>-1</sup> [9, 60]. Another study on naphthalene oxidation over ceria at temperatures ranging 100 to 350 °C revealed that naphthalene was completely oxidised to CO<sub>2</sub> at 350 °C [61]. In this study, the feedstock was composed of naphthalene at 450 vppm, 20 % O<sub>2</sub> and 80 % Helium by volume, while the GHSV was ranged from 20,000 to 75,000 h<sup>-1</sup>. Similar findings have been reported when air was employed as the carrier gas for naphthalene oxidation over ceria catalysts [41, 42]. On the other hand, oxygenated compounds such as phenols are easily oxidised at lower temperatures compared to aromatic compounds. Phenol oxidises readily over CeO<sub>2</sub>/Al<sub>2</sub>O<sub>3</sub> catalyst at temperature around 180 °C [62].

Copper (II) oxide (CuO) is another catalyst used for oxidation of hydrocarbons. CuO oxidises benzene, toluene and naphthalene with air as the carrier gas at temperatures around 350 °C and GHSV between 20,000 and 60,000 h<sup>-1</sup> [63-65]. The use of CuO for CO and H<sub>2</sub> oxidation has been reported elsewhere [66]. The temperatures required for these reactions are similar to those of hydrocarbons. Therefore, the overall reaction depends on the adsorption capacity of the reactants on the catalyst surface.

Catalysts such as CeO<sub>2</sub>, CuO and NiO catalyst have found great applications in catalytic converters owing to the high capability in promoting redox reactions [67, 68]. Additionally, the oxides promote not only the water-gas shift reaction and steam reforming, but also control the oxygen levels in the gas stream as they can switch between different oxidation states. For instance the oxidation states of cerium are Ce<sup>4+</sup> and Ce<sup>3+</sup> [69]. Similarly, copper exists as Cu<sup>0</sup>, Cu<sup>+</sup> or Cu<sup>2+</sup> while nickel is Ni<sup>2+</sup>, Ni<sup>3+</sup> and Ni<sup>4+</sup> [70-72]. These features suggest that redox catalysts can be employed for partial oxidation of hydrocarbons present in the syngas. However, the presence of other gas species such as H<sub>2</sub>, CO and CO<sub>2</sub> and other complex hydrocarbons from a real gasification process can affect the catalyst selectivity, therefore, an investigation of their effect is important.

### 2.2.5 Catalyst supports

Catalyst supports are usually employed to enable the formation of catalyst particles that are held relatively immobile and thus cannot coalesce. There are important criteria for selecting a catalyst support. The desirable features include: inertness, resistance to attrition, high surface area, porosity and low cost. Based on these criteria, only alumina, silica and activated carbon can be used as catalyst support. However, their cost is relatively high compared to natural occurring pumice. Another catalyst support material is kaolin. Kaolin is a clay mineral composed of mainly silica and alumina. Although these materials suffer attrition, its high alumina content suggests possession of thermal stability and can be utilised in gasification process. Other researchers have used kaolin in fluidised bed gasification to reduce alkali metals in the syngas as it can react to form alkali-silicate. The resulted silicate has higher melting point, thus ensuring stable operations [73].

Previous studies have proved the viability of doping pumice with transition metals to improve catalytic selectivity [74, 75]. The formation and characterisation of pumice have been reported elsewhere [76-78]. The generalisation of this overview has shown that pumice possesses excellent properties as a catalyst support. The major beneficial features of pumice include comparatively high porosity which ensures low pressure drop in packed bed reactors [79, 80]. It also maintains thermal stability to about 900 °C due to its high silica and alumina content [81]. The presence of alkali compounds or metal oxides on support materials can have a promoting

effect on syngas reactions. These oxides can be dispersed over the support surface using impregnation.

In Tanzania pumice deposits are found in Langijave (Arusha), Holili (Kilimanjaro) and Rungwe (Mbeya) as illustrated in Figure 2.8. Pumice deposits at Langijave, Holili and Rungwe originates from Mount Meru, Kilimanjaro and Rungwe volcano respectively. Kaolin deposits are found at Pugu Hills in the Coastal region of Tanzania as well as in Chimala (Mbeya) and Malangali (Iringa). In most cases, pumice is used as aggregate for production of light weight concrete. Other uses of pumice include abrasive and polishing materials, filter and landscaping. Although pumice has shown possession of good properties as a catalyst support, information on its use in biomass gasification is very limited.



Figure 2.8 Map of Tanzania showing locations of pumice and kaolin deposits [82]

### **2.2.6 Preparation and characterisation of supported metal catalysts**

Supported catalysts are often used in gas-phase reactions owing to high dispersion of active surface with high thermostability of the catalytic component. These catalysts are usually prepared by precipitation and impregnation methods [83]. The precipitation involves mixing the metal salt solution with the catalyst support. Enough alkali solution is then added to cause precipitation and the catalyst is dried to remove water. Further treatments include calcination to decompose the metal salt and where necessary, reduction to metal is carried out.

Catalyst preparation using impregnation method involves filling the pores of the support with the solution of metal salt. The support is then dried to remove embedded liquids followed by calcining to decompose the metal salt. The resulting oxide can be reduced to metal depending on the application of the catalyst. The concentration of the metal catalyst over the support can be increased by carrying out several successive impregnations. Another approach is to increase the strength of the impregnation solution to increase the number of pores containing crystallites [83]. Impregnation method is usually applied to the preformed catalyst support including porous materials, an example of which is pumice.

Characterisation of supported catalysts can be achieved in different ways. There are three main characteristics to be determined in terms of (i) support properties, (ii) metal dispersion and location, and (iii) nature of active component. These properties can be determined using a range of methods and equipments as summarised in Table 2.6. Although all properties are important, the state of catalyst is crucial during reforming reactions.

Table 2.6 Properties and characterisation methods of heterogeneous catalysts [84, 85]

Category	Properties	Analysis Methods	Application
Catalyst support	Total surface area	BET method	<ul style="list-style-type: none"> <li>• Monitor the activity and stability of catalysts</li> </ul>
	Porosity and Pore structure	Natural stone method, Nitrogen isotherms	<ul style="list-style-type: none"> <li>• Modeling pore diffusion and film-mass transfer resistance</li> </ul>
	Thermal stability	Thermogravimetric analysis (TGA)	<ul style="list-style-type: none"> <li>• To establish working temperature limits</li> </ul>
	Surface chemical properties	XPS analysis	<ul style="list-style-type: none"> <li>• Determine the oxidation state of supports</li> </ul>
Metal dispersion	Metal area	BET method	<ul style="list-style-type: none"> <li>• To determine catalyst coverage</li> </ul>
	Crystallite size	SEM	<ul style="list-style-type: none"> <li>• Determine catalyst crystallite sizes</li> </ul>
	Concentration	XRD, ICP-OES, XRF	<ul style="list-style-type: none"> <li>• Determine catalyst loading</li> </ul>
Nature of active component	Oxidation state	XPS, XRD	<ul style="list-style-type: none"> <li>• Examine oxidation state of the catalyst</li> </ul>

BET = Brunauer Emmett Teller  
 ICP-OES = Inductive Coupled Plasma-Optical Emission Spectroscopy  
 TGA = Thermo Gravimetric Analysis  
 XPS = X-ray Photoelectron Spectroscopy  
 XRD = X-Ray Diffraction  
 XRF = X-Ray Fluorescence

### 2.2.7 Catalyst screening

There are two main criteria used for evaluating the suitability of a catalyst for a particular application. These criteria are activity and selectivity. Activity refers to a measure of reaction rate promoted by the catalyst. In practice the activity is determined in different ways [53]:

- (i). Conversion under constant reaction conditions. Conversion  $X_F$ , is used to express a fraction of the feed materials that has reacted to the initial amount and is determined using Equation 2.2.

$$X_F = \frac{n_{F,0} - n_F}{n_{F,0}} \quad [\text{mol/mol or \%}] \quad (2.2)$$

Where  $n_{F,0}$  and  $n_F$  are number of moles of the feed and product materials respectively.

- (ii). Space Velocity (SV) or Gas Hourly Space Velocity (GHSV) for a given constant conversion. SV is a ratio of the volume flow rate of the fluid ( $\dot{V}_o$ ) passing through a catalytic reaction space to the volume (or mass) of the catalyst ( $V_{cat}$  or  $m_{cat}$ ) through which the fluid passes. This term is also used to describe the condition at which catalytic processed was carried out. It is determined according to Equation 2.3.

$$SV = \frac{\dot{V}_o}{V_{cat}} \text{ or } SV = \frac{\dot{V}_o}{m_{cat}} \text{ [h}^{-1} \text{ or m}^3/\text{kg s]} \quad (2.3)$$

- (iii). Space-Time Yield (STY). STY is the quantity of product formed per unit time per unit volume of the reactor for a given feed rate. This parameter is used for comparing the performances of different catalytic reactors based on the catalyst mass or volume. It is determined using Equation 2.4.

$$STY = \frac{\text{Desired product quantity}}{\text{Catalyst volume} \cdot \text{Time}} \text{ [mol L}^{-1} \text{ h}^{-1}] \quad (2.4)$$

- (iv). The ability of the catalyst to resist coking caused by the gasification product gas can be used to determine the catalyst activity. This is determined by quantifying the amount of carbon deposited for a given variable parameter [86-88].

Selectivity is a measure of a catalyst performance in converting the feed materials to the desired product. For catalytic screening the reaction conditions of the temperature and space velocity are kept constant. Selectivity is determined based on stoichiometric coefficients of the catalytic reactions [53]. As the catalytic reactions of the gasification product gas are complex, the process can be treated as independent of the stoichiometric coefficients. Different researchers have determined catalyst selectivity to carbon-containing gases as the ratio of an individual gas to their sum in the product gas [89-91]. For  $H_2$ , the selectivity has been expressed as the

ratio of moles of H<sub>2</sub> produced to the product of the carbon atoms in the gas phase and the H<sub>2</sub>/CO<sub>2</sub> ratio [92].

## **2.3 Modeling in Gasification and Catalysis**

### **2.3.1 Background**

Modeling of a gasification process considers mainly the feedstock composition, the thermodynamics of the process and the product gas composition for given operating conditions. Gasification modeling provides guidance before manufacturing a prototype and during plant operation. Normally the inputs needed for gasification trials are feedstock properties, temperatures, feed rate of the fuel and gasifying agents. The former is obtained through proximate and ultimate analyses. Similarly, modeling provides detailed information of the complex catalytic reactions in industrial processes, an example of which is gasification. Various gaseous reactions using solid catalysts can be modeled using the major influencing factors including temperature and concentration of reactants as well as the active sites.

There are various gasification and catalytic reaction modeling tools available including ANSYS FLUENT software. This software consists of a number of combustion models that can be employed for gasification predictions. Among these models are Non-Premixed, Partially Premixed and Premixed Combustion. The suitability of each model depends on the reactor design and the operation conditions. The software also has two other useful functions: a Discrete Phase Model (DPM) and a Species Transport model. The former can be incorporated to study the thermodynamics of fuel particles. The latter is employed in predicting catalytic reactions. As the entrained flow gasifier reactors operate in partially premixing mode, Partially Premixed Combustion, DPM and Species Transport models are discussed in the following sections.

### **2.3.2 Partially Premixed Combustion Model**

The Partially Premixed Model solves a transport equation for the mixture of fuel and oxidizer. This mixture is composed of a mass of fuel  $f$  and the balance  $(1 - f)$  is the mass of the oxidiser. The specie fractions of the reactants and products as well as the process temperature are determined using density weighed mean scalars  $\bar{\phi}$ . These scalars are calculated from the probability density function (PDF) of fuel  $f$  and flame position  $c$  as per Equation 2.5.

$$\bar{\phi} = \int_0^1 \int_0^1 \phi(f, c) p(f, c) df dc \quad (2.5)$$

Where  $c = 0$  for unburnt mixture (i.e. reactants) and  $c = 1$  for burnt mixture (i.e. products)

The partially premixed model requires laminar flame speed which depends on composition (equivalence ratio), temperature and pressure of the reactants. The chemistry calculations and PDF integrations for the burnt mixture are performed in ANSYS FLUENT software. Properties such as density, temperature, specific heat and thermal diffusivity of reactant mixture are fitted to a third-order polynomial of mean mixture fraction ( $\bar{f}$ ) using linear least squares Equation 2.6.

$$\bar{\phi}_u = \sum_{n=0}^3 c_n \bar{f}^n \quad (2.6)$$

### 2.3.3 Discrete Phase Model

The discrete phase model can be used to study the characteristics of wood particles under gasification conditions. The model predicts the trajectory of a discrete phase particle by integrating the force balance on the particle. This force balance equates the particle inertia ( $\frac{du_p}{dt}$ ) with the forces acting on the particle as a result of interaction with the continuous phase, and can be expressed using Equation 2.7.

$$\frac{du_p}{dt} = F_D(u - u_p) + \frac{g_x(\rho_p - \rho)}{\rho_p} + F_x \quad (2.7)$$

Where  $F_x$  is the additional force due to acceleration (force/per unit particle mass) and  $F_D(u - u_p)$  is the drag force per unit particle mass and is determined according to Equation 2.8.

$$F_D = \frac{18\mu}{\rho_p d_p^2} \frac{c_D Re}{24} \quad (2.8)$$

Where,  $u$  and  $u_p$  are fluid phase and particle velocities respectively,  $\mu$  is the fluid viscosity,  $\rho$  is the fluid density,  $\rho_p$  is the density of the particle, and  $d_p$  is the particle diameter.  $Re$  is the relative Reynolds number which is defined using Equation 2.9.

$$Re = \frac{\rho d_p |u_p - u|}{\mu} \quad (2.9)$$

The dispersion of particles due to turbulence in the gas stream is usually predicted using a stochastic tracking model (random walk). This model takes into account the effect of instantaneous turbulent fluctuation of velocity on the particle trajectories.

### 2.3.4 Species Transport Model

The Species Transport model is used to predict both non-reacting and reacting gaseous flows. These flows can be through porous or non-porous materials. In heterogeneous catalysis modeling, porous materials are used to describe the catalyst support and packed bed reactors. Chemical reactions are solved based on local mass fraction of each species  $Y_i$  using a conservation Equation 2.10.

$$\frac{\partial}{\partial t} (\rho Y_i + \nabla \cdot (\rho \vec{v} Y_i)) = -\nabla \cdot \vec{J}_i + R_i + S_i \quad (2.10)$$

Where  $R_i$  is the net rate of production of species  $i$  by chemical reaction and  $S_i$  is the rate of creation by addition of dispersed phase.  $\vec{v}$ ,  $\rho$  and  $\vec{J}_i$  are averaged velocity, density and diffusion flux of species  $i$ .

Chemical reactions can be predicted using chemical kinetics. Kinetics is a tool used to describe the rate at which a chemical reaction occurs in relation to the process parameters such as concentration, pressure and temperature. In practice, chemical reaction rates are determined by energy needed to enable the reaction to proceed, usually termed the activation energy. This energy is mainly dependent on the temperature to which the reactants are exposed. The change of free energy during reaction determines the number of molecules to be converted.

In ANSYS FLUENT software, there are various kinetic models including the Arrhenius kinetic equation. The Arrhenius kinetic equation is widely employed in modeling temperature dependent reactions. The reactions can be treated as a single elementary step in a limited temperature range. In heterogeneous catalysis, there are several factors apart from temperature that affects the catalytic reaction. Some of these factors include (1) adsorption of reactants on the catalyst surface, (2) desorption of products from the catalyst surface, (3) catalyst loading and (4) the state of the active sites. According to Langmuir Adsorption Isotherms, adsorption can be described as associative, dissociative and competitive depending on the number of reactants [93]. The first two are ideally limited for single specie reactant, while the other two are an appropriate approximation for multiple species which is common in catalytic gasification reactions. For competitive adsorption, the rate at which species adsorb or desorb depends on the binding energy of the reactant as well as the concentration of the feed. The overall reaction rate taking into account the effect of temperature and concentration of active sites  $S_i$  can be determined using Equation 2.11 [94, 95].

$$k = Ae^{-E_a/RT} S_i \quad (2.11)$$

Where  $A$  = pre-exponential factor,  $E_a$ =Activation energy (kJ/mol),  $R$  = Universal gas constant, and  $S_i$  =Concentration of active site determined using Equation 2.12.

$$S_i = \rho_{site} Z_i \quad (2.12)$$

Where  $Z_i$  and  $\rho_{site}$  are surface site coverage and surface site density (kgmol/m<sup>2</sup>) of specie  $i$  respectively. Site density can be determined using Equation 2.13 [96].

$$\rho_{site} = \frac{\text{Concentration of active sites [mol]}}{\text{Number of volumes} \times \text{Specific surface area of support } \left[ \frac{m^2}{kg} \right]} \quad (2.13)$$

Where the specific area of the pumice particles ranging 1-8 mm is between 9 and 11 m<sup>2</sup>/g [97] and the number of volumes is the total number of particles of the total mass of support.

## 2.4 Summary

The literature review on biomass gasification and catalysis studies on syngas treatment has been conducted. The gasification process has been highlighted as well as the development of entrained-flow gasifier reactors employing biomass as a feedstock. Factors affecting the gasification process have been reviewed and measures to alleviate the shortcomings are presented. Other biomass conversion methods are also highlighted.

In catalysis studies, the types of catalysts for selective oxidation of hydrocarbons are described. Preparation and characterisation methods are described for the understanding of the experimental procedures. In addition, factors affecting the performance of catalysts are highlighted, as well as catalyst screening criteria. Furthermore, Pumice as catalyst supports has been described in detail. The modeling of gasification and catalytic processes using CFD software has been described. In both cases, appropriate models for predicting a particular process are highlighted. The overall review suggests that:

- (i) Biomass is an alternative fuel to fossil and can be gasified to produce green fuel. Effective biomass gasification process using air as gasifying agent can be achieved at temperatures ranging 800 °C to 900 °C. The corresponding equivalence ratio is between 0.20 and 0.25.
- (ii) Entrained flow gasifiers can be configured in different orientations to enhance fuel conversion.
- (iii) Pumice and Kaolin can be used as catalyst support. The former possess high surface area and the latter catalytic characteristic. Moreover, tar formation during gasification depends on the process temperatures. These compounds can be oxidised using metal oxides at temperatures as low as 350 °C.
- (iv) CFD modeling can be used to study the effect of orientation of the entrained-flow gasifier reactor to the overall gasification process.

The next chapter describes the materials and methods for characterisation studies.

### 3 MATERIALS AND METHODS OF CHARACTERISATION STUDIES

#### 3.1 Introduction

This chapter describes the materials and characterisation methods used in investigating the performance of the horizontal entrained flow gasifier and the effect of catalysts on the gasification product gas. Procedures used in characterising wood powder as fuel feedstock materials are provided. The chemical and physical properties of the feedstock were determined for establishing appropriate operating conditions such as air-fuel ratio, process temperatures, feedstock rate and others. Similarly, preparation and characterisation methods for various catalysts are described in detail. The selection of ceria ( $\text{CeO}_2$ ), copper oxide ( $\text{CuO}$ ), Nickel oxide ( $\text{NiO}$ ) and zirconia ( $\text{ZrO}_2$ ) as catalysts was based on their redox characteristics which promote partial oxidation and reduction of the gasification product gas.

#### 3.2 Characterisation of Sawdust

##### 3.2.1 Sample preparation

Commercial pine sawdust from a commercial supplier (Batleys) was prepared for characterisation according to BS EN 15413:2011 standard [98]. As received samples (typically 3 mm size), were reduced to pass a test sieve with an aperture of 250  $\mu\text{m}$  using a grinding mill as shown in Figure 3.1. The test samples were then dried at 90  $^\circ\text{C}$  in an oven for 16 hours. Following this, the samples were cooled to room temperature and stored in sealed bags.



(a) As received sawdust



(b) Wood powder

Figure 3.1 Feedstock samples

### 3.2.2 Proximate analysis

Proximate analysis expresses the properties of a particular fuel with regard to moisture, ash, fixed carbon, and volatile matter. These properties are important in assessing the characteristics of a particular fuel during combustion. The approach and methods used to determine individual properties are described as follows:

#### 3.2.2.1 Moisture content

The moisture content in the sawdust was determined according to BS EN 1477-3:2009 standard [99]. The analysis was conducted in triplicate to monitor the repeatability between the test samples. Three ceramic dishes with lids were pre-conditioned to remove moisture by heating at 105 °C for 2 hours in a drying oven and then cooled to room temperature in a desiccator. After cooling, the dishes and their lids were weighed to nearest 0.1 mg. After weighing the dishes, a minimum fuel sample of 1 g weighed to nearest 0.1 mg was spread evenly over the respective dishes and heated in the drying oven at 105 °C for 2 hours. Before removing the samples from the oven, the lids were replaced and the assemblies transferred to the desiccator for cooling to room temperature. The moisture content (MC) expressed in percentage was calculated according to Equation 3.1.

$$MC[\%] = \left( \frac{M_2 - M_3}{M_2 - M_1} \right) \times 100 \quad (3.1)$$

Where:

$M_1$  is the mass of the empty crucible and lid

$M_2$  is the mass of the crucible and lid and sawdust before heating

$M_3$  is the mass of the crucible, lid and residue after heating

#### 3.2.2.2 Ash content

Ash content is the measure of mass of the inorganic matter left after ignition of a fuel under standardised conditions [100]. The analysis was carried out in triplicate to monitor the repeatability between the test samples. Prior to combustion of the fuel samples, three empty ceramic dishes were preconditioned in the muffle furnace to remove volatile matter by heating to 550 °C for 2 hours. After conditioning, the dishes were cooled to room temperature in a desiccator and

weighed. Approximately 1 g of dried sawdust sample weighed to the nearest 0.1 mg was spread over each dish and then heated in the furnace at 550 °C for 2 hours to ensure complete combustion. The dishes with residues were then transferred to the desiccator, cooled to room temperature and weighed. The ash content (AC) on dry basis was calculated using Equation 3.2.

$$AC [\%] = \left( \frac{M_2 - M_3}{M_2 - M_1} \right) \times 100 \times \frac{100}{100 - M_{ad}} \quad (3.2)$$

Where:

$M_1$  is the mass of the empty crucible and lid

$M_2$  is the mass of the crucible and lid and sawdust before heating

$M_3$  is the mass of the crucible, lid and residue after heating

$M_{ad}$  is the mass fraction of moisture of the general analysis sample on wet basis, as percent

### 3.2.2.3 Volatile matter content

Volatile matter expresses the mass of the material loss, deducting that due to moisture, when a test sample is subjected to heat in the absence of air under specific conditions. Volatile matter normally consists of various hydrocarbons which affect burning characteristics of the solid carbonaceous fuel such as biomass. In this study, the volatile matter was determined according to CEN/TS 15148:2009 [101] standard procedure. Three fused silica crucibles with lids were preconditioned to remove volatiles by heating at 900 °C for 7 minutes and then cooled to room temperature in the desiccator. When cool, the crucibles with lids were weighed to the nearest 0.1 mg. A minimum sample of 1 g was then spread evenly over the respective crucibles and heated in a muffle furnace at 900 °C for 7 min. After this time, the crucibles with residues were cooled in the desiccator to room temperature and weighed. The net weight loss of the material was determined by subtracting the loss due to moisture content. The volatile matter (VM) content on dry basis was calculated using Equation 3.3. The analysis was carried out in triplicate to monitor the repeatability between the test samples.

$$VM[\%] = \left( \frac{M_2 - M_3}{M_2 - M_1} \right) \times 100 - M_w \times \frac{100}{100 - M_{ad}} \quad (3.3)$$

where:

$M_1$  is the mass of the empty crucible and lid

$M_2$  is the mass of the crucible and lid and sawdust before heating, in grams

$M_3$  is the mass of the crucible and lid and residue after heating

$M_w$  is the mass fraction of moisture in the sawdust as a percentage

$M_{ad}$  is the mass fraction of moisture of the general analysis sample on wet basis as a percentage

#### 3.2.2.4 Fixed carbon content

The solid residue left after the determination of volatile matter of the wood powder is known as fixed carbon (FC). This type of carbon is linked to the carbon-related reactions during gasification process as reported in Table 2.1. Increased fixed carbon content in the feedstock can reduce the rate of the fuel conversion in the gasifier reactor where combustion mechanism such as fragmentation and attrition are limited [102]. In this study, fixed carbon was calculated by difference using Equation 3.4.

$$FC [\%] = 100 - \text{Moisture content} (\%) - \text{Ash content} (\%) - \text{Volatiles} (\%) \quad (3.4)$$

#### 3.2.3 Calorific value

Calorific value is the specific energy of combustion of a unit mass of a substance combusted in oxygen. Calorific value is expressed as a gross calorific value or lower calorific value. The former gives the total energy released when water in the combustion products is in liquid state and the latter, vapour. In this work, a bomb calorimeter, Parr 6100 (Figure 3.2) from Parr Instrument Company was used to determine the gross heating value of the biomass feedstock according to BS ISO 1928:2009 [103] standard procedure. Prior to analysis, the bomb calorimeter was calibrated by three certified benzoic acid pellets. After calibration was completed, 1 g of sawdust was analysed in the bomb. This analysis was done in triplicate to monitor the repeatability between the fuel samples. The net calorific value was determined by using Equation 3.5 specified in [103].

$$q_{wv,net,m} = [q_{v,gr,d} - 206w_{H,d}]x(1 - 0.01M_T) - 23.05M_T \quad (3.5)$$

where  $q_{v,gr,d}$  and  $w_{H,d}$  represent the gross calorific value at constant volume in J/g and hydrogen content (% wt), of the moisture-free (dry) fuel respectively, while  $M_T$  is the total moisture content (% wt).



Figure 3.2 Bomb calorimeter (Parr 6100)

### 3.2.4 Ultimate analysis

Ultimate analysis involves determination of the elemental composition of a fuel. Most commonly, carbon, hydrogen, nitrogen, sulphur and oxygen (CHNSO) are measured in a particular fuel through complete combustion. These elements are important in determining an appropriate air-fuel ratio for the combustion or gasification process. Additionally, any catalyst activity depends on the concentration of poisoning elements in the feed an example of which is sulphur. In this study, ultimate analysis of pine sawdust was analysed in a CHNSO-IR spectrometry (LECO) analyser according to the BS 1016:1996 standard [104]. About 0.5 g of wood powder weighed to nearest 0.1 mg was spread evenly over the clean dry combustion boat. The sample was then completely covered with 0.5 g of aluminium oxide and loaded to the analyser.

### 3.2.5 Thermo gravimetric analysis (TGA)

Thermogravimetric analysis involves heating a test sample on a highly sensitive microbalance with a controlled temperature programme in a given atmosphere BS EN ISO 11358:1997 [105]. TGA investigates the relationship between decomposition rate and temperature by varying the temperature and measuring the mass loss. This analysis was conducted to establish the appropriate working temperatures in the gasifier and the catalyst reactor. In this study, 8.6 mg of the ‘as received’ sawdust was weighed to the nearest 0.01 mg and heated to 800 °C using a STA-780 series thermal analyser shown in Figure 3.3. Helium was used at a flow rate of 20 ml/min to ensure an inert environment while the heating rate was 10 °C/min. Mass change and temperatures were recorded at 1 second intervals using Picolog software.



Figure 3.3 Thermogravimetric analyser (STA-780 series)

### 3.2.6 Particle shape and size distribution

Particle size influences the gasification products as discussed in Section 2.4.1. Prior to particle grading, the ‘as received’ sawdust was ground to give a maximum particle size of 0.3, 0.5 and 1.0 mm. The determination of the particle size distribution for each sample was performed using the vibrating screen method according to the BS EN 15149:2010 [106] standard. To prevent the particles from agglomerating due to the moisture content, the bulk sample was dried in the oven at 100 °C for 16 hours. In ascertaining the repeatability of the measurements, three test

portions were prepared from the bulk preconditioned material. The sieve sizes employed in this study were 0.056 mm, 0.106 mm, 0.180 mm, 0.250 mm, 0.300 mm, 0.500 mm and 1.18 mm. For each subsample, 50 g of sawdust weighed to the nearest 0.01 g was spread on the top sieve and the sieving operation was fixed at a duration of 30 minutes.

The particle sizes were classified in ranges as below 0.056 mm, 0.056 mm to 0.106 mm, 0.106 mm to 0.180 mm, 0.180 mm to 0.250 mm, 0.250 mm to 0.300 mm, 0.300 mm to 0.500 mm, 0.500 mm to 1.18 mm and above 1.18. In each class, the respective mass of the collected sawdust was weighed and expressed as a fraction of the total mass. The median particle size distribution ( $d_{50}$ ) was determined by interpolating the points between the 50 % line on the cumulative distribution curve. The experimental error was determined by calculating the difference between the total mass of the test portion and the total mass of all fractions using Equation 3.6.

$$m_d[\%] = \left( \frac{M_s - M_f}{M_s} \right) \times 100 \quad (3.6)$$

Where  $M_s$  is the total mass of the test portion and  $M_f$  is the total mass of all fractions

Another analysis involved scanning fuel particles using a ZEISS scanning electron microscope (SEM). Sawdust test samples were spread over the holder with carbon background and then scanned at a magnification of 120. The electron high tension (EHT) was set at 25 kV while the working distance (WD) was 10.5 mm. This investigation was to identify the shape necessary for discrete phase modeling. The modeling approach was important to study the particle trajectories during injection and verify the operating parameters, specifically the air flow rate.

### **3.3 Characterisation of Pumice**

#### **3.3.1 Major and trace elements analysis**

The analysis of the major elements of the pumice was performed using ICP-OES, (PerkinElmer Optima 4300 DV) shown in Figure 3.4. Three samples of the powdered pumice were processed in an Anton Parr microwave digester to obtain the final samples for elemental analysis. 2 ml of 47-51 % HF was added to a 0.1 g test sample of pumice weighed to the nearest 0.1 mg and left for 16 hours to fully

dissolve. Another 6 ml composed of 32 % HCl and 70 % HNO<sub>3</sub> at 1:1 volume ratio, was added to each sample in a Teflon vessel before transferring into the digester. The microwave was programmed to digest the sample by heating to 200 °C at a ramp rate of 15 °C/min and held for 30 min. After cooling, the HF acid in the digestate was neutralized by adding 12 ml of 4 % boric acid and reheated to the previous temperature in the microwave ramped at 5 °C/min and held for 15 min. Finally, the deionised water was added to the solution to make 50 ml in a plastic bottle for loading to the ICP-OES. The targeted elements were phosphorous, silicon, titanium, aluminium, iron, manganese, magnesium, calcium, sodium and potassium [107].



Figure 3.4 ICP-OES analyser (PerkinElmer Optima 4300 DV)

The trace elements in the pumice were determined using X-ray Fluorescence (XRF), (InnovXsystem X-50) shown in Figure 3.5. A minimum weight of 2 g of the powdered pumice was spread over an ultralene film, 4 µm thick and 64 mm diameter. Prior to analysis, the XRF analyser was calibrated using standard 316 specimens. A Soil 3 Beam method was employed to detect trace elements in the test sample. The method utilizes 3 beams with voltage levels at 50, 35 and 15 kV respectively. These voltages were chosen to detect the elements commonly found in minerals. The final results were averaged from all 3 beams and expressed in parts per million (ppm).

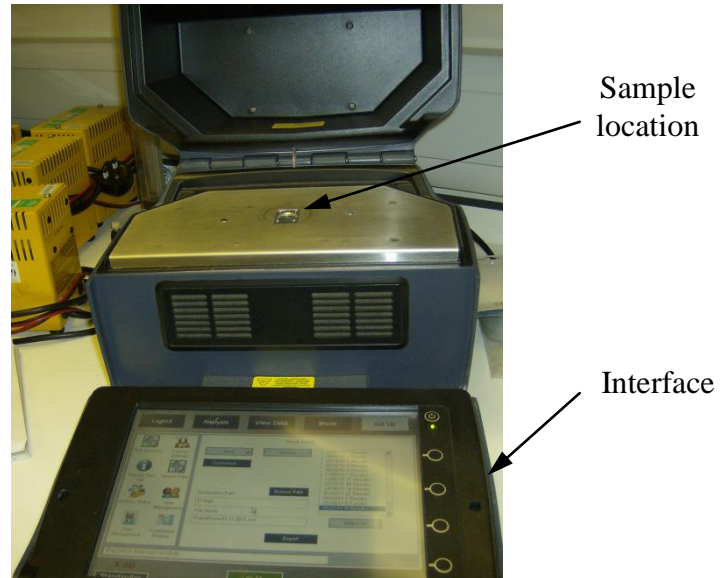


Figure 3.5 XRF analyser (InnovXsystem X-50)

### 3.3.2 Thermogravimetric analysis

The purpose of thermogravimetric analysis has been partially described in Section 3.2.6. In addition, the analysis provides information on the thermal stability of the material at the elevated temperatures, typically used in gasification and catalysis processes. Unlike the common equipment used for sawdust, the mass loss of the pumice samples was determined using a muffle furnace. The equipment allows for a larger sample size compared to the standard thermogravimetric analyser (TGA), thus increasing the accuracy of the measurements. Three samples weighing 1 g measured to nearest 1 mg were heated in a furnace for 1 hour at discrete temperatures ranging from 200 to 1000 °C. The mass loss was calculated according to Equation 3.7 and the final result was obtained from the average of the triplicate trials.

$$M_{loss}[\%] = \left( \frac{M_2 - M_T}{M_2 - M_1} \right) \times 100 \quad (3.7)$$

Where:

$M_1$  is the mass of the empty crucible

$M_2$  is the mass of the crucible and pumice before initial heating

$M_T$  is the mass of the crucible and residue after heating at the respective temperature

### 3.3.3 Porosity of the packed bed and surface area of pumice

The porosity of the packed bed reactors is an important parameter in catalysis studies as it affects pressure drop [108], thus, limiting species diffusion into the active sites. There are various methods available for measuring the porosity of the materials including using a porosimeter or the natural stone test method BS EN 1936:2006 [109]. The former was used to determine the surface area of pumice particles (2-4 mm) while the latter packed bed porosity. The surface area of the pumice particles was determined using Surface area and Pore size analyser (NOVA 2000e). Pumice sample from Arusha weighing 302.6 mg was heated in a vacuum at 120 °C for 1 hour to remove any adsorbed volatiles such as water and oil. Once clean, the sample was brought to constant temperature (-196 °C) under nitrogen atmosphere for overnight. The adsorption data for specific surface area and pore size distribution were calculated employing Brunauer–Emmett–Teller (BET) and Barrett–Joyner–Halenda (BJH) methods respectively, using a Quantachrome NovaWin software. The sample from Arusha was chosen due to its high resistance to attrition compared to that Mbeya as observed during particle size reduction.

The natural stone test method was adopted to determine the porosity of the test bed materials. Pumice samples dried at 120 °C were filled to 40 ml in a graduated 50 ml beaker and transferred to a vacuum assisted flask as illustrated in Figure 3.6. The flask was then connected to a vacuum line and left for 2 hours to remove air trapped in the pores. Following this, deionised water from a graduated pipette was introduced into the bed material until all the particles were immersed. The porosity of the packed bed was calculated from the volume of water absorbed divided by the total volume of the bed material and expressed as a percentage.

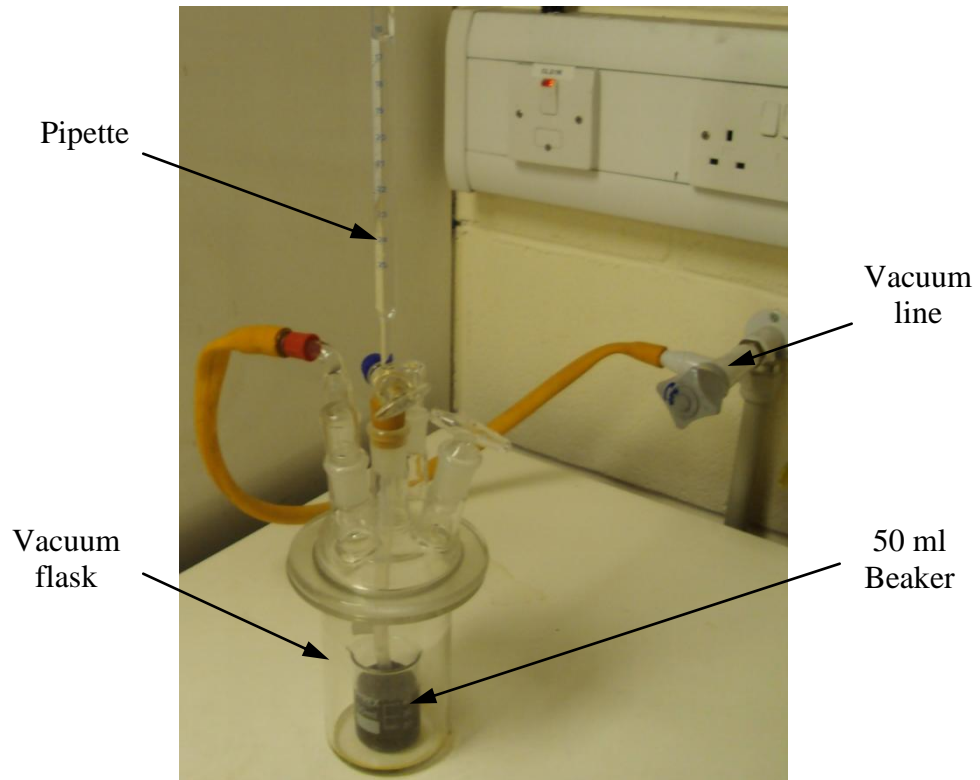


Figure 3.6 Experimental layout for determining the porosity of pumice

### 3.3.4 Loss on ignition (LOI)

The term “Loss on ignition” is used to measure the content of organic matter such as carbon or volatiles that could be present in a substance such as pumice which is itself not combustible. In this study, the LOI of pumice was determined according to BS EN 15169:2007 [110] and preEN 1744-7:2010 [111]. Three crucibles with lids were preconditioned by heating to 550 °C for 1 hour and then cooled to room temperature in the desiccator and weighed to nearest 0.1 mg. A minimum pumice sample of 1 g was spread evenly over each crucible and heated in a muffle furnace at 550 °C for 4 hours. The crucibles with residues were then cooled to room temperature in a desiccator and weighed. The loss on ignition was calculated from the weight loss dividing by the weight of the original sample and expressed as a percentage.

### 3.4 Preparation of Ceria ( $\text{CeO}_2$ ) doped pumice

#### 3.4.1 Experimental rig set-up

Depositing ceria over the particle surface of pumice was carried out using an impregnation method. The process involved preparation of the ceria precursor solutions before mixing with the pumice particles. Figure 3.7 illustrates the experimental set-up employed during preparation of the ceria precursor solution and the impregnation process of the pumice samples described in Section 3.4.2. The solutions were prepared by mixing the reagents at required ratios in a flask and stirring with a magnetic bar stirrer. A metal plate was used to heat the mixture and the evolving gases were scrubbed in 2 dreschel bottles filled with water. A similar configuration was adopted while impregnating the pumice support. As the emitted gas products including acid vapor are harmful, the assembly was installed in the fume hood equipped with an extraction fan.



Figure 3.7 Experimental set-up for preparation of ceria doped pumice

#### 3.4.2 Impregnation process

Impregnating ceria ( $\text{CeO}_2$ ) over pumice particle surfaces involved precursor preparation, impregnation, drying and calcination. Three solutions were prepared at different mixing ratios of the reagents. In the first batch, 10 g of  $\text{CeO}_2$  weighed to the nearest 0.1 mg was placed in a flask. 100 ml of 70 %  $\text{HNO}_3$  was added and the

mixture heated to 90 °C while stirring with a magnetic bar. After the set temperature was reached, 100 ml of peroxide ( $\text{H}_2\text{O}_2$ ) was introduced dropwise until the solution cleared. Addition of peroxide was necessary to promote ceria reduction under acidic conditions [112]. Heating continued until the solution cleared. The resulting precursor solution was cooled and stored in a glass bottle. The mixing proportion for the second precursor solution was 20 g  $\text{CeO}_2$  and 90 ml 70%  $\text{HNO}_3$  and 30 %  $\text{H}_2\text{O}_2$ . While the third was 30 g  $\text{CeO}_2$  and 90 ml 70%  $\text{HNO}_3$  and 30 %  $\text{H}_2\text{O}_2$ . These batches were named as B1, B2 and B3 respectively. All reagents were sourced from Fisher Scientific.

Three bulk samples of the pumice (2-4 mm) were impregnated with the prepared precursor solutions of ceria. The first sample was prepared by mixing 50 g of dried pumice with 200 ml of B1 and left for 24 hours. Following this, the treated pumice was filtered and dried at 120 °C for 36 hours before degassing at 550 °C for 2 hours in the muffle furnace. After cooling to room temperature, the final catalyst was stored in a dark glass bottle to avoid photocatalytic activity. The same technique was employed for the second and third samples using solution B2 and B3 respectively.

### **3.5 Preparation of nickel doped pumice**

Impregnating nickel over the pumice support employed nickel nitrate ( $\text{Ni}(\text{NO}_3)_2 \cdot 6\text{H}_2\text{O}$ ) from Fisher Scientific as a nickel source. Two catalysts samples were prepared in a 250 ml conical flask at different nickel source concentrations. The first catalyst was prepared by dissolving 10 g of nitrate in a 100 ml of deionised water at room temperature and stirred gently with a magnetic bar for 2 hours. The resulting precursor solution was mixed with 40 g of pumice and left for 24 hours to adsorb. Following this, the treated pumice were filtered and heated at 120 °C to vaporise water. Once drying was completed, the treated pumice was air-calcined at 450 °C for 4 hours to remove nitrites. After cooling to room temperature, the catalyst was stored in a dark glass bottles. A similar approach was employed for the second catalyst samples. However, the mass of nickel nitrate was 20 g.

### **3.6 Preparation of copper doped pumice**

Copper doped pumice was prepared in a 250 ml conical flask using copper sulphate salt as a copper source. Three samples were prepared by varying the concentration of salt as shown in Table 3.1. In each sample, copper sulphate (from

Fisher Scientific) and deionised water were mixed and heated at 60 °C for 2 hours while stirring gently with a magnetic bar. The resulting precursor solution was cooled to room temperature and transferred to a flask containing pumice. The mixture was left for 24 hours to cause adsorption of species into the support pores. Following this, the treated pumice was filtered and heated at 120 °C to vaporise water. Finally, the treated pumice was air-calcined at 900 °C for 4 hours to decompose sulphates. The calcined catalyst was then cooled to room temperature and stored in the dark glass bottles to prevent photocatalytic activity.

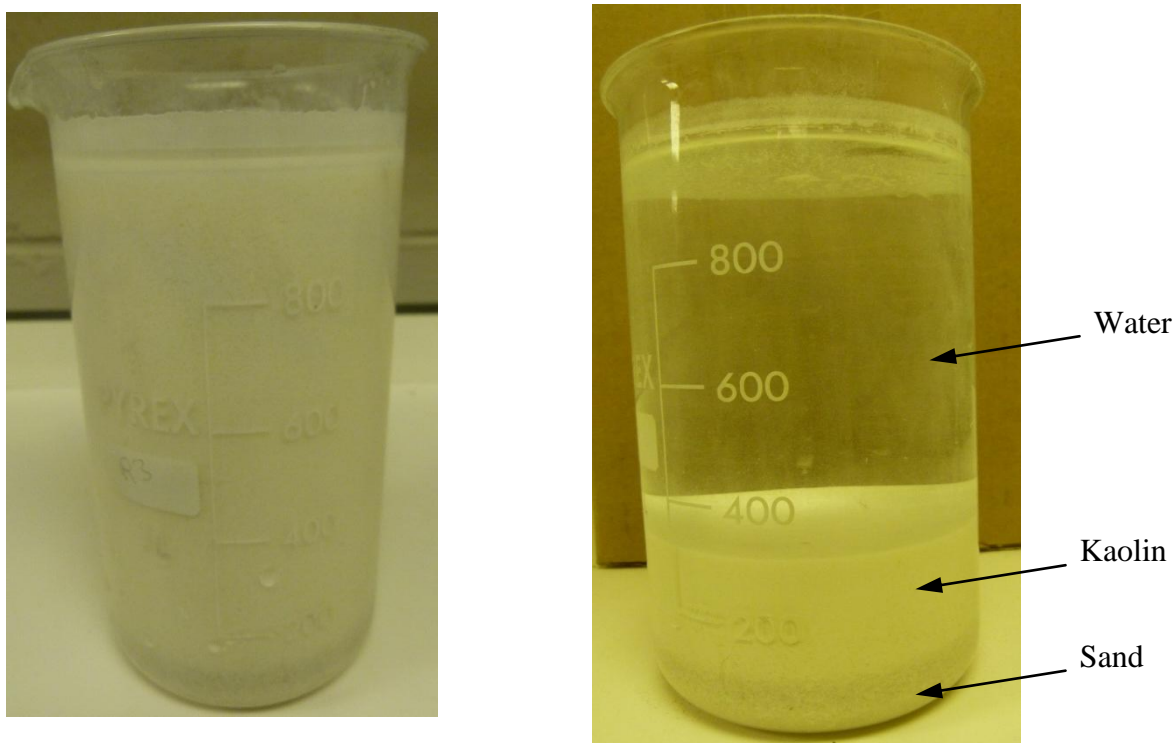
Table 3.1 Mixing ratios for the preparation of copper doped pumice

S/N	Material	Catalysts		
		Sample 1	Sample 2	Sample 3
1	Copper sulphate (g)	20	30	40
2	Deionised water (ml)	150	150	150
3	Pumice (g)	40	40	40

### 3.7 Preparation of kaolin catalysts

#### 3.7.1 Extraction of kaolin

Kaolin from Pugu Hills, Tanzania was extracted by dissolving raw kaolin in deionised water and left for 24 hours for mixture separation as shown in Figure 3.8 (a). Due to density differences, three distinct layers were formed as seen in Figure 3.8 (b). Starting at the bottom the layers were: sand particles, fine kaolin and clear water. After settling, the water and kaolin were decanted respectively in different flasks. The extracted kaolin was dried in an oven at 120 °C for 16 hours and then cooled to room temperature.



(a) Kaolin after mixing with distilled water (b) Distinct layers formed after 16 hours

Figure 3.8 Extraction of kaolin from raw sample

### 3.7.2 Kaolin-Ceria (KL/CeO<sub>2</sub>)

The extracted kaolin was mixed with ceria at different concentrations as shown in Table 3.2. It should be noted that the density of ceria is 3 times that of kaolin, thus, a high viscous solution was required to enhance dispersion of ceria. For each catalyst set-up, the materials were mixed with 100 ml of deionised water and stirred for 30 minutes. Following this, the mixture was spread over flat glass dishes at a maximum depth of 5 mm and dried in the oven at 120 °C for 16 hours. The dried sample was then crushed to give 2-4 mm particles. These particles were calcined at 800 °C for 4 hours in the muffle furnace. The calcined catalyst was then cooled to room temperature and stored in a dark glass bottle.

Table 3.2 Mixing proportions of kaolin and ceria

No.	Mass of kaolin (g)	Mass of ceria (g)	Percentage ceria
1	90	10	10
2	85	15	15
3	80	20	20

### **3.7.3 Kaolin-Ceria-Zirconia (KL/CeO<sub>2</sub>/ZrO<sub>2</sub>)**

Kaolin/CeO<sub>2</sub>/ZrO<sub>2</sub> was prepared using similar procedures described in the previous Section 3.7.2. Pure zirconia particles were mixed with ceria and kaolin. The mixing proportion for this catalyst was 15 g CeO<sub>2</sub>, 15 g ZrO<sub>2</sub> and 70 g kaolin. Addition of zirconia was aimed to improve OSC of the catalyst [113]. The calcined catalyst was stored in a dark glass bottle.

### **3.8 Characterisation of Catalysts**

Characterisation of the prepared and the spent catalysts were carried out to quantify and examine the state of the active sites. Quantification of active sites was performed using ICP-OES as described in Section 3.3.1. The oxidation state of catalysts was examined using X-ray diffraction (XRD), (Philips PW 3830) controlled with xPert industry software. The Cu K- $\alpha$ 1 X-ray tube was set at 2 $\theta$  ranging between 0 and 80° to include the phase of cerium, copper and nickel oxides. Additionally, pure samples of these additives were analysed to confirm their chemical state in the catalysts.

### **3.9 Summary**

The materials and methods used in characterising the feedstock and catalysts are presented herein. Materials considered include sawdust as fuel while pumice, ceria, nickel, kaolin and copper represent catalysts. These materials were characterised according to various standard procedures. Characterisation of sawdust involved proximate and ultimate analyses as well as thermogravimetric analysis and particle grading. Proximate analysis was used to determine fuel characteristics. The ultimate analysis was necessary to quantify the combusting elements for determining the appropriate equivalence ratio (ER). In establishing the working conditions, thermogravimetric analysis was deployed to investigate the evolution of volatiles as a function of temperature and time. It should be noted that volatile release depends on particle size and a small particle size was required for effective fuel injection.

Similarly, catalysts were characterised using various methods and classical equipments such as X-ray diffraction X-ray fluorescence and inductive coupled plasma-optical electron spectroscopy. Chemical composition analysis was performed on fresh and spent catalysts to investigate the chemical change and deposits. Subsamples of pumice were treated with ceria and nickel using an impregnation

method. Other catalysts composed of kaolin and ceria at different weight ratios were prepared by solid mixing in deionised water. All catalysts were calcined between 550 and 900 °C to remove salts and other volatiles.

The next chapter presents the test rig and detailed description of the experimental procedures used during gasification trials.

## **4 GASIFICATION TRIALS AND MEASUREMENTS**

### **4.1 Introduction**

This chapter describes detail of the experimental rig and other equipment used during gasification trials and data measurements. Geometrical dimensions of the horizontal entrained-flow gasifier are presented. Testing parameters for gasification and catalysis studies are also provided. The fuel feedstock and catalysts employed have been discussed in Chapter 3. Procedures used in determining the fuel conversion and cold gas efficiency for evaluating the performance of the gasifier are provided. Similarly, the activity, selectivity and coking resistance of catalysts are described in detail. Furthermore, as the gasification products are potentially hazardous, safety considerations are also highlighted.

### **4.2 Testing Parameters**

#### **4.2.1 Performance of the horizontal entrained-flow gasifier**

Prior to catalytic reforming of the gasification products, the gasifier was examined for smooth operation. Due to the horizontal configuration, a specific particle size range was necessary to optimise pneumatic fuel injection and the gasification process. Three different particle size ranges were used in this study as shown in Table 4.1. Other parameters were chosen using different methods. For instance, equivalence ratio was based on preliminary CFD modeling while the gasification temperature was chosen for optimal tar yield. Similarly, a gas hourly space velocity (GHSV) of  $8000 \text{ h}^{-1}$  and catalyst temperatures of  $350 \text{ }^\circ\text{C}$  have been reported to be sufficient for hydrocarbon oxidation [9, 42, 60]. Tar sampling temperature and volumetric requirement of isopropanol were chosen according to a current existing standard proposed for tar capture in biomass gasification [114].

In all test phases, syngas and tar composition were measured as well as carbon in the residues as described in Section 4.5. Syngas composition was important for determining the cold gas efficiency. Both syngas and tar composition were required for catalyst performance comparisons. The unburnt carbon in the residues was analysed for determining fuel conversion.

Table 4.1 Parameter settings for testing of the gasifier performance

Parameters	Unit	Test Experiment Phases		
		1	2	3
Equivalence ratio	-	0.23	0.23	0.23
Gas hourly space velocity (GHSV)	h <sup>-1</sup>	8000	8000	8000
Gasification temperature	°C	800	800	800
Catalytic reactor temperature	°C	350	350	350
Tar sampling temperature	°C	-15	-15	-15
Total isopropanol volume	ml	400	400	400
Wood particle size	mm	< 1.0	< 0.5	< 0.3

#### 4.2.2 The effect of catalysts on gasification products

An investigation on the effect of various catalysts on gasification products was performed after the optimisation of the gasifier performance tests as described in Section 4.2.1. Unless otherwise stated, operating conditions were kept constant during catalytic reforming tests. A study matrix for testing the effect of selected catalysts on the gasification products is shown in Table 4.2. These catalysts were prepared in different concentrations for determining the optimal loading. Loading refers to a concentration of active sites over the support materials. In examining their effects, the composition of the syngas and tar and the deposited carbon were measured.

Table 4.2 Study matrix for catalytic processing of gasification product gas

Test	Catalyst	Function	Main Indicators
1	Pumice (calcined-800°C)	Base catalyst and support	<ul style="list-style-type: none"> <li>• Syngas composition</li> <li>• Tar composition</li> <li>• Carbon deposition</li> </ul>
2	Ceria doped pumice (2-7 % CeO <sub>2</sub> )	CeO <sub>2</sub> possess excellent redox properties necessary for improving coking resistance of catalysts	<ul style="list-style-type: none"> <li>• Syngas composition</li> <li>• Tar composition</li> <li>• Carbon deposition</li> </ul>
3	Copper doped pumice (2-9 % CuO)	CuO can oxidise hydrocarbon at lower temperatures ( ~ 350 °C)	<ul style="list-style-type: none"> <li>• Syngas composition</li> <li>• Tar composition</li> <li>• Carbon deposition</li> </ul>
4	Nickel doped pumice (2-6 % NiO)	NiO can oxidise hydrocarbon at lower temperatures ( ~ 350 °C)	<ul style="list-style-type: none"> <li>• Syngas composition</li> <li>• Tar composition</li> <li>• Carbon deposition</li> </ul>
5	Kaolin-Ceria (0-21 % CeO <sub>2</sub> )	Kaolin is composed of several metal oxides that can oxidise hydrocarbons	<ul style="list-style-type: none"> <li>• Syngas composition</li> <li>• Tar composition</li> <li>• Carbon deposition</li> </ul>

### 4.3 Equipment

#### 4.3.1 The experimental rig

Figure 4.1 shows the schematic layout and the experimental test rig used in this study. The rig consisted of a gasification reactor fitted in a tube furnace, a fuel feeder (with injector), a tar sampling system, a catalyst reactor, a vacuum pump and a gas chromatograph (GC). These components included standard fittings to provide connection to other components using either 316 stainless steel pipes or Un-Reinforced PVC Tube. Air rotameters (from Fisher Controls Ltd) were used for measuring the air inflow rate and the syngas outflow. Their operating limit ranged between 0 and 24 l/min at  $\pm 5\%$  accuracy of full scale. The air rotameter for syngas measurement was adjusted based on the density difference to take account of the syngas composition. The density of syngas ( $\rho_{gas}$ ) was determined using Equation 4.1 and the volume flow rate ( $\dot{V}_{gas}$ ) was determined using Equation 4.2. The general set-up allowed sampling the whole gas stream to avoid bias caused by flow dynamics.

$$\rho_{gas} = \sum_{i=1}^n \rho_i \quad (4.1)$$

$$\dot{V}_{gas} = \frac{\rho_{air}}{\rho_{gas}} \dot{V}_{air} \quad (4.2)$$

Where  $i$  is the gas component in the syngas as determined by GC in the preliminary tests while  $\rho_{air}$  and  $\dot{V}_{air}$  are density and volume flow rate of air respectively.

#### 4.3.2 The fuel feeder

Wood particles of a pre-determined size were fed to the gasifier reactor using the feed mechanism illustrated in Figure 4.3 (a). The unit was comprised of a vibrator with a hopper (from Triton Engineering Co. Ltd, UK), and a pneumatic injector. The vibrator employs agitation to cause particles to flow. Depending on the density of the material, mass flow rate was set in the range of 0 to 100 % and the rate was measured by collecting mass of the wood powder at a specific time.

Commissioning tests showed that the fuel injection mechanism was the crucial part of the feed unit because of particle dynamics. It consisted of an air injector and a premixing zone as detailed in Figure 4.3 (a). The air injector was made using a 316 stainless steel pipe with outside diameter (OD) 3.2 x 0.889 mm while the

premixing zone was OD 10 x 40 x 2.11 mm. A distance of 40 mm from the gasifier reactor inlet to the injector nozzle was sufficient to cause mixing before entering the gasifier. The two parts and the second hopper were connected with a T-socket. All pipes and fittings were sourced from RS components.

### 4.3.3 The furnace

The tube furnace that was used as a source of heat during warming-up and thermal insulator throughout the gasification process is shown in Figure 4.3 (a). The furnace (TF 825) from Severn Furnaces Ltd comprised of a ceramic tube with an inside diameter of 40 mm and a length of 515 mm. The tube was heated by a series of seven heater bands which were controlled individually with PID temperature controllers manufactured by CAL controls. The rated power output of the furnace was 1.5 kW while the maximum and nominal operating temperatures were 1200 °C and 850 °C respectively.

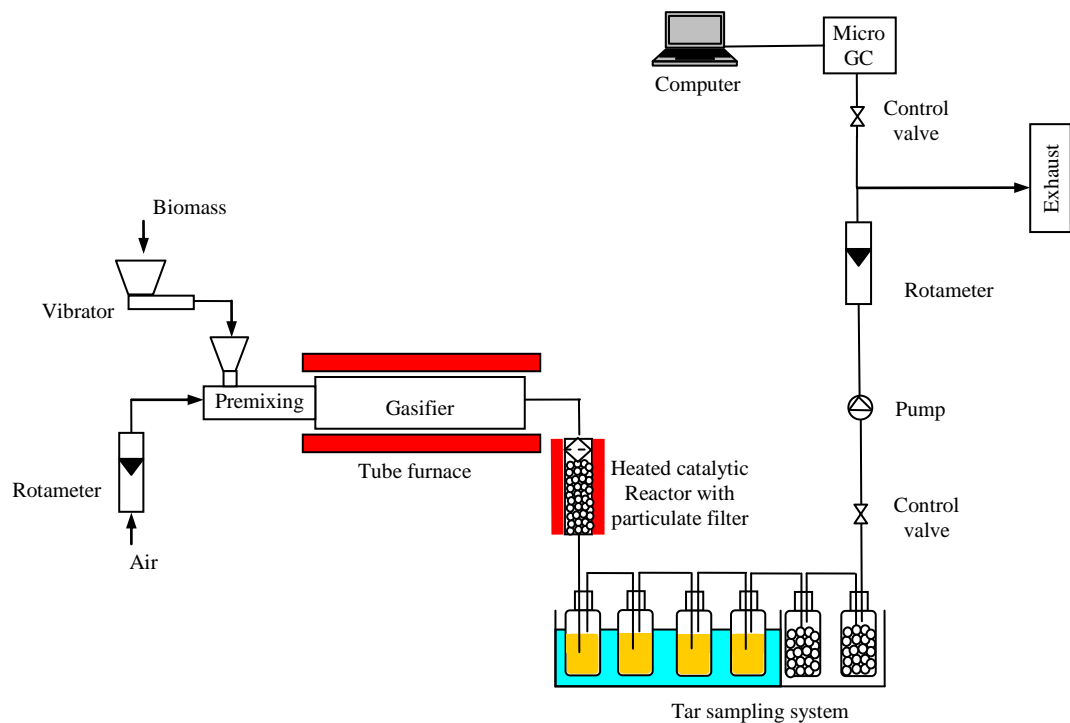


Figure 4.1 Schematic layout of the gasification trials set-up

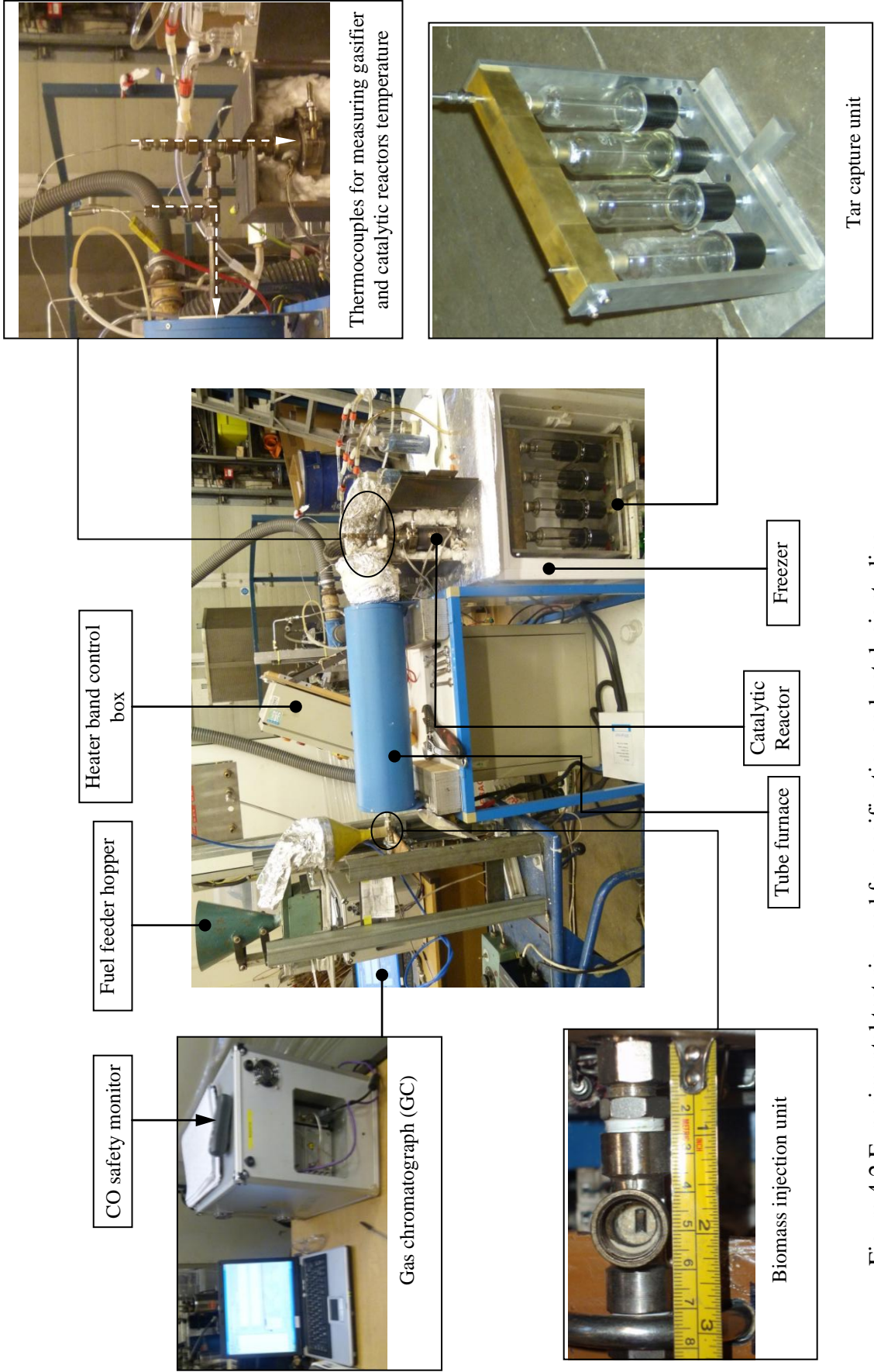


Figure 4.2 Experimental test rig used for gasification and catalysis studies

#### 4.3.4 The gasifier

Due to the rig's horizontal configuration, interaction of particles with the flow was important to ensure scavenging of residues. Accumulation of residues such as ashes and un-gasified carbon in the gasifier reactor resulted in gasification efficiency loss. Accumulation of residues was primarily dependent on the flow velocity, which is related to the chamber cross-section area. In accounting for this drawback, the use of appropriate diameter ratios of the inlet and outlet pipes to the gasifier was proposed. A ratio of 0.5 was sufficient to enhance scavenging of ash and unburnt carbon particles as revealed using a complementary method highlighted in Section 4.6. Additionally, this ratio ensured homogeneous mixing of the resulting gasification products. Detailed geometrical parameters are presented in Figure 4.3 (b).

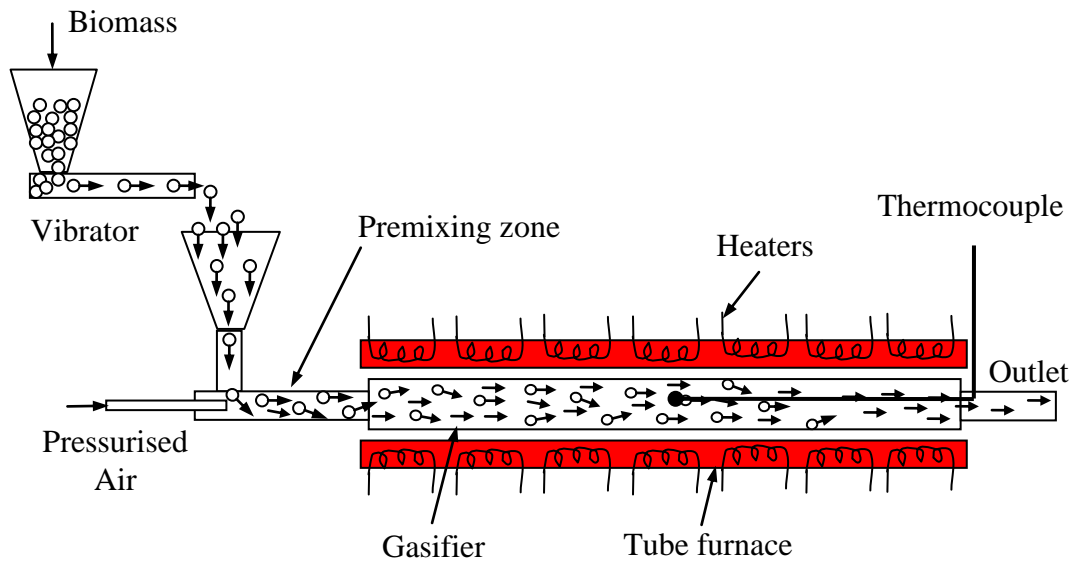
Figure 4.3 (a) illustrates the gasifier with the feeding mechanism used in this study. The gasifier was made of a 316 stainless steel pipe  $\text{Ø } 21.34 \times 450 \times 2.77$  mm (NPS  $\frac{1}{2}$  SCH 40 S) supplied by Swagelok. At both ends, male connectors,  $\frac{1}{4}$  in. Tube OD  $\times \frac{1}{2}$  in. male NPT were welded to provide connection for the fuel injector and the syngas outlet. These materials were selected for its ability to withstand a continuous working temperature up to 900 °C.

#### 4.3.5 Catalytic reactor and the heating system

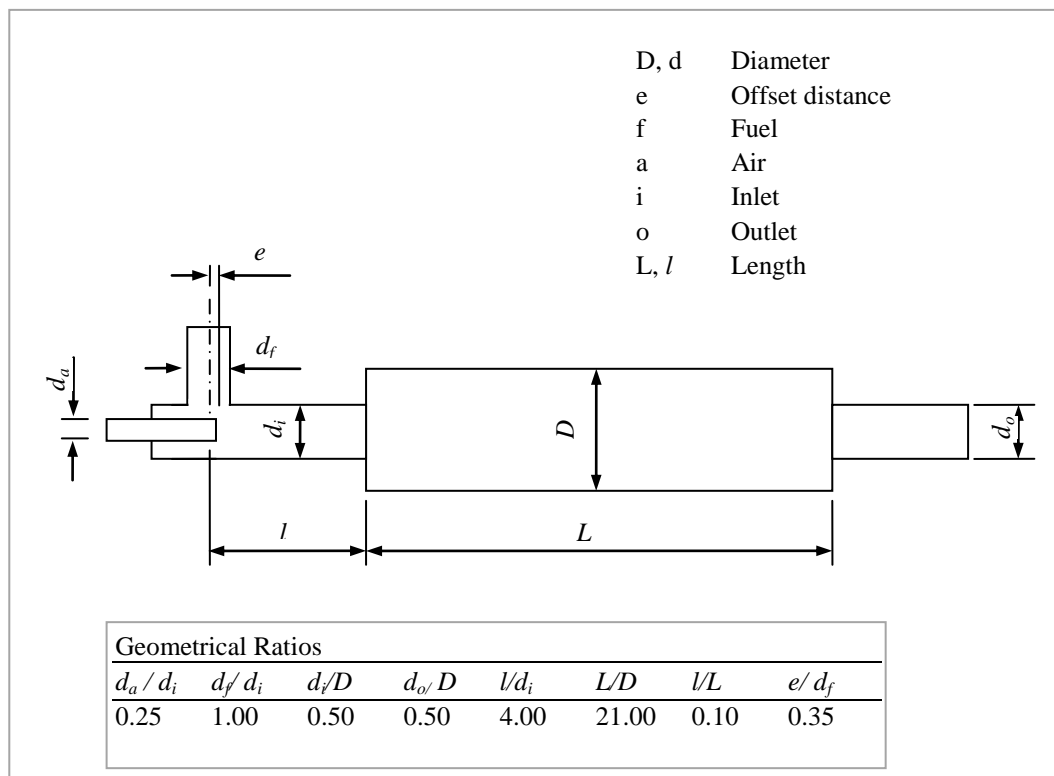
Figure 4.4 shows the reactor and heating system used for catalytic reforming of the gasification products. This reactor is similar to the one used for isokinetic tar sampling according to the European standard CEN/TS 15439 [114]. It was manufactured using 316 grade stainless steel and sized  $\text{Ø } 48.3 \times 115 \times 3.69$  mm (NPS  $1 \frac{1}{2}$  SCH 40S). Both the inlet and outlet holes were made to fit M 6 adaptors.

Heating of the catalytic reactor was achieved through Two heater bands  $\text{Ø } 2'' \times 2''$  size, from Dynisco Company. These heaters were rated 750 W and maximum operating temperature of 450 °C. The heating system was controlled using a Watlow 93 PID temperature controller with inputs from two K-type thermocouples. The first thermocouple was attached to the surface of the heater band for setting the reactor working temperature, as well as monitoring the working temperature limits of the heater bands. The temperature in the reactor was measured directly using a K-Type thermocouple and was recorded in a thermometer data logger (YCT YC-737D) described in Section 4.5.1. The second thermocouple was attached at the surface of

the insulation box to avoid overheating that could damage the freezer and the surrounding tubing. This input was set at 50 °C as a safety limit.

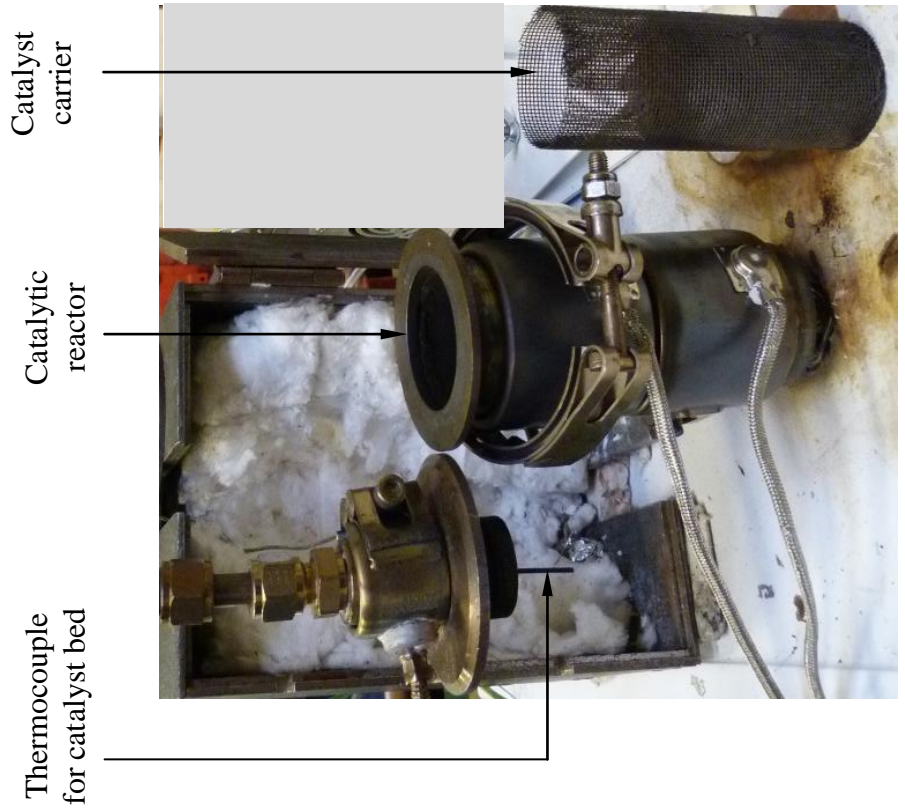


(a) Gasifier and feed mechanism illustrating material flow

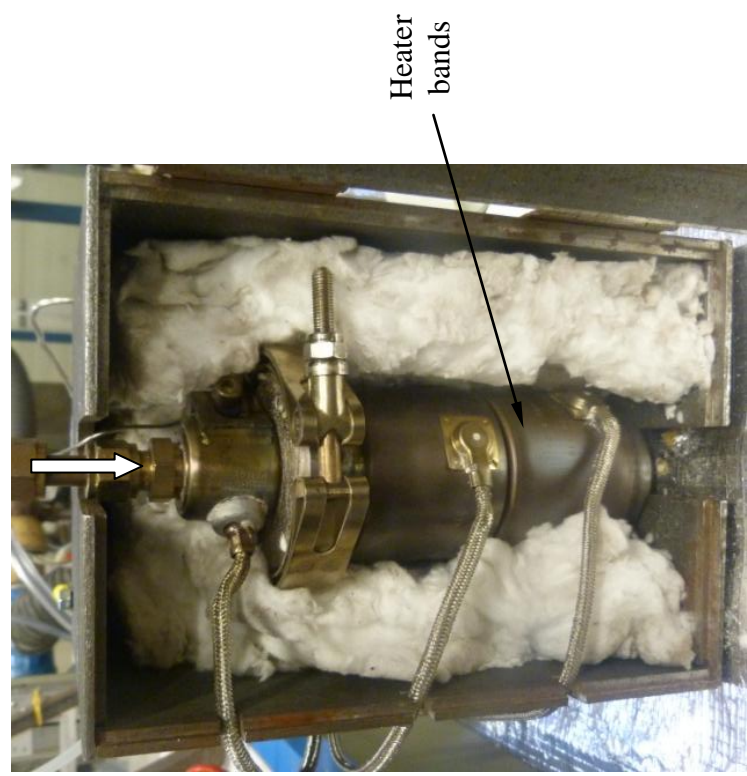


(b) Geometrical parameters

Figure 4.3 Schematic diagram for the gasifier reactor and the fuel feed mechanism



(a) Exploded view

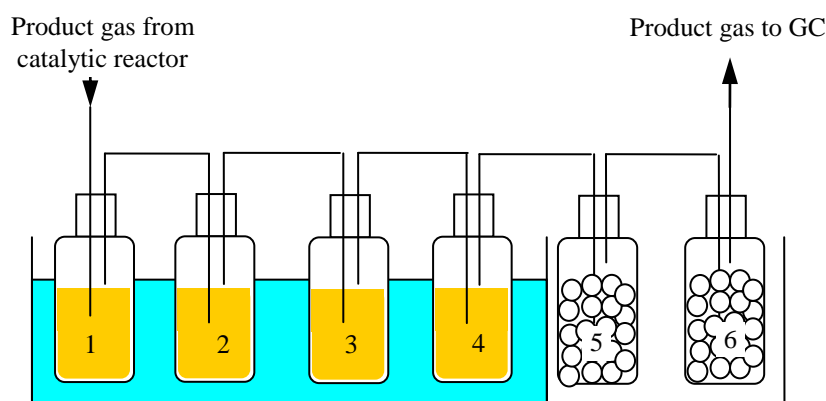


(b) Assembled view

Figure 4.4 Catalytic reactor and the heating system

### 4.3.6 Tar sampling system

The tar sampling system was designed according to the standard method for sampling and analysing tar from gasification processes [114]. The design consisted of four positions for fixing standard dreschel bottles MF 29/3/250 as detailed in Figure 4.2. The inner tubes for each bottle position were made from 316 stainless steel pipe  $\text{\O} 6 \times 145 \times 1$  mm. This pipe size is similar to the standard 250 ml dreschel bottle head. Solvent cooling was achieved using a freezer (BEKO, ZA630W) rated 50 W and minimum temperature of  $-15$  °C. The freezer was able to accommodate the impinger bottles assembly. On the top side of the freezer, 2 holes  $\text{\O} 10$  mm were drilled for connecting the inlet pipe from the reactor and the outlet to the remaining bottle train. Selective screening of tar compounds was performed using isopropanol (99.8 %) from Fisher Scientific. The use of silica gel ensured complete removal of water vapor in the gas stream. A schematic diagram of the tar sampling system is shown in Figure 4.5.



Tar sampling system. Impinger bottles 1-4 (each 100 ml of isopropanol) in the freezer at  $-15$  °C. Bottles 5 and 6 contain silica gel and kept in dry bath at  $20$  °C

Figure 4.5 Schematic diagram of the tar sampling system

### 4.3.7 Vacuum pump

A vacuum pump was necessary to provide a flow of syngas by overcoming the pressure drop resulting from the pipe bends and constriction, bed material and tar sampling solvent. The pump was sourced from Heidolph with a maximum rated speed of 1200 rev/min at 75 W. This pump was installed after the tar sampling unit to provide smooth gas flow.

#### **4.3.8 Sundry equipment**

In setting-up the experimental rig, various accessories were used including pipes and fittings, tubing and rotameters. The connections between components were made according to the material and size. Stainless steel pipes and fittings of grade 316 were used for connecting the gasifier to the tar sampling system through the catalytic reactor. These materials were selected for their ability to withstand higher temperatures from the syngas stream. As the syngas cools in the tar sampling unit, further connections to the GC and the exhaust were made of 9 mm diameter Un-Reinforced PVC Tube.

### **4.4 Gasification Process Procedures**

#### **4.4.1 Gasification operating procedures**

The biomass gasification and catalytic reforming of the product gas were conducted according to the set-up described in Section 4.3. Prior to gasification trials, the gasifier was preheated to the required operating temperature. Wood powder from the vibrating fuel feeder was introduced under gravity and the pressurised air conveyed the particles to the mixing chamber where partial premixing was achieved. As a result of higher pressure in the mixing chamber than in the reactor, the air-fuel mixture was propelled into the preheated gasifier reactor. The resulting gas product was passed through the preheated catalytic reactor. The product gas from the reactor was passed through the tar sampling system. In order to provide consistent gas outflow, a constant outflow rate was used. This flow rate was achieved by adjusting the control valve located before the pump (Figure 4.1) and the rate was measured using a rotameter. Finally, the gas composition was analysed using a gas chromatograph at discrete time intervals before exhausting the gas to the extraction duct.

#### **4.4.2 Preparation procedures**

Prior to experimental operation, the rig was tested with regard to safety and consistent operation. The preparation procedures for the set-up were as follows:

- (i) To assemble the rig and ensure that all joints were securely fixed as well as venting the exhaust to the extraction system.
- (ii) Preconditioning the 250 ml dreschel bottles by cleaning using laboratory detergent and dried at 120 °C for 4 hours, to remove any contaminants.

- (iii) All gas pipe lines were checked for leakage by purging with air at 15 l/min for 30 minutes. This flow rate was sufficient to create positive pressure high enough to cause detectable leaks.
- (iv) Testing for proper functioning of freezer, suction pump, heater bands and the tube furnace. The freezer was switched on for 24 hours to confirm that cooling effect was as per specifications provided (measured with a thermocouple). The pump was powered and the outflow was measured using the air rotameter. The pump's function was demonstrated by showing changes to the outflow as the inlet control was altered. The heater bands were activated and the temperature was monitored using a K-Type thermocouple. Similarly, the tube furnace was tested for the operating temperatures and protection against overheating. The controllers were set to 800 °C and the temperature rise monitored through the controller. An external K-Type thermocouple was connected to the thermometer. Protection against overheating the furnace was confirmed by auto-shut off at 900 °C.
- (v) The fuel feeder was tested for consistent flow of the wood particles. About 10 g of wood powder was fed to the hopper and the mass flowrate was measured by collecting the wood powder at an interval of 1 minute. Measurements were taken three times to monitor the repeatability. In accounting the external influences to the vibrator feed mechanism, it was decided to calibrate the fuel flow rate just before the gasification test starts.

#### **4.4.3 Operation procedures**

The overall experimental procedures undertaken for the operation of the rig were as follows:

- (i) 100 ml of isopropanol measured at room temperature was filled in each of the four 250 ml dreschel bottles in the tar sampling system. The second bottle was also filled with 80 ml of 5 mm diameter glass beads to increase aerosol formation [115], which enhance hydrocarbons screening.
- (ii) After assembling the tar sampling system, the catalytic reactor and the tube furnace were activated and the temperatures monitored.

- (iii) When the gasifier temperature reached 200 °C, the extraction system in the laboratory was activated to remove any resulting combustible or toxic gases.
- (iv) A vibrating feeder was then calibrated gravimetrically to give 5 g/min of sawdust by direct weighing of the fuel for 1 minute. This procedure was repeated 3 times to ensure repeatability was achieved. Thereafter, about 60 g of sawdust measured at 1 mg scale was filled in the hopper ready for the gasification trial. However, in the catalyst deactivation trials, 100 g of fuel was used.
- (v) When the temperature in the gasifier reached 750 °C and the solvent was below -15 °C, the outflow rotameter control needle valve was opened fully before activating the suction pump. This was necessary to avoid back pressure that could damage the meter. Once the valve was opened, the pump was activated. Following this, the inlet air flow rate was set at 5 l/min to give an equivalence ratio of 0.23 (by mass) and the outflow rate of 15 l/min on the air rotameter. This setting was equivalent to a GHSV of 8000 h<sup>-1</sup>. The fuel feeder was then activated to start the gasification process and the temperature data logging was initiated.
- (vi) After the gasification process stabilised (about 1-2 min), the outflow sampling pipe was connected to the gas chromatograph to analyse the syngas composition. Gas measurements were repeated until the test sample was completely gasified. In most cases, the gasification test took 10 minutes.
- (vii) To ensure there were no gas leaks at the end of the test, the suction pump was left on for further 5 minutes to remove all gases in the pipelines.
- (viii) When shutting down, the air inlet valve was closed and then the freezer, furnace, feeder and the heater band controller. The pump was shut down in accordance with step (vii).
- (ix) Finally, the content of the impinger bottles were decanted into a storage bottle. The impinger bottles were rinsed with isopropanol and the resulting solvent was combined with the actual sample. These samples were kept in the freezer below 5 °C for immediate analysis. Similarly, the spent catalysts were stored in the dark glass bottles to prevent photocatalytic reactions. While the tar containing samples were analysed

by GC-MS, the catalysts were analysed for chemical composition using a variety of equipments including carbon and sulphur analyser and XRD as described in Chapter 3, Section 3.2.

## **4.5 Experimental Data Measurements**

### **4.5.1 Temperatures**

The gasification process is highly dependent on operating temperatures as temperature affects the product gas composition. Similarly, temperature controls the catalytic reaction rates of the reactants over the active sites. Furthermore, the isopropanol solvent solution requires low temperatures to prevent vaporisation which reduces the performance of the tar sampling system [114]. Measuring these temperatures was important in controlling the overall process.

Throughout the experimental work, the temperatures were recorded using a thermometer (YCT YC-737D) data logger manufactured by TMS Europe Ltd. The thermometer has 3 thermocouple input channels with data logging up to 10,000 records per channel at resolution of 0.1 °C. A range of thermocouples can be accepted including K-type and J-type. The accuracy of the thermometer using these thermocouples is  $\pm 0.1$  % full scale reading + 0.7 °C at a range of 100 ~ 1300 °C.

Prior to gasification trials, the temperature distribution along the gasifier was measured to ensure uniform heating and establish a reference position for the thermocouple. The furnace was heated to 800 °C where the temperatures were taken at an interval of 50 mm using a K-type thermocouple, while purging air at a flow rate of 5 l/min. The temperatures in the catalytic reactor and tar sampling system were measured using a K-type and J-type thermocouples respectively. In the latter, the thermocouple was attached to the fourth bottle of the sampling system. The choice of this location was based on the fact that, the fourth bottle experiences the lowest temperature compared to the others. During the gasification trials, the time interval for data acquisition was set at 30 seconds.

### **4.5.2 Syngas analysis**

A variety of gas analysers are available with different detection ranges and types of gas components. These factors are the major criteria for selecting an appropriate analyser for a particular application such as gasification. A gas chromatograph (GC) was chosen for measuring the composition of the product gas.

In this study, the syngas composition was analysed using a micro gas chromatograph (Varian, CP-4900) shown in Figure 4.2. The GC was controlled with a Galaxie Workstation using software version 1.9.3.2. Gas analyses were performed using a programmed method where 2 chromatography channels and the sample line were controlled independently. For channel 1, the measured gases were H<sub>2</sub>, O<sub>2</sub>, N<sub>2</sub>, CO, and CH<sub>4</sub> with argon (Ar) as a carrier gas. During analysis, the column and injector temperatures were kept at 70 °C while the column pressure was 150 kPa. On the channel 2, four gases were measured under helium (He) atmosphere. These gases were CO<sub>2</sub>, C<sub>2</sub>H<sub>6</sub>, C<sub>3</sub>H<sub>8</sub> and C<sub>4</sub>H<sub>10</sub>. In this channel, the column and the injector were heated at 109 °C and a pressure of 75 kPa was maintained in the column. The sample line was kept at 70 °C. The channels and sample line conditions were design to minimise condensation and to ensure sample integrity.

Prior to measurements, the GC was calibrated on air and a standard syngas mixture (sourced from Scientific & Technical Gases Ltd). The standard was composed of 15 % H<sub>2</sub>, 15 % CO, 15 % CO<sub>2</sub>, 5 % CH<sub>4</sub>, 2 % C<sub>2</sub>H<sub>6</sub>, 2 % C<sub>3</sub>H<sub>8</sub>, 1 % n-Butane and the balance was nitrogen in volume percentage. This gas composition is typically found in gasification processes where air is employed as an oxidizing agent. Once the calibration was completed, the outflow syngas was sampled at an interval of 3 minutes. In order to monitor the accuracy of the experimental data, the GC was calibrated after every 10 readings. On average, the accuracy of the GC for the calibration gas was found to be ± 1 % error.

### **4.5.3 Tar Analyses**

#### **4.5.3.1 Reagents**

Various reagents were employed in quantifying a selection of the tar compounds using a gas chromatograph-mass spectrometer (GC-MS) described in Section 4.5.3.3. These reagents were mainly isopropanol and certified reference standards listed in Table 4.2. Isopropanol was used as the rinsing solvent during the analysis of the test samples. The reference mixes were chosen for confirming the presence of similar compounds in the gasification products. All standards were sourced from Restek Corporation (Appendix A).

Table 4.3 Reference standards for identifying tar compounds

No.	Standard	Compounds
1	8040 Phenols mix #1	Phenols
2	BTEX standard	Volatile Organic Compounds (VOC)
3	OLM 01.1 Revised SV MegaMix	Semi Volatile Organic Compounds (SVOC)
4	SV calibration mix #5	Polycyclic Aromatic Hydrocarbon (PAH).

#### 4.5.3.2 Sample preparation

Prior to analysis, a bulk tar containing solution from gasification test was mixed thoroughly to ensure homogeneity. Following this, a 10 ml sub-sample of the solution was filtered through a 47 µm filter to remove any particles that could block the chromatogram column. After filtration was complete, 2 ml of the filtrate was transferred to a 2 ml vial and then capped to prevent loss by evaporation. The concentrated standards were diluted to give calibration mixtures of 50, 100 or 200 ppm. Another sample of blank solution of isopropanol was also prepared. The prepared sample was then loaded into the GC-MS against the standards and the blank isopropanol. Depending on the type of compounds to be determined, the analysis method was set according to the specifications of the respective reference standard as detailed in Appendix A.

#### 4.5.3.3 The Gas Chromatograph- Mass Spectrometer (GC-MS)

The tar samples produced from the gasification trials were analysed using a PerkinElmer GC-MS (Clarus 500GC). The analyser was fitted with a capillary column (Elite-5MS), autosampler and mass spectrometer. The column has an internal diameter of 0.25 mm x 30000 mm long and operated between -60 and 350 °C. The column separates the individual compounds as the mixture flows through. After the sample had been injected and separated in the column, the compounds were detected using a mass spectrometer (MS). The MS was interfaced with the GC through TurboMass version 5.0.0 software. The software was calibrated to search specific components based on the actual retention time and mass spectrum. Identification of an individual compounds present in the test sample was performed by comparing the unknown peak spectrum with the respective reference standards and mass spectra library. Commercial standards shown in Table 4.3 were used to verify the PAH, phenols, volatile organic aromatics (VOA) and semi-volatiles (SV) compounds. The

concentration ( $C_i$ ) of the individual compound is demonstrated using Figure 4.6 and was determined according to Equation 4.3 based on the ratio between the area of the test specimen and the standard.

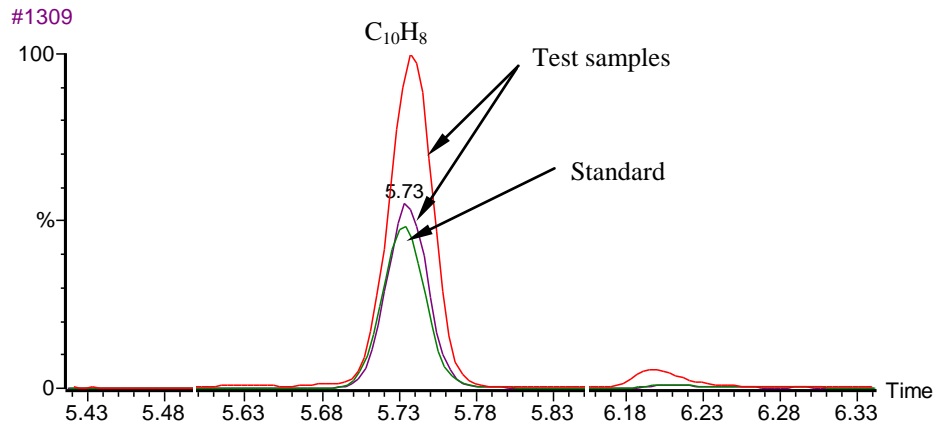


Figure 4.6 GC-MS spectra for naphthalene ( $C_{10}H_8$ )

$$C_i [ppm] = \frac{A_i \times D_{std}}{A_{std}} \quad (4.3)$$

Where  $A_i$  and  $A_{std}$  are the area under the peak of the individual compound in the test sample and the standard respectively and  $D_{std}$  is the concentration of the compound in the standard (ppm by mass).

#### 4.5.4 Pressure drop across the catalyst reactor

Pressure drop is an important parameter in determining the superficial velocity required for estimation of the residence time of the gas stream through the catalyst bed as described in Chapter 2. Figure 4.7 shows the experimental layout for pressure drop measurements across the pumice-packed reactor using a Digitron P200 H manometer. A typical pumice sample after size reduction is shown in Figure 4.8. Pumice particles were graded according to their diameter size as small (1-2 mm), medium (2-4 mm) and large (4-5 mm). For each grade, the pressure drop was measured at 20 mm, 70 mm and 100 mm bed heights respectively. Different particle sizes and bed heights were chosen to study their effect on the pressure drop in the catalytic reactor. In each case, the air was purged through the reactor at various flow

rates ranging 3 to 24 l/min with accuracy of  $\pm 5\%$  of full scale. Both air and reactor were kept at room temperature.

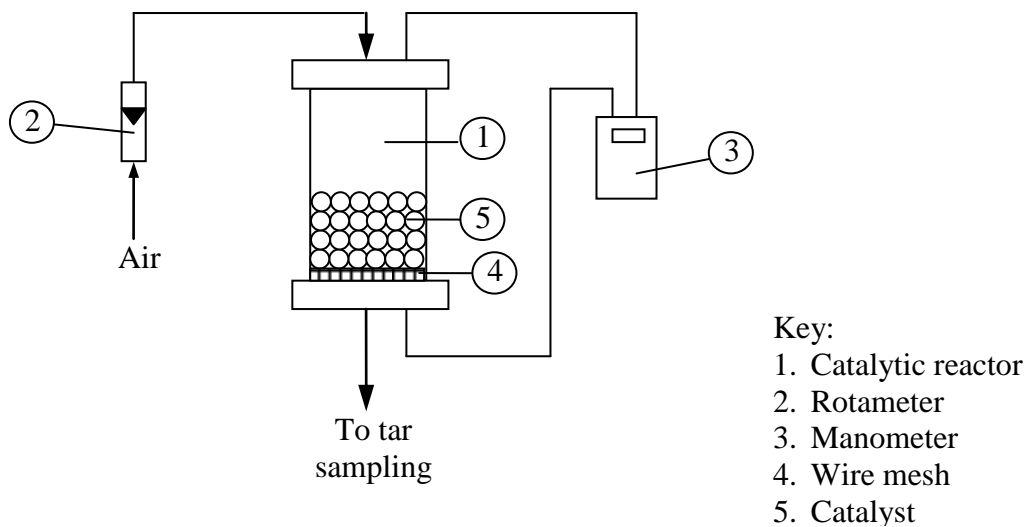


Figure 4.7 Schematic layout for the pressure drop experiments



Figure 4.8 Pumice sample for 2-4 mm size

#### 4.5.5 Fuel conversion and cold gas efficiency

Fuel conversion and cold gas efficiency (CGE) are major parameters for assessing the performance of the gasification process. The former expresses the fuel proportion converted into gas products. While the latter, is defined as the ratio of energy content in the syngas to the biomass energy content. Fuel conversion was calculated using Equation 4.4 and the CGE was calculated using Equation 4.5 [43]. The fractions of char in the gasification residues were determined using a Leco SC-144DR, total carbon analyser shown in Figure 4.9. Procedures used are described in Section 3.2.4.

$$X_f[\%] = \left[ 1 - \frac{m_c}{m_f} \right] \times 100 \quad (4.4)$$

$$\eta_{CGE}[\%] = \left[ \frac{m_g \times LHV_g}{m_f \times LHV_f} \right] \times 100 \quad (4.5)$$

Where  $m_c$ ,  $m_g$  and  $m_f$  are the mass of unburnt carbon, syngas and fuel respectively.  $LHV_g$  is the lower heating value of syngas and  $LHV_f$  for the parent solid fuel.



Figure 4.9 Carbon-Sulphur analyser (Leco SC-144DR)

#### 4.5.6 Catalyst activity and selectivity

Catalyst activity and selectivity are important criteria for assessing the performance of the catalysts. In this work, the activity of the catalysts was

investigated based on the coking resistance. The coking profile along the reactor was obtained by determining the deposited carbon on the spent catalyst at different reactor bed heights. The bed heights were measured using a depth gauge vernier calliper and were classified as 0 to 20 mm, 20 to 30 mm, 30 to 40 mm, 40 to 50 mm, 50 to 60 mm and 60 to 70 mm. The classified samples were then ground to a powder and the deposited carbon was determined using a Leco SC-144DR analyser. The analysis was conducted in triplicate employing subsamples of 0.35 g weighed to nearest 0.1 mg.

The selectivity of the catalysts to carbon-containing gases (CO, CO<sub>2</sub>, CH<sub>4</sub>, C<sub>2</sub>H<sub>6</sub> and C<sub>3</sub>H<sub>8</sub>) was determined using Equation 4.6. A similar equation was employed in determining the selectivity to tar cracking for the identified compounds. Since the tar compounds were quantified by mass, the ratio was calculated on a mass basis. For the case of H<sub>2</sub>, the catalyst selectivity was determined according to Equation 4.7.

$$S_j[\%] = x_j \times 100 / \sum_{j=1}^n x_j \quad (4.6)$$

$$H_2[\%] = \frac{\text{Molecules } H_2 \text{ produced}}{(C \text{ atoms in gas phase}) \times RR} \times 100 \quad (4.7)$$

Where  $x_j$  is the mole fraction of a gas  $j$  containing carbon atoms and the summation is for all  $n$  gases containing carbon atoms.  $RR$  is the H<sub>2</sub>/CO<sub>2</sub> reforming ratio which accounts for H<sub>2</sub> consumed during reverse water-gas shift reaction (RWGS) (i.e. CO<sub>2</sub> + H<sub>2</sub> → CO + H<sub>2</sub>O)

#### 4.5.7 Feed rate settings

Air–fuel ratio is one of the major determining factors governing the gasification process as discussed in Chapter 2. An appropriate air–fuel ratio was important to provide momentum for pneumatic injection as well as restricting O<sub>2</sub> quantity for the specified equivalence ratio. The amount of air required was determined based on the stoichiometric reactions of the fuel components as summarised in Table 4.4. The combustion equations were used only as indicator to determine a stoichiometric air–fuel ratio, and then calculate the required air–fuel flow rate at equivalence ratio of 0.23 (by mass). The elemental compositions of the wood

powder were obtained as detailed in Section 4.2.4. In this study, an equivalence ratio of 0.23 was selected as the optimal value according to the previous studies discussed in Section 2.1.2.4. The relationship between equivalence ratio and stoichiometric and actual air-fuel ratios was expressed using Equation 4.8.

$$ER = \frac{\text{Actual Air Fuel Ratio}}{\text{Stoichiometric Air Fuel Ratio}} \quad (4.8)$$

The stoichiometric O<sub>2</sub> was determined according to the balanced combustion equation with the respective combustible species in the fuel (C, H, O, and S). The required amount to cause complete combustion was calculated using Equation 4.9. The total amount of O<sub>2</sub> ( $m_{O_2,T}$ ) was obtained by summing the required O<sub>2</sub> subtracting the inherent oxygen atoms in the fuel. Total amount of air required was determined using Equation 4.10.

$$m_{O_2,i} = \frac{n_{O_2,i} M_{O_2,i} \times m_i}{n_i M_i} \quad (4.9)$$

Where  $n_{O_2,i}$  and  $M_{O_2,i}$  are the number of moles and the molecular weight of oxygen respectively, required for stoichiometric combustion of specie  $i$  in the fuel. Similarly,  $n_i$  and  $M_i$  are number of moles and molecular weight of the combustible specie  $i$  while  $m_i$  is the mass fraction of the combustible specie  $i$  in the fuel determined in the proximate analysis.

$$m_a = \frac{m_{O_2,T} \times m_{O_2,a}}{M_a} \quad (4.10)$$

Where  $m_{O_2,T}$  and  $m_{O_2,a}$  are the total mass of oxygen required and mass of O<sub>2</sub> in standard air (7.424 g/mol) respectively and  $M_a$  is the molecular weight of air (28.556 g/mol).

The Air-fuel ratio (AFR) was determined by dividing the mass of air required to the mass of fuel at a given equivalence ratio. The relationship between fuel flow rate ( $\dot{m}_f$ ) and air flow rate ( $Q_a$ ) were expressed using Equation 4.11.

$$Q_a = \frac{\dot{m}_f \times AFR}{\rho_a} \quad (4.11)$$

Where  $\rho_a$  is the density of air at ambient temperature ( $1.2 \text{ kg/m}^3$ ). The fuel flow rate was chosen in the range 1 to 20 g/min and the equivalent air flow rates were calculated and expressed in l/min.

Table 4.4 Air-Fuel ratio for gasification process at ER=0.23

Combustion equation	Fuel composition			Stoichiometric O <sub>2</sub> (g)	Actual at ER=0.23
		(% wt)	Mass (g)		
C+O <sub>2</sub> =CO <sub>2</sub>	C	49.40	0.4940	1.3173	0.3030
H <sub>2</sub> +0.5O <sub>2</sub> =H <sub>2</sub> O	H	5.90	0.0590	0.4720	0.1086
	O	40.68	0.4068	-0.4068	-0.0936
	N				
S+O <sub>2</sub> =SO <sub>2</sub>	S	0.02	0.0002	0.0002	0.0001
	Total	96.00	0.9600		
	Total O <sub>2</sub> required			1.3827	0.3180
	Total Air required			5.3185	1.2232
	Air -Fuel Ratio (by mass)			5.5401	1.2742

Due to the horizontal orientation of the gasifier used in this work, the air flow rate had to be high enough to cause pneumatic injection of the sawdust. Thus, the chosen fuel flow rates in the range of 1 to 20 g/min and the equivalent air flow rates were used to determine the optimal feed settings. An alternative approach to defining the fuel flow rate was through modeling using computational fluid dynamics (CFD) highlighted in Section 4.6. The preliminary trials revealed smooth operation at 5 g/min of fuel and 5 l/min of air. Below these rates blockages occurred at the fuel inlet due to insufficient injection momentum, while solvent carry-over in the tar capture system occurred for the higher flow rates. A general relationship between consistent air flow rate ( $Q_a$  in l/min) and mass flow rate of wood particles ( $\dot{m}_f$  in g/min) was expressed using Equation 4.12, based on calibration tests carried out prior to experimentation. This expression was used to establish different AFR settings for preliminarily experimental tests.

$$\dot{m}_f = 1.0619Q_a \quad (4.12)$$

## **4.6 Summary**

In this chapter the approaches used during gasification trials and data measurements are presented. The designed experimental rig set-up provides capability for investigating the performance of the horizontal entrained flow gasifier and the effect of catalysts on the gasification products. In the gasification procedure section, the overall process is described in detail including setting up and operating procedures. Similarly, all parameters necessary for the investigation are presented in the section of experimental data measurements. Flow parameters such as velocities and particle trajectories are important in evaluating the performance of the gasifier and the catalytic reactor. These parameters provide the visualisation of the flow field in which areas with detrimental recirculation zones can be identified and rectified. However, their experimental studies are intensive and costly. An alternative approach is through modeling using a CFD. Through this tool, optimal experimental operating parameters such as feed rate and syngas outflow can be determined at low cost. The next chapter describes the modeling procedures for the gasification process and catalysis studies.

## **5 MODEL DEVELOPMENT**

### **5.1 Introduction**

This chapter presents the development models for the gasification process and catalytic processing of the gasification products. The gasification models were used to investigate the performance of an entrained flow gasifier in a horizontal configuration. In addition a vertical configuration is presented for comparison purposes. The principle operating theories of the gasification unit under consideration are not yet known in terms aerodynamics and gasification characteristics. Since the experimental study of the former requires intensive velocity measurements, computational fluid dynamics (CFD) adopting FLUENT 12.1 software models were employed as an alternative tool. Non-isothermal flow field prediction was important as it helps to establish appropriate experimental operating parameters such as air-fuel flow rates and temperatures. The gasification process can be modeled using a partially premixed model and compared to the experimental data [116]. Furthermore, wood particle combustion and particle trajectories are predicted using a discrete phase model. Particle combustion along the gasifier provide clear evidence on the effect of configuration on the gasifier performance.

Modeling the catalytic processes was intended to investigate selective oxidation of gasification products using catalysts with reduction oxidation (redox) characteristics. The catalysed gas-solid modeling was performed using a species model available in the FLUENT software. The species model consisted of chemical kinetic laws which allow the determination of reaction rates and catalytic parameters for the specified reactions. The gas species input to this model are derived from the gasification model described earlier and the numerical results can be compared with the experimental data. This research covered only modeling of the gasification process using the entrained-flow gasifier reactor and catalytic processing of the product gas. Both horizontal and vertical configurations were simulated to compare their performances. The effect of catalyst loading on the product gas was studied using ceria doped pumice.

## 5.2 Gasification Predictions

### 5.2.1 The model geometry

The configuration of the experimental set-up used in this study is shown in Section 4.3.1 was adapted in developing the model for gasification predictions. Since the gasification processes were carried out in the gasifier and the products were processed in the reactor, only these two parts were considered for simulations. Figure 5.1 shows the model geometry comprised of a gasifier and a catalytic reactor. The two parts were connected with a pipe, 10 mm diameter of the same material. It should be noted that the air-fuel mixture requires partial premixing before injection into the gasifier. This process was achieved in a pipe ( $\text{Ø}10 \times 40 \text{ mm}$ ) connected at the inlet of the gasifier. Coupling the gasifier and the catalytic reactor provided accurate predictions by accounting the effect of porosity in the catalytic bed materials. Similar components were generated for predicting the performance of the entrained flow gasifier in a vertical configuration.

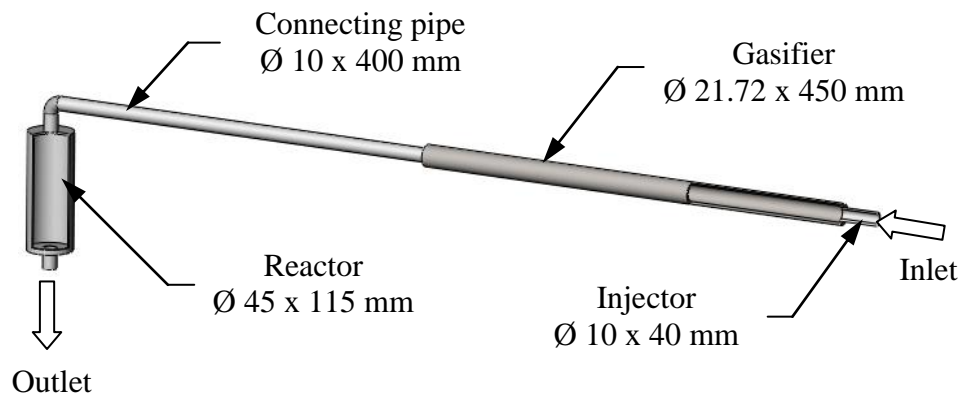


Figure 5.1 The Model geometry representing the experimental rig

### 5.2.2 The computational domain and grid quality

The computational domain represents the area in which the gasification process and the resulting products were predicted. This region includes the swept volumes of the gasifier, reactor and the connecting pipes as described in the model geometry in Section 5.2.1. Since the geometry was symmetrical, the computational domain could be treated as 2D or 3D. Although the former simplifies the computation, treating it in 3D was necessary to capture the particle trajectories [95].

In performing numerical computations using FLUENT software, the particular domain is discretised into mesh grids. The software provides various 3D mesh cells including tetrahedron, hexahedron, polyhedron, pyramid and wedge as shown in Figure 5.2. The selection of cell type depends on the complexity of model geometry, nevertheless, hexahedral cells are recommended. Although it is time-consuming in generating these mesh cells, it has great advantages in reducing computational expense. Furthermore, the mesh quality is important in increasing the accuracy of the numerical solution. There are different criteria used to define the mesh quality including skewness, which is defined as the difference between the shape of the cell and the shape of an equilateral cell of equivalent volume. Highly skewed cells can decrease accuracy and destabilize the solution. Skewness is expressed as Equiangle Skew ( $Q_{EAS}$ ) and Equivolume Skew ( $Q_{EVS}$ ). The former is defined using Equation 5.1 while the later Equation 5.2 [95]. The acceptable quality of the mesh based on skewness range between 0 and 0.95 on a 0 to 1 scale.

$$Q_{EAS} = \max \left[ \left( \frac{\theta_{max} - \theta_{eq}}{180 - \theta_{eq}} \right), \left( \frac{\theta_{eq} - \theta_{min}}{\theta_{eq}} \right) \right] \quad (5.1)$$

$$Q_{EVS} = \left[ \frac{S_{eq} - S}{S_{eq}} \right] \quad (5.2)$$

Where  $\theta_{max}$  and  $\theta_{min}$  are maximum and minimum angles in degrees between the edges of the element respectively, while  $\theta_{eq}$  is the characteristic angle corresponding to an equilateral cell of similar form (for hexahedral elements,  $\theta_{eq}=90$ ). Parameter  $S_{eq}$  is the maximum volume of an equilateral cell and  $S$  represents the volume of the similar mesh element.

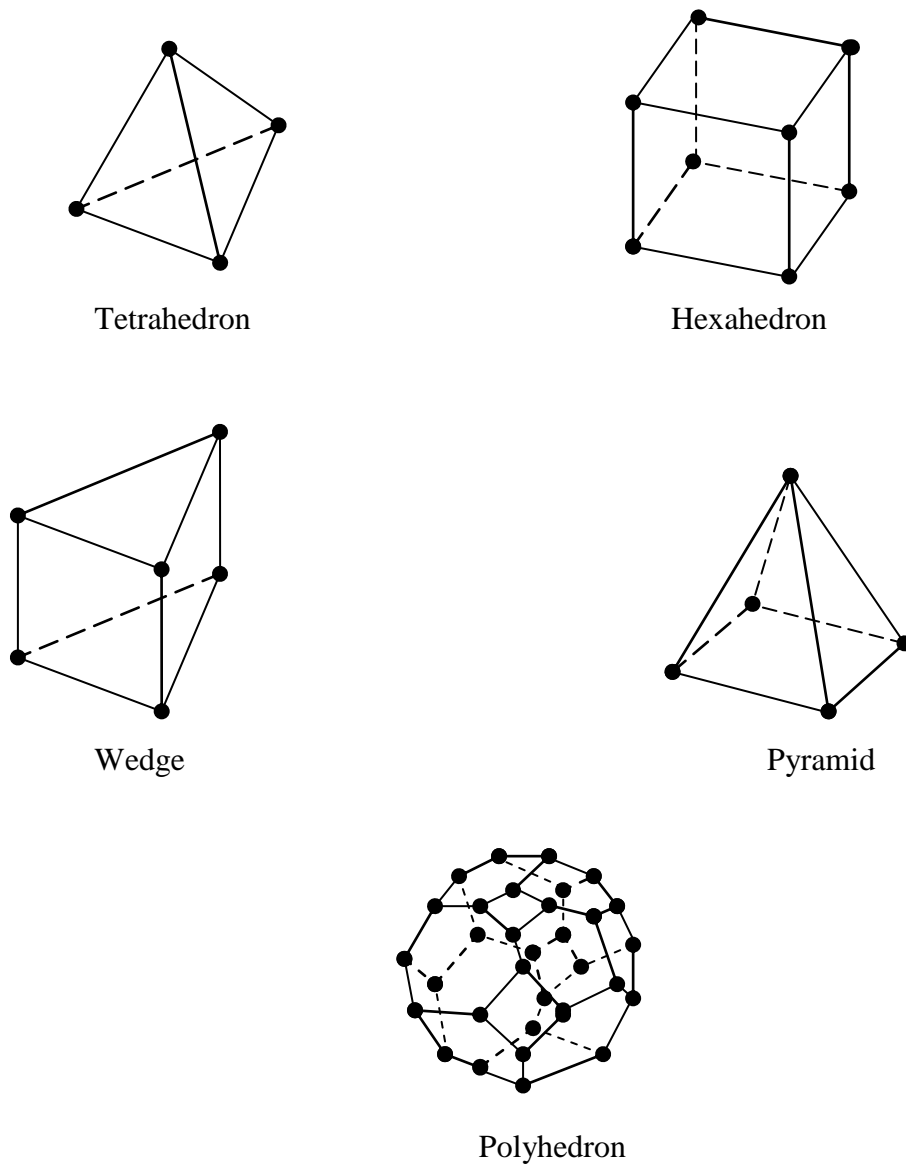


Figure 5.2 Types of 3D mesh cells

Figure 5.3 shows the mesh grids on the computational domain. The gasifier and reactor were modeled using hexahedral cells. Although tetrahedral meshes were generated on the connecting pipe between the gasifier and reactor, its consequence on computation cost was negligible. The maximum skewness achieved was 0.78 and average of 0.22 which were in good agreement with the recommended value of less than 0.95 and 0.33 respectively [95].

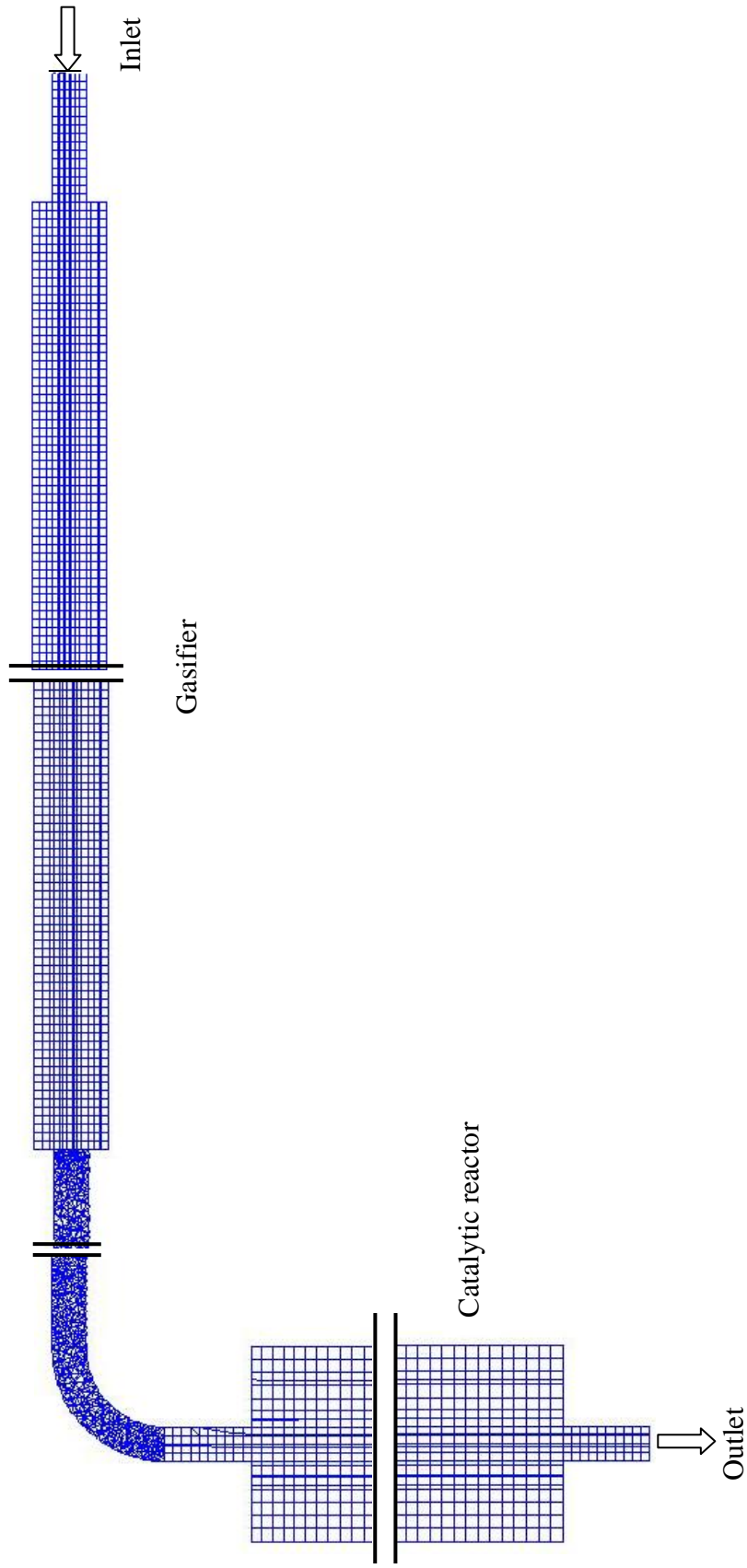


Figure 5.3 The meshed computational domain

### 5.2.3 Gasification models

The gasification process was predicted using partially premixed combustion and discrete phase models. The partially premixed combustion model discussed in Section 2.3.2 was selected based on the experimental procedures employed during the study. The model solves the transport equations for the species fractions and temperature. It employs the beta Probability Density Function in computing the chemistry interaction of the reactants. As the sawdust contains volatile matter, the secondary stream was enabled to treat separately the volatile matter and char. The gasification process yields many species and varies with operating conditions. Sixteen species were chosen based on the experimental results of this study. These components include: C, H, O, N, S, CH<sub>4</sub>, H<sub>2</sub>, N<sub>2</sub>, O<sub>2</sub>, C(s), CO, CO<sub>2</sub>, H<sub>2</sub>O, OH, C<sub>2</sub>H<sub>6</sub> and C<sub>3</sub>H<sub>8</sub>. Although OH and H<sub>2</sub>O were not measured in this study, these species are typically found in biomass gasification process [116]. While the concentration of the product species is dependent on the overall gasification process, the profile along the gasifier explains the effect of configuration.

The discrete phase model was employed to study the characteristics of wood particles under gasification conditions. The model predicts the trajectory of a discrete phase particle by integrating the force balance on the particle including the effect of heat, momentum and mass transfer. Fuel injection into the gasifier was defined by an inlet face with three tries to capture possible particle trajectories. As wood particles were non-spherical (Figure 6.3), a shape factor of 0.7 was chosen to affect the drag force in order to improve the prediction of particle velocity [116]. Based on the sawdust characterisation results, the maximum particle size was set at 500  $\mu\text{m}$  while the minimum size was assumed to be 1  $\mu\text{m}$ . The size distribution of wood particles was modeled to match the Rosin-Rammler equation with mean diameter of 388  $\mu\text{m}$ . The dispersion of particles due to turbulence in the gas stream was predicted using a stochastic tracking model (random walk). This model takes into account the effect of instantaneous turbulent fluctuation of velocity on the particle trajectories, which improves the accuracy of the simulation. Particle properties were set as shown in Table 5.1.

Table 5.1 Particle properties of pine sawdust [116]

Property	Unit	Value
Density	kg/m <sup>3</sup>	540
Specific heat capacity, Cp	J/kg-K	1000
Thermal conductivity	W/m-K	0.13
Latent heat		0
Vaporisation temperature	K	400
Volatile component fractions (% wt)		82
Binary diffusivity	m <sup>2</sup> /s	0.0005
Particle emissivity		0.9
Particle scattering factor		0.5
Swelling coefficient		0.7
Burnout stoichiometric ratio		2.7
Combustible fraction		19.3

#### 5.2.4 Boundary conditions

Gasifiers are sensitive to inlet conditions, specifically, air-fuel ratio and feed rate [44]. Boundary conditions used in this model were derived from the experimental data and are summarised in Table 5.2 and Appendix C. The mass flow inlet was set as normal to the boundary while particle injection was selected as from the inlet face shown in Figure 5.3. Furthermore, the mean mixture fraction was estimated from the probability density function (PDF) curve shown in Figure 5.4. As it can be seen from the figure, the appropriate fuel mixture fractions for gasification conditions range between 0.2 and 0.3. Thus, a fraction of 0.21 was selected for further simulation studies. The relationship between the mixture fraction ( $f$ ) and equivalence ratio ( $ER$ ) is given by Equation 5.1.

$$f = \frac{ER}{ER+r} \quad (5.1)$$

Where  $r$  is the air-to-fuel ratio on mass basis.

Furthermore, in enhancing smooth flow, a pressure of -50 Pa absolute was set at the outlet face to overcome the pressure drop in the bed material. This value chosen based on the experimental measurement at air low rate of 5 l/min as will be discussed in Section 6.4. Temperatures at the inlet and outlet were set to 300 K to represent ambient conditions.

Table 5.2 Parameters setting for boundary conditions

Parameter	Unit	Inlet	Outlet
Mass flow rate	kg/s	0.0003	
Temperature	K	300	300
Mean mixture fraction		0.21	
Pressure outlet	Pa		-50
Mean particle diameter	mm	0.388	

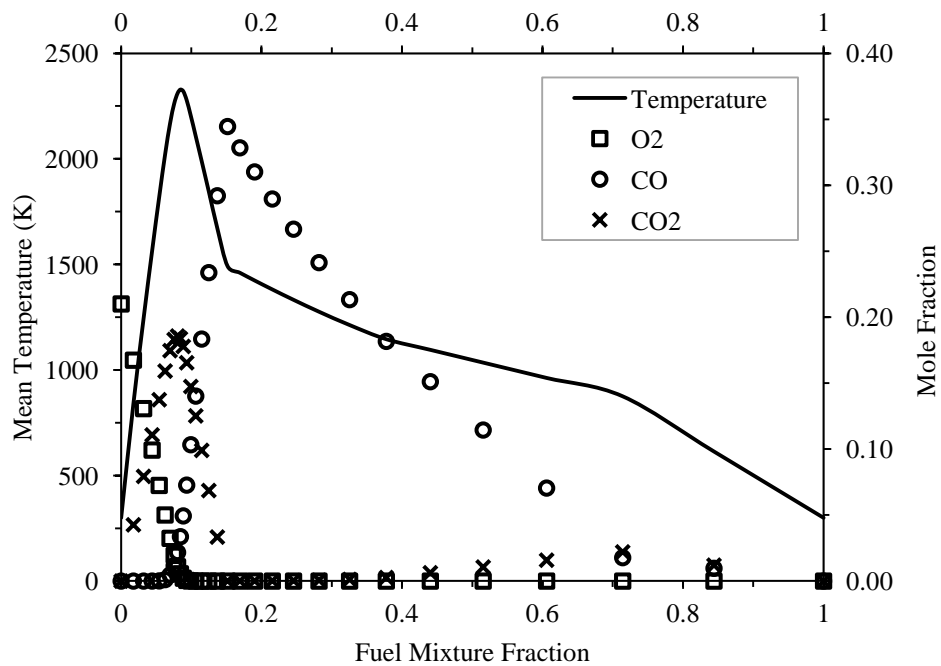


Figure 5.4 PDF curve for biomass combustion

### 5.3 Modeling of the Catalytic Processing of Gasification Products

#### 5.3.1 The model geometry

Figure 5.5 shows the model geometry used for catalytic processing of the gasification products. The geometry represents the setup employed for the experimental study. The system comprised of a reactor with inlet and outlet ports just as the configuration of the rig in the Chapter 4. The inlet ports represented the pipe connecting the gasifier and the reactor while the outlet port represented the reactor to the tar sampling system. All parts were made from a 316 stainless steel. Bed materials represented the catalysts used for selective oxidation of the gasification products. The reactor was kept vertical and the gas flow direction was top to bottom.

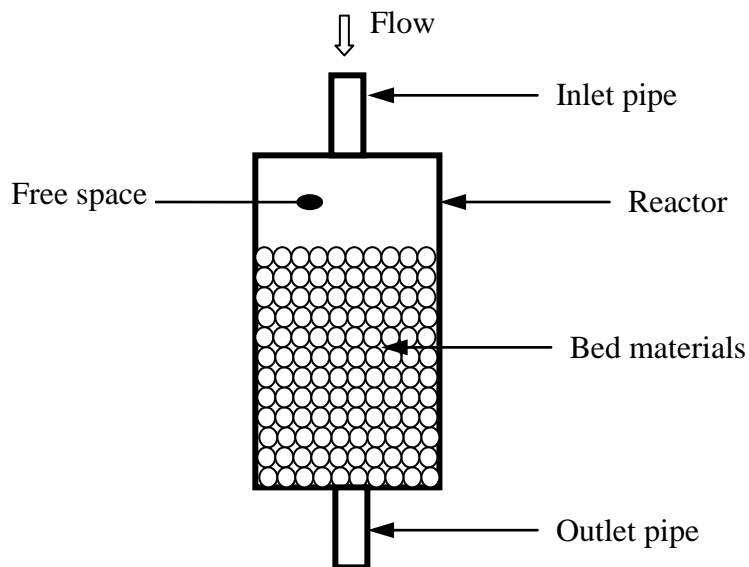


Figure 5.5 Model geometry of the catalytic reactor

#### 5.3.2 The computational domain

Figure 5.6 shows the computational domain for the catalytic reactor used in selective oxidation of the gasification products. The reactor was divided into fluid and porous zones. The fluid part comprised of the top section of the reactor and the connecting pipes at the inlet and outlet port. This region represents the syngas species transport and no chemical reactions take place. On the other hand, the porous zone represents the catalyst bed materials where the catalytic reactions occur. It should be noted that the empty space in the top portion of the reactor was intended to

enhance uniform diffusion of the reactants across the substrate through flow expansion.

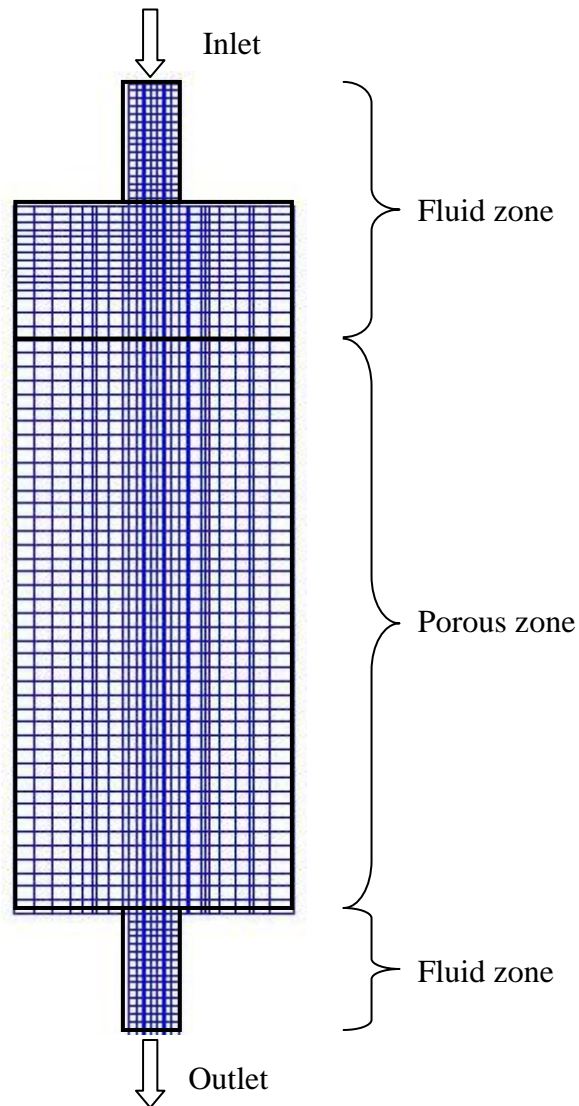


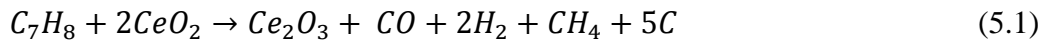
Figure 5.6 Computational domain of the catalytic reactor

### 5.3.3 Modeling approach

Catalyst bed and packing simulation involves modeling through porous media. The nature of the gas flow influences the performance of the catalytic reactor. The pressure gradient and velocity distribution through the substrate are of particular importance. These parameters are used to explain how the catalyst materials are loaded during the process and they can be investigated using a Species Transport

Model. The model is able to predict the species transport both with and without reactions.

In modeling the selective oxidation of gasification product gas, both wall and particle surface reactions were utilised. The former was used to predict the deposition of carbon causing catalyst deactivation (coking), while the latter used gaseous catalysed reactions. It was proposed that hydrocarbons were the main source of carbon deposition over the catalysts. Based on the experimental results, toluene showed decreasing trend compared to other hydrocarbons. Thus, toluene oxidation was chosen to represent other hydrocarbons as per reaction Equation 5.1. The produced carbon was reacted with ceria according to Equation 5.2 [117].



The interaction of catalyst and syngas components was also considered. The suggested reduction of ceria through H<sub>2</sub> reaction is described using reaction Equation 5.3 while oxidation with CO<sub>2</sub> is Equation 5.4.



#### 5.3.4 Boundary conditions

Model inputs for simulating the catalytic processing of the gasification products were derived from the gasification model described in Section 5.2 and the experimental conditions. The gas species extracted from the gasification tests are summarised in Table 5.3. The inlet temperature was set according to the measured value during the experimental tests. Pressure of -50 Pa absolute was set at the outlet as described for the gasification model Section 5.2.4. Catalyst loading was varied using surface site density described in Section 2.3.4. The calculated site densities of ceria at specific surface area of pumice (0.627 m<sup>2</sup>/g) and number of volumes (particles) of 1,227 were 4.91x10<sup>-9</sup>, 1.09x10<sup>-8</sup> and 1.31x10<sup>-8</sup> kgmol/m<sup>2</sup> for 0.65 g, 1.44 g and 1.73 g loading respectively.

Table 5.3 Boundary conditions for catalysis trials as measured experimentally

Parameter	Inlet	Outlet
Mass flow rate (kg/s)	0.00021	
Temperature (K)	623	623
Pressure outlet (Pa)		-50
<i>Syngas composition (mole fraction)</i>		
H <sub>2</sub>	0.1410	
CO	0.2175	
CO <sub>2</sub>	0.1374	
CH <sub>4</sub>	0.0356	
C <sub>2</sub> H <sub>6</sub>	0.0163	
C <sub>3</sub> H <sub>8</sub>	0.0037	
N <sub>2</sub> (by difference)	0.4321	
<i>Tar (mole fraction)</i>		
Phenol	0.0015	
Cresol isomers	0.0006	
Benzene	0.0085	
Toluene	0.0028	
Ethylbenzene	0.0004	
Xylene isomers	0.0015	
Naphthalene	0.0007	
Acenaphthylene	0.0002	

#### 5.4 Solution Algorithms and Accuracy

The computations of process parameters for predictions of gasification and catalytic processing of the product gas were performed adopting the Pressure-Based Segregated Algorithm. This algorithm was chosen due to memory-efficient compared to the Pressure-Based Coupled Algorithm [95]. In the segregated algorithm, the governing equations are solved sequentially and the solution loop is

carried out iteratively to obtain converged numerical solution. The solution steps for the segregated algorithm are illustrated in Figure 5.7.

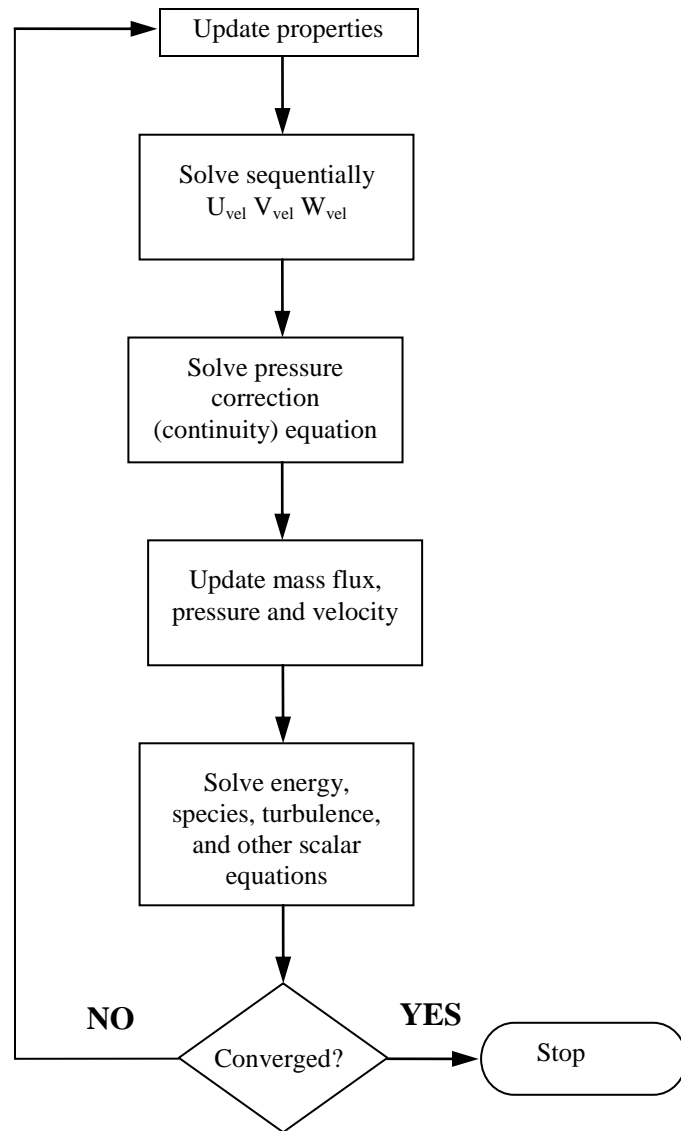


Figure 5.7 Pressure-Based Segregated Algorithm

As illustrated in Figure 5.7, steps in each iteration involve updating fluid properties such as viscosity, density, specific heat and others based on the current solution. Momentum equations are then solved using recent updated values of pressure and face mass fluxes to obtain new values of velocity field and mass-flux. The updated velocity and mass-flux are then used in solving the pressure correction (continuity) equation. Face mass fluxes, pressure, and velocity field are then solved using the recent updated pressure. The obtained values are used to solve additional

scalars such as energy, species, turbulent, quantities, radiation intensity and others. The outcome at this stage is updated and checked for numerical solution convergence. The solution loop continues until the convergence criteria are met.

The accuracy of the numerical solution was based on the second-order upwind discretisation scheme. In this approach, higher-order accuracy is achieved at cell faces through a Taylor series expansion. The under relaxation values were used to control the convergence. For gas species these values were set in the range of 0.5 to 1, while for the pressure, energy and momentum were 0.3, 0.8 and 0.4 respectively. Furthermore, skewness of less than 0.8 was used as a driver for the grid sensitivity [95]. The residue values for solution convergence were set at  $10^{-4}$  for all parameters except energy which was  $10^{-6}$ .

## **5.5 Summary**

Modeling of gasification processes and selective oxidation of gasification products have been reported. The introduction highlights the research topic, the purpose of the modeling approach and the use of FLUENT 12.1 as the software used for modeling. In the gasification model, the chapter describes the layout of the model geometry representing the experimental rig as well as the quality of mesh cells. In addition, theories relevant to the gasification process are explained in terms of a partially premixed combustion model. To account for the effect of wood particle thermodynamics, a discrete phase model has been incorporated. Furthermore, boundary conditions are provided to simulate the experimental conditions.

For catalytic processing of gasification products, the model geometry describes the catalytic reactor and the bed material while the computational domain details the grid cells and the quality. The theories on catalytic process are based on the Species Transport Model using particle surface reaction. Detailed descriptions of major chemical reactions and boundary conditions are also provided.

## 6 EXPERIMENTAL RESULTS

### 6.1 Introduction

This chapter presents and discusses the research findings obtained from the experimental study. The results for characterisation of wood powder, pumice and other catalyst are presented and discussed. Analysis of the gasification product gas from non-catalytic tests is provided to evaluate the performance of the entrained-flow gasifier in a horizontal configuration. Similarly, catalytic gasification results are discussed to explain the effect of the catalysts on the gasification product gas.

### 6.2 Material Characterisation

#### 6.2.1 Characterisation of the feedstock

Table 6.1 highlights the proximate and ultimate analysis of a commercial wood powder. It can be seen that the fuel is composed of mainly volatile matter (approximately 82 %) with fixed carbon around 14 %, while ash content is considered to be of trace amount. The observed low moisture content (2.47 %) is a result of preconditioning the fuel through a drying process. Drying increases energy density of the feed fuel and is of particular importance as it enhances the pneumatic feed which is crucial in entrained flow gasification. The ultimate analysis show that carbon and hydrogen values are 49.40 % and 5.90 % respectively. The oxygen content is high at 40.68 which must be taken into account during the gasification process. Sulphur is found in trace amount (0.02 %) which ensures low formation of hydrogen sulphide (H<sub>2</sub>S) that could poison the catalysts.

Table 6.1 Proximate and ultimate analysis of sawdust

Proximate Analysis (% wt)		Ultimate Analysis (% wt)	
Moisture content	2.47	C	49.40
Ash	0.43	H	5.90
Volatile matter	82.73	S	0.02
Fixed carbon	14.37	N	0.30
Total	100.00	O by difference	40.68
Gross calorific value, (MJ/kg)	19.09		

### 6.2.2 Thermogravimetric analysis

Investigation on the thermal behavior of sawdust is presented in Figure 6.1. The figure shows four distinct phases of mass loss. These losses are due to moisture release at temperatures below 105 °C followed by a large loss of volatiles between 130-300 °C. Further heating to 300-500 °C results in significant loss of volatile and above 500 °C the loss is considered a trace amount. The volatiles released at 130-150 °C has been identified as hemicellulose while at 300-500 °C are mixed cellulose and lignin and above 500 °C mainly lignin [118, 119]. From these results it can be concluded that, most of the hydrocarbon compound leaves the biomass at about 500 °C, thus suggesting being a minimum working temperature for wood powder devolatilisation. This temperature is important in setting the range at which the gasifier reactor need to be preheated before feeding the feedstock fuel.

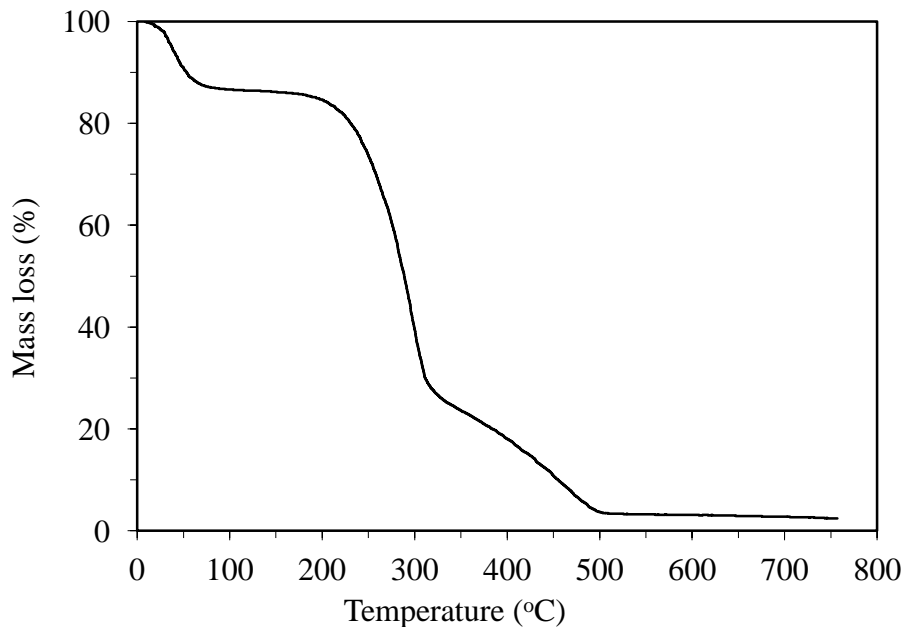


Figure 6.1 Thermogravimetric behavior of pinewood sawdust

### 6.2.3 Particle size distribution

Figure 6.2 shows the particle size distribution for the wood powder employed during gasification tests. It can be observed that about 80 % of particles falls below 0.5 mm and the balance ranges from 0.5 to 1.18 mm. It should be noted that, although all particles were screened using 0.5 mm mesh size in a cutting mill machine, the presence of the balance is mainly due to nonspherical shape as revealed

by Scan Electron Microscope (SEM) as shown in Figure 6.3. The  $d_{50}$  value particle distribution was found to be 0.39 mm as determined by interpolation. The averaged difference between the total mass of the test portion and the total mass of all fractions was 0.77 % which is within a recommended range (<2.0 %) by BS EN 15149:2010 [106].

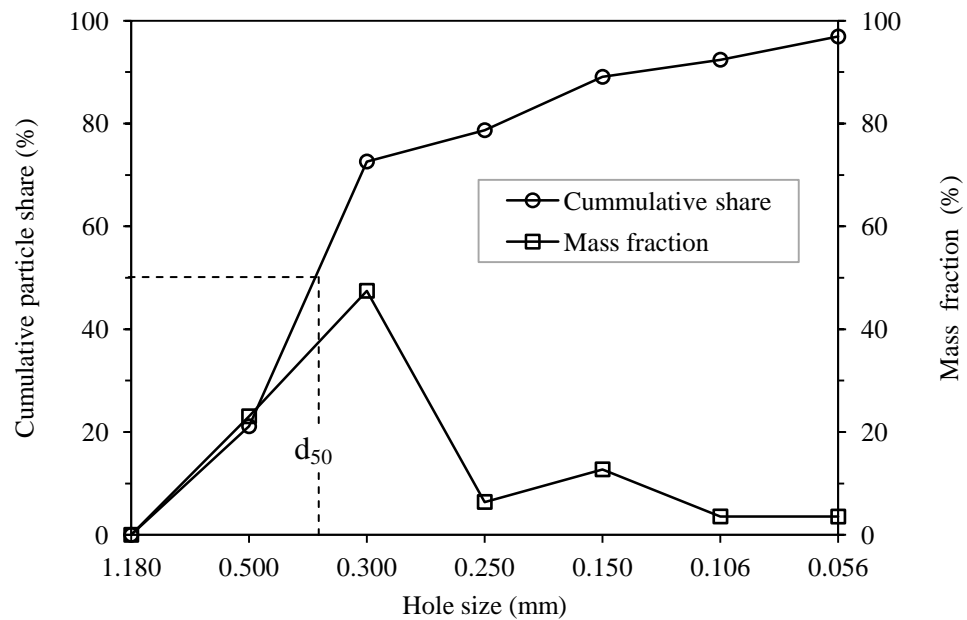


Figure 6.2 Particle size distribution of the wood powder

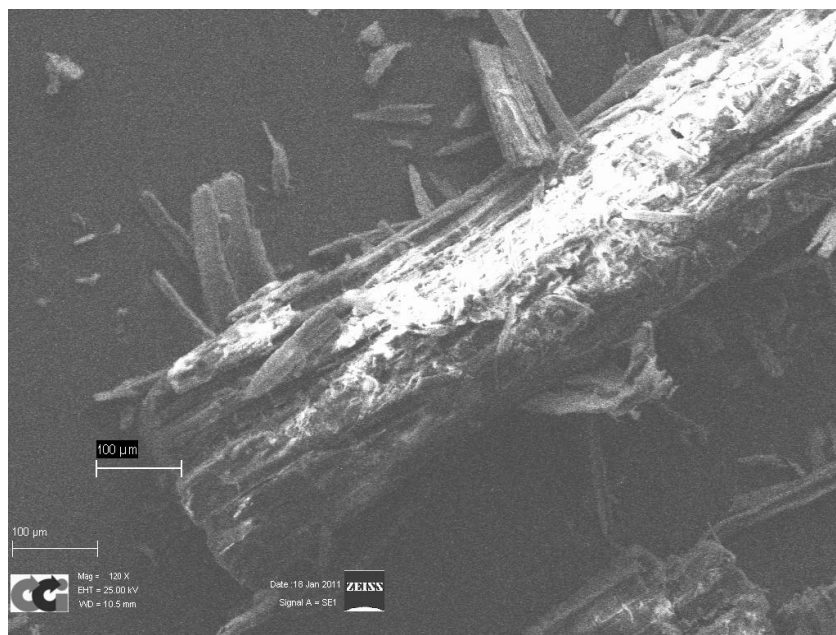


Figure 6.3 Particle size and shape of wood powder

### 6.3 Characterisation of Pumice and Kaolin

#### 6.3.1 Major and trace elements

Figure 6.4 shows the XRD pattern of the three different pumice samples and one for kaolin. From Figure 6.4 (a-d), the peak at  $2\theta=20.865^\circ$ ,  $26.651^\circ$  and  $50.164^\circ$  confirms the presence of quartz. Moreover, the diffraction band for Mexican pumice was broad at  $2\theta = 12-35^\circ$  compared to those from Arusha and Mbeya Tanzania. This difference highlights that Mexican pumice was more amorphous compared to the other pumice samples as indicated in Figure 6.4 (c). Although amorphous silica was not detected by XRD, other researchers have reported similar finding has also been reported by Singh and Gilkes [120]. For kaolin, the observed peaks at  $2\theta=12.407^\circ$ ,  $19.869-21.229^\circ$ ,  $23.126-26.510^\circ$ ,  $24.963^\circ$ ,  $26.510^\circ$  and  $35.023-39.544^\circ$  confirms the presence of kaolinite. The presence of quartz was confirmed by the peaks occurring at  $2\theta = 20.865^\circ$ ,  $26.651^\circ$ ,  $54.120^\circ$  and  $62.180^\circ$ . Thus, pumice samples were mainly composed of amorphous silica and quartz, while kaolin was composed of kaolinite and quartz [121, 122].

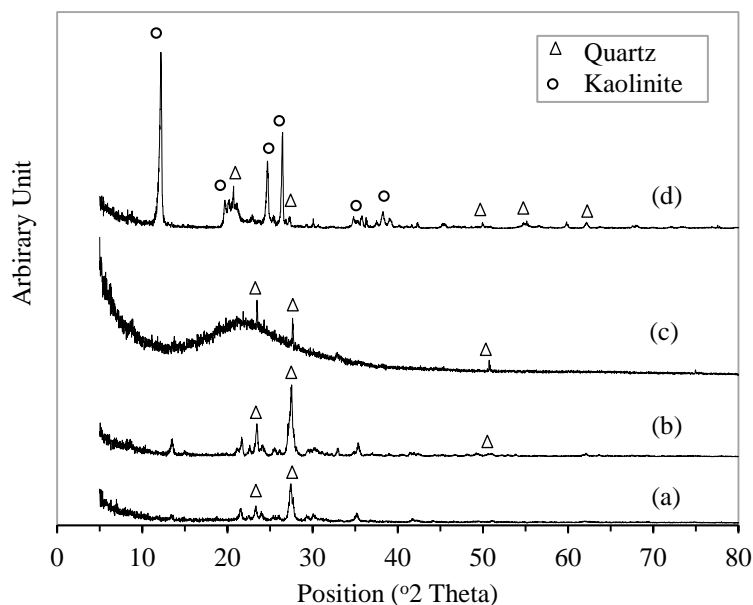


Figure 6.4 XRD pattern for the calcined (a) Pumice from Arusha, Tanzania (b) Pumice from Mbeya, Tanzania and (c) Pumice from Mexico and (d) Kaolin from Pugu Hills , Tanzania

Table 6.2 presents elemental analysis of the pumice and kaolin samples. This analysis was conducted to determine the chemical composition of the catalyst

supports. It can be seen from the table that, regardless of the sample source, pumice exhibited similar elemental composition as revealed by XRD analysis (Figure 6.4). The observed high concentration of alkali metals ( $\text{Na}_2\text{O}+\text{K}_2\text{O}$ ) of about 10 wt % suggests that pumices are basic in nature. Furthermore, high silica and alumina content ensures possession of good thermal stability. Although the composition of pumice is similar to that of kaolin, the concentration of some major elements is different. For instance, kaolin has a high concentration of alumina and volatiles compared to the pumice. The difference in alkali metals content suggests different acid-base characteristics of these catalyst supports. Trace element analysis revealed concentration of Zr (3753-4760 ppm) in pumice and kaolin (9119 ppm) for samples from Tanzania. Although zirconium was in trace amount, it may contribute to the oxygen storage capacity of the support. It is also noticed that both Tanzanian pumice have high values of S, Cl, Rb, Sr and Ba. This difference could be due to the variation of mineralogy of the location and geological formation of volcanic pumice [97].

Table 6.2 Elemental analyses of the pumice from Mexico (MEX), Arusha (ARU), Mbeya (MBY) and Kaolin (KL) from Pugu Hills

	Major elements (wt %) <sup>a</sup>				Trace elements (ppm) <sup>b</sup>				
	Pumice			Kaolin		Pumice			Kaolin
	MEX	ARU	MBY	KL		MEX	ARU	MBY	KL
SiO <sub>2</sub>	55.50	50.02	46.79	49.66	S	673	1764	1273	1004
TiO <sub>2</sub>	0.26	0.65	0.68	0.35	Cl	565	1775	1477	nd
Al <sub>2</sub> O <sub>3</sub>	14.13	15.49	16.3	32.85	V	92	bd	bd	bd
Fe <sub>2</sub> O <sub>3</sub>	2.20	4.70	5.13	0.74	Cr	55	109	108	107
MnO	0.10	0.16	0.17	0.01	Co	8	13.6	16.7	1.6
MgO	0.36	1.37	1.38	0.04	Cu	9	bd	bd	bd
CaO	1.35	2.67	2.56	0.01	Zn	132	54	64	bd
Na <sub>2</sub> O	5.28	5.96	5.24	0.18	Ga	34	27	33	42
K <sub>2</sub> O	3.18	3.17	3.30	1.71	As	35	17	bd	bd
P <sub>2</sub> O <sub>5</sub>	0.09	0.42	0.39	0.07	Rb	66	606	682	455
LOI	3.24	3.02	4.35	10.20	Sr	804	1268	1631	150
Total	85.69	87.28	85.61	96.12	Zr	636	3753	4760	9117
Si/Al	3.47				Mo	6	12	bd	bd
CeO <sub>2</sub>	8.53*	bd	bd	bd	Ag	42	65	80	31
C <sup>c</sup>	0.009	0.012	0.031	0.078	Ba	1057	3365	3443	461
					Pb	7	bd	bd	76
					Th	195	565	565	114
					U	4	bd	bd	5.9

• Concentration in ppm; bd=below detection limit; nd=not determined; a=major element by ICP-OES; b=trace element by XRF; c=determined by carbon and sulphur analyser; LOI=loss on ignition.

### 6.3.2 Thermogravimetric analysis

Thermogravimetric analysis was important in determining the thermal stability of the catalyst support. Figure 6.5 presents thermal characterisation of pumice and it can be observed that mass loss is higher in the temperature ranging from 200 to 500 °C and remains constant thereafter until 1000 °C. This loss is due to removal of volatiles that could be present in the pumice sample as confirmed by the loss on ignition (LOI) reported in Table 6.2. Moreover, at temperatures above 900 °C, pumice particles shrunk significantly showing a sign of phase change. According to thermal analysis (DTA-TG), shrinking and melting have been linked to the change of amorphous structure in the pumice particle [97]. The present findings support the hypothesis that pumice has good thermal stability.

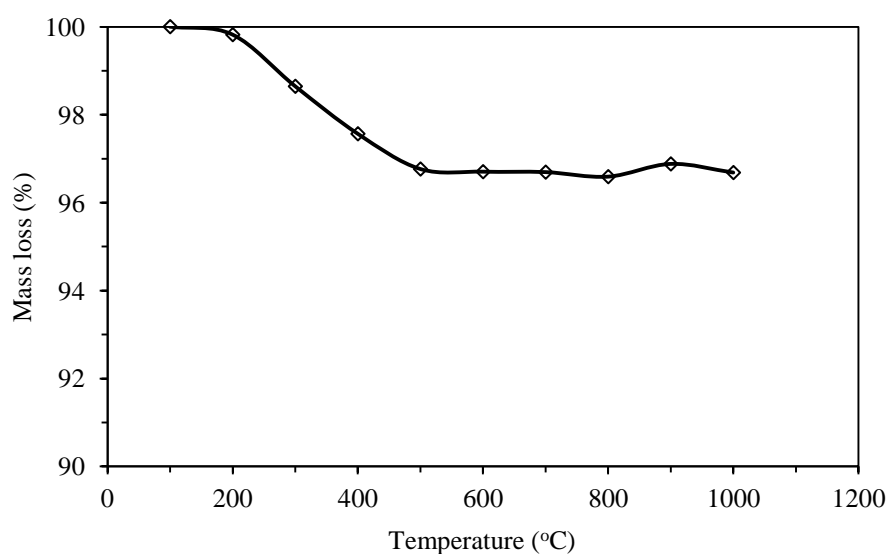


Figure 6.5 Mass loss analysis of the dried pumice

### 6.3.3 Characterisation of catalysts

The prepared catalysts were characterised based on the concentration on the catalyst support and the results are presented in Table 6.3. The concentration of active sites was determined by ICP-OES, while XRD was employed for determining the oxidation state of the catalysts. These compositions were used to determine the total mass of the catalyst used for each test, respectively.

Table 6.3 Prepared catalysts and their composition as determined by ICP-OES

Catalyst	Active site	Catalyst composition (% wt)		
		Batch 1	Batch 2	Batch 3
Ceria doped pumice	CeO <sub>2</sub>	2.49	5.75	6.87
Nickel doped pumice	NiO	3.20	5.70	
Copper doped pumice	CuO	2.02	5.86	9.41
Kaolin-Ceria	CeO <sub>2</sub>	9.2	14	21
Kaolin-Ceria-Zirconia	CeO <sub>2</sub> /ZrO <sub>2</sub>	14/14		

Figure 6.6 compares the XRD spectrum of pumice and the derived catalysts to investigate the oxidation state of ceria on the pumice support. The spent catalysts are also presented to study the effect of coking on the oxidation state of the active sites. A good agreement of ceria peaks was observed on the ceria doped pumice spectrum as well as for the spent catalyst. It can therefore be confirmed that the active sites were in the form of cerium (IV) oxide. The observed intensities of the quartz peaks in the fresh pumice as detailed in Figure 6.4 were completely suppressed in the spent pumice. A possible attribute to the suppression of these peaks could be due to coke deposition on the pumice surface resulted from the gasification product.

Figure 6.7 shows the XRD spectra for copper doped pumice catalysts. The occurrence of peaks at  $2\theta=35.3^\circ$  and  $38.6^\circ$  confirms the existence of CuO in the pumice support. The observed clear peaks of CuO indicate that the active sites were well dispersed over the pumice support. These peaks were almost suppressed for the spent catalyst as seen from Figure 6.7 (c). The disappearance of the copper peaks could be due to coking as a result of hydrocarbon dissociation and adsorption over the catalyst as discussed in Section 6.8.

The oxidation state of kaolin/CeO<sub>2</sub> was determined by XRD as shown in Figure 6.8. It can be seen from the figure that the XRD spectra for the prepared kaolin/CeO<sub>2</sub> consist of specific peaks of ceria, thus, confirming the oxidation state of the catalyst. The remaining peaks correspond to the existence of kaolinite which indicates that both ceria and kaolinite were equally dispersed over the surface. Similar findings can be seen for the spent catalyst. However, the disappearance of some peaks in the spent catalyst can be explained as a deactivation caused by coking as discussed in Section 6.8.

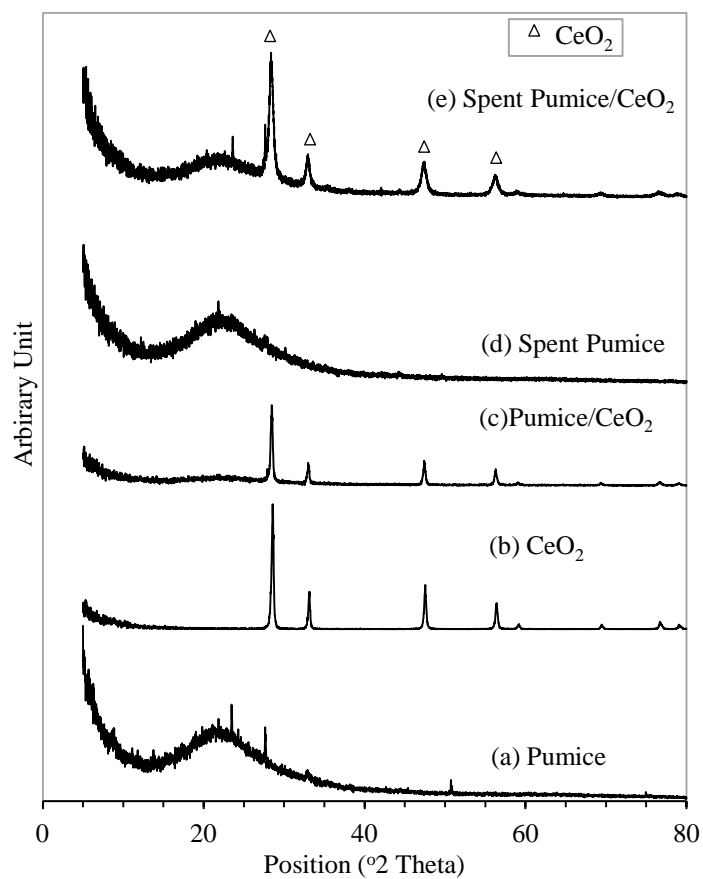


Figure 6.6 XRD analysis of the pumice and the derived ceria doped pumice catalysts

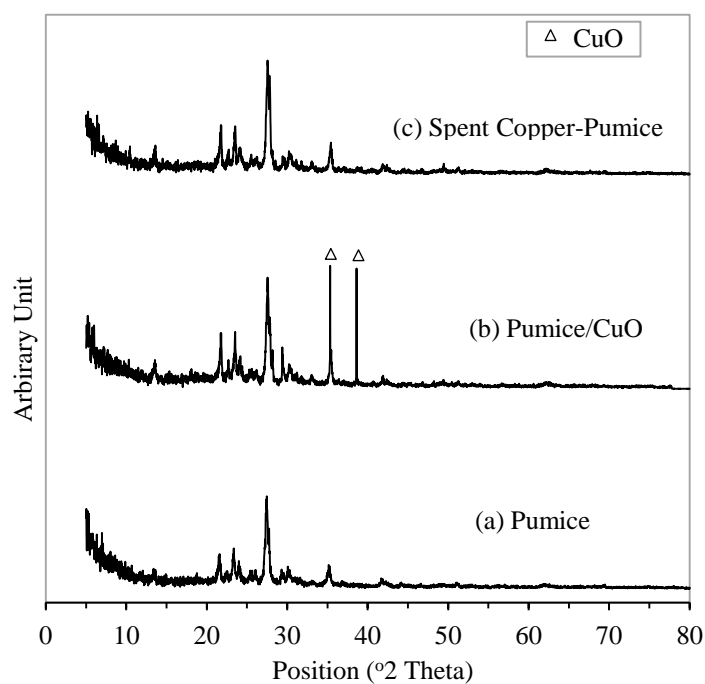


Figure 6.7 XRD analysis of the pumice and the derived copper doped pumice catalysts

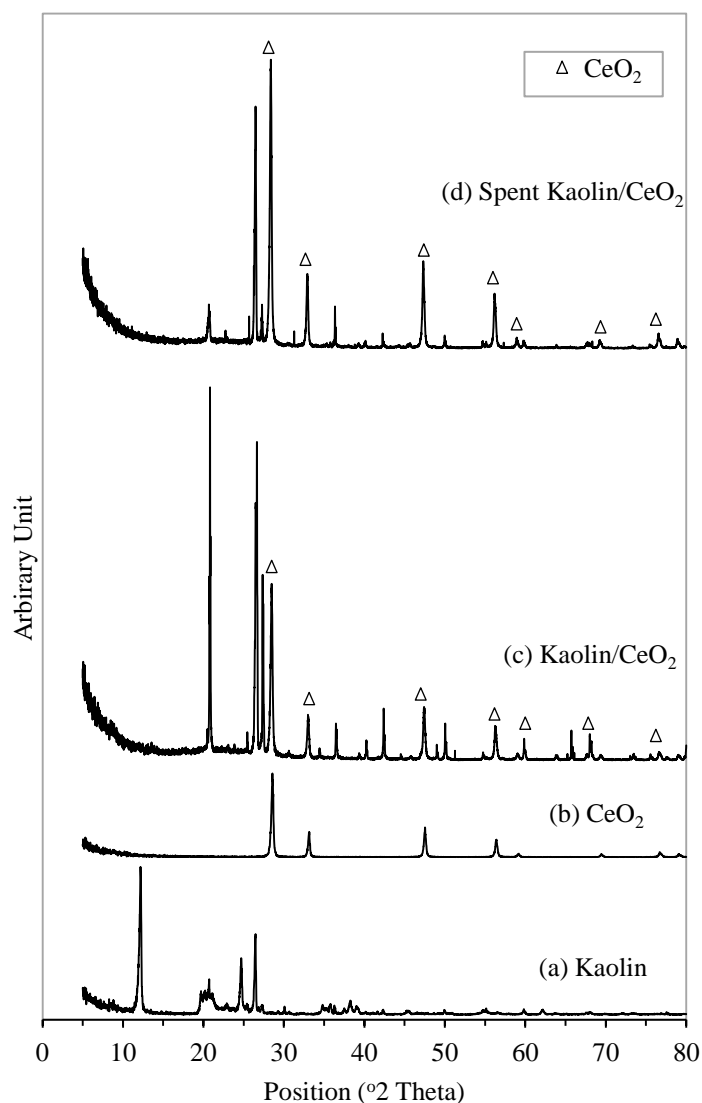


Figure 6.8 XRD analysis of the pumice and the derived ceria doped kaolin catalysts

XRD spectra of the calcined kaolin treated with  $\text{CeO}_2$  and  $\text{ZrO}_2$  is presented in Figure 6.9. It can be seen from the figure that the peaks occurring at  $2\theta=28.34^\circ$ ,  $32.88^\circ$ ,  $47.27^\circ$  and  $56.16^\circ$  correspond to the cerium (IV) oxide. In addition the peaks for zirconia were not detected indicating that zirconia inserted into the framework of ceria and form solid solution of ceria-zirconia compound. The formation of ceria-zirconia improves catalytic activity towards volatile organic compounds [60]. Furthermore, the disappearance of the peak at  $2\theta=12.2^\circ$  can be explained as transformation of crystalline kaolinite to amorphous phase due to thermal treatment [121].

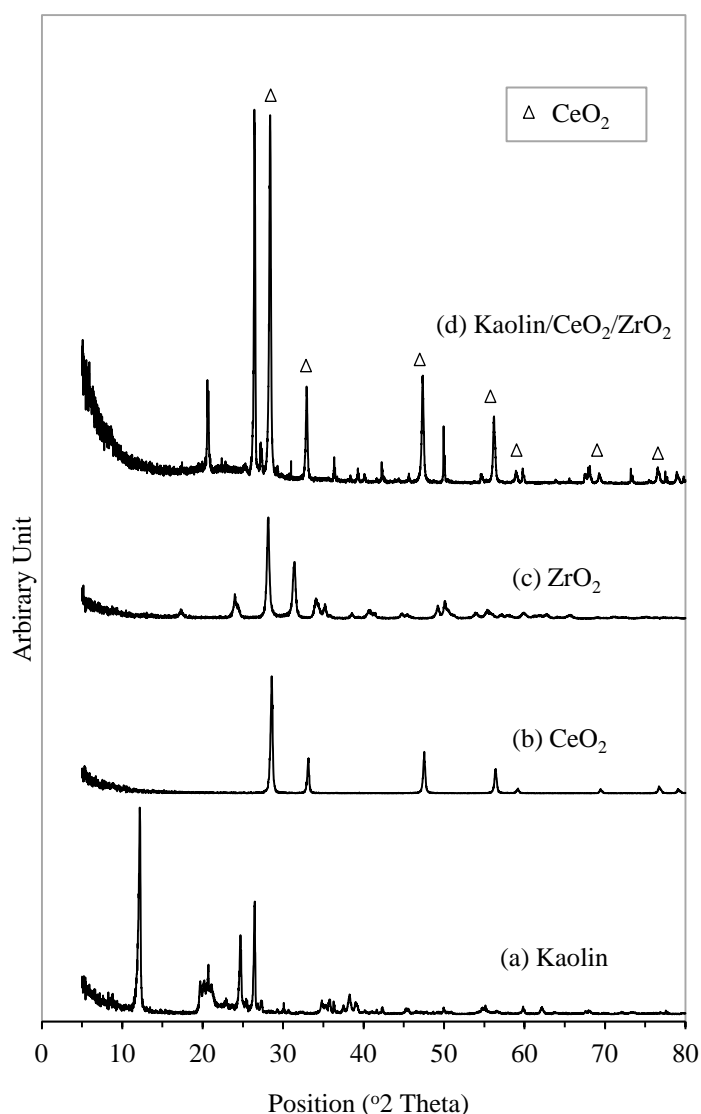


Figure 6.9 XRD analysis of the pumice and the derived ceria and zirconia doped kaolin catalysts

XRD analysis of nickel doped pumice is shown in Figure 6.10. From Figure 6.10 (b) it can be seen that the spectrum for pumice/NiO shows major peaks at  $2\theta=37.344^\circ$ ,  $43.290^\circ$  and  $62.922^\circ$  which confirm the existence of nickel in form of nickel (II) oxide (NiO). In addition the clear peaks of NiO indicate that the active sites were well dispersed over the pumice support. Similar findings have been reported on the characterisation of NiO by Deraz et al [123]. For the spent catalyst, NiO peaks are almost suppressed as seen in Figure 6.10 (c). The disappearance of nickel (II) oxide peaks can be linked to the catalyst deactivation as result of carbon deposition as discussed in Section 6.8. Hydrocarbons present in the syngas dissociate on the nickel oxide surface to produce carbon which is then gasified to CO according

to the reaction ( $NiO + C \rightarrow Ni + CO$ ). The excess deposited carbons encapsulate nickel sites thus inhibiting the redox cycle which is necessary for catalytic activity [124].

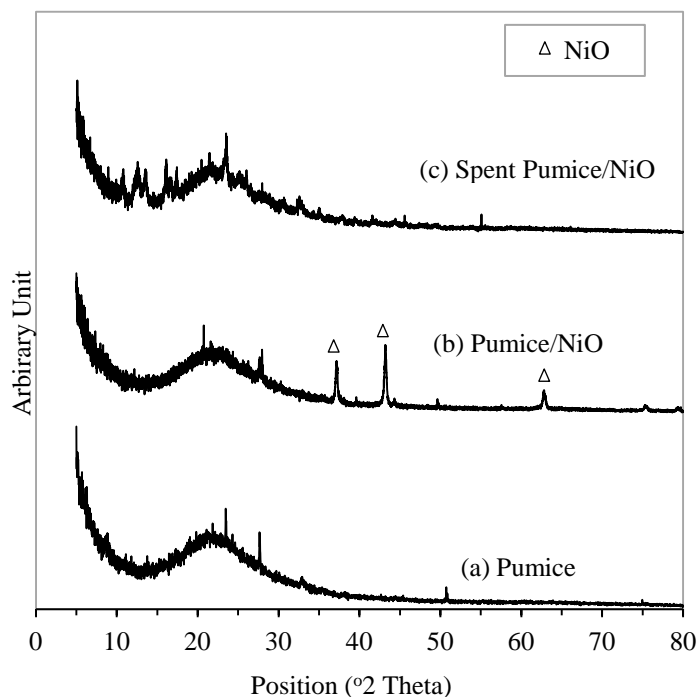


Figure 6.10 XRD analysis of the nickel doped pumice catalysts

The overall results from characterisation of wood powder show that minimum temperature required for preheating the gasifier reactor to initiate the gasification process is 500 °C. Wood particles are non-spherical, therefore a shape factor is required in improving the accuracy of the gasification modeling. Moreover, pumice and kaolin materials are mainly composed of amorphous silica and kaolinite respectively. While kaolinite possesses active sites [125], the formation of amorphous state on pumice suggests limitation on chemical reactivity [126]. Furthermore, the clear peaks of metal oxides indicate that the active sites were well dispersed over the pumice and kaolin support.

#### 6.4 Pressure Drop in the Catalytic Bed

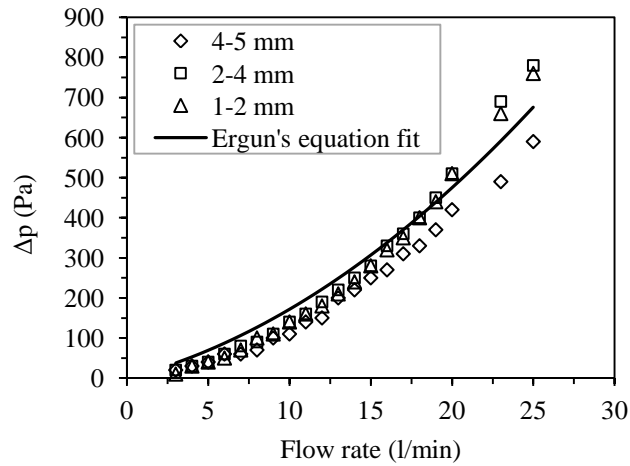
Pressure drop in the catalytic reactor with pumice as a bed material is shown in Figure 6.11. As can be seen from the figure, pressure drop was independent of the pumice particle size and bed length. This could be attributed to the high porosity of

pumice as discussed latter in this section. However, the correlation is limited to the particle size in the range of 1-5 mm. This finding suggests that a partial bed length can be employed to enhance uniform gas diffusion across the catalytic reactor due to flow expansion. The observed low pressure drop difference between the tests provides additional evidence that pumice is porous and is potential catalyst support in heterogeneous catalysis. In general, the experimental data are in good agreement with Ergun equation which is expressed by Equation 6.1. This equation takes into account the viscous and kinetic energy losses at a given gas flow rate through the bed material [127].

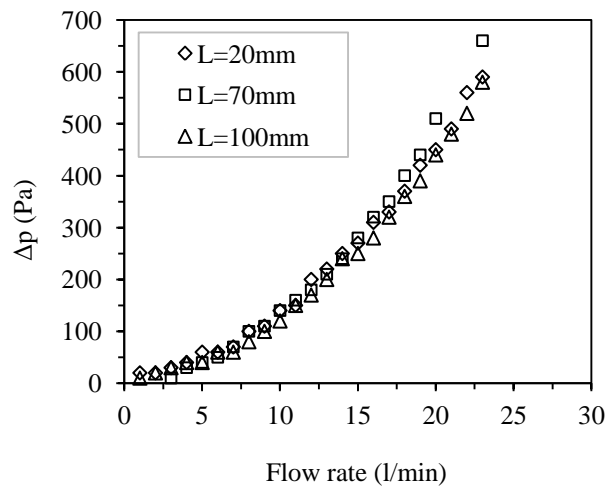
$$\frac{|\Delta p|}{L} = A \frac{\mu(1-\varepsilon)^2}{D_p^2 \varepsilon^3} v_s + B \frac{\rho(1-\varepsilon)}{D_p \varepsilon^3} v_s^2 \quad (6.1)$$

Where  $\mu$  is the fluid viscosity,  $D_p$  is the mean particle diameter,  $L$  is the bed depth,  $\rho$  is the fluid density,  $v_s$  is the superficial velocity and  $\varepsilon$  is the void fraction, defined as the volume of voids divided by the volume of the packed bed region. In this study constants  $A$  and  $B$  are 554 and 1.05 respectively.

The surface area, pore volume and pore diameter size of the pumice from Arusha determined using BET and BJH methods. The specific surface area was found to be 0.627 m<sup>2</sup>/g while pore volume and pore diameter were 0.006 cc/g and 3.892 nm. Another analysis for the catalytic reactor involved determining the bed porosity. The porosity of bed material was determined for the three types of pumice materials. Based on the natural stone method, the results showed that the Arusha pumice was highly porous (92 %) compared to those from Mbeya (89 %) and Mexico (75 %). These values are in good agreement with those reported by Asgari et al [128]. This finding suggests that pumice from Arusha has higher surface area and could be a potential catalyst support.



(a) Effect of particle diameter on pressure drop



(b) Effect of bed length on pressure drop

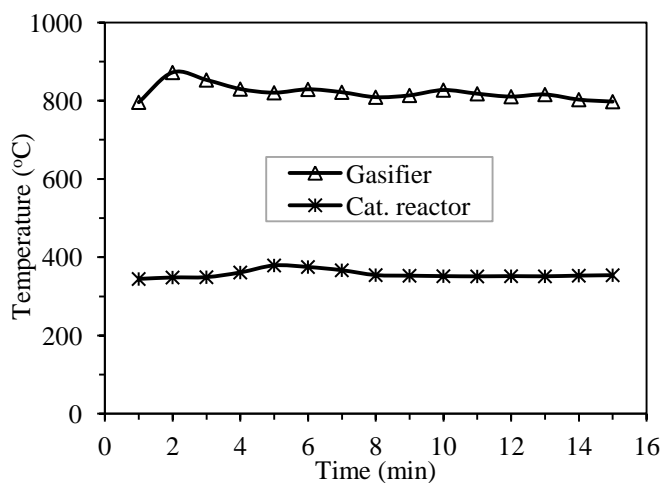
Figure 6.11 Pressure drop profile in the catalyst reactor

## 6.5 Gasification Conditions

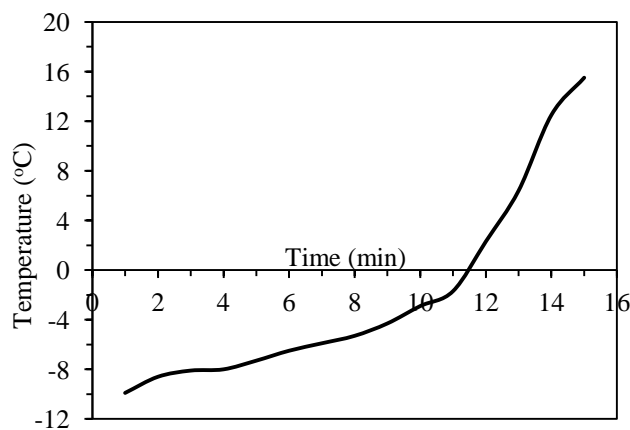
This section highlights the nominal conditions for the gasification process used during the experimental study. The results are being used as a control from which comparison with catalytic results can be made. The temperature in the gasifier reactor was taken at the center which was 250 mm from the gasifier inlet. For the catalytic reactor and tar sampling system the temperatures were taken at the void space and the fourth bottle respectively. The measured temperatures for the gasifier, catalytic reactor and tar sampling system during biomass gasification test are shown in Figure 6.12 (a and b). It can be seen from the Figure 6.12 (a) that temperature in the gasifier peaked at the start of the gasification test and stabilises thereafter. The peak reached 872 °C and thereafter remains in the range of 853 °C to

798 °C. The temperature in the catalytic reactor was between 379 °C and 345 °C. From Figure 6.12 (b) it can be seen that the temperature in the tar sampling system increased with time from -10 °C to 16 °C.

The observed peak in the gasifier highlights the existence of the combustion process favoured by high air-fuel ratio for the gasification process. The temperature difference in the catalytic reactor could be attributed to the additional heat due to catalytic reactions as well as the temperature fluctuations of the feed gas. For the tar sampling system, the rise in temperature can be linked to the heat exchange between syngas and isopropanol solution. It should be noted that tar compounds such as benzene and toluene can slip in the tar sampling system at ambient temperatures due to their low volatility [129]. Therefore, a combination of sampling time and temperature of the isopropanol can affect the concentration of tar compounds. The loss of isopropanol due to temperature rise has also been reported by Malhotra [130].



(a) Temperature profile in the gasifier and catalytic reactor



(b) Temperature profile in the tar sampling system

Figure 6.12 Temperature pattern of the experimental set-up

## **6.6 Performance of the Horizontal Entrained-flow Gasifier Reactor**

### **6.6.1 Fuel conversion**

The performance of the horizontal entrained-flow gasifier on fuel conversion (FC) is shown in Table 6.4. The maximum fuel conversion attained for non-catalytic gasification was found to be 99.0 % compared to 91.4 % by Hernandez et al [43] and 87.4 % by Zhao et al [38] who used a vertical configuration. A possible attribute to this higher conversion could be due to the particle to metal contact. It should be noted that the gasifier wall acts as a heat source to initiate and sustain the gasification process in addition to the heat of combustion from the feedstock. Stainless steel is believed to have good heat transfer properties, thus, improving fuel conversion. Another attributing factor could be the geometrical ratios of the gasifier reactor which enhances low temperature gradient across the reactor. The typical geometrical parameters for the design used in this study are provided in Section 4.3.4.

### **6.6.2 Cold Gas Efficiency (CGE)**

Although a comparative high fuel conversion was achieved in the gasifier reactor, the higher conversion could be attributed to the combustion rather than intended gasification process. Thus, further verification of the performance was determined and expressed in terms of cold gas efficiency (CGE) as described in Section 4.5.5. The CGE is the measure of conversion of the chemical energy in the primary fuel (wood powder) to the secondary fuel (syngas). The maximum CGE achieved in this gasifier reactor was 70 %. With the exception of sensible heat, the balance is the loss of energy mainly in the form of tar and fractions of char. Comparing with the previous studies for the vertical entrained flow gasifier undertaken at similar conditions, the highest CGE achieved was in the range of 40.77 to 62.8 % [38, 48, 131]. The observed increase on CGE substantiates the conversion efficiency of the horizontal entrained-flow gasification of biomass feedstock.

### **6.6.3 Syngas composition**

Table 6.4 shows the syngas composition from gasification of biomass using a horizontal entrained-flow gasifier reactor. These results were obtained when the catalytic reactor was empty in order to establish a baseline for comparison with catalysis studies. It can be seen from the table that the maximum H<sub>2</sub> achieved was

14.33 %, while CO, CO<sub>2</sub> and CH<sub>4</sub> were 13.97 %, 22.11 % and 3.62 % by volume respectively. Moreover, light hydrocarbons such as ethane (C<sub>2</sub>H<sub>6</sub>) and propane (C<sub>3</sub>H<sub>8</sub>) were detected in trace amounts. With this gas composition, the corresponding low heating value was found to be 6.67 MJ/Nm<sup>3</sup>. Furthermore, the CO/CO<sub>2</sub> and H<sub>2</sub>/CO<sub>2</sub> ratios were more than 1 and the yield of total energy containing gases (H<sub>2</sub>, CO, CH<sub>4</sub>, C<sub>2</sub>H<sub>6</sub> and C<sub>3</sub>H<sub>8</sub>) was 0.85 Nm<sup>3</sup>/kg of fuel.

An interpretation to these results can be explained by a number of factors. The observed high CO/CO<sub>2</sub> and H<sub>2</sub>/CO<sub>2</sub> ratios confirm the existence of partial oxidation atmosphere which favours the gasification process. The observed high concentration of H<sub>2</sub> and CH<sub>4</sub> could also be related to the tar cracking in the gasifier reactor promoted by low temperature gradient.

Table 6.4 Syngas composition and yields from biomass gasification using a horizontal entrained-flow gasifier reactor

Parameter	Gas Composition (vol. %, db)	Gas yield (Nm <sup>3</sup> /kg fuel, db)
H <sub>2</sub>	14.33	0.29
CO	22.11	0.45
CO <sub>2</sub>	13.97	0.29
CH <sub>4</sub>	3.62	0.07
C <sub>2</sub> H <sub>6</sub>	1.66	0.03
C <sub>3</sub> H <sub>8</sub>	0.38	0.01
N <sub>2</sub>	43.93	0.90
Char (g)	0.18	
<i>Gas ratios</i>		
CO/CO <sub>2</sub>	1.58	
H <sub>2</sub> /CO <sub>2</sub>	1.03	
CH <sub>4</sub> /CO <sub>2</sub>	0.12	
H <sub>2</sub> /CO	0.65	
LHV (MJ/Nm <sup>3</sup> )	6.67	
Fuel Conversion (%)	99.0	
Cold gas efficiency (%)	70.0	

#### 6.6.4 Tar composition

Table 6.5 presents the composition of tar compounds screened from the non-catalytic gasification of wood powder. The reported compounds are grouped as oxygenated and aromatic compounds. It can be observed that more than 80 % of the tar yields are in the form of aromatic compounds. In this fraction, benzene and toluene share 50 % and 20 % respectively. The oxygenated compounds were found

at approximately 15 % of the total tar detected and the balance was contributed by trace amounts of both aromatic and oxygenated hydrocarbons. Phenol and cresols were observed as major compounds representing oxygenated compounds resulted from the gasification of wood powder. Moreover, the chlorophenol family were below detection limit. The overall results indicate that, the total tar yield was almost 5 % wt of the wood powder (i.e. 50 g of tar per kg of fuel).

There are several factors that can be associated with the composition and yield of tar from gasification of wood powder. The observed high concentration of aromatic compounds compared to the oxygenated compounds suggests limited partial oxidation of volatiles in the gasifier reactor. The presence of nitrogen (as inert) in the gas stream is one of the factors limiting the reactivity of volatiles with the oxidant [132]. It should be noted that, excessive partial oxidation can lead to combustion of combustible gases such H<sub>2</sub>, CO and CH<sub>4</sub>. Thus, lowering the heating value of the syngas as revealed in the study by Cao et al [133]. Although tar yield exceeded the threshold recommended for internal combustion engines (<100 mg/Nm<sup>3</sup>), the resulted syngas (Table 6.4) highlights the viability for application in internal combustion engines [134].

Another possible explanation of the high yield of aromatic compounds can be related to the high volatile matter in the wood powder as reported in Table 6.1. These volatiles are mainly composed of hydrocarbons in form of C<sub>x</sub>H<sub>y</sub> and C<sub>x</sub>H<sub>y</sub>O. The undetected chlorophenols could be attributed to the low chlorine content in the feedstock [135]. It is important to note that, the derivatives of chlorophenol compounds are classified as highly toxic, mutagenic and carcinogenic for living organisms [136]. With the exception of other hydrocarbon compounds, biomass tars are mainly composed of benzene, toluene, xylene isomers, phenol, naphthalene and cresol isomers. These findings are in good agreement with those obtained by Zhang et al [8] in the gasification of hinoki cypress sawdust at 800 °C.

Table 6.5 Tar yield from biomass gasification using a horizontal entrained-flow gasifier reactor

No.	Compound	Formula	Mwt	Tar Yield	
				(mg/Nm <sup>3</sup> )	(g/kg fuel)
	<i>Oxygenated compounds (OC)</i>				
1	Phenol	C <sub>6</sub> H <sub>5</sub> -OH	94	1427.04	4.99
2	Cresol isomers	C <sub>6</sub> H <sub>4</sub> -OH, CH <sub>3</sub>	108	662.08	2.32
3	Dimethylphenol isomers	C <sub>6</sub> H <sub>3</sub> -OH, CH <sub>3</sub>	122	33.28	0.12
4	Acetophenone	C <sub>8</sub> H <sub>8</sub> O	120	30.40	0.11
5	Dibenzofuran	C <sub>12</sub> H <sub>8</sub> O	168	14.53	0.05
		Total OC		2167.33	7.59
	<i>Aromatic compounds</i>				
6	Benzene	C <sub>6</sub> H <sub>6</sub>	78	6705.23	23.47
7	Toluene	C <sub>6</sub> H <sub>5</sub> -CH <sub>3</sub>	92	2624.17	9.18
8	Ethylbenzene	C <sub>6</sub> H <sub>5</sub> CH <sub>2</sub> CH <sub>3</sub>	102	394.98	1.38
9	Xylene isomers	C <sub>6</sub> H <sub>4</sub> -CH <sub>3</sub> , CH <sub>3</sub>	106	1613.92	5.65
10	Naphthalene	C <sub>10</sub> H <sub>8</sub>	128	939.34	3.29
11	Acenaphthylene	C <sub>12</sub> H <sub>8</sub>	152	307.15	1.08
12	Acenaphthene	C <sub>12</sub> H <sub>10</sub>	154	24.12	0.08
13	Biphenyl	C <sub>12</sub> H <sub>10</sub>	154	43.28	0.15
14	Fluorene	C <sub>13</sub> H <sub>10</sub>	166	18.06	0.06
15	Phenanthrene	C <sub>14</sub> H <sub>10</sub>	178	16.02	0.06
16	Anthracene	C <sub>14</sub> H <sub>10</sub>	178	24.53	0.09
17	Fluoranthene	C <sub>16</sub> H <sub>10</sub>	202	18.06	0.06
18	Pyrene	C <sub>16</sub> H <sub>10</sub>	202	16.02	0.06
19	Benz (a) anthracene	C <sub>18</sub> H <sub>12</sub>	228	2.27	0.01
20	Chrysene	C <sub>18</sub> H <sub>12</sub>	228	1.66	0.01
21	Benzo (b) fluoranthene	C <sub>20</sub> H <sub>12</sub>	252	1.39	0.00
23	Benzo (a) pyrene	C <sub>20</sub> H <sub>12</sub>	252	0.27	0.00
24	Dibenz (a, h) anthracene	C <sub>22</sub> H <sub>14</sub>	278	0.99	0.00
		Total AC		12751.46	44.63
		Total tar detected		14918.79	52.22

## **6.7 Catalytic Gasification Results**

This section presents and discusses the results from the catalytic processing of the gasification product gas. The results for syngas and tar composition are compared to the non-catalytic test described in the Section 6.6. In addition, cold gas efficiency, gas ratios and catalyst selectivity are also compared.

### **6.7.1 Effect of Catalyst Support on the Gasification Product Gas**

Table 6.6 compares the effect of pumice on syngas composition from the gasification of biomass. The results for “None” are from the gasification tests reported in Section 6.6.3. Glass beads were selected to represent non-reactive materials. As it can be seen, H<sub>2</sub>, CO and CH<sub>4</sub> yield for the gasification without catalyst support is almost similar to that of glass beads and Mexican pumice. The CO concentration for the pumice from Arusha, Tanzania was 22.71 % vol. similar to other catalyst supports. However, H<sub>2</sub> was found to be 7.75 % vol. compared to 14-15 % vol. of glass beads and Mexican pumice. Kaolin showed low concentration of H<sub>2</sub> and CH<sub>4</sub> compared to other catalyst supports, consequently, reducing the syngas LHV.

The observed small difference on gas composition between pumice samples and glass beads can be explained as a limitation of chemical reactivity of the catalyst supports on the gasification product gas. Although pumice from Arusha showed low concentration of H<sub>2</sub> compared to other pumice supports, a good agreement of CO<sub>2</sub> concentration and CO provide no evidence on the existence of oxidation reactions. It can therefore be suggested that natural pumice has little chemical effect on the syngas composition. For the Kaolin support, a small difference in CO, CO<sub>2</sub> and CH<sub>4</sub> concentrations compared to those of the None highlights no chemical effect on the gas product. A previous study by Siedlecki and de Jong [73] also showed insignificant effect on the gas composition due to addition of kaolin in sand bed material during gasification of wood.

Table 6.6 Comparison of syngas composition from different catalyst supports

Bed material	Syngas Composition (% Vol.)				
	None	Glass Beads	Mexico Pumice	Arusha Pumice	Kaolin
H <sub>2</sub>	14.33	15.05	14.64	7.75	7.93
CO	22.11	21.27	20.95	22.71	20.74
CO <sub>2</sub>	13.97	12.29	13.39	12.01	10.67
CH <sub>4</sub>	3.62	3.84	3.80	3.92	3.33
C <sub>2</sub> H <sub>6</sub>	1.66	1.68	1.59	1.23	1.13
C <sub>3</sub> H <sub>8</sub>	0.38	0.53	0.65	0.32	0.27
LHV (MJ/Nm <sup>3</sup> )	6.02	6.31	6.19	5.01	5.34

Table 6.7 compares the yield of the major tar compounds at different catalyst supports. The results for an empty catalytic reactor “None” are also presented as a baseline for studying the effect of supports on the tar yield. From the table it can be seen that the oxygenated compounds decreased for all pumice supports and kaolin compared to that of None. This decrease was mainly contributed by decrease of phenol compound. A similar trend was observed for aromatic compounds in which decrease was contributed by benzene, toluene and ethylbenzene. The overall results showed that tar yield using pumice from Arusha Tanzania was low as 9842.57 mg/Nm<sup>3</sup> compared to 10882.28 mg/Nm<sup>3</sup> and 13584.55 mg/Nm<sup>3</sup> of Mexican pumice and Kaolin from Pugu Hills Tanzania. These concentrations were found to be lower than those obtained when the catalytic reactor was empty (14918.79 mg/Nm<sup>3</sup>).

There are several explanations on the effect of these catalyst supports on the tar yield. The observed decrease of phenol and other aromatic hydrocarbons such as acenaphthene and acenaphthylene can be linked to the adsorption on the catalyst support. Anis and Zainal [7] also reported tar reduction with porous materials such as activated carbon is mainly through adsorption. Although benzene and toluene are difficult to condense at given operating temperature of 350 °C, their decrease could be due to limited desorption from the support pores. Macropores and mesopores of the porous support are easily blocked with heavy hydrocarbons thus reducing desorption of the adsorbed species. The observed low tar yield for pumice from Arusha can be attributed to its high porosity compared to other support as discussed in Section 6.4.

Table 6.7 Comparison of tar yield from different catalyst supports

No.	Compound	Formula	Mwt	Tar yield (mg/Nm <sup>3</sup> )				
				None	Glass Beads	Mexico Pumice	Arusha Pumice	Kaolin
	<i>Oxygenated compounds</i>							
1	Phenol	C <sub>6</sub> H <sub>5</sub> -OH	94	1427.04	962.78	1076.52	840.27	1258.21
2	Cresol isomers	C <sub>6</sub> H <sub>4</sub> -OH, CH <sub>3</sub>	108	662.08	534.92	420.87	645.06	623.30
3	Dimethylphenol isomers	C <sub>6</sub> H <sub>3</sub> -OH, CH <sub>3</sub>	122	33.28	13.07	10.90	48.67	53.13
4	Acetophenone	C <sub>8</sub> H <sub>8</sub> O	120	30.40	0.00	24.33	35.12	31.96
5	Dibenzofuran	C <sub>12</sub> H <sub>8</sub> O	168	14.53	0.00	6.38	29.76	19.68
		Total		2167.33	1510.77	1538.99	1598.88	1986.28
	<i>Aromatic compounds</i>							
6	Benzene	C <sub>6</sub> H <sub>6</sub>	78	6705.23	4831.73	3729.65	3458.17	5992.98
7	Toluene	C <sub>6</sub> H <sub>5</sub> -CH <sub>3</sub>	92	2624.17	3163.79	2343.44	1424.77	2496.84
8	Ethylbenzene	C <sub>6</sub> H <sub>5</sub> CH <sub>2</sub> CH <sub>3</sub>	102	394.98	485.08	302.43	299.57	330.97
9	Xylene isomers	C <sub>6</sub> H <sub>4</sub> -CH <sub>3</sub> , CH <sub>3</sub>	106	1613.92	1758.80	1667.40	1282.43	1285.02
10	Naphthalene	C <sub>10</sub> H <sub>8</sub>	128	939.34	606.96	960.49	1114.62	966.93
11	Acenaphthylene	C <sub>12</sub> H <sub>8</sub>	152	307.15	120.82	207.57	347.67	253.91
12	Acenaphthene	C <sub>12</sub> H <sub>10</sub>	154	24.12	9.28	9.32	0.00	0.00
13	Biphenyl	C <sub>12</sub> H <sub>10</sub>	154	43.28	0.00	48.91	75.81	50.95
14	Fluorene	C <sub>13</sub> H <sub>10</sub>	166	18.06	24.76	36.93	62.10	55.12
15	Phenanthrene	C <sub>14</sub> H <sub>10</sub>	178	16.02	48.16	52.55	93.24	93.71
16	Anthracene	C <sub>14</sub> H <sub>10</sub>	178	24.53	14.49	14.75	34.93	31.40
17	Fluoranthene	C <sub>16</sub> H <sub>10</sub>	202	18.06	9.06	8.80	23.46	17.86
18	Pyrene	C <sub>16</sub> H <sub>10</sub>	202	16.02	7.33	8.08	18.74	15.45
19	Benz (a) anthracene	C <sub>18</sub> H <sub>12</sub>	228	2.27	1.51	1.22	3.15	2.41
20	Chrysene	C <sub>18</sub> H <sub>12</sub>	228	1.66	0.87	0.58	2.41	1.61
21	Benzo (b) fluoranthene	C <sub>20</sub> H <sub>12</sub>	252	1.39	0.05	0.06	2.13	1.55
22	Benzo (a) pyrene	C <sub>20</sub> H <sub>12</sub>	252	0.27	0.02	0.01	0.48	0.48
23	Dibenz (a, h) anthracene	C <sub>22</sub> H <sub>14</sub>	278	0.99	0.02	0.02	0.00	1.10
		Total		12751.46	11082.73	9392.21	8243.69	11598.27
		TOTAL		14918.79	12593.5	109331.20	9842.57	13584.55

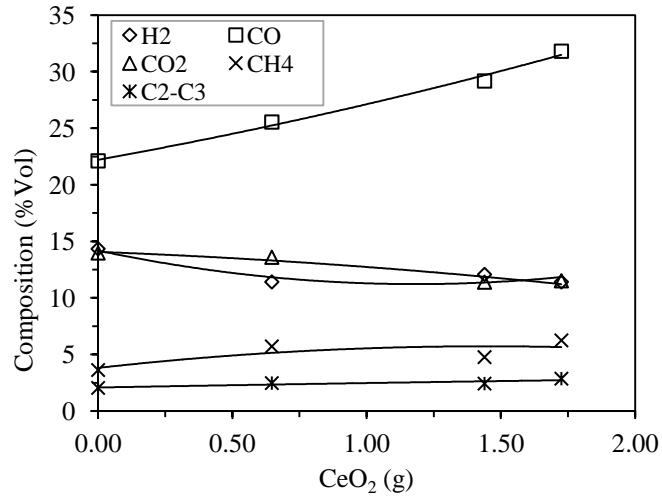
## 6.7.2 Ceria (CeO<sub>2</sub>) Doped Pumice

### 6.7.2.1 Effect of ceria doped pumice on syngas composition

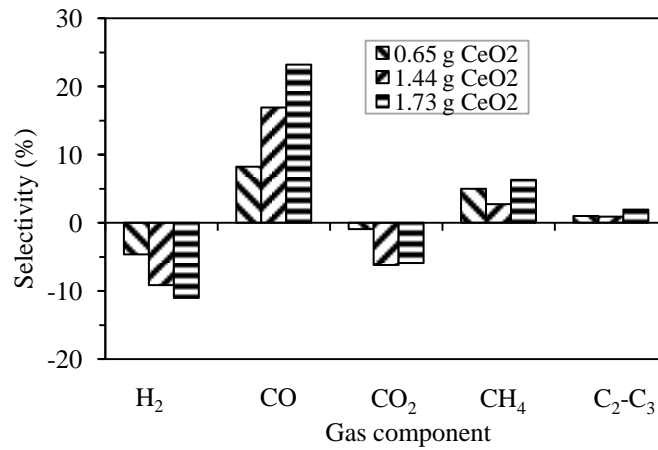
Figure 6.13 presents the experimental results on the effect of ceria doped pumice on syngas composition from biomass gasification. Figure 6.13 (a) provides the trends of an individual gas species (H<sub>2</sub>, CO, CO<sub>2</sub>, CH<sub>4</sub>) and total light hydrocarbons (C<sub>2</sub>H<sub>6</sub> and C<sub>3</sub>H<sub>8</sub>) at different ceria loading. It can be observed that the increase of CeO<sub>2</sub> concentration on pumice resulted in a decrease in H<sub>2</sub> and CO<sub>2</sub> in the produced syngas. The decrease was in the range of 2-3 % by volume. The concentration of CO and CH<sub>4</sub> increased with increasing ceria loading. Their increase was in the range of 3-10 % and 1-3 % respectively. Furthermore, there was no significant effect on light hydrocarbons for all tested catalysts. In Figure 6.13 (b), the performance of catalyst on specific gas products is provided. These results were obtained by subtracting the selectivity of non-catalytic gasification from those of catalytic gasification. It can be seen from the figure that H<sub>2</sub> and CO<sub>2</sub> decreased for all catalysts trials, while CO and CH<sub>4</sub> increased significantly. Another observation is a slight increase of light hydrocarbons with increasing ceria concentration on the pumice particles. The syngas heating value was found to be 7.80, 7.94 and 8.97 MJ/Nm<sup>3</sup> for catalyst loading of 0.65, 1.44 and 1.73 g respectively.

Figure 6.13 (c) presents the corresponding changes in cold gas efficiency (CGE) as a result of catalytic effects on syngas composition. Additional analyses on CO/CO<sub>2</sub> and H<sub>2</sub>/CO<sub>2</sub> (all in percentage by volume) were provided to investigating the reforming reactions environment. The former ratio was used to assess the oxidation conditions, while the latter aimed at exploring the correlation between H<sub>2</sub>, CO<sub>2</sub> and CeO<sub>2</sub>. The results showed that CGE increased with increasing ceria concentration on the pumice support. Similar trend was observed with the CO/CO<sub>2</sub> and CH<sub>4</sub>/CO<sub>2</sub> ratios while the H<sub>2</sub>/CO<sub>2</sub> ratio highlighted a decrease.

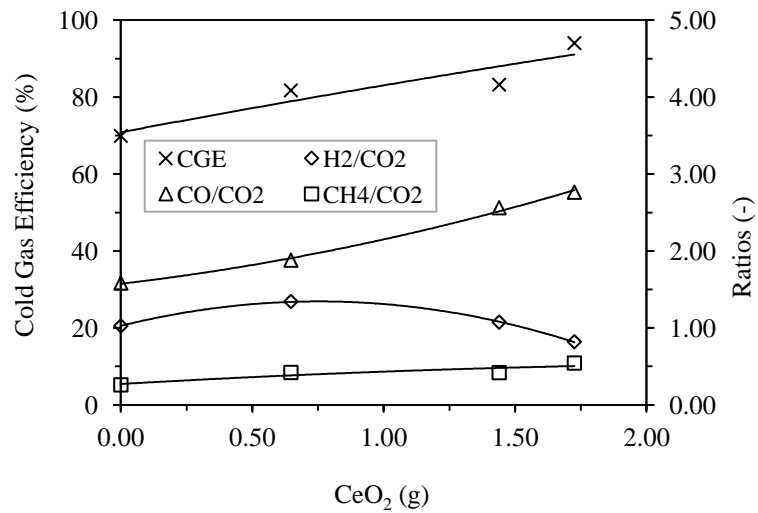
There are several possible explanations for these results. The observed increase in CGE can be linked to the increase in CO and CH<sub>4</sub> as revealed in Figure 6.13 (a). Comparing the data in Figure 6.13 (a and b), a positive correlation can be found between H<sub>2</sub>, CO<sub>2</sub> and CeO<sub>2</sub>. A combination of CO/CO<sub>2</sub> and CH<sub>4</sub>/CO<sub>2</sub> rise and the decrease of H<sub>2</sub>/CO<sub>2</sub> ratio confirm the existence of a redox atmosphere dominated with Ce<sup>4+</sup> and Ce<sup>3+</sup> oxides. A previous study<sup>4</sup> by Holmgren [137] reported on the interaction of O<sup>2-</sup> exchange between CeO<sub>2</sub> and H<sub>2</sub> was higher compared to CO and the reduced cerium oxide reacts rapidly with CO<sub>2</sub> to produce CO.



(a) Syngas composition



(b) Selectivity to gaseous products



(c) Cold gas efficiency (CGE) and gas ratios

Figure 6.13 The effect of CeO<sub>2</sub> loading on (a) syngas composition, (b) Selectivity to gaseous products and (c) Cold gas efficiency (CGE) and gas ratios

These findings support the theory that the decrease of the H<sub>2</sub> can be explained using reaction Equation 6.2, while the corresponding decrease in CO<sub>2</sub> could be due to oxidation of the reduced ceria as per reaction Equation 6.3. An implication to the involvement of H<sub>2</sub> in redox reactions is detrimental to the syngas heating value. Although the CGE increased with increasing ceria, higher concentrations can decrease the syngas heating value due to hydrogen oxidation. Thus optimal operating conditions including ceria loading are necessary.



#### 6.7.2.2 Effect of Ceria doped pumice on tar yield

Table 6.8 compares the yield of the major tar compounds at different ceria loading on the pumice support. From the table it can be seen that benzene was a major compound in the biomass derived tar. Other compounds with concentration above 100 mg/Nm<sup>3</sup> were toluene, xylene isomers, phenol, naphthalene, cresol isomers and acenaphthylene. The effect of increasing ceria loading resulted in a decrease of naphthalene and acenaphthylene. Other aromatic compounds such as benzene and ethylbenzene increased with increasing ceria loading. Furthermore, an increase in the oxygenated hydrocarbons was also observed. This increase was mainly attributed to cresol and dimethylphenol isomers. Phenol showed a slight decrease for all catalytic gasification trials. Although acetophenone and dibenzofuran were found in trace amounts, a notable increase was observed with increasing ceria loading.

These findings can be explained by a range of different factors. The increase of acetophenone and dibenzofuran can be correlated to the decrease of naphthalene and acenaphthylene as a result of oxidation. Similar findings have been reported during oxidation of naphthalene [42] and anthracene [138]. These reactions are mainly dominated with intermediate free radicals promoted by O<sup>2</sup> [139]. Furthermore, benzene and toluene are believed to be stable one-ring aromatic compounds. Compared with the reactivity of H<sub>2</sub> and CO<sub>2</sub>, the conversion of these compounds over the catalyst could be limited.

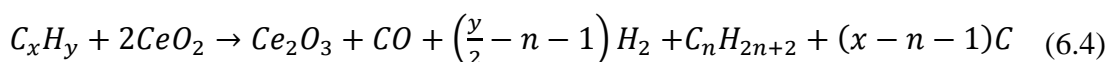
Table 6.8 Tar yield at different ceria loading (FP, CeO<sub>2</sub>=0 g; CeO<sub>2</sub>-1=0.65 g; CeO<sub>2</sub>-2=1.44 g; CeO<sub>2</sub>-3=1.73 g)

No.	Compound	Formula	Mwt	Tar yield (mg/Nm <sup>3</sup> )			
				FP	CeO <sub>2</sub> -1	CeO <sub>2</sub> -2	CeO <sub>2</sub> -3
	<i>Oxygenated compounds</i>						
1	Phenol	C <sub>6</sub> H <sub>5</sub> -OH	94	1076.52	794.47	927.60	890.36
2	Cresol isomers	C <sub>6</sub> H <sub>4</sub> -OH, CH <sub>3</sub>	108	420.87	636.31	521.38	621.96
3	Dimethylphenol isomers	C <sub>6</sub> H <sub>3</sub> -OH, CH <sub>3</sub>	122	10.90	58.20	45.42	50.36
4	Acetophenone	C <sub>8</sub> H <sub>8</sub> O	120	24.33	37.26	23.08	41.05
5	Dibenzofuran	C <sub>12</sub> H <sub>8</sub> O	168	6.38	13.61	8.54	11.75
		Total		1538.99	1539.86	1526.02	1615.48
	<i>Aromatic compounds</i>						
6	Benzene	C <sub>6</sub> H <sub>6</sub>	78	3729.65	4610.39	4174.51	4949.89
7	Toluene	C <sub>6</sub> H <sub>5</sub> -CH <sub>3</sub>	92	2343.44	2389.09	2069.02	1952.37
8	Ethylbenzene	C <sub>6</sub> H <sub>5</sub> CH <sub>2</sub> CH <sub>3</sub>	102	302.43	375.95	317.39	419.08
9	Xylene isomers	C <sub>6</sub> H <sub>4</sub> -CH <sub>3</sub> , CH <sub>3</sub>	106	1667.40	1293.73	1231.23	1499.10
10	Naphthalene	C <sub>10</sub> H <sub>8</sub>	128	960.49	364.16	571.64	455.96
11	Acenaphthylene	C <sub>12</sub> H <sub>8</sub>	152	207.57	89.77	148.44	107.07
12	Acenaphthene	C <sub>12</sub> H <sub>10</sub>	154	9.32	14.78	12.04	14.65
13	Biphenyl	C <sub>12</sub> H <sub>10</sub>	154	48.91	20.19	21.29	28.48
14	Fluorene	C <sub>13</sub> H <sub>10</sub>	166	36.93	25.53	30.20	27.91
15	Phenanthrene	C <sub>14</sub> H <sub>10</sub>	178	52.55	39.89	49.08	40.53
16	Anthracene	C <sub>14</sub> H <sub>10</sub>	178	14.75	16.03	15.53	16.03
17	Fluoranthene	C <sub>16</sub> H <sub>10</sub>	202	8.80	6.99	10.43	7.70
18	Pyrene	C <sub>16</sub> H <sub>10</sub>	202	8.08	5.17	8.30	5.94
19	Benz (a) anthracene	C <sub>18</sub> H <sub>12</sub>	228	1.22	1.09	2.04	0.54
20	Chrysene	C <sub>18</sub> H <sub>12</sub>	228	0.58	0.77	1.15	1.17
21	Benzo (b) fluoranthene	C <sub>20</sub> H <sub>12</sub>	252	0.06	0.21	0.03	0.03
22	Benzo (a) pyrene	C <sub>20</sub> H <sub>12</sub>	252	0.01	0.01	0.02	0.01
23	Dibenz (a, h) anthracene	C <sub>22</sub> H <sub>14</sub>	278	0.02	0.01	0.01	0.00
		Total		9392.21	9253.77	8662.35	9526.47

In addition, the increase of intermediates such as xylene, cresol, ethylbenzene and dimethylphenol isomers in the product gas explains the inhibition of further tar conversion to gases over CeO<sub>2</sub> sites. According to the literature [9, 42, 60] benzene, toluene and phenol can undergo complete oxidation at 350 °C using ceria as catalyst. Therefore it is possible that the presence of gases such as H<sub>2</sub>, CO, CO<sub>2</sub> inhibits tar conversion over the ceria catalyst. These results are in good agreement with Laosiripojana and Assabumrungrat [140] who revealed that H<sub>2</sub> suppresses CH<sub>4</sub> conversion during dry reforming of methane over ceria. In general, these findings suggest that tar conversion over ceria at GHSV (~ 8000 h<sup>-1</sup>) and 350 °C results in formation of intermediate hydrocarbons.

### 6.7.2.3 Effect of ceria doped pumice on coking resistance

Figure 6.14 shows the diffusion profile of carbon deposition in the catalytic bed materials. In this analysis the aim was to investigate the dispersion of carbon causing deactivation of the catalyst. It can be seen from the Figure 6.14, carbon concentration in the doped pumice is less than that of untreated pumice (FP). This difference could be attributed to the primary reaction Equation 6.4 for tar cracking and further reaction Equation 6.5 for carbon conversion. These reactions provide another possible source of CO increase in the product gas. A similar conclusion has been proposed based on the ability of ceria to oxidise carbon at temperature between 300 °C and 400 °C [141, 142]. Furthermore, the noted high carbon concentration at the bed heights above 45 mm in the untreated pumice material could be a result of the decrease of bed porosity thus accelerating deposition of hydrocarbons. The decrease of carbon with increasing ceria over pumice provides evidence of the resistance to coking. Analysis on coked ceria catalyst using TGA has also shown similar results as reported by Wu and Williams [143].



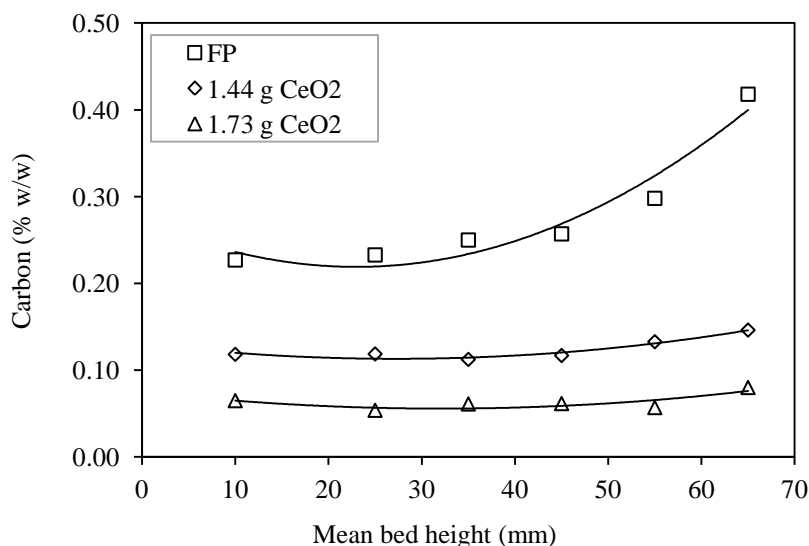


Figure 6.14 Carbon deposition profile in the catalytic reactor with fresh pumice (FP) and ceria treated pumice

### 6.7.3 CuO doped pumice

#### 6.7.3.1 The effect of copper doped pumice on syngas composition

Figure 6.15 presents the effect of catalyst loading on the syngas composition. It can be observed that increasing the CuO loading has a significant effect on the syngas composition. The CO concentration increased from 22.11 % to 31.87 % by volume when CuO on pumice was increased from 0 to 2.81 g. Similarly, CH<sub>4</sub> concentration increased from 3.62 % to 6.50 % by volume. It was also noted that H<sub>2</sub> and CO<sub>2</sub> decreased from 14.33 % to 9.93 % and 13.97 % to 11.22 % by volume respectively. Further observations revealed an insignificant effect on light hydrocarbons (C<sub>2</sub>H<sub>6</sub> and C<sub>3</sub>H<sub>8</sub>) with increasing CuO loading. The syngas heating value was found to be 7.67, 8.20 and 8.66 MJ/Nm<sup>3</sup> for catalyst loading of 0.74, 1.79 and 2.81 g respectively.

Figure 6.16 shows the effect of CuO loading on the selectivity to gas components in the syngas. It can be observed that CuO decrease H<sub>2</sub> and CO<sub>2</sub>, while promoting CO, CH<sub>4</sub> and light hydrocarbons. However, there was no significant change of catalyst selectivity on CO and CH<sub>4</sub> at higher CuO loading as revealed at 1.79 g and 2.81 g compared to 0.74 g doping.

The gas ratios and cold gas efficiency at different CuO loading are provided in Figure 6.17. It can be observed from the figure that CO/CO<sub>2</sub> and CH<sub>4</sub>/CO<sub>2</sub> ratios increased with increasing CuO loading. This increase almost doubled that of the non-

catalytic test. The  $H_2/CO_2$  decreased from 1.03 to approximately 0.7 at CuO loading between 0.74 g and 1.79 g. Moreover, there was no significant difference of  $H_2/CO_2$  ratio at 2.81 g CuO loading when compared with the non-catalytic test as seen in Table 6.4.

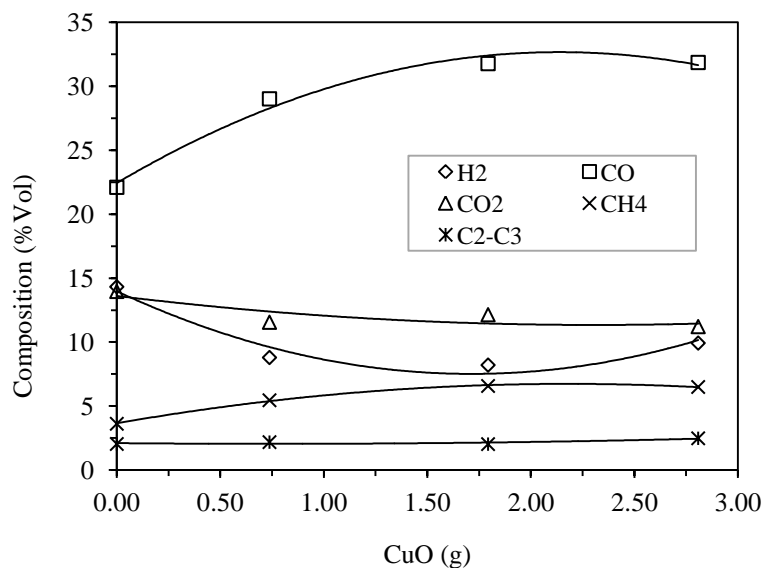


Figure 6.15 Syngas composition at different CuO loading

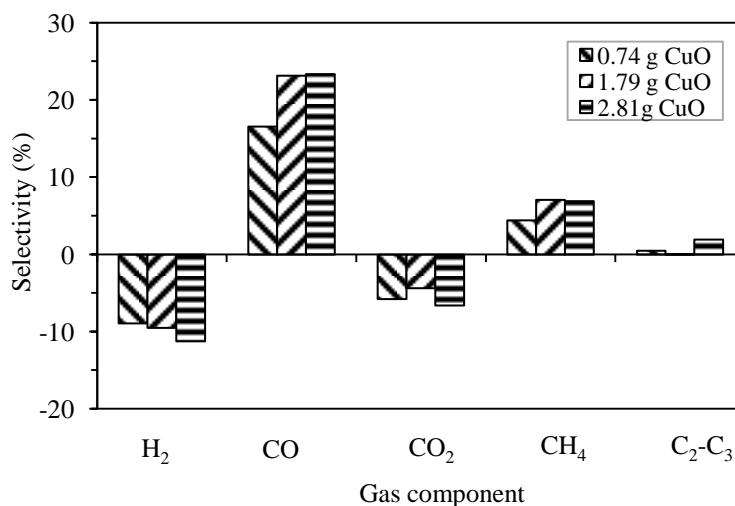


Figure 6.16 Catalyst selectivity on gaseous product at different CuO loading

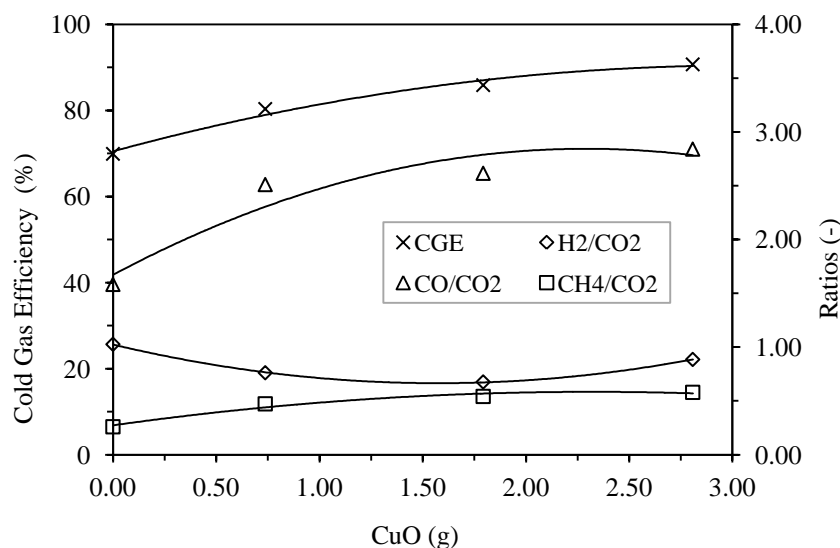


Figure 6.17 The effect of CuO loading on cold gas efficiency

There are several possible explanations for the involvement of CuO in syngas reforming reactions. The decrease of H<sub>2</sub> highlights the activity of the catalyst on the reduction reaction. Jiang et al [144] studied the CuO catalyst on H<sub>2</sub> uptake and CO oxidation using a Temperature Programmed Reduction (TPR) method and found that H<sub>2</sub> was rapidly consumed at temperatures below 400 °C explained by reduction reaction ( $\text{CuO} + \text{H}_2 \rightarrow \text{Cu} + \text{H}_2\text{O}$ ). The reduced Cu is believed to have high CO<sub>2</sub> adsorption capability compared to hydrocarbons and CO [145]. As a result, further interaction of CO in the reformed gas and the catalyst is suppressed. Similar finding was reported by Tanaka et al [146] in their study on the effect of CO<sub>2</sub> on water gas shift reaction over Cu/MnO catalyst. Other studies have reported the increase of CH<sub>4</sub> is a result of side reaction Equation 6.6 when the adsorbed CO<sub>2</sub> on Cu surface interacts with H atoms [147, 148].



### 6.7.3.2 Effect of copper doped pumice on tar yield

Table 6.9 shows the tar yield at different CuO loading on the pumice support. It can be seen that for pure pumice, the aromatic compound yields between three and five times the values for the oxygen containing hydrocarbons. Benzene shares about one-half of the aromatic compounds, while toluene was about one-fourth. Although

at 0.74 g CuO loading showed an increase of benzene yield by 1088 mg/Nm<sup>3</sup>, higher catalyst loading decreased these compounds in the range of 400-1100 mg/Nm<sup>3</sup>. Other aromatic hydrocarbons such as toluene, ethylbenzene, xylene isomers and naphthalene showed a noticeable decrease. However, their concentrations were still above the recommended threshold for internal combustion engines (100 mg/Nm<sup>3</sup>). Moreover, acenaphthylene and fluorene showed a slightly decrease with increasing catalyst loading. Biphenyl was not detected in all catalyst loading experiments. For oxygenated compounds, phenol was found to be the largest concentration contributing to more than two-third of the total yield. Cresol isomers were also detected at concentration ranging 400-500 mg/Nm<sup>3</sup> for all catalyst tests. These compounds showed a slight increase with increasing catalyst loading.

Further analysis on the effect of CuO on tar destruction is highlighted in Figure 6.18 and Figure 6.19. These results were expressed as percentage of the non-catalytic tests, whereas at zero concentration of CuO represented the untreated pumice support. Comparison between catalyst tests revealed a decreasing trend of the aromatic compounds with increasing copper concentration as observed in Figure 6.18. Also noted was that oxygenated compounds showed a slight increase with increasing CuO on pumice. Light tar showed a decreasing trend with increasing CuO concentration on the catalyst support as well. The decrease ranged 5-20 % compared to the untreated pumice. For heavy tar, there was no significant change with increasing catalyst concentration.

The effect of CuO loading on tar destruction can be explained by several factors. The decrease of aromatic and the increase of oxygenated compounds can be correlated to the partial oxidation of hydrocarbons which favours formation of CO, CO<sub>2</sub>, alcohols and acids. This interpretation is further highlighted by the observed increase of CO as shown in Figure 6.15. The increase of dibenzofuran has been coupled to the partial oxidation of fluorene and biphenyl over the CuO catalysts [149]. The increase of phenol derivatives can be associated with benzene oxidation over CuO catalyst as reported by Parida and Rath [150]. The increase of methane as a result of benzene and toluene conversion has also been reported by Grimes et al [151] and Lee et al [152] during the decomposition of aromatic hydrocarbons on the copper (II) oxide catalyst. Another possible explanation for the decrease of aromatic hydrocarbons could be due to cracking which favours coke formation and methane yield.

Table 6.9 Tar yield at different copper loading (FP=0 g CuO, CuO-1=0.74 g, CuO-2=1.79 g, CuO-3=2.81 g)

No.	Compound	Formula	Mwt	Tar yield (mg/Nm <sup>3</sup> )			
				FP	CuO-1	CuO-2	CuO-3
<i>Oxygenated compounds</i>							
1	Phenol	C <sub>6</sub> H <sub>5</sub> -OH	94	1076.52	890.89	1126.21	1077.35
2	Cresol isomers	C <sub>6</sub> H <sub>4</sub> -OH, CH <sub>3</sub>	108	420.87	441.94	559.52	518.04
3	Dimethylphenol isomers	C <sub>6</sub> H <sub>3</sub> -OH, CH <sub>3</sub>	122	10.90	32.73	52.48	51.49
4	Acetophenone	C <sub>8</sub> H <sub>8</sub> O	120	24.33	26.44	21.44	20.68
5	Dibenzofuran	C <sub>12</sub> H <sub>8</sub> O	168	6.38	24.60	19.69	18.24
	Total			1538.99	1416.60	1779.35	1685.80
<i>Aromatic compounds</i>							
6	Benzene	C <sub>6</sub> H <sub>6</sub>	78	3729.65	4818.54	3283.32	2644.43
7	Toluene	C <sub>6</sub> H <sub>5</sub> -CH <sub>3</sub>	92	2343.44	1781.21	1433.33	1375.94
8	Ethylbenzene	C <sub>6</sub> H <sub>5</sub> CH <sub>2</sub> CH <sub>3</sub>	102	302.43	231.92	204.82	194.87
9	Xylene isomers	C <sub>6</sub> H <sub>4</sub> -CH <sub>3</sub> , CH <sub>3</sub>	106	1667.40	1104.03	916.83	917.95
10	Naphthalene	C <sub>10</sub> H <sub>8</sub>	128	960.49	517.23	697.24	650.17
11	Acenaphthylene	C <sub>12</sub> H <sub>8</sub>	152	207.57	116.99	165.60	178.03
12	Acenaphthene	C <sub>12</sub> H <sub>10</sub>	154	9.32	0.00	40.72	35.23
13	Biphenyl	C <sub>12</sub> H <sub>10</sub>	154	48.91	0.00	0.00	0.00
14	Fluorene	C <sub>13</sub> H <sub>10</sub>	166	36.93	22.19	31.13	31.03
15	Phenanthrene	C <sub>14</sub> H <sub>10</sub>	178	52.55	38.05	60.90	51.77
16	Anthracene	C <sub>14</sub> H <sub>10</sub>	178	14.75	11.93	21.96	18.21
17	Fluoranthene	C <sub>16</sub> H <sub>10</sub>	202	8.80	9.25	15.65	13.28
18	Pyrene	C <sub>16</sub> H <sub>10</sub>	202	8.08	8.34	8.24	6.71
19	Benz (a) anthracene	C <sub>18</sub> H <sub>12</sub>	228	1.22	1.56	3.43	2.51
20	Chrysene	C <sub>18</sub> H <sub>12</sub>	228	0.58	1.10	2.56	1.86
21	Benzo (b) fluoranthene	C <sub>20</sub> H <sub>12</sub>	252	0.06	0.80	2.07	1.44
22	Benzo (a) pyrene	C <sub>20</sub> H <sub>12</sub>	252	0.01	0.56	0.37	0.28
23	Dibenz (a, h) anthracene	C <sub>22</sub> H <sub>14</sub>	278	0.02	0.00	2.08	1.46
	Total			9392.21	8663.71	6890.27	6125.16

nd=not determined

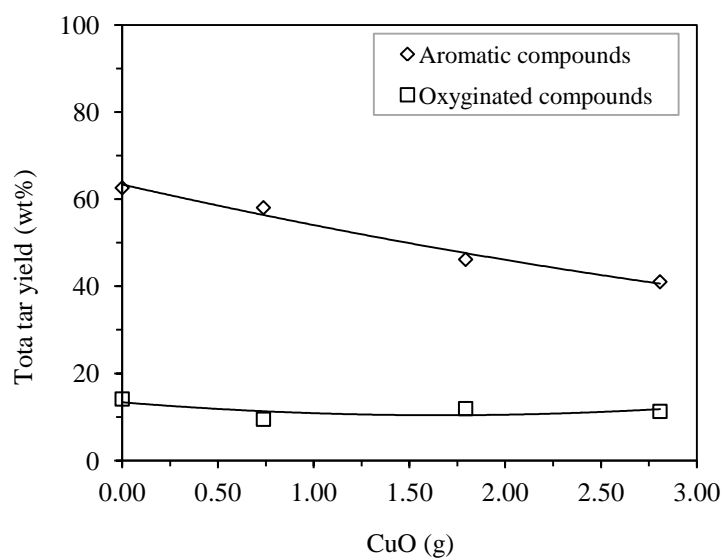


Figure 6.18 The effect of CuO loading on tar yield

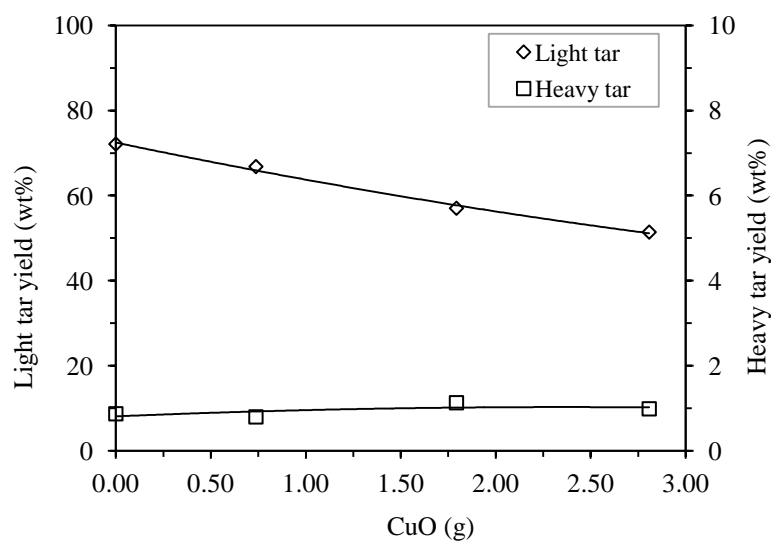


Figure 6.19 The effect of CuO loading on light tar yield

These findings suggest that the activity of copper doped pumice on biomass tar at 350 °C is governed by the redox characteristics of the catalyst. Other researchers have related the activity of CuO as a result of good dispersion over the catalyst support and also promote reduction reactions [153]. These reactions involve ions exchange with a reduced copper ( $\text{Cu}^{2+}$ ).

## 6.7.4 Nickel doped pumice

### 6.7.4.1 The effect of nickel doped pumice on gasification products

Nickel doped pumice was studied during the catalytic processing of the gasification product gas at 350 °C. Based on the non-catalytic tests, the feed was mainly composed of gases (H<sub>2</sub>, CO, CO<sub>2</sub>, CH<sub>4</sub>, C<sub>2</sub>-C<sub>3</sub>) and tar as reported in Table 6.4 and Table 6.10 respectively. The tested catalysts were prepared at concentration of 1.07 g and 2.04 g of nickel oxide on the pumice support.

Figure 6.20 shows the measured composition of syngas at different NiO loading. It can be seen from the figure that CO and CH<sub>4</sub> increased significantly with increasing NiO. With a 2.04 g loading, the concentration of CO increased from 22.11 % to 28.01 % by volume. Similarly, CH<sub>4</sub> increased from 3.62 to 5.06 %. Furthermore, the concentration of the H<sub>2</sub> decreased from 14.33 % to 8.16 %, while CO<sub>2</sub> decreased from 13.97 % to 10.61 %. There was no significant difference in light hydrocarbon between non-catalytic and catalytic tests. The syngas heating value was found to be 6.71 and 7.26 MJ/Nm<sup>3</sup> for catalyst loading of 1.07 and 2.04 g respectively.

The selectivity of NiO to gaseous components is shown in Figure 6.21. The negative selectivity means consumption of a particular species, while positive selectivity means the species was generated by the catalytic reactions. It can be seen from the figure that NiO consumed H<sub>2</sub>, CO<sub>2</sub> and light hydrocarbons slightly. With an increase of NiO loading from 1.07 g to 2.04 g, the H<sub>2</sub> selectivity increased from 13.02 % to 17.08 % by volume. Similarly, the selectivity to CO<sub>2</sub> rose from 5.85 % to 8.05 %. Under similar catalyst loading, CO selectivity increased from 8.89 % to 14.14 %. Although the selectivity to CH<sub>4</sub> was positive, there was no significant change with the doubling of the catalyst concentration.

Figure 6.22 presents the gas ratios and cold gas efficiency obtained at different NiO loading. The results show that CO/CO<sub>2</sub> and CH<sub>4</sub>/CO<sub>2</sub> ratios increased with increasing NiO concentration on pumice support. This increase almost doubled that of the non-catalytic test. However, the H<sub>2</sub>/CO<sub>2</sub> ratio decreased to 0.77 compared to 1.03 of the non-catalytic test. The cold gas efficiency showed no significant change with all tested catalysts.

There are several possible explanations for these results. A combination of CO/CO<sub>2</sub> and CH<sub>4</sub>/CO<sub>2</sub> ratios increase at decreasing H<sub>2</sub>/CO<sub>2</sub> ratio confirms the activity of the NiO on partial oxidation of hydrocarbon that were present in the

gasification product gas. This activity could be a possible source for the increase of CO and CH<sub>4</sub> in the product gas identified in Figure 6.20. Moreover, the increased selectivity to H<sub>2</sub> destruction correlates with an insignificant change of cold gas efficiency for all gasification tests as shown in Figure 6.22.

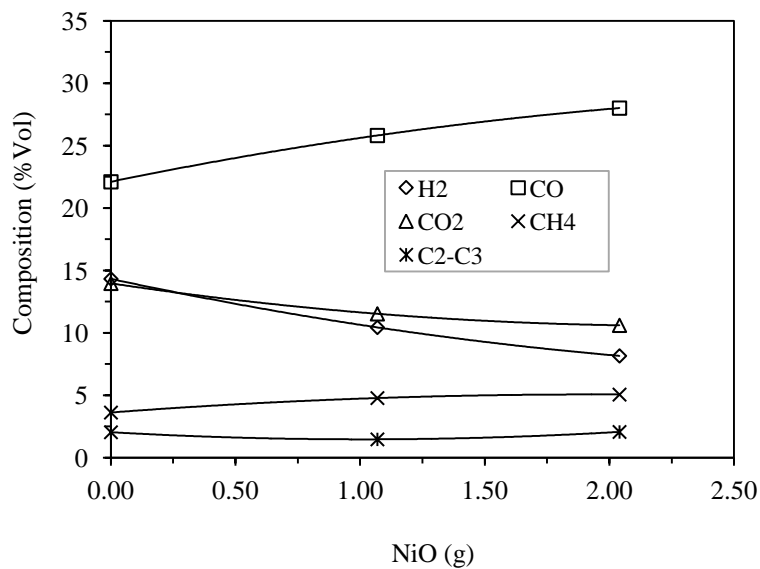


Figure 6.20 Syngas composition at different NiO loading

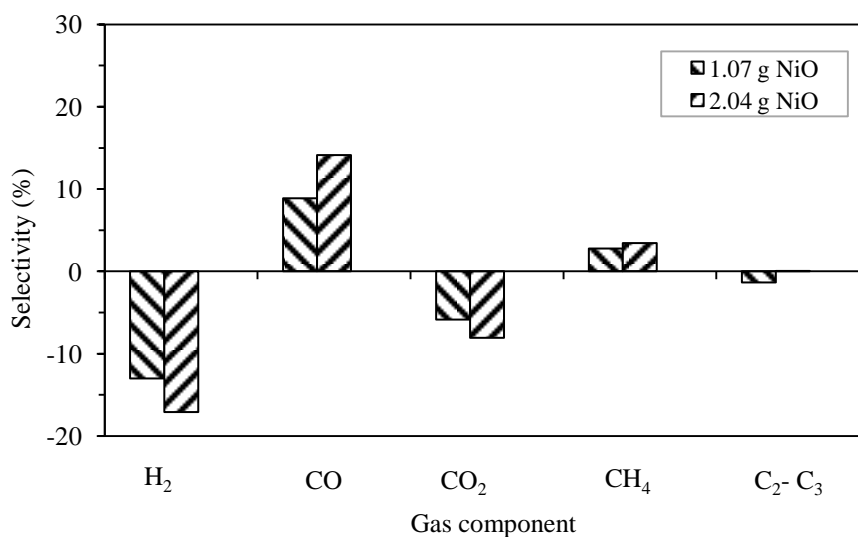


Figure 6.21 Catalyst selectivity at different NiO loading

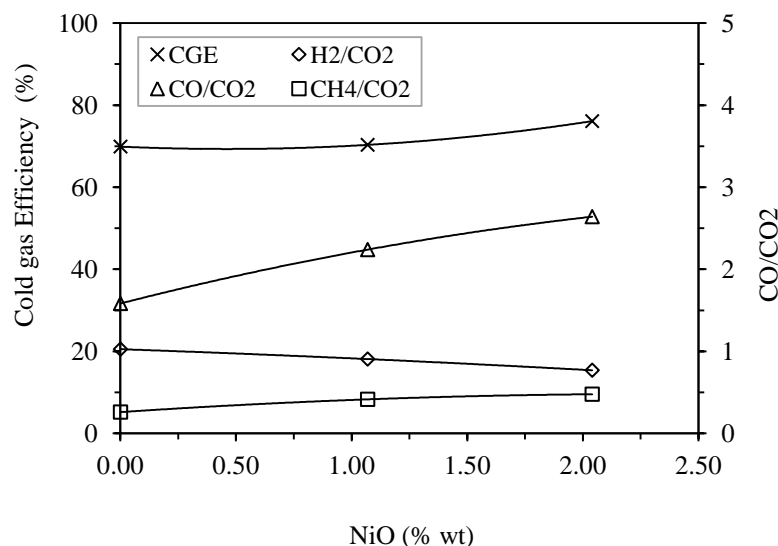


Figure 6.22 The effect of NiO loading on cold gas efficiency and gas ratios

#### 6.7.4.2 The effect of nickel doped pumice on tar yield

The composition and yields of tar forming compounds as detected by the GC-MS during testing of nickel doped pumice catalysts are shown in Table 6.10. As seen from the table, the main tar forming compounds were benzene, toluene, xylene, phenol, naphthalene and cresol isomers. From these compounds, only phenol and cresol isomers are oxygen containing hydrocarbons. With the increase of NiO loading from 0 to 1.07 g, the concentration of aromatic compounds decreased from 9343 mg/Nm<sup>3</sup> to 7780 mg/Nm<sup>3</sup>. This decrease was mainly contributed by the decrease of toluene and xylene isomers to about 880 and 870 mg/Nm<sup>3</sup> respectively. In addition, naphthalene contributed to a decrease of 280 mg/Nm<sup>3</sup>. With the exception of benzene, further increase of NiO loading to 2.04 g resulted in increase of all aromatic compounds. However, the increase was still lower compared to the untreated pumice. The oxygenated compounds presented similar a trend to that of aromatic hydrocarbons. At the 1.07 g NiO loading, the observed decrease of oxygenated compound was mainly contributed by phenol. Further increase of NiO loading to 2.04 g, resulted in an increase of all oxygen containing hydrocarbons. Furthermore, there was no significant effect on the tar destruction as revealed in Figure 6.23 and Figure 6.24.

Table 6.10 Tar yield at different NiO loading (FP, NiO=0 g; NiO-1=1.07 g; NiO-2=2.04 g)

No.	Compound	Formula	Mwt	Tar yield (mg/Nm <sup>3</sup> )		
				FP	Ni-1	Ni-2
	<i>Oxygenated compounds</i>					
1	Phenol	C <sub>6</sub> H <sub>5</sub> -OH	94	1076.52	814.29	1273.19
2	Cresol isomers	C <sub>6</sub> H <sub>4</sub> -OH, CH <sub>3</sub>	108	420.87	405.42	452.00
3	Dimethylphenol isomers	C <sub>6</sub> H <sub>3</sub> -OH, CH <sub>3</sub>	122	10.90	33.36	0.00
4	Acetophenone	C <sub>8</sub> H <sub>8</sub> O	120	24.33	13.13	26.93
5	Dibenzofuran	C <sub>12</sub> H <sub>8</sub> O	168	6.38	14.69	30.29
		Total		1538.99	1280.89	1782.40
	<i>Aromatic compounds</i>					
6	Benzene	C <sub>6</sub> H <sub>6</sub>	78	3729.65	4345.34	3154.64
7	Toluene	C <sub>6</sub> H <sub>5</sub> -CH <sub>3</sub>	92	2343.44	1459.06	1964.91
8	Ethylbenzene	C <sub>6</sub> H <sub>5</sub> CH <sub>2</sub> CH <sub>3</sub>	102	302.43	178.94	254.36
9	Xylene isomers	C <sub>6</sub> H <sub>4</sub> -CH <sub>3</sub> , CH <sub>3</sub>	106	1667.40	793.68	1195.42
10	Naphthalene	C <sub>10</sub> H <sub>8</sub>	128	960.49	682.40	1228.13
11	Acenaphthylene	C <sub>12</sub> H <sub>8</sub>	152	207.57	205.05	393.72
12	Acenaphthene	C <sub>12</sub> H <sub>10</sub>	154	9.32	32.29	0.00
13	Biphenyl	C <sub>12</sub> H <sub>10</sub>	154	48.91	0.00	69.23
14	Fluorene	C <sub>13</sub> H <sub>10</sub>	166	36.93	17.85	44.00
15	Phenanthrene	C <sub>14</sub> H <sub>10</sub>	178	52.55	8.46	40.32
16	Anthracene	C <sub>14</sub> H <sub>10</sub>	178	14.75	20.23	54.72
17	Fluoranthene	C <sub>16</sub> H <sub>10</sub>	202	8.80	17.85	44.00
18	Pyrene	C <sub>16</sub> H <sub>10</sub>	202	8.08	8.46	40.32
19	Benz (a) anthracene	C <sub>18</sub> H <sub>12</sub>	228	1.22	3.10	6.84
20	Chrysene	C <sub>18</sub> H <sub>12</sub>	228	0.58	2.23	4.91
21	Benzo (b) fluoranthene	C <sub>20</sub> H <sub>12</sub>	252	0.06	2.14	4.36
22	Benzo (a) pyrene	C <sub>20</sub> H <sub>12</sub>	252	0.01	0.44	0.88
23	Dibenz (a, h) anthracene	C <sub>22</sub> H <sub>14</sub>	278	0.02	2.21	5.39
		Total		9343.32	7779.74	8506.13

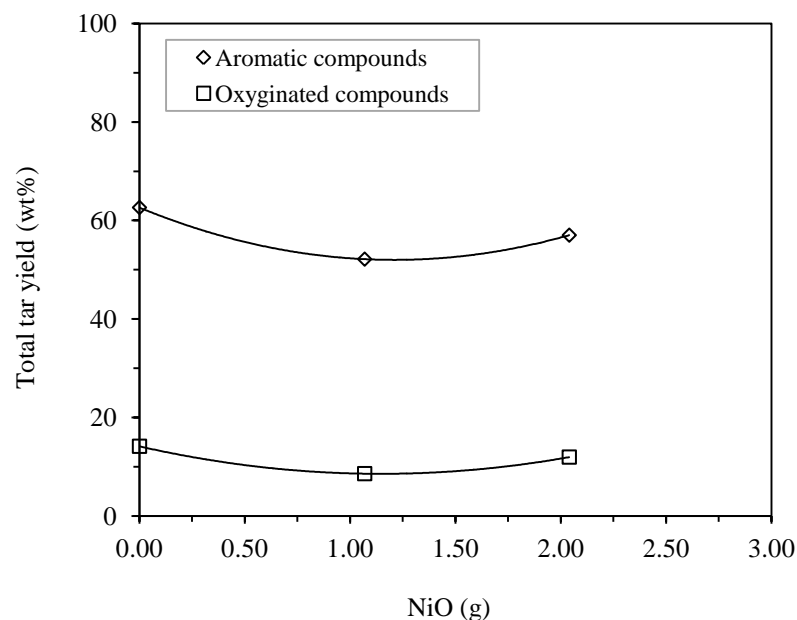


Figure 6.23 The effect of NiO loading on tar yield

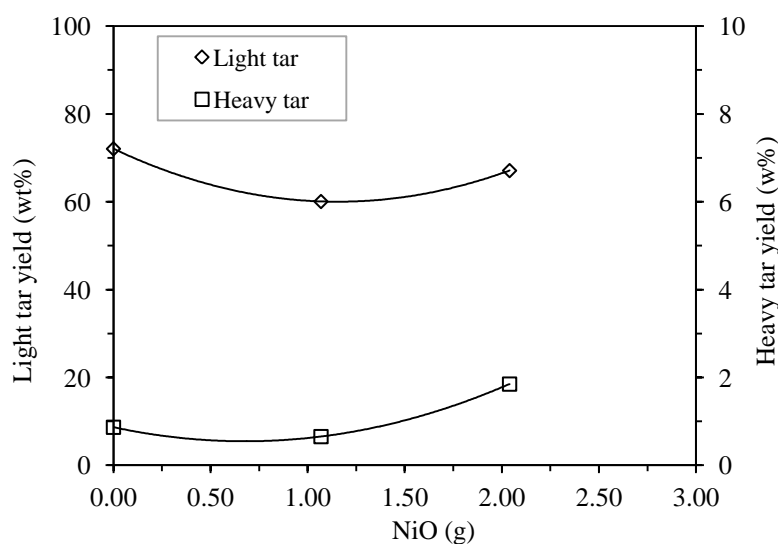


Figure 6.24 The effect of NiO loading on light tar yield

There are several possible explanations for the effect of nickel doped pumice on biomass tar. A noted decrease of tar at 1.07 g NiO loading compared to 2.04 g loading can be explained as a concentration limiting factor. At higher concentration, the structure of nickel oxide reduces the surface area of the active sites and consequently reducing the catalyst activity. Another possible explanation for the decrease of tar could be cracking as confirmed by the increase of methane and coke

formation highlighted in Figure 6.20 and Figure 6.32 respectively. Furthermore, the increase of oxygenated compounds can be linked to the catalytic partial oxidation of hydrocarbons. A previous study by Patcas and Patcas [154] showed that NiO oxidises hydrocarbons yielding various products including CO, CO<sub>2</sub>, alcohols and acids. This activity can be correlated to the increase of CO as shown in Figure 6.20. Other researchers [155] have also reported that toluene and naphthalene could be converted into CO and CH<sub>4</sub> over a NiO catalyst under similar reaction conditions. Furthermore, the observed increase and decrease of compounds between 1.07 g and 2.04 g NiO loading can be explained as catalyst concentration dependency while the decrease of xylene could be due to the partial oxidation [156]. In general, the increase of cold gas efficiency and the decrease of tar, while preliminary, suggests that nickel doped pumice could be employed for catalytic reforming of the gasification product gas.

### **6.7.5 Kaolin-Ceria (KL/CeO<sub>2</sub>)**

#### **6.7.5.1 The effect of Kaolin-Ceria catalysts on gasification product gas**

Kaolin catalysts were prepared at different blends with ceria as active sites. The use of ceria aimed at increasing the mobile oxygen which was responsible for the oxidation of tar present in the biomass gasification product gas. A typical composition of the feed for gas species is provided in Table 6.4 and for the tar in Table 6.10. The concentration of ceria in the Kaolin mix for the tested catalysts was 0, 9.2, 14, 21 g respectively.

Figure 6.25 shows the composition of syngas at different kaolin-ceria mix ratios. It can be seen that CO reached its maximum value of 28 % by volume at ceria loading between 9.2 g and 14 g. At higher catalyst loading (21 g CeO<sub>2</sub>), CO decreased to approximately 24 %. Unlike CO, the CH<sub>4</sub> showed an increasing trend with increasing ceria in the kaolin. The increase was more than one-half of that measured in the non-catalytic tests. Although H<sub>2</sub> and CO<sub>2</sub> showed no difference at CeO<sub>2</sub> loading of 9.2 g and 14.0 g, their concentrations were about 6 % and 3 % lower compared to that of the non-catalytic test. Furthermore, for all catalytic tests, there was no significant effect on the concentration of light hydrocarbons. The syngas heating value was found to be 7.34, 7.13 and 6.24 MJ/Nm<sup>3</sup> for catalyst loading of 9.20, 14 and 21 g respectively.

The selectivity of the kaolin-ceria to gas components in the syngas is shown in Figure 6.26. These results were obtained by subtracting the selectivity of the non-catalytic test from those of catalytic tests. The negative values means consumption, while the positive selectivity means generation. It can be observed that for all catalytic tests, H<sub>2</sub>, CO<sub>2</sub> as well as light hydrocarbon were consumed while CO and CH<sub>4</sub> were generated. Both H<sub>2</sub> and CO<sub>2</sub> reached a maximum decrease of 12 % at a kaolin-mix of 21 g CeO<sub>2</sub>. For light hydrocarbon the increase was only 1 %. Under the same catalyst loading, the selectivity to CO and CH<sub>4</sub> showed the lowest positive values of 4 % and 3 % respectively. The maximum selectivity to CO and CH<sub>4</sub> of kaolin mix catalyst reached 14 % and 4 % at ceria concentration of 9.2 and 14 g respectively.

The effect kaolin-ceria catalyst on gas ratios and cold gas efficiency is shown in Figure 6.27. For the gas ratios, a significant increase was observed for CO/CO<sub>2</sub> with increasing the CeO<sub>2</sub> in the kaolin mix. This rise (1.58 to approx. 2.50) remained unchanged despite the increasing ceria loading. The CH<sub>4</sub>/CO<sub>2</sub> reached a maximum value of 0.67 at 9.2 g CeO<sub>2</sub> in the mix and gradually decreased with increasing ceria. Furthermore, there was a decrease of H<sub>2</sub>/CO<sub>2</sub> ratio in the range of 0.15 to 0.30. The performance of the catalysts are also presented by the cold gas efficiency curve in Figure 6.27. The CGE reached its maximum value of 77 % at 9.2 g CeO<sub>2</sub> loading and gradually decreased with increasing ceria in the kaolin mix.

The effect of kaolin-ceria catalyst on syngas composition can be explained by the atmosphere in which the reactions were taking place. The decreasing trend of gas ratios confirms the existence of partial oxidation reactions. These reactions may be attributed to the interaction of O<sup>2-</sup> released from the catalyst and the hydrocarbons that are present in the gasification product gas. Furthermore, the observed decrease of H<sub>2</sub> can be explained as a result of oxidation in which O<sup>2-</sup> could be responsible [137]. The consequence of this side reaction is the decrease of cold gas efficiency as shown in Figure 6.27. Another finding was the low concentration of CO produced compared to that of ceria doped pumice catalysts discussed in Section 6.6.1. Although kaolin-ceria mix catalyst consisted high ceria compared to that of pumice support, the results suggest that catalytic activity was mainly on the surface rather than the bulk catalyst.

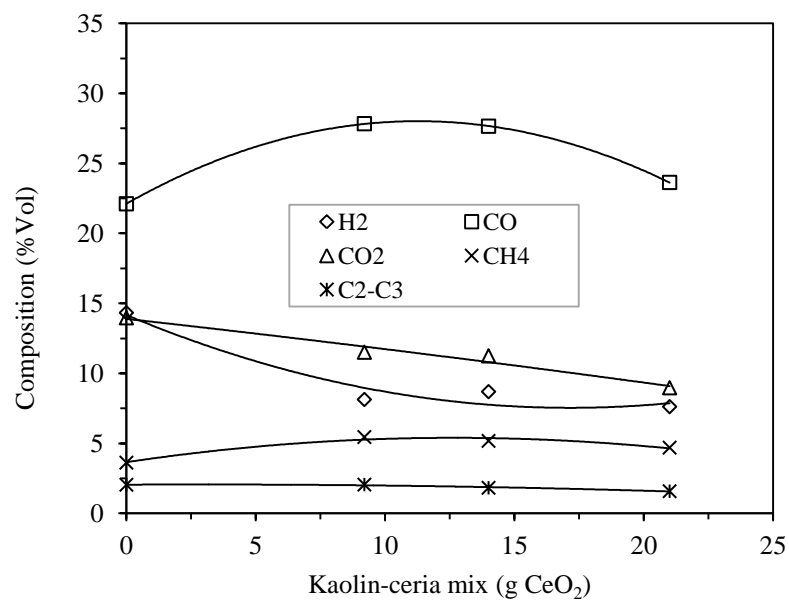


Figure 6.25 Syngas composition at different CeO<sub>2</sub> loading in the Kaolin-ceria mix catalysts

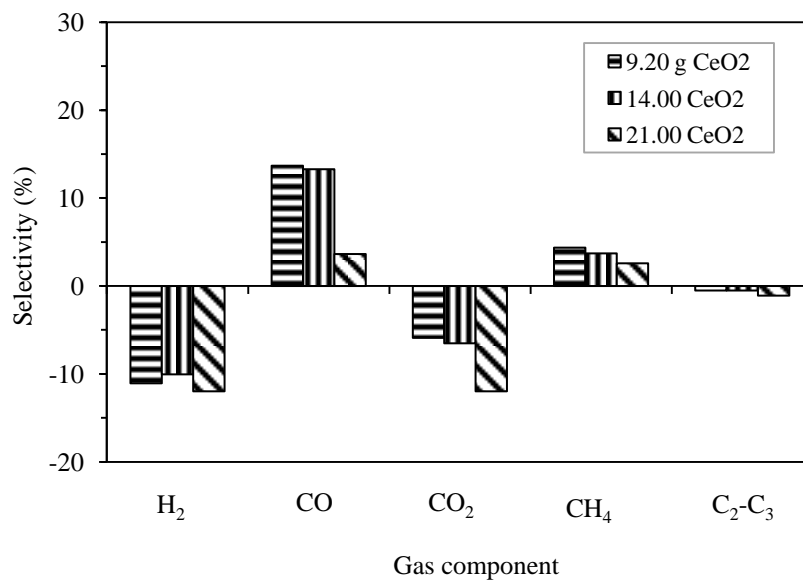


Figure 6.26 Catalyst selectivity at different CeO<sub>2</sub> loading in the kaolin-ceria mix catalysts

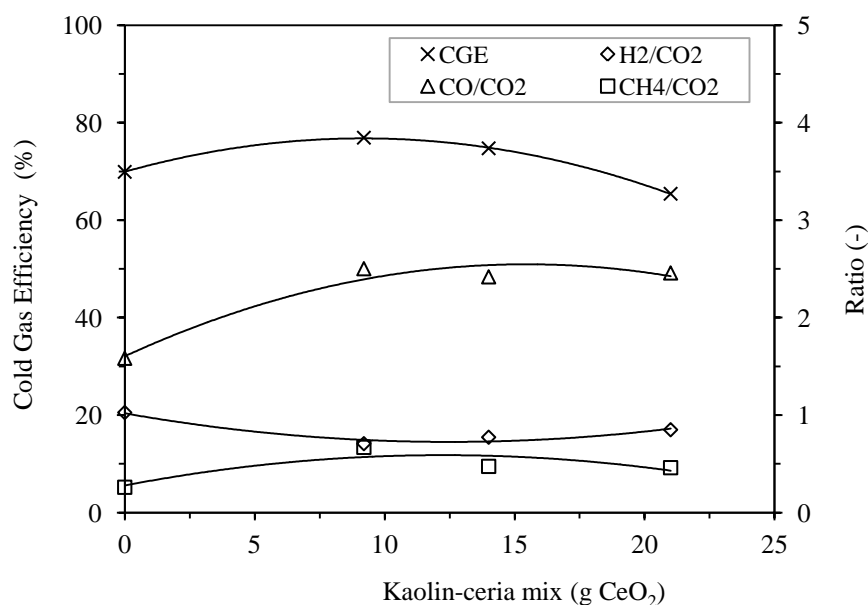


Figure 6.27 The effect of CeO<sub>2</sub> loading on cold gas efficiency in the kaolin-ceria mix

### 6.7.5.2 The effect of Kaolin-Ceria catalysts on tar yield

Table 6.11 shows the yield of tar forming compounds over kaolin catalysts as detected by the GC-MS. It can be seen from the table that pure kaolin presented high tar slip compared to the ceria doped kaolin. While tar reduction was observed at 14 g CeO<sub>2</sub> loading, further increase of CeO<sub>2</sub> concentration to 21 g showed an insignificant effect on the total yield for both oxygenated and aromatic compounds. Specifically, benzene and toluene showed a further decrease of more than one-fourth at 14 g CeO<sub>2</sub> compared to 9.2 g. Other aromatic compounds such as xylene isomers, naphthalene, acenaphthylene and phenanthrene decreased with increasing catalyst loading. Furthermore, the effect of kaolin catalysts on the light and heavy tar compounds is presented in Figure 6.28 and Figure 6.29 respectively. It can be seen that light tar decreased in the range of 20-30 % with ceria concentration between 9 and 21 g. In this range there was no significant change for the heavy tar destruction.

The effect of ceria doped kaolin on tar from biomass gasification can be associated with several factors. The decreasing trend of the total tar yield as highlighted in Figure 6.28 can be correlated to the increase of CH<sub>4</sub> and CO in the product gas as previously shown in Figure 6.26. A combination of these findings can be explained as catalytic cracking and partial oxidation of hydrocarbons respectively.

Table 6.11 Tar yield at different copper loading (Kaolin-1, CeO<sub>2</sub>=0 g; Kaolin-2, CeO<sub>2</sub>=9.2 g; Kaolin-3, CeO<sub>2</sub>=14 g; Kaolin-4, CeO<sub>2</sub>=21 g)

No.	Compound	Formula	Mwt	Tar yield (mg/Nm <sup>3</sup> )			
				Kaolin-1	Kaolin-2	Kaolin-3	Kaolin-4
<i>Oxygenated compounds</i>							
1	Phenol	C <sub>6</sub> H <sub>5</sub> -OH	94	1258.21	713.52	912.20	786.38
2	Cresol isomers	C <sub>6</sub> H <sub>4</sub> -OH, CH <sub>3</sub>	108	623.30	491.93	389.56	351.67
3	Dimethylphenol isomers	C <sub>6</sub> H <sub>3</sub> -OH, CH <sub>3</sub>	122	53.13	42.46	33.21	39.54
4	Acetophenone	C <sub>8</sub> H <sub>8</sub> O	120	31.96	17.87	33.29	48.87
5	Dibenzofuran	C <sub>12</sub> H <sub>8</sub> O	168	19.68	5.18	20.50	27.29
		Total		1986.28	1270.96	1388.76	1253.74
<i>Aromatic compounds</i>							
6	Benzene	C <sub>6</sub> H <sub>6</sub>	78	5992.98	4832.53	3745.62	3885.94
7	Toluene	C <sub>6</sub> H <sub>5</sub> -CH <sub>3</sub>	92	2496.84	2438.14	1560.52	1278.67
8	Ethylbenzene	C <sub>6</sub> H <sub>5</sub> CH <sub>2</sub> CH <sub>3</sub>	102	330.97	337.45	206.86	235.79
9	Xylene isomers	C <sub>6</sub> H <sub>4</sub> -CH <sub>3</sub> , CH <sub>3</sub>	106	1285.02	243.02	803.14	878.43
10	Naphthalene	C <sub>10</sub> H <sub>8</sub>	128	966.93	864.49	604.33	633.85
11	Acenaphthylene	C <sub>12</sub> H <sub>8</sub>	152	253.91	191.33	158.70	150.46
12	Acenaphthene	C <sub>12</sub> H <sub>10</sub>	154	nd	nd	nd	nd
13	Biphenyl	C <sub>12</sub> H <sub>10</sub>	154	50.95	39.69	53.07	68.67
14	Fluorene	C <sub>13</sub> H <sub>10</sub>	166	55.12	43.17	34.45	33.67
15	Phenanthrene	C <sub>14</sub> H <sub>10</sub>	178	93.71	64.71	58.57	56.15
16	Anthracene	C <sub>14</sub> H <sub>10</sub>	178	31.40	22.20	19.62	19.56
17	Fluoranthene	C <sub>16</sub> H <sub>10</sub>	202	17.86	10.49	11.16	13.06
18	Pyrene	C <sub>16</sub> H <sub>10</sub>	202	15.45	9.45	9.66	11.12
19	Benz (a) anthracene	C <sub>18</sub> H <sub>12</sub>	228	2.41	3.95	1.50	2.84
20	Chrysene	C <sub>18</sub> H <sub>12</sub>	228	1.61	1.22	1.01	2.07
21	Benzo (b) fluoranthene	C <sub>20</sub> H <sub>12</sub>	252	1.55	1.46	0.97	2.19
22	Benzo (a) pyrene	C <sub>20</sub> H <sub>12</sub>	252	0.48	0.52	0.30	0.58
23	Dibenz (a, h) anthracene	C <sub>22</sub> H <sub>14</sub>	278	1.10	1.03	0.69	1.75
		Total		11598.27	9104.86	7270.15	7274.78

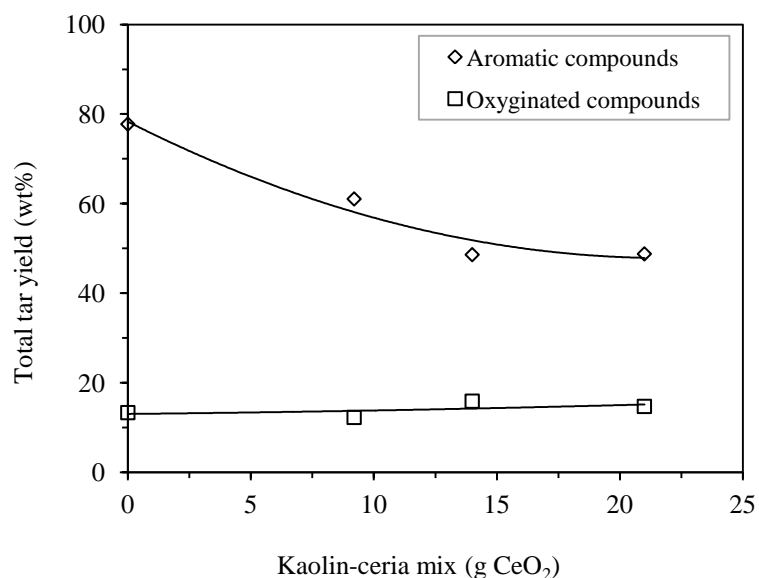


Figure 6.28 The effect of CeO<sub>2</sub> loading on tar yield using kaolin-ceria mix catalysts

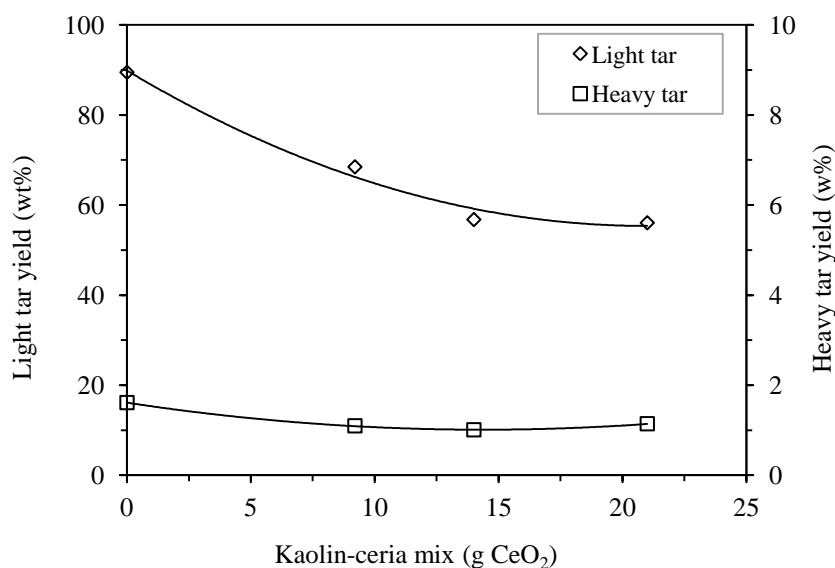


Figure 6.29 The effect of CeO<sub>2</sub> loading on light tar yield using kaolin-ceria mix catalysts

The observed low reactivity of heavy tar with catalysts could be attributed to the competitive adsorption to the active sites. Heavy tar has low adsorption capacity compared to the light tar fraction and the reactive gases such as hydrogen and carbon monoxide. The observed decrease of light and heavy PAH can also be linked to condensation over the catalyst surface as revealed by carbon analysis discussed in the next section of catalyst screening.

## 6.7.6 Kaolin-Ceria-Zirconia (KL/CeO<sub>2</sub>/ZrO<sub>2</sub>)

### 6.7.6.1 The effect of Kaolin-CeO<sub>2</sub>-ZrO<sub>2</sub> on biomass gasification product gas

The effect of doping zirconia with ceria doped kaolin on gasification product gas has been examined. Addition of zirconia on the kaolin-ceria blend aimed at increasing the oxygen storage capacity (OSC) of the resulting catalyst. Increasing OSC promotes redox reactions due to the enhanced atmosphere of mobile oxygen responsible for the oxidation of hydrocarbons. Feed composition employed during the study is provided in Section 6.5. The comparison was made between ceria doped kaolin with a 14 g CeO<sub>2</sub> loading and the kaolin-ceria-zirconia composed of 14 CeO<sub>2</sub> g, 14 g ZrO<sub>2</sub> with kaolin making up the balance to a 100 g total product.

Table 6.12 compares the performance of the kaolin-ceria and kaolin-ceria-zirconia catalysts on the biomass gasification product gas. It can be seen from the table that addition of zirconia in the kaolin-ceria system resulted in an increase of hydrogen and methane in the product gas. H<sub>2</sub> increased from 8.69 to 11.32 (% vol.) as well as CH<sub>4</sub> increased 5.17 % to 7.40 %. Contrary to the expectations, this study did not find a significant increase of CO in the product gas. The syngas heating value increased from 7.13 MJ/Nm<sup>3</sup> to 7.74 MJ/Nm<sup>3</sup>.

Table 6.12 The effect of doping zirconia in the kaolin-ceria mix catalyst on the biomass gasification product gas

Parameter	Catalysts	
	KL/CeO <sub>2</sub>	KL/CeO <sub>2</sub> /ZrO <sub>2</sub>
<i>Syngas composition (% vol.)</i>		
H <sub>2</sub>	8.69	11.32
CO	27.65	27.39
CO <sub>2</sub>	11.25	11.52
CH <sub>4</sub>	5.17	7.40
C <sub>2</sub> H <sub>6</sub>	1.53	0.99
C <sub>3</sub> H <sub>8</sub>	0.29	0.23
<i>Gas ratios</i>		
CO/CO <sub>2</sub>	2.46	2.38
H <sub>2</sub> /CO <sub>2</sub>	0.77	0.98
CH <sub>4</sub> /CO <sub>2</sub>	0.46	0.64
H <sub>2</sub> /CO	0.31	0.41
LHV (MJ/Nm <sup>3</sup> )	7.13	7.74
Cold gas efficiency (%)	74.73	81.07

These results may be explained by a number of factors. The observed increase of methane and hydrogen in the product gas could be attributed to the tar cracking. The slightly decrease of light hydrocarbons can be associated with partial oxidation over the active sites. In addition the possible interference of competitive adsorption of the species over the catalyst can not be ruled out. The increase of cold gas efficiency from 74.73 % to 81.07 % highlights the contribution of CH<sub>4</sub> and H<sub>2</sub> in the syngas heating value.

#### **6.7.6.2 The effect of Kaolin-CeO<sub>2</sub>-ZrO<sub>2</sub> on tar destruction**

The effect of adding zirconia in kaolin-ceria mixes (kaolin-3, 14 g CeO<sub>2</sub>) on tar destruction is shown in Table 6.13 and Figure 6.30. It can be seen from the table that addition of 14 g ZrO<sub>2</sub> resulted in a significant decrease in the aromatic and oxygenated compounds. The former decreased by more than 60 %, while the latter decreased by 25 %. The decrease of aromatic compounds was highly related to the decrease of benzene and toluene. Light hydrocarbons decreased by 50 % as shown in Figure 6.30. In addition, there was no significant effect on heavy tar as result of doping zirconia with the kaolin-3.

The effect of doping zirconia with kaolin-ceria catalyst can be explained by various factors. A significant decrease of aromatic compounds with a slight decrease of oxygenated compounds suggests the existence of the partial oxidation of hydrocarbons. Moreover, the interpretation can be correlated to the increase of CO as observed in Table 6.12. These findings are in good agreement with the study by Juutilainen et al [157] and Viinikainen et al [158] who examined the effect of zirconia on toluene and naphthalene conversion. In their study, zirconia catalysts showed a remarkable conversion of toluene and naphthalene at temperatures around 500 °C. A high activity of zirconia on tar decomposition is mainly promoted by its basicity characteristics. Another possible attribute to the tar conversion is through cracking as confirmed by the increase of methane reported in Table 6.12. Therefore it is possible that zirconia increases the heating of the syngas from biomass gasification by promoting tar cracking.

Table 6.13 Tar yield at different copper loading (KL/CeO<sub>2</sub>, CeO<sub>2</sub>=14 g; KL/CeO<sub>2</sub>/ZrO<sub>2</sub>, CeO<sub>2</sub>=14 g, ZrO<sub>2</sub>=14 g)

No.	Compound	Formula	Mwt	Tar yield (mg/Nm <sup>3</sup> )	
				KL/CeO <sub>2</sub>	KL/CeO <sub>2</sub> /ZrO <sub>2</sub>
	<i>Oxygenated compounds</i>				
1	Phenol	C <sub>6</sub> H <sub>5</sub> -OH	94	912.20	707.21
2	Cresol isomers	C <sub>6</sub> H <sub>4</sub> -OH, CH <sub>3</sub>	108	389.56	354.35
3	Dimethylphenol isomers	C <sub>6</sub> H <sub>3</sub> -OH, CH <sub>3</sub>	122	33.21	27.82
4	Acetophenone	C <sub>8</sub> H <sub>8</sub> O	120	33.29	6.90
5	Dibenzofuran	C <sub>12</sub> H <sub>8</sub> O	168	20.50	3.65
		Total		1388.76	1099.94
	<i>Aromatic compounds</i>				
6	Benzene	C <sub>6</sub> H <sub>6</sub>	78	3745.62	864.63
7	Toluene	C <sub>6</sub> H <sub>5</sub> -CH <sub>3</sub>	92	1560.52	303.82
8	Ethylbenzene	C <sub>6</sub> H <sub>5</sub> CH <sub>2</sub> CH <sub>3</sub>	102	206.86	41.44
9	Xylene isomers	C <sub>6</sub> H <sub>4</sub> -CH <sub>3</sub> , CH <sub>3</sub>	106	803.14	160.62
10	Naphthalene	C <sub>10</sub> H <sub>8</sub>	128	604.33	705.05
11	Acenaphthylene	C <sub>12</sub> H <sub>8</sub>	152	158.70	193.47
12	Acenaphthene	C <sub>12</sub> H <sub>10</sub>	154	nd	nd
13	Biphenyl	C <sub>12</sub> H <sub>10</sub>	154	31.84	10.00
14	Fluorene	C <sub>13</sub> H <sub>10</sub>	166	34.45	40.75
15	Phenanthrene	C <sub>14</sub> H <sub>10</sub>	178	58.57	71.36
16	Anthracene	C <sub>14</sub> H <sub>10</sub>	178	19.62	24.47
17	Fluoranthene	C <sub>16</sub> H <sub>10</sub>	202	11.16	15.90
18	Pyrene	C <sub>16</sub> H <sub>10</sub>	202	9.66	13.15
19	Benz (a) anthracene	C <sub>18</sub> H <sub>12</sub>	228	1.50	1.81
20	Chrysene	C <sub>18</sub> H <sub>12</sub>	228	1.01	1.30
21	Benzo (b) fluoranthene	C <sub>20</sub> H <sub>12</sub>	252	0.97	1.04
22	Benzo (a) pyrene	C <sub>20</sub> H <sub>12</sub>	252	0.30	0.11
23	Dibenz (a, h) anthracene	C <sub>22</sub> H <sub>14</sub>	278	0.69	0.91
		Total		7248.94	2449.83

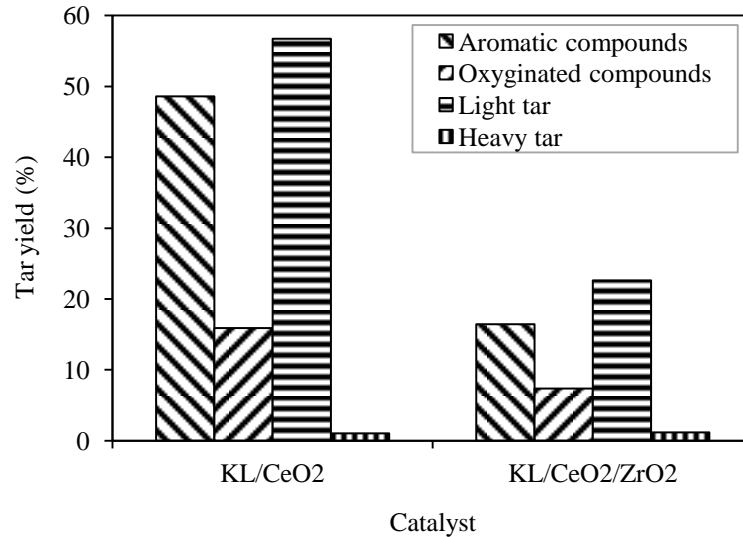


Figure 6.30 The effect of adding ZrO<sub>2</sub> in the CeO<sub>2</sub> doped kaolin on tar yield, (KL=kaolin)

## 6.8 Catalyst Screening

This section provides a comparison on the activity of catalysts employed for catalytic processing of the biomass gasification product gas. The criteria used for catalyst screening were selectivity, coking resistance and cold gas efficiency. These parameters are described in detail in Section 4.5. A summary of all experimental tests are also provided.

Figure 6.31 (a-e) compares the catalyst selectivity of pumice treated with CeO<sub>2</sub>, CuO and NiO at different catalyst loading. From Figure 6.31 (a) it can be seen that all catalysts showed a decrease of hydrogen concentration in the product gas. The decrease was found to be in the range of 4.64 % to 11.03 % for catalyst loading of 0.65 g to 1.73 g. Ceria doped pumice showed a lowest conversion of H<sub>2</sub> at 0.65 g loading compared to other catalysts and it exhibited highest conversion at 1.73 g loading. While copper doped pumice showed a slight difference in H<sub>2</sub> conversion at different catalyst loading, nickel doped pumice increased with increasing catalyst loading.

Figure 6.31 (b) indicates that the increase in selectivity of catalysts to gases range from 5.40 % to 23.22 % at 0.65 g to 1.73 g loading. At 0.65 g loading, copper doped pumice showed highest selectivity to CO, while the nickel doped pumice showed least selectivity. Similarly, at 1.23 g loading, nickel catalyst showed low

selectivity to CO compared to ceria and copper doped pumice catalysts. Moreover, ceria catalyst exhibited highest selectivity to CO at 1.73 g loading.

From Figure 6.31 (c) it can be seen that all catalysts showed a decrease of CO<sub>2</sub> concentration in product gas. This decrease was in the range of 0.91 % to 6.18 % for the reported catalyst loading and was dependent on the catalyst type and loading. High CO<sub>2</sub> conversions were achieved using ceria doped pumice and at 1.23 g and 1.73 g loading compared to other catalysts. At 0.65 g loading, copper doped pumice showed highest CO<sub>2</sub> conversion.

Further comparison as seen in Figure 6.31 (d), shows that the catalyst selectivity to CH<sub>4</sub> also depends on the type of catalyst and loading. While ceria doped pumice showed highest selectivity at 0.65 g and 1.73 g loading, the copper doped pumice catalysts was highest at 1.23 g loading. Nickel doped pumice showed least selectivity to CH<sub>4</sub> at given catalyst loading. The selectivity to light hydrocarbons shown in Figure 6.31 (e), shows that ceria and copper doped pumice increases the concentration of these gases, while nickel showed a decrease compared to non-catalytic gasification tests. A noticeable increase of selectivity of these catalysts was observed at 1.23 g and 1.73 g loading.

Kaolin catalysts showed both beneficial and detrimental effects to the syngas composition. The comparison was made between kaolin with 14 wt% CeO<sub>2</sub> and kaolin with 14 wt% CeO<sub>2</sub> and 14 wt% ZrO<sub>2</sub> as identified in Figure 6.31 (f). From this figure it can be seen that, the highest reduction of H<sub>2</sub> was observed for ceria doped kaolin compared to all other tested catalysts. However, the addition of zirconia improved significantly the CH<sub>4</sub> yield for ceria doped kaolin compared to all other catalysts.

These findings can be explained by a number of factors. The decrease of catalyst selectivity to H<sub>2</sub> indicates that all catalysts exhibited oxidation characteristic with the gasification product gas. Traditionally, H<sub>2</sub> conversion is important in promoting the catalyst redox cycle, higher conversions can lead to reduction of the syngas heating value. Although CO<sub>2</sub> is considered as inert gas, the observed reduction in concentration can be explained as a result of dissociation over the catalyst sites according to reaction ( $CO_2 \rightarrow CO + O$ ) [159]. This finding highlights a possible source of CO increase and the liberated oxygen could be responsible for sustaining catalyst redox cycles and partial combustion reactions of the product gas.

Furthermore, catalyst selectivity to gaseous product depends on the type and concentration of the catalyst.

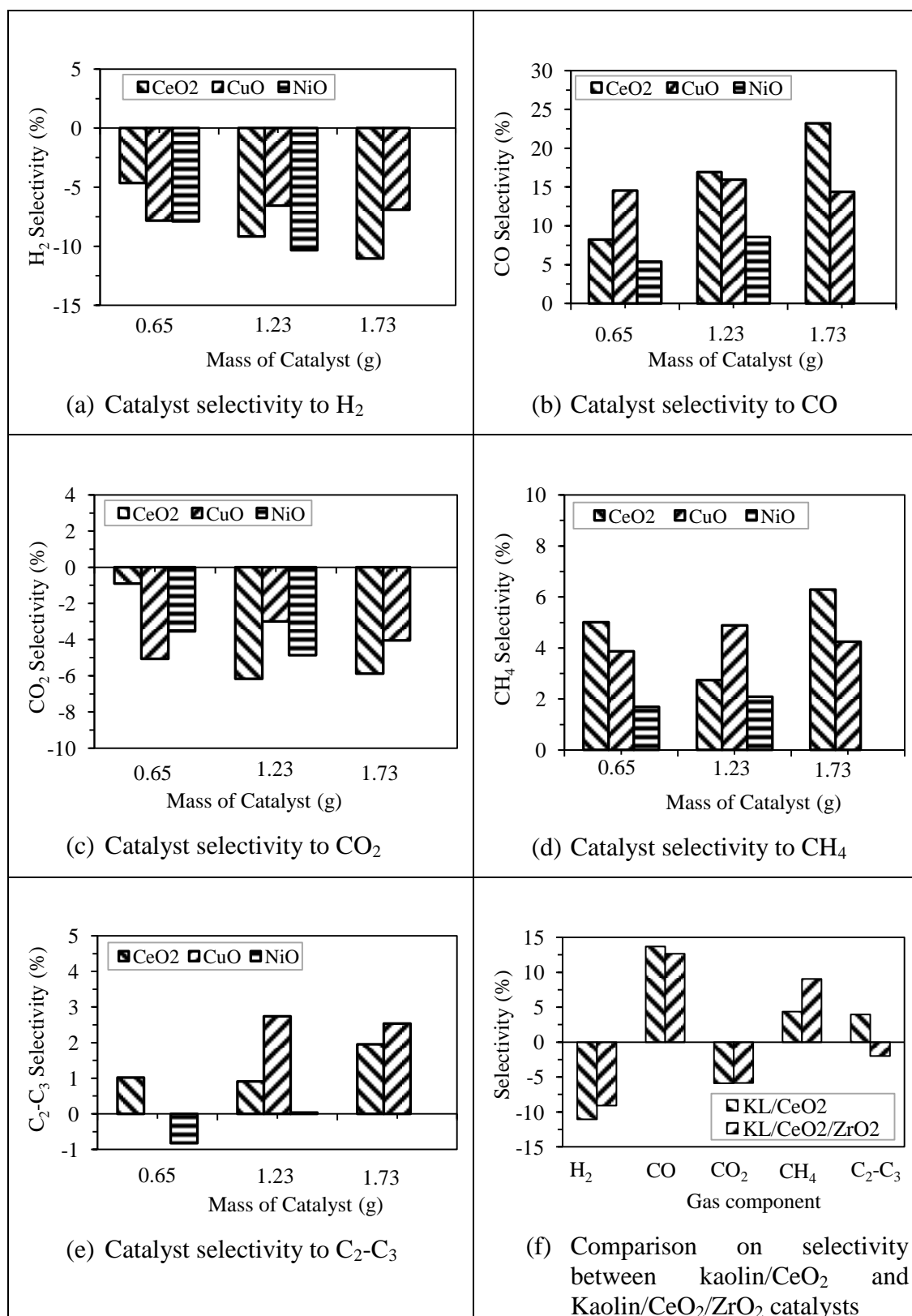


Figure 6.31 Comparison on the selectivity of catalysts to gaseous products

Overall results suggest that ceria and copper doped pumice can be employed where high selectivity to CO, CH<sub>4</sub>, and light hydrocarbons are required. Specifically, copper doped pumice can also be used for catalytic dry reforming processes which have also been reported by Laosiripojana and Assabumrungrat [140].

The carbon deposit on the CeO<sub>2</sub>, CuO and NiO doped pumice catalysts is presented in Figure 6.32. The carbon deposit over the catalyst was chosen to compare the activity of the catalysts on the coking resistance. It can be seen from the figure that the carbon deposition on fresh pumice (FP) and Kaolin (KL) were almost similar (0.40 %). Kaolin-ceria catalyst showed high deposited carbon compared to other catalysts. Treating these supports with redox catalysts resulted in a noticeable decrease of deposited carbon. For instance doping pumice with ceria decreased carbon deposition to 0.06 %, while with CuO and NiO decreased to 0.15-0.2 %. A similar trend was observed for the kaolin mix catalysts. The observed high carbon deposition on kaolin-ceria catalysts can be explained as a result of light and heavy tar deposition as reported in the previous Section 6.7.5.2. This could be attributed to the limited dispersion of ceria over the catalyst surface as revealed by XRD analysis (Figure 6.8). The overall results suggest that ceria doped pumice exhibits highest coking resistance compared to other catalysts.

Figure 6.33 compares the maximum cold gas efficiency achieved by each catalyst employed in this study. These catalysts were pumice doped with CeO<sub>2</sub>, CuO and NiO and kaolin treated with CeO<sub>2</sub>, and ZrO<sub>2</sub>. From the figure it can be seen that ceria and copper doped pumice showed highest cold efficiency indicating that they are potential catalysts for catalytic processing of the gasification product gas. Furthermore, the performance of the ceria doped kaolin can be improved by further doping with zirconia.

Table 6.14 summarises the results from both non-catalytic and catalytic experimental tests. For non catalytic tests, maximum LHV was 6.67 MJ/Nm<sup>3</sup> composed of H<sub>2</sub>, CO, CO<sub>2</sub>, CH<sub>4</sub> and C<sub>2</sub>H<sub>6</sub>, C<sub>3</sub>H<sub>8</sub> at 14.33, 22.11, 13.97, 3.62, 1.66, 0.38 % vol. respectively. The corresponding tar yield and cold gas efficiency was 70.78 %. Maximum LHV for doped pumice was 8.97 MJ/Nm<sup>3</sup> and the concentration of H<sub>2</sub>, CO, CO<sub>2</sub>, CH<sub>4</sub> and C<sub>2</sub>H<sub>6</sub>, C<sub>3</sub>H<sub>8</sub> was 11.41, 31.80, 11.51, 6.24, 2.26 and 0.60 % vol., while tar yield and CGE were 11.14 g/Nm<sup>3</sup> and 94.02 % respectively. Kaolin doped with ceria and zirconia showed highest LHV of 7.74 MJ/Nm<sup>3</sup> and the CGE was 81.07 %. This catalyst system also showed highest CH<sub>4</sub> and least tar yield.

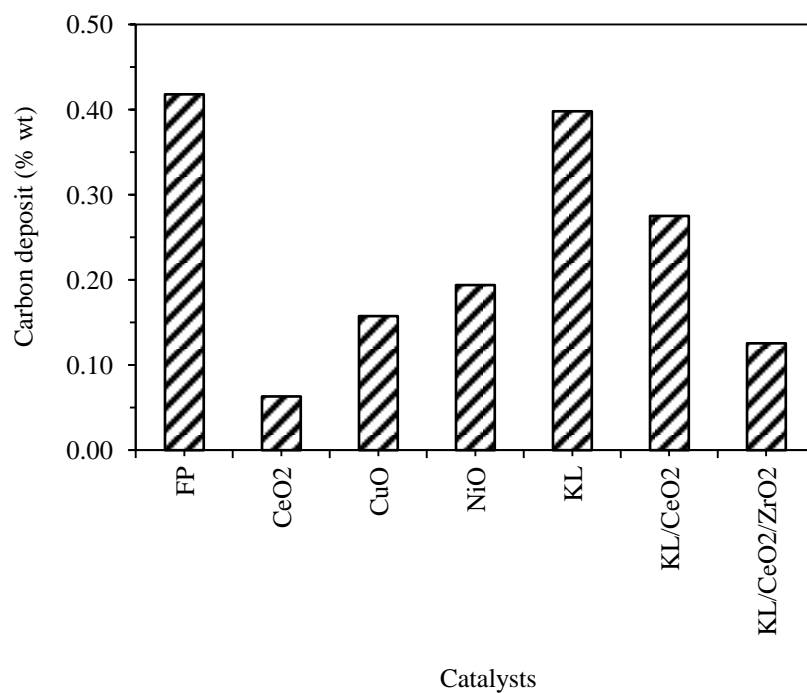


Figure 6.32 Activity of different catalysts based on coking resistance

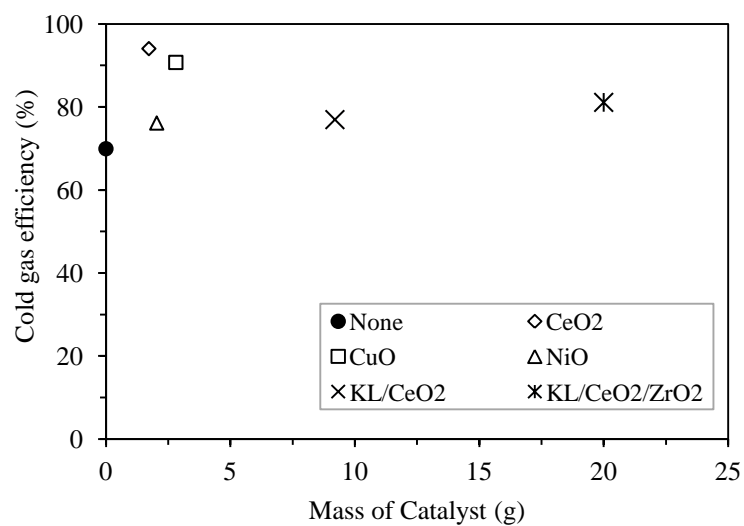


Figure 6.33 A comparison on the maximum cold gas efficiency achieved by different catalysts

Table 6.14 Summary of results from all experimental tests

Experimental Test	Gas Composition (% vol.)						LHV (MJ/Nm <sup>3</sup> )	Tar Yield (g/Nm <sup>3</sup> )	CGE (%)
	H <sub>2</sub>	CO	CO <sub>2</sub>	CH <sub>4</sub>	C <sub>2</sub> H <sub>6</sub>	C <sub>3</sub> H <sub>8</sub>			
None	14.33	22.11	13.97	3.62	1.66	0.38	6.67	14.92	70.78
Mexican Pumice	14.64	20.95	13.39	3.80	1.59	0.65	6.46	10.93	65.49
Arusha Pumice	7.75	22.71	12.01	3.92	1.23	0.32	5.01	9.84	56.87
Kaolin	7.93	20.74	10.67	3.33	1.13	0.27	5.34	13.58	55.98
Glass Beads	15.05	21.27	12.29	3.84	1.68	0.53	6.31	12.62	73.18
<i>Pumice supported catalysts</i>									
0.65 g CeO <sub>2</sub>	11.41	25.54	13.59	5.71	1.89	0.57	7.80	10.79	81.73
1.44 g CeO <sub>2</sub>	12.07	29.17	11.39	4.76	1.89	0.53	7.94	10.19	83.20
1.73 g CeO <sub>2</sub>	11.41	31.80	11.51	6.24	2.26	0.60	8.97	11.14	94.02
0.74 g CuO	8.80	29.02	11.56	5.46	1.72	0.46	7.67	10.08	80.74
1.79 g CuO	8.21	31.78	12.15	6.58	1.67	0.36	8.20	8.67	86.31
2.81 g CuO	9.93	31.87	11.22	6.50	2.02	0.46	8.66	7.81	91.16
1.07 g NiO	10.44	25.82	11.53	4.78	1.31	0.16	6.71	9.06	70.32
2.04 g NiO	8.16	28.01	10.61	5.06	1.65	0.42	7.26	10.29	76.10
<i>Kaolin supported catalysts</i>									
9.2 g CeO <sub>2</sub> /kaolin	8.13	27.83	11.51	5.45	1.70	0.35	7.34	10.38	76.91
14 g CeO <sub>2</sub> /kaolin	8.69	27.65	11.25	5.17	1.53	0.29	7.13	8.62	74.73
21 g CeO <sub>2</sub> /kaolin	7.62	23.64	8.97	4.69	1.25	0.33	6.24	8.53	65.40
14 g CeO <sub>2</sub> -14 g ZrO <sub>2</sub> -kaolin	11.32	27.39	11.52	7.40	0.99	0.23	7.74	3.58	81.07

## 6.9 Material and Energy Balances

Material and energy balances in the gasification system were conducted to monitor the conversion of wood powder into desired product gas as well as the residues as shown in Figure 6.34. Wood powder and air were fed to the gasifier as described in Section 4.4.3 and the products were classified as volatiles and char. The latter represented the unburnt carbon from the gasification residues while the former represented tar, carbonaceous gases ( $\text{CO}$ ,  $\text{CO}_2$ ,  $\text{CH}_4$ ,  $\text{C}_2\text{H}_6$ ,  $\text{C}_3\text{H}_8$ ) and non-carbonaceous gases ( $\text{H}_2$  and  $\text{N}_2$ ). These classes were considered as main streams in determining the mass, carbon and energy balances of the whole gasification system for all experimental tests.

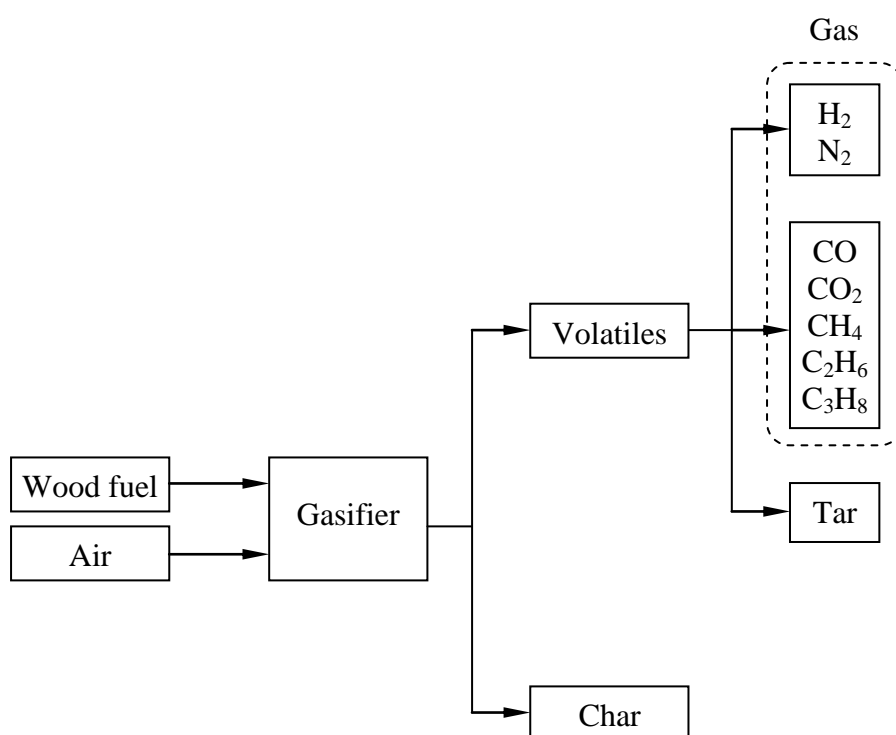


Figure 6.34 Distribution of the material flow in the gasification system

Mass balance in the gasification system was determined using Equation 6.7. the mass of fuel and char were weighed using a laboratory scale, while the mass of tar was taken as a sum of all compounds detected by GC-MS. The mass of air and gas were calculated using Equation 6.8 and Equation 6.9 respectively.

$$m_{air} + m_{fuel} = m_{char} + m_{tar} + m_{gas} \quad (6.7)$$

$$m_{air} = \frac{Q_{air}t}{\rho_{air}} \quad (6.8)$$

$$m_{gas} = Q_{gas} * t \sum X_i M_i \quad (6.9)$$

Where  $Q_{air}$  and  $\rho_{air}$  are flow rate (5 l/min) and density (1.2 kg/m<sup>3</sup>) of air respectively.  $Q_{gas}$  is the gas outflow rate (15 l/min) and  $t$  is the duration of the experiment (average 11 minutes).

Carbon balance was used to monitor the conversion of wood powder to gases, tar and char. Since air has negligible carbon content, only fuel wood was considered as a main source of carbon in the input stream. In the output stream, carbon distribution was considered to be in the gas ( $C_{gas}$ ), tar ( $C_{tar}$ ) and char ( $C_{char}$ ). The overall carbon balance was determined using Equation 6.10.

$$C_{fuel} = C_{gas} + C_{tar} + C_{char} \quad (6.10)$$

The carbon content in the fuel, gas, tar and char were determined using Equation 6.11, 6.12, 6.13 and 6.14 respectively.

$$C_{fuel} = m_{fuel} C C_{fuel} \quad (6.11)$$

$$C_{char} = m_{char} C C_{char} \quad (6.12)$$

$$C_{gas} = \frac{12nm_i}{M_{i,c}} \quad (6.13)$$

$$C_{tar} = \frac{12nm_j}{M_{j,c}} \quad (6.14)$$

Where  $CC$  is the measured carbon content expressed in mass fraction.  $M_{i,c}$  and  $M_{j,c}$  is the molar mass of carbon containing gas species  $i$  and tar compound  $j$  respectively.  $n$  is the number of carbon in the respective compound.

Furthermore, energy balance was used to monitor the efficiency of the gasification system in producing useful energy in the form of clean fuel gas. Since the air and wood powder were fed at ambient temperatures, only chemical energy in the fuel was considered in the input stream. Similar approach was used for the output stream as the product gases, tar and char were measured at room temperature. Sensible heat resulted from combustion of gas products to sustain the gasification process was considered as losses. The overall energy balance was determined using Equation 6.12.

$$m_{fuel}LHV_{fuel} = m_{char}LHV_{char} + m_{tar}LHV_{tar} + m_{gas}LHV_{gas} \quad (6.15)$$

The LHV for fuel ( $LHV_{fuel}$ ), char ( $LHV_{char}$ ) and tar ( $LHV_{tar}$ ) were determined using Equation 3.5, while for gas ( $LHV_{gas}$ ) was determined using Equation 6.16.

$$m_{gas} = \sum X_i(LHV)_i \quad (6.16)$$

Where  $(LHV)_i$  is the LHV of species  $i$  summarised in Table 6.15.

Table 6.15 LHV and density of gases typically found in gasification process [160].

	H <sub>2</sub>	CO	CO <sub>2</sub>	CH <sub>4</sub>	C <sub>2</sub> H <sub>6</sub>	C <sub>3</sub> H <sub>8</sub>	N <sub>2</sub>
LHV (MJ/Nm <sup>3</sup> )	10.22	11.97	-	33.95	60.43	86.42	-
LHV (MJ/kg)	121	10.1	-	50	47.8	46.35	-
Density (kg/m <sup>3</sup> )	0.07	0.967	1.842	0.554	1.038	1.522	1.165

The comparison of material and energy balance parameters between input and output streams were determined using Equation 6.17.

$$\% \text{ Error} = \frac{\text{Inflow} - \text{Outflow}}{\text{Inflow}} \quad (6.17)$$

Table 6.16 outlines an example of the material and energy balances of a gasification system based on experimental data obtained from the non-catalytic test. It can be seen from the table that the mass of gas was more than 75 % of the total input and the balance was tar and char. The overall mass balance between input and output stream was at 8.05 % error. Analysis on the carbon balance showed high carbon content was in the gas stream compared to that of tar and char. The carbon balance was found to be at 22.39 % error. Energy content in the gas stream was also found to be high compared to that of tar and char. The deviation between input and output was 30.82 % error.

Table 6.16 Material and energy balances for non-catalytic test

Stream	Mass balance (g)			Carbon balance (g)			Energy balance (MJ)		
	In	Out	% error	In	Out	% error	In	Out	% error
Wood powder	60.00			29.64			1.01		
Air	45.83								
Gas		94.00			20.04			0.63	
Tar		3.13			2.87			0.07	
Char		0.18			0.10			0.00	
Total	105.83	97.31	8.05	29.64	23.00	22.39	1.01	0.70	30.82

Table 6.17 summarises the material flow and energy balance of all gasification tests and their detailed streams are shown in the Appendix D. It can be seen from the table that at given constant mass inflow of 105.83 g, the mass outflow for all tests ranged between 90 g and 105 g. The mass balance compares in the range from 1 % to 14 % error. Total carbon input was 29.64 g and in the output stream showed a total ranging 20 g to 29 g. The carbon balance compared at 5-32 % error. For the energy balance, the output stream was in the range of 0.63 MJ to 0.93 MJ compared to 1.01 MJ input. The corresponding deviation was found to be 15-38 % error.

Figure 6.35 shows the comparison trends for mass, carbon and energy balances of a gasification system used in this study. It can be seen from this figure that a linear relationship existed for all balancing parameters. Increase in mass output also resulted in an increase in carbon and energy in the outflow stream.

Table 6.17 Material and energy balances for all experimental tests

Test	Mass balance (g)			Carbon balance (g)			Energy balance (MJ)		
	In	Out	% error	In	Out	% error	In	Out	% error
None	105.83	97.31	8.05	29.64	23.00	22.39	1.01	0.70	30.82
0.65 g CeO <sub>2</sub>	105.83	104.65	1.12	29.64	25.54	13.85	1.01	0.81	19.75
1.44 g CeO <sub>2</sub>	105.83	100.84	4.72	29.64	25.56	13.76	1.01	0.82	18.84
1.73 g CeO <sub>2</sub>	105.83	104.68	1.09	29.64	28.07	5.31	1.01	0.93	8.58
0.74 g CuO	105.83	99.50	5.99	29.64	24.96	15.78	1.01	0.77	23.75
1.79 g CuO	105.83	103.41	2.29	29.64	26.74	9.80	1.01	0.82	19.47
2.81 g CuO	105.83	103.72	2.00	29.64	26.36	11.08	1.01	0.86	15.56
1.07 g NiO	105.83	96.12	9.18	29.64	22.55	23.90	1.01	0.68	33.11
2.04 g NiO	105.83	98.10	7.30	29.64	23.69	20.08	1.01	0.74	27.42
9.2 g CeO <sub>2</sub> /kaolin	105.83	99.40	6.08	29.64	24.33	17.90	1.01	0.74	26.66
14 g CeO <sub>2</sub> /kaolin	105.83	98.04	7.36	29.64	23.65	20.21	1.01	0.72	29.40
21 g CeO <sub>2</sub> /kaolin	105.83	91.04	13.98	29.64	20.20	31.85	1.01	0.63	37.69
14 g CeO <sub>2</sub> -14 g ZrO <sub>2</sub> -kaolin	105.83	96.88	8.46	29.64	23.44	20.91	1.01	0.75	26.06

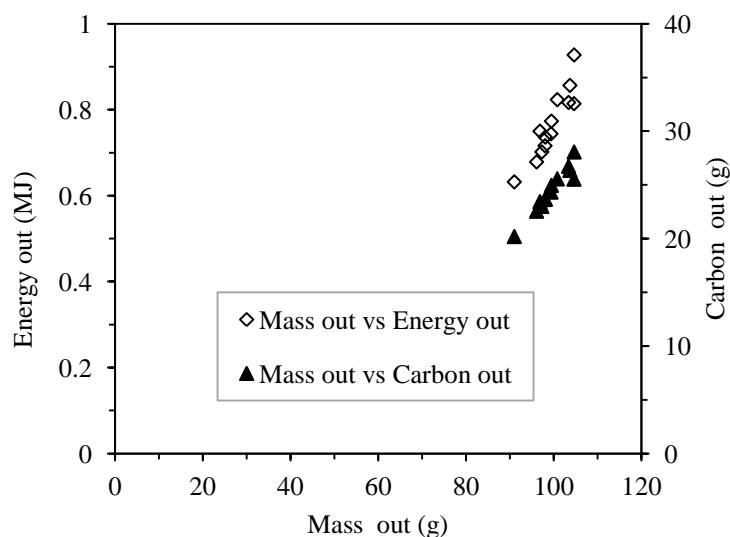


Figure 6.35 Relationship between material and energy balance in a gasification system

These results can be explained by a number of factors. The observed decrease for mass balance could be attributed to the loss of material in the form of water and undetected tar. As the latter contains carbon, loss of these compounds could also be a source for deviations in the analysis of carbon and energy balances. Moreover, the high deviation on energy balance can be explained as the loss of product gas due to combustion. Combusting part of the product gas was necessary to provide sufficient heat for sustaining the gasification process. A clear linear trend for mass vs carbon

output shown in Figure 6.35 highlights the dependency of energy output on the carbonaceous gases excluding CO<sub>2</sub>. In general, the material and energy balances results suggest that catalytic processing of gasification product gas exhibit a noticeable variation of gas components for different catalysts.

## **6.10 Summary**

This chapter has shown the viability of using a horizontal entrained-flow gasifier and the possible utilisation of pumice and kaolin as catalyst support for improving syngas quality. The performance of pumice and kaolin doped with redox catalysts on the gasification product gas has been discussed in detail. The major findings show that pumice has limited catalytic activity on the gasification product gas. However, the activity can be improved by doping with cerium, copper, and nickel oxides. Similarly, Ceria and zirconia improves catalytic activity of kaolin on the gasification product gas. Although all tested catalysts increased the syngas heating value, the concentration of hydrogen gas showed a noticeable decrease and further tar conversion was limited.

The following chapter presents and discusses the prediction results from gasification process and catalytic processing of the product gas. In addition, a comparison between the model and the experimental data measured from a horizontal entrained flow gasifier reactor are provided.

## 7 MODELLING RESULTS

### 7.1 Introduction

This chapter presents and discusses the modeling results for the biomass gasification using an entrained-flow gasifier reactor. Gasification predictions are provided for the gasifier reactor while the catalytic predictions considered a catalyst reactor only. The effect of the gasifier orientation on the gasification process is provided by comparing between the vertical and horizontal designs.

### 7.2 Gasification Predictions

Figure 7.1 shows the temperature profile in the gasifier reactor under gasification conditions. It can be seen that the steady operating temperature was between 978 and 1010 K. This temperature was attained at 75 mm from the gasifier reactor inlet and remained constant thereafter. A temperature gradient exists between the gasifier inlet and 75 mm distance. The observed temperature gradient at the inlet could be due to heat consumed by feed materials. These results confirm the existence of favourable temperature to enhance the gasification process. Furthermore, the constant temperature along the reactor ensures stable gasification conditions are attained.

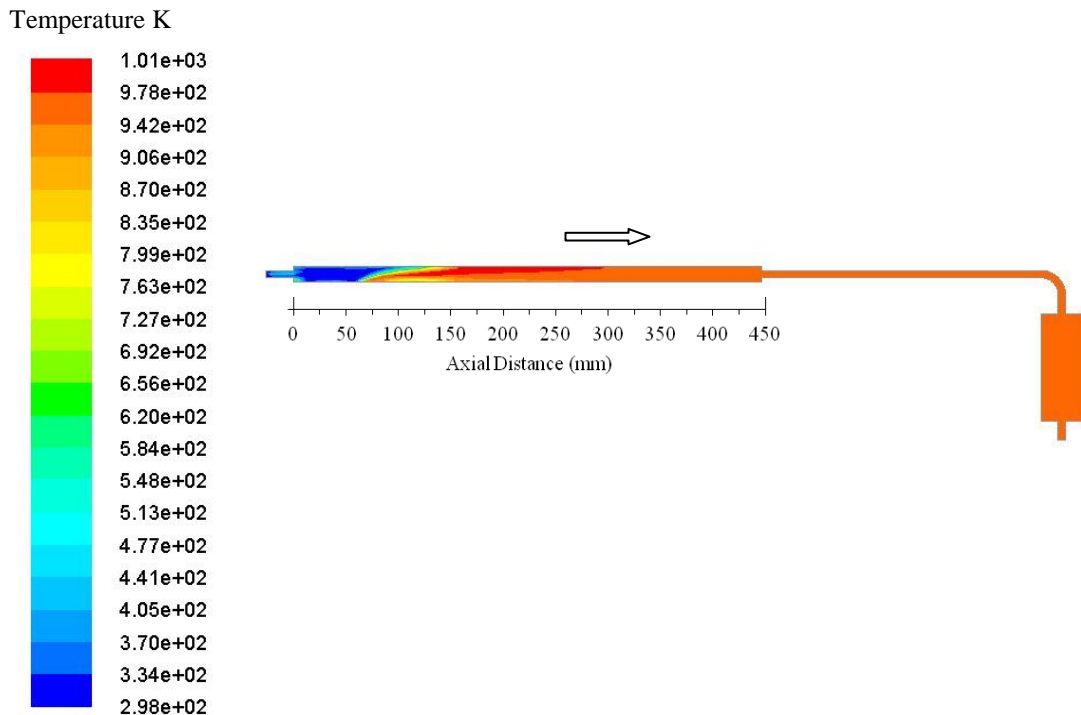


Figure 7.1 Predicted temperature profile in the gasifier reactor

Figure 7.2 through Figure 7.9 show the concentration of gas species according to biomass gasification modeling. It can be seen from Figure 7.2 that the maximum mole fraction of CO was 0.242 (24.4 %). The distribution of CO concentration after generation is almost uniform throughout the gasifier reactor. Prediction for CO<sub>2</sub> reached a maximum mole fraction of 0.0942 (9.42 %) as seen in Figure 7.3. Moreover, the maximum mole fraction of H<sub>2</sub> and CH<sub>4</sub> were 0.398 (39.8 %) and 0.0431 (4.31 %) as shown in Figure 7.4 and Figure 7.5 respectively. The consumption of O<sub>2</sub> and char (C(s)) is shown in Figure 7.6 and Figure 7.7 respectively. It can be seen that O<sub>2</sub> was completely consumed during gasification process while char fraction was found to be 0.193 (19.3 %) as residues. Furthermore, Figure 7.8 and Figure 7.9 show the particle residence time and volatile fraction as it moves along the gasifier reactor during gasification process. It can be seen from these figures that the particle residence time in the gasifier reactor was around 0.52 s and the volatile fraction was completely released into gas. In general the gasification conditions were attained at a distance between 150 mm and 200 mm from the gasifier reactor inlet.

There are several possible explanations of these results. A combination of high char, high H<sub>2</sub> and low CO<sub>2</sub> fractions can be correlated to the O<sub>2</sub> deficiency. This is due to the limitation of a single oxidising stream available in the partially premixed combustion model. Similar findings have been reported by Fraser [116] in predicting the gasification process in an inverted cyclone gasifier. Oxygen is responsible for partial oxidation of both volatiles and char during gasification process. Thus, providing additional oxidizing stream could result in an effective char conversion. Poor char conversion could also be attributed to the limited particle fragmentation not considered in this study. Char fragments when it comes into contact with the gasifier reactor wall at temperatures above 350 °C [116, 161]. Since gasification conditions were attained at almost half length of the reactor, it can be suggested that a length of 350-450 mm was sufficient for the gasification process under given operating conditions described in Section 4.4. Comparisons of these results with the experimental data are discussed in Chapter 8.

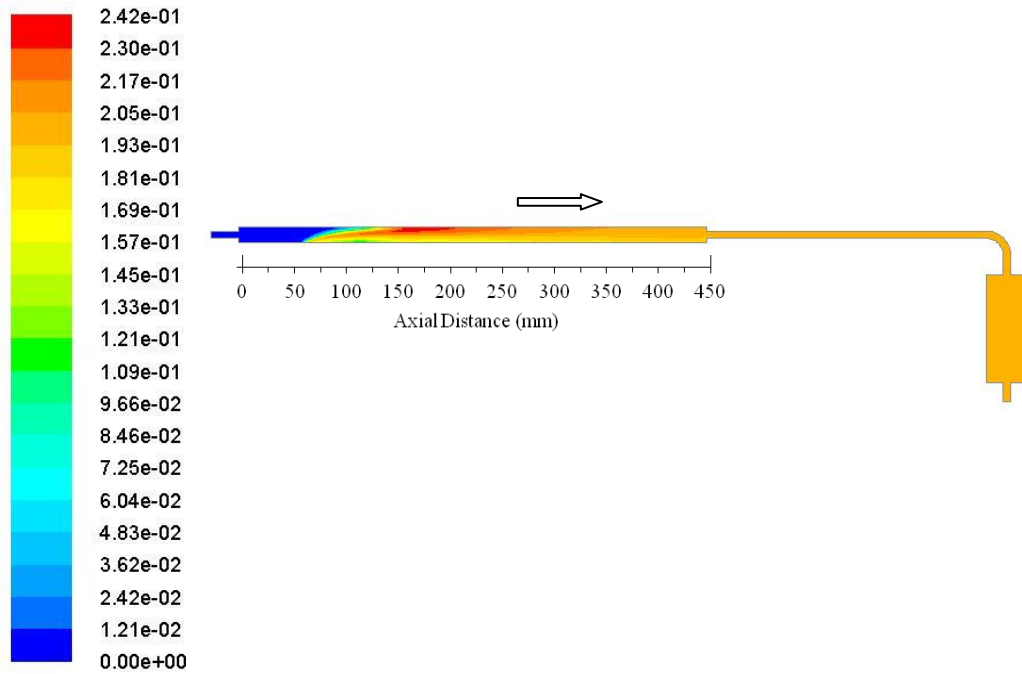


Figure 7.2 Contours of mole fraction of CO

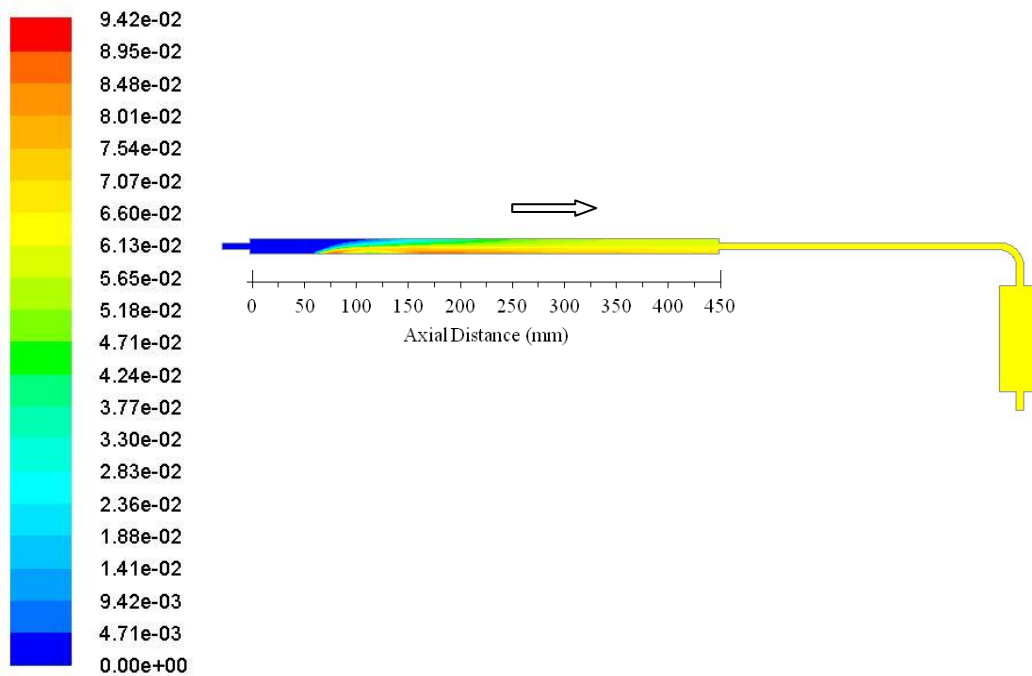


Figure 7.3 Contours of mole fraction of CO<sub>2</sub>

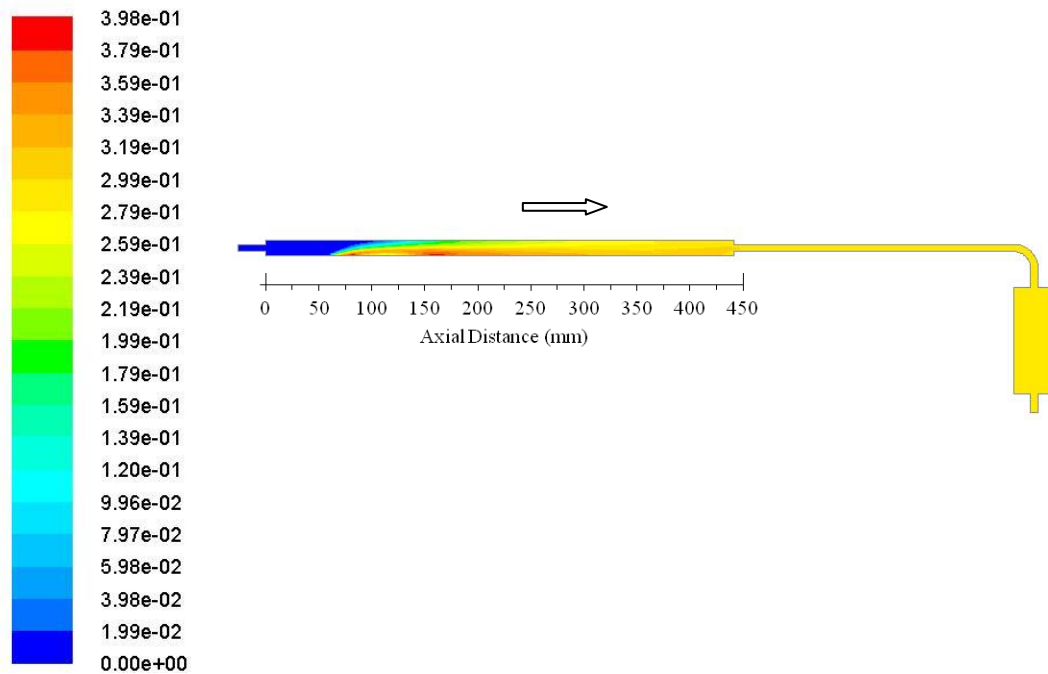


Figure 7.4 Contours of mole fraction of H<sub>2</sub>

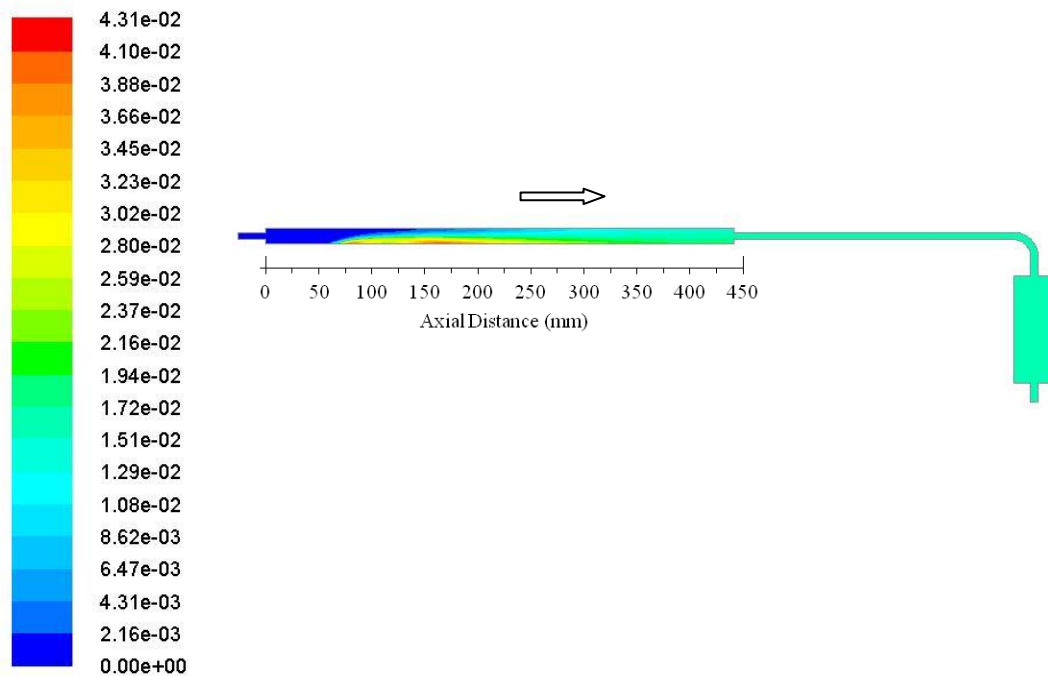


Figure 7.5 Contours of mole fraction of CH<sub>4</sub>

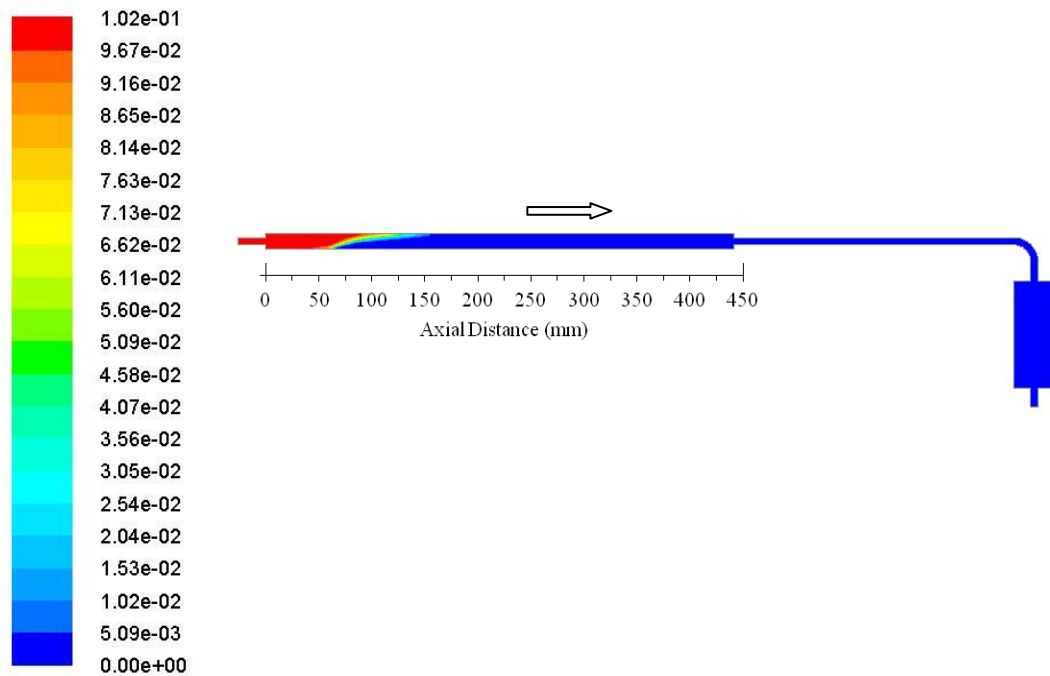


Figure 7.6 Contours of mole fraction of  $O_2$

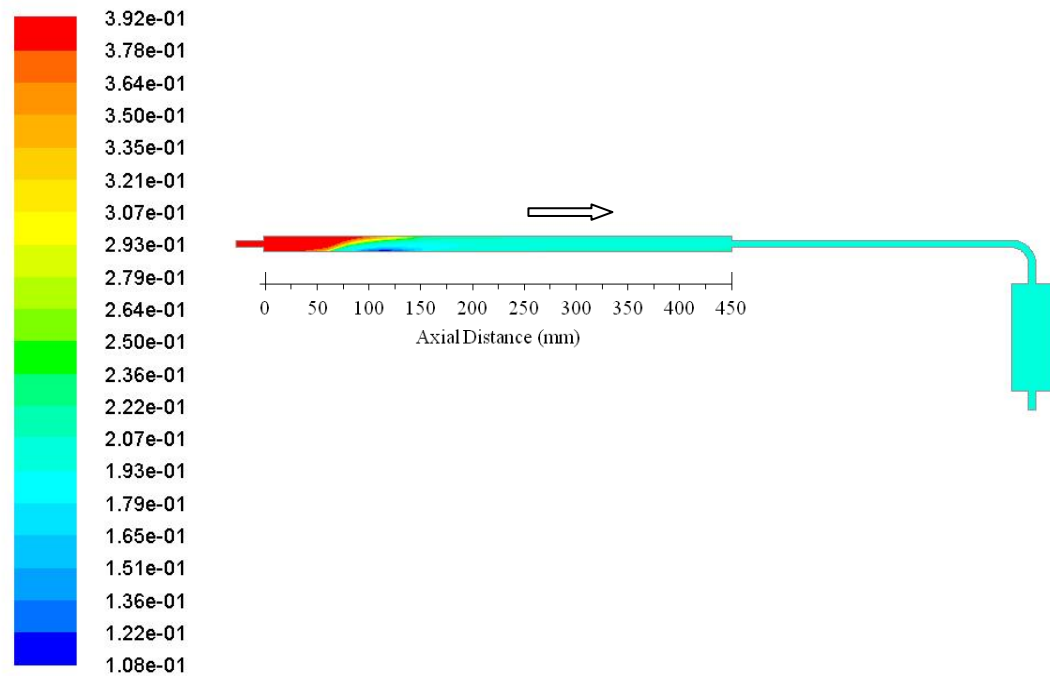


Figure 7.7 Contours of mole fraction of  $C(s)$

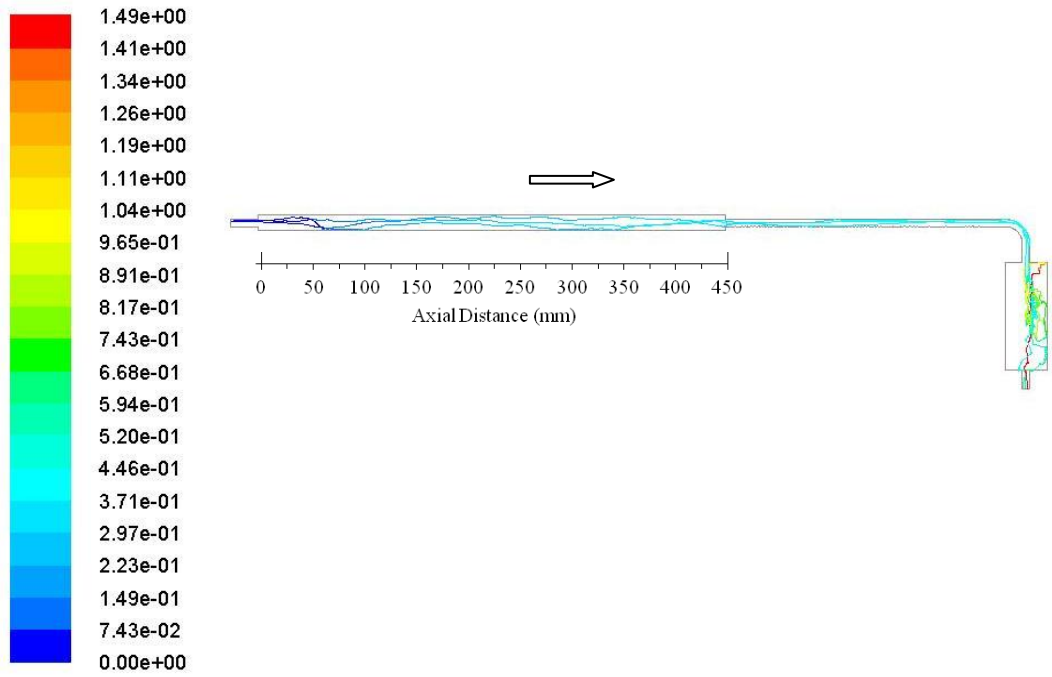


Figure 7.8 Particle traces colored by particle residence time (s)

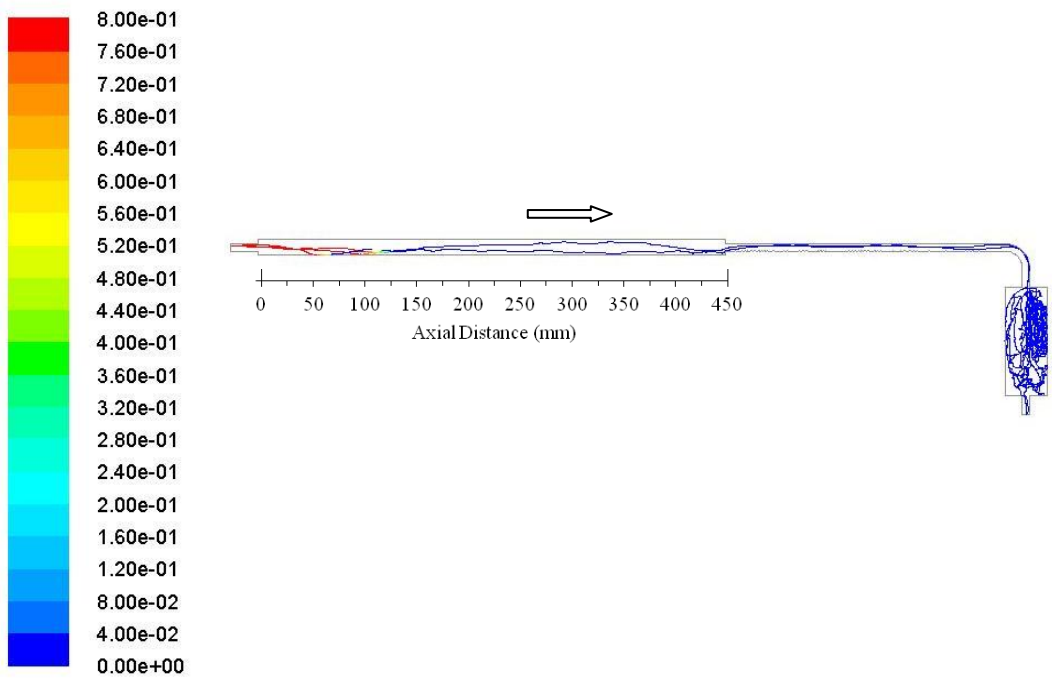


Figure 7.9 Particle traces colored by particle volatile fraction

### 7.3 Predictions for Catalytic Processing of the Product Gas

This section presents and discusses the findings from the modeling of the catalytic processing of the gasification product gas described in Section 5.3. A central plane was created in the reactor geometry to study the areas of interest including dispersion of species. The dispersion of species in the catalytic reactor was studied using contour plots. However, these results are only limited to ceria doped pumice catalysts which presented a highest syngas heating value during the experimental investigations.

Figure 7.10 shows the vector plot of the axial velocity along the catalytic reactor. It can be seen from the figure that the flow expands in all directions after entering the void space. High velocity was seen at the inlet central axis as expected and the recirculation zones at the corners of the catalytic reactor were not significant. Although the axial velocity was not uniform at the void space, in the bed materials was found to be uniformly distributed. This could be attributed to the flow expansion in the void space and the porous bed materials. Uniform flow distribution in the bed materials ensures effective catalyst utilisation.

Figure 7.11 shows the simulated and experimental results for CO and CO<sub>2</sub> concentration after catalytic processing of the gasification product gas. It can be seen from the Figure 7.11 (a), CO concentration increased with increasing catalyst bed length while CO<sub>2</sub> showed a decreasing trend. Although CO could be generated from a number of chemical reactions, it can clearly be suggested that coke oxidation Equation 7.1 and CO<sub>2</sub> reduction Equation 7.2 also contribute the increase of CO in the catalysed syngas.



The H<sub>2</sub> and CH<sub>4</sub> concentration are shown in Figure 7.12 (a) and Figure 7.12 (b) respectively. It can be seen from Figure 7.12 (a) that H<sub>2</sub> decreased with increasing catalyst bed length. The decrease of mole fraction ranged from 0.141 to 0.110. From Figure 7.12 (b) it can be seen that the mole fraction of CH<sub>4</sub> increased slightly with increasing catalyst bed length. The increase ranged between 0.0356 and

0.0359. Although the model under-predicted the concentration of CH<sub>4</sub>, its trend was relatively similar to that measured experimentally. While the decrease of H<sub>2</sub> may be explained by the activity of hydrogen with ceria via the reduction reaction Equation 7.3, the increase of CH<sub>4</sub> could be attributed to the tar cracking according to Equation 7.4.



Tar conversion over ceria doped pumice was predicted and the results are shown in Figure 7.13 (a). It can be seen from the contour plot that the mole fraction of toluene (C<sub>7</sub>H<sub>8</sub>), decreased from 0.0280 to 0.0238 with increasing catalyst bed length. The decrease of toluene and the increase of CH<sub>4</sub> confirmed the possibility of tar cracking over ceria treated pumice and can be explained by reaction Equation 7.4. In this reaction, toluene was chosen to represent the aromatic hydrocarbons. Similarly, the low conversion of tar can be explained as a result of competing reactions of H<sub>2</sub> and CO<sub>2</sub> with the active sites on the pumice support.

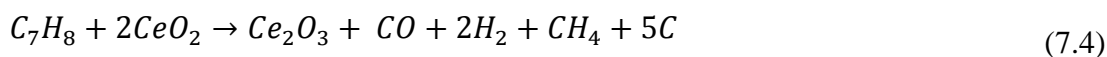


Figure 7.13 (b) shows the temperature profile in the catalytic reactor. It can be seen from the contour plot that high temperature occurred at halfway along the bed material highlighting a region of high catalytic activity. At this region, there was an increase of 5 K compared to the inlet temperature (623 K). A typical reaction contributing to this temperature rise could be reduction of ceria over hydrogen as described using Equation 7.3.

Surface coverage which expresses the fraction of surface sites on the catalyst support is presented in Figure 7.14. This analysis was determined to study the chemical state of the catalyst in the catalytic reactor. Comparing the results from Figure 7.14 (a) and Figure 7.14 (b), it can be seen that the surface coverage of reduced ceria (Ce<sub>2</sub>O<sub>3</sub>) was higher compared to that of CeO<sub>2</sub>. These results are contrary to the XRD analysis for the spent ceria doped pumice shown in Figure 6.6 (e). The observed high surface coverage of the reduced ceria suggests the existence of the reduction reaction of CeO<sub>2</sub> with hydrogen, coke, tar or carbon dioxide under

given operation conditions. Furthermore, the observed difference between model and XRD results could be due to the re-oxidation of  $Ce_2O_3$  on the spent catalyst in air during experimental shutdown. This is due to the unstable characteristics of  $Ce_2O_3$  in air at room temperature [162].

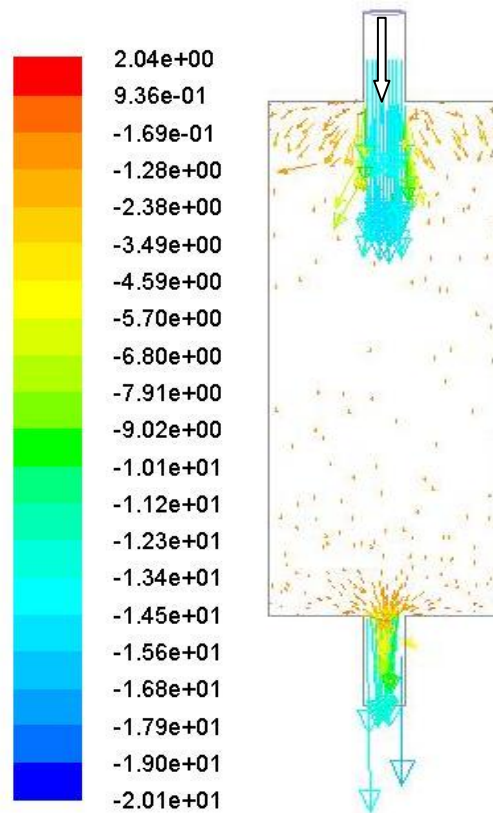


Figure 7.10 Vector plot of the axial velocity along the catalytic reactor

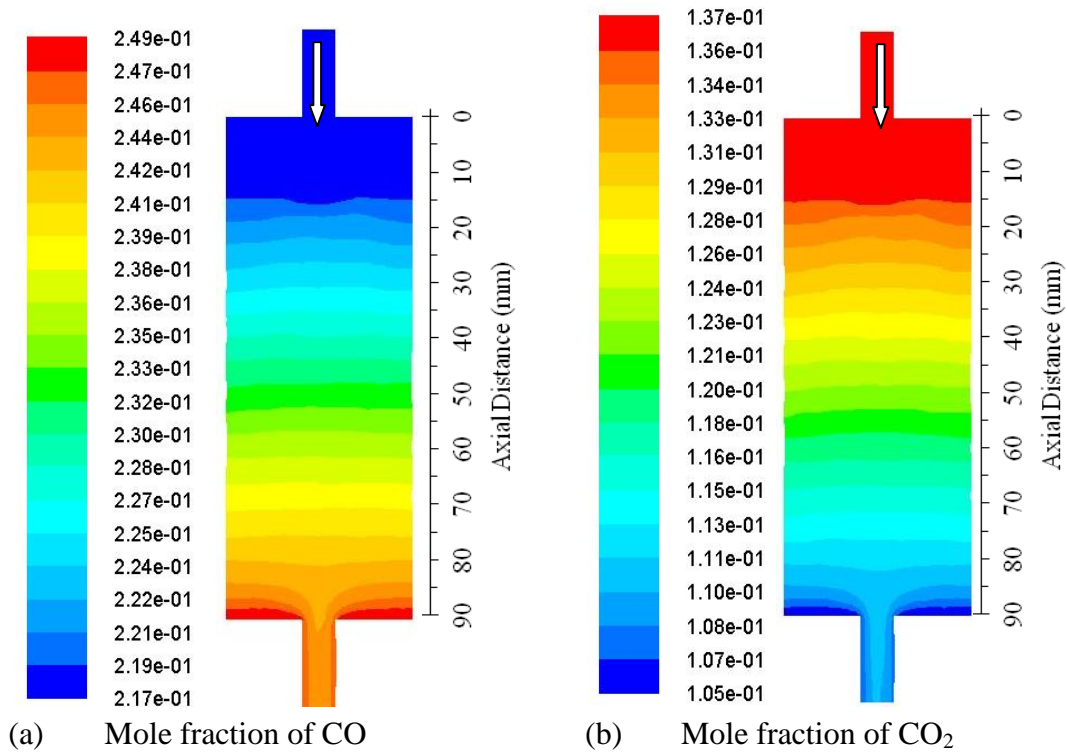


Figure 7.11 Contour plots for CO and CO<sub>2</sub> concentration

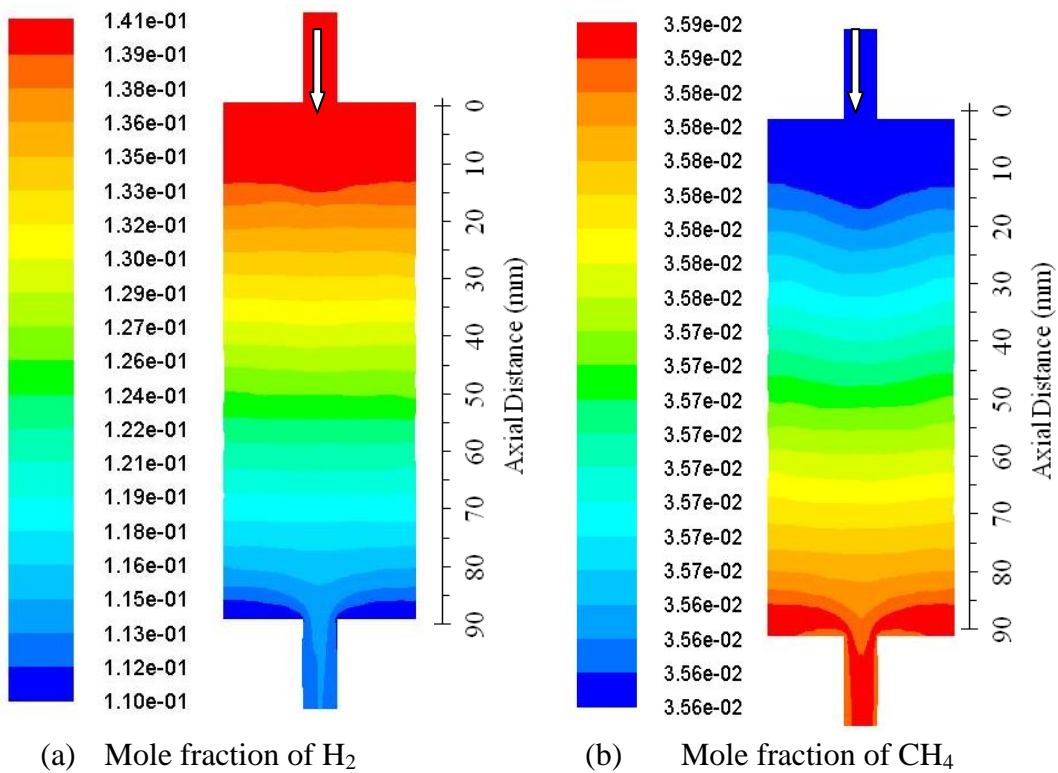


Figure 7.12 Contour plots for H<sub>2</sub> and CH<sub>4</sub> concentration

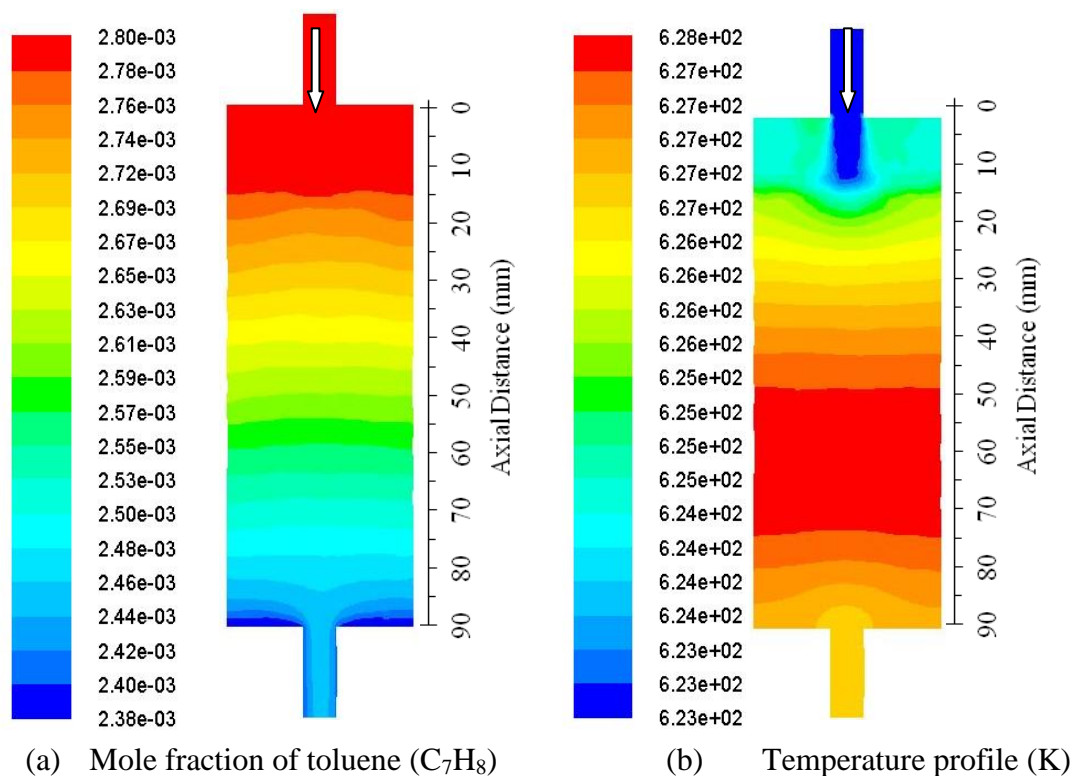


Figure 7.13 Contour plots for tar conversion and temperature profile

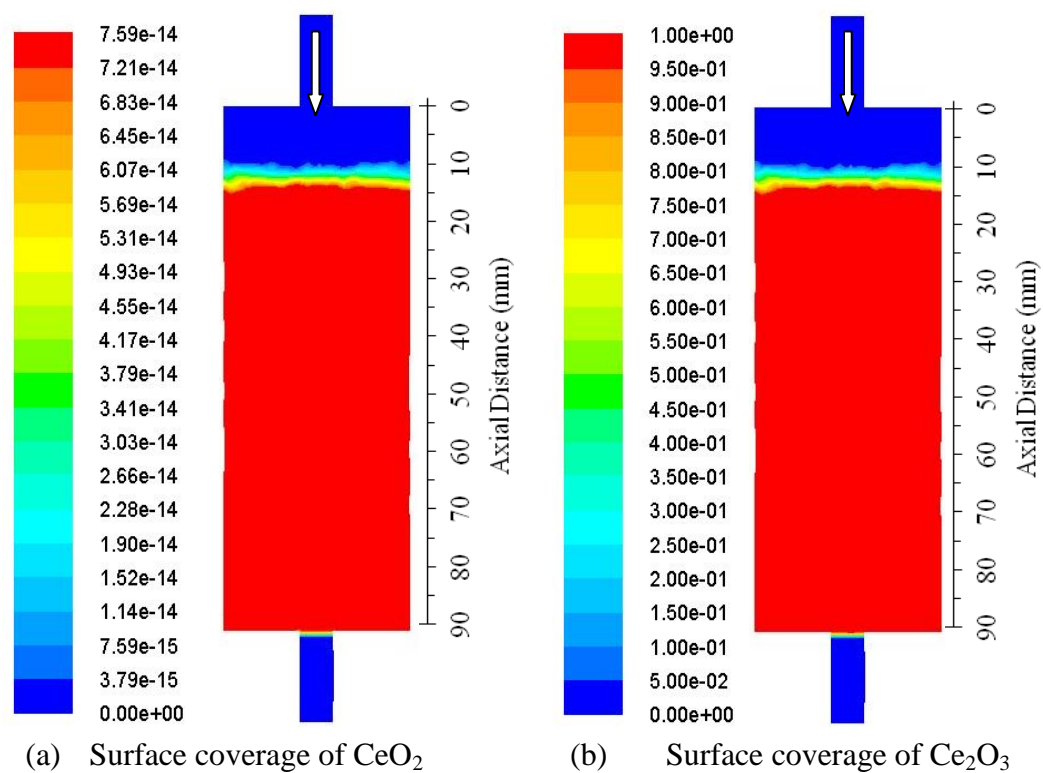


Figure 7.14 Contours of surface coverage of catalysts

## 7.4 Gasifier Reactor Orientation

The effect of gasifier orientation on the gasification process was studied considering the horizontal and vertical designs. The results of these designs were obtained using CFD modeling described in Chapter 5. Figure 7.15 (a) compares the temperatures along the reactor length. It can be seen from the figure that the maximum temperature in the horizontal design was achieved at 100 mm distance from the gasifier reactor inlet while for the vertical occurred at 300 mm. In addition the temperature profile for the horizontal design showed a single rise while the vertical design showed two distinct stages of increase. In the vertical design, the first rise occurred at 50 mm distance with an increase of 300 K and the second stage occurred at 300 mm with a further 378 K rise. All designs attained a maximum temperature of 1010 K.

Figure 7.15 (b-f) compares the major product gas components. It can be seen from Figure 7.15 (b) that the profile for CO generation for all designs are almost similar to those of temperature shown in Figure 7.15 (a). For the vertical design, the mole fraction of CO increased to 0.10 and 0.242 at 50 mm and 300 mm respectively. In the horizontal design the mole fraction of CO rose suddenly to 0.242 at 100 mm distance. Moreover, a slightly different profile was observed for CO<sub>2</sub>, H<sub>2</sub> and CH<sub>4</sub> compared to that of CO for the vertical design. CO<sub>2</sub> increased gradually from the gasifier inlet with a sharp rise at 340 mm distance as seen in Figure 7.15 (c). Similar trend was seen for H<sub>2</sub> and CH<sub>4</sub> as seen in Figure 7.15 (d) and Figure 7.15 (e) respectively. The mole fraction of char decreased gradually along the gasifier reactor as seen in Figure 7.15 (f).

These results can be explained by a number of factors. Comparing the trends of temperature and CO for the vertical design, it can be suggested that CO generation during gasification process is highly dependent on temperature. In addition, carbon monoxide is the primary gas product during biomass thermal decomposition. The correlation between gradual increase of CO<sub>2</sub>, H<sub>2</sub> and CH<sub>4</sub> with decreasing char mole fractions explains that these gases are secondary products and the formation depends on the particle surface reactions. In addition the sharp rise at 340 mm distance highlights the occurrence of the devolatilisation in the fuel particle. The observed long distance at which the devolatilisation occurred can be associated with limited heat transfer due to high particle velocity. Unlike vertical design, the horizontal type showed particle surface reactions occurs rapidly in a short transport distance. The

finding from the horizontal design suggests that both pyrolysis and partial oxidation reactions occurs almost simultaneously. The implication of this is enhanced gas yield during the gasification process as also reported by Higman and van der Burgt [4]. Hence the results demonstrate that there exists a sensitivity to the gasifier reactor orientation on the overall gasification process.

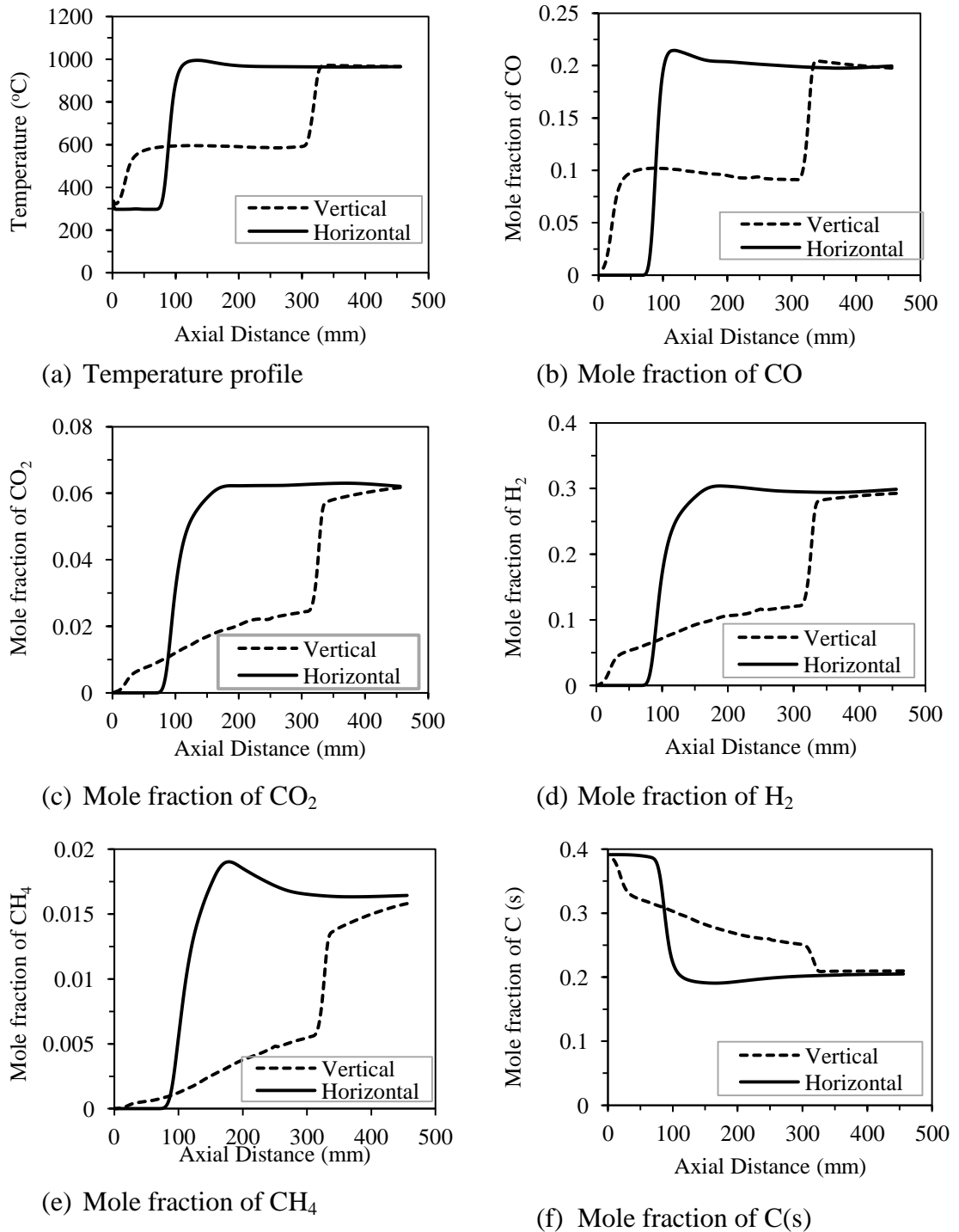


Figure 7.15 Comparison between a horizontal and vertical gasifier configurations on the gasification process

## 7.5 Summary

This chapter has shown the effect of gasifier orientation on the performance of the horizontal and vertical configuration using CFD modeling. Similarly, catalytic processing of the product gas has been presented and discussed, however, only ceria doped pumice was considered taking into account possible major reactions. The major findings are summarised hereunder:

- (i). There exists a sensitivity to the gasifier reactor orientation on the overall gasification process. Particle surface reactions are enhanced in the horizontal compared to the vertical gasifier reactor design.
- (ii). Kinetic study has shown that reduction of hydrogen and carbon dioxide in the gas stream is due to the redox characteristics of ceria doped pumice. Consequently, tar conversion over the catalyst is inhibited.
- (iii). Prediction of gasification process showed limited char combustion reaction for the partially premixed combustion model. This is attributed to the single oxidising stream compared to the double fuel streams.

## 8 COMPARISON OF EXPERIMENTAL AND MODEL RESULTS

### 8.1 Introduction

This chapter presents and discusses the comparison between the modeling results and the experimental data. The experimental data were obtained from biomass gasification using a horizontal entrained-flow gasifier reactor and catalytic processing of product gas using ceria doped pumice catalyst. The study on whether the gasifier orientation has an effect on the gasification process is also provided by comparing the vertical and horizontal designs. The interaction of product gas with the catalyst is also provided. The results from all simulation tests were taken at the axial axis of the respective reactor.

### 8.2 Gasification Model Results

Table 8.1 compares the temperature and gas composition between the model and experimental data from a horizontal entrained-flow gasifier reactor. For the model, the temperature was taken at 250 mm from the gasifier inlet, while the concentration of gases was taken at the exit of the catalytic reactor. It can be seen from the table that the comparison for temperature and CO concentration shows good agreement between the model and experimental data. This agreement was found to be within 10 % error. Moreover, the predicted concentrations for H<sub>2</sub>, CO<sub>2</sub> and CH<sub>4</sub> deviated from those measured experimentally by a factor ranging 1.5 to 2. Although light hydrocarbons C<sub>2</sub>H<sub>6</sub> and C<sub>3</sub>H<sub>8</sub> were considered in the PDF mixture, the model under-predicted the concentration of these compounds as seen in the Table 8.1.

Table 8.1 Comparison between model and experimental data

Parameter	Model	Experimental	% error
Temperature (°C)	769	800	-4.03
<i>Gases (% vol.)</i>			
H <sub>2</sub>	29.88	14.33	52.05
CO	19.96	22.11	-10.79
CO <sub>2</sub>	6.2	13.97	-125.36
CH <sub>4</sub>	1.64	3.62	-120.86
C <sub>2</sub> H <sub>6</sub>	0	1.66	-
C <sub>3</sub> H <sub>8</sub>	0	0.38	-
C(s) (% wt)	13.78	1.00	92.74

The observed difference in predicting the concentration of H<sub>2</sub>, CO<sub>2</sub> and CH<sub>4</sub> can be linked to the low carbon conversion as shown previously in Figure 7.7. While the predicted char mass fraction at the outlet of the gasifier reactor was 0.1378, the experimental data showed only 0.01. Further improvement on char combustion may also result in increasing the predicted temperature due to heat generated from combustion of H<sub>2</sub> and CO. Consequently, H<sub>2</sub> is expected to decrease while CO<sub>2</sub> is likely to increase accordingly.

### 8.3 Catalytic Processing of the Syngas

This section provides comparison between the model and experimental results for the catalytic processing of gasification product gas. For the model results, the catalyst loading was varied using surface site density described in Section 2.3.4 and Section 5.3.4. The accuracy of the model in percentage error was determined using Equation 8.1.

$$\% \text{ Error} = 100 * \left( \frac{E_d - M_d}{E_d} \right) \quad (8.1)$$

Where  $E_d$  and  $M_d$  are experimental and model data respectively.

The comparison between model and experimental data on CO concentration is shown in Figure 8.1 (a). It can be seen from the figure that the model predicted well the CO concentration at 0.65 g CeO<sub>2</sub> loading and under-predicted at 1.44 g and 1.73 g loading. The deviation was found to be within 17 % error. Both the model and the experimental results showed an increasing trend of CO concentration with increasing ceria loading. Figure 8.1 (b) compares the CO<sub>2</sub> concentration at different ceria loading. It can be seen from the figure that while the experimental data showed a linear decrease of CO<sub>2</sub> concentration, the model showed the decrease was limited to the catalyst concentration. The model also underpredicted the concentration of CO<sub>2</sub> for all catalyst loading. The comparison between the model and experimental results was in the range of 10-37 % error. The comparison for H<sub>2</sub> prediction and the experimental data is shown in Figure 8.1 (c). It can be seen from the figure that the model underpredicted the H<sub>2</sub> concentration for all catalyst loading tests, however, the trend was similar to that of experimental data. The deviation between the model and

the experimental data was within 25 % error. Moreover the prediction for CH<sub>4</sub> showed a noticeable deviation as seen in Figure 8.1 (d). This deviation was found to be 65 % error.

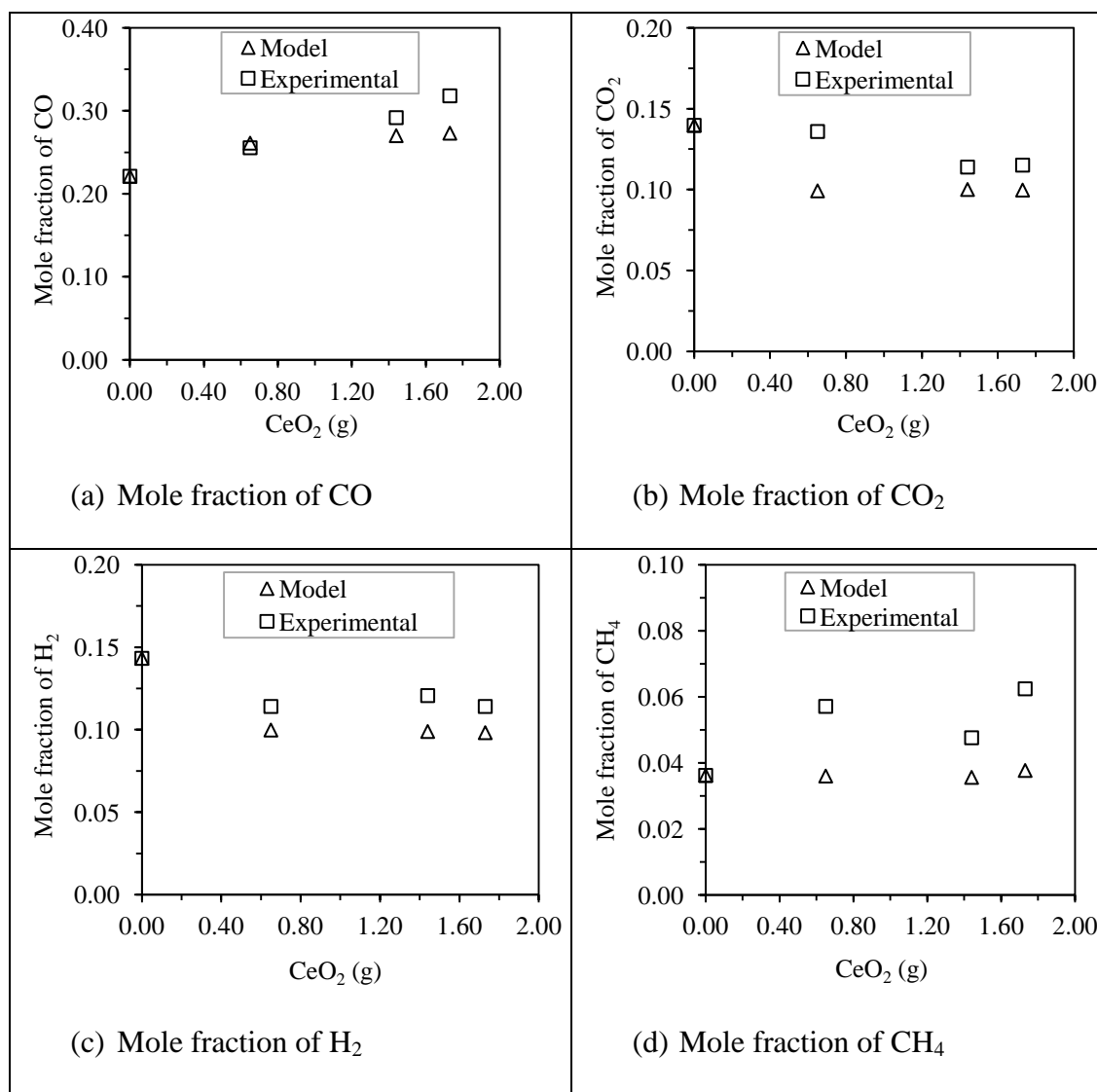


Figure 8.1 Comparison between model and experimental data on catalytic processing of gasification product gas

Findings from the comparison between the model and the experimental data can be explained by a number of factors. A good agreement of H<sub>2</sub> trend confirms the existence of reduction reaction of ceria with hydrogen as per previous Equation 7.3. Similarly the decrease of CO<sub>2</sub> can be explained as the oxidation of ceria according to Equation 7.2. The observed deviation of CO and CH<sub>4</sub> prediction could be due to the limited reactions considered in this model. These gases can be produced from various

complex hydrocarbon reactions through oxidation, reduction, cracking or reforming [57].

#### 8.4 Interaction of Gasification Product Gas with Redox Catalysts

Figure 8.2 summarises the findings from this study for the interaction of the gasification product gas with redox catalysts doped on pumice or kaolin supports. When the syngas undergoes redox reaction, H<sub>2</sub> and CO<sub>2</sub> dominate the interaction with the catalyst yielding CO and vapour according to reactions Equations 8.2 and reaction Equation 8.3. The H<sub>2</sub> is responsible for the reduction of metal oxide (MO) due to its higher reactivity compared to the remaining species. Soon after reduction, the active sites (M<sup>\*</sup>) are re-oxidised with CO<sub>2</sub> and the cycle continues until the catalyst deactivates. Although the oxidative cleavage of tar is complex, there are possible pathways to describe the cracking mechanism. For instance, aromatic hydrocarbons could have three pathways during the oxidation process. The first route leads to formation of oxygenated hydrocarbons such as phenols and alcohol derivatives. Another route is the direct conversion to quinones derivatives, as well as aldehydes and carboxylic acids [163]. The remaining pathway could be direct conversion to H<sub>2</sub>, CH<sub>4</sub>, C<sub>2</sub>-C<sub>3</sub> and vapour. Similarly, the resulting aldehydes, carboxylic acids and quinones derivatives can undergo deoxygenation and dehydrogenation over reduced metal oxides to yield H<sub>2</sub>, CH<sub>4</sub>, C<sub>2</sub>-C<sub>3</sub> and vapour.



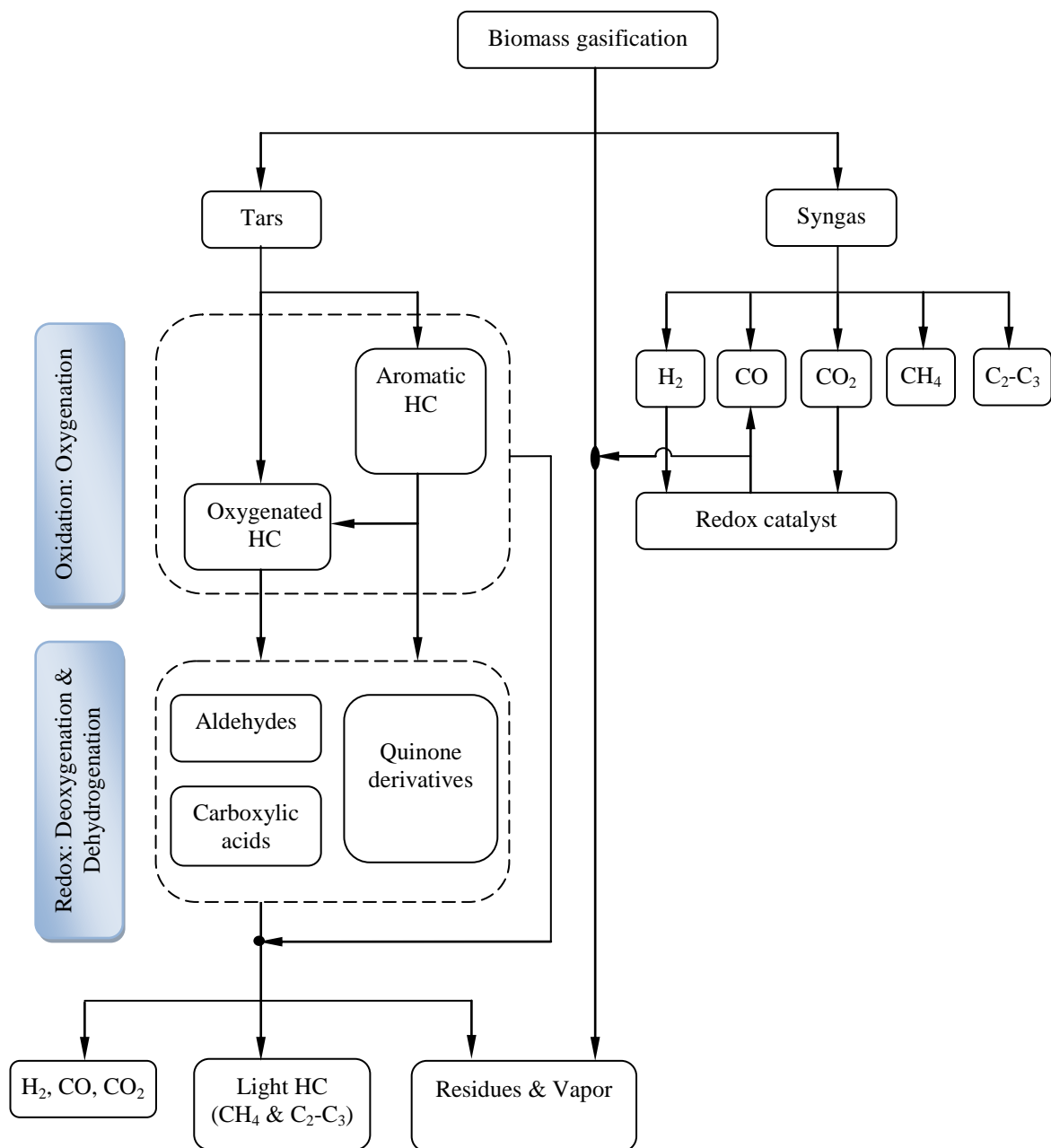


Figure 8.2 The conceptual model for the interaction of biomass gasification product gas over pumice and kaolin treated with redox catalysts

## 8.5 Summary

This chapter has validated the modeling results and those measured experimentally. The major findings are summarised hereunder:

- (i). The partially premixed combustion model exhibited limited char combustion reaction for gasification process compared to the experimental results. This limitation can be attributed to the single oxidising stream compared to the double fuel streams.
- (ii). Although the Species Transport Model predicted well the temperature and the reduction of  $H_2$  and  $CO_2$ , the model under-predicted the concentration of  $CO$  and  $CH_4$ .

## 9 CONCLUSIONS AND RECOMMENDATIONS

### 9.1 Conclusions

It has been shown that there exists a sensitivity to the gasifier orientation on the overall gasification process. The horizontal configuration showed high fuel conversion compared to the vertical design. The maximum fuel conversion was 99 % while syngas heating value and cold gas efficiency were 6.67 MJ/Nm<sup>3</sup> and 70 % respectively. Total tar concentration without catalyst support was found to be 14.92 g/Nm<sup>3</sup> (55.22 g/kg wood fuel). Furthermore, using a horizontal configuration, the gasifier reactor length can be reduced from 1000-2000 mm to 500 mm with an inlet to the reactor diameter ratio of 0.5.

The experimental investigations have shown that pumice is an inert material, thus it has limited chemical effect on the gasification product gas. In addition, pumice has good resistance to concentrated acidic solutions. Although different pumice materials may have similar chemical composition, other properties such as strength and porosity are different. While the strength is important as it ensures resistance to attrition, the porosity ensures high surface area at low pressure drop. Furthermore, pumice can be used for tar reduction in the product gas. The reduction was found to be in the range of 4-6 g/Nm<sup>3</sup>. However, the reduction was mainly through adsorption. From the studied samples, pumice from Arusha Tanzania showed highest porosity which is an important feature in heterogeneous catalysis.

It has also been shown that the catalytic properties of pumice can be improved by doping with ceria. The observed low carbon deposition on the ceria doped pumice confirms the coking resistance possessed by ceria. In addition the syngas heating value increases with increasing ceria content on the pumice support. The maximum heating value achieved was 8.97 MJ/Nm<sup>3</sup> at 1.74 g CeO<sub>2</sub> loading. Furthermore, tar conversion over ceria doped pumice results in the formation of intermediates which are mainly oxygenated hydrocarbons. The concentration of CO and CH<sub>4</sub> increased with in the product gas, while H<sub>2</sub> and CO<sub>2</sub> showed a slightly decrease. Although tar conversion was limited, the observed conversion was found to be through cracking and partial oxidation reactions. The presence of H<sub>2</sub> and CO<sub>2</sub> in the product gas could be responsible for the inhibition of tar conversion.

The experimental results of this study have shown that copper doped pumice has an effect on the gasification product gas. While H<sub>2</sub> and CO<sub>2</sub> decreased, CO and CH<sub>4</sub> increased with increasing CuO concentration. The maximum heating value of

syngas was found to be 8.66 MJ/Nm<sup>3</sup> at 2.81 g CuO loading. Furthermore, tar concentration in the product gas decreases with increasing CuO concentration on the pumice surface. The governing reactions between tar and the catalyst are through cracking and oxidation as confirmed by increasing of CO and CH<sub>4</sub> concentration in the syngas. The lowest tar yield was found to be 6.12 g/Nm<sup>3</sup> at 2.81 CuO loading compared to 10.93 g/Nm<sup>3</sup> of untreated pumice. These findings suggest that copper doped pumice can be employed for tar conversion into gas product during biomass gasification.

This study has shown that increasing nickel loading on pumice support increases CO and CH<sub>4</sub> in the product gas while H<sub>2</sub> and CO<sub>2</sub> decreases. Moreover, nickel oxide has limited effect on the light hydrocarbons. The maximum heating value of the syngas was found to be 7.26 MJ/Nm<sup>3</sup> at 2.04 g NiO loading. It was also shown that nickel doped pumice possesses tar cracking and partial oxidation properties with respect to the gasification product gas. However, the performance can be limited by the carbon deposition over the catalyst surface. The lowest tar yield was found to be 7.78 g/Nm<sup>3</sup> at 1.07 g NiO loading.

It has also been shown that ceria improves catalytic activity of kaolin on the gasification product gas. The selectivity to H<sub>2</sub> and CO<sub>2</sub> conversion increases with increasing ceria concentration in the kaolin, while CO and CH<sub>4</sub> yield were promoted. The maximum heating value of the syngas was found to be 7.13 MJ/Nm<sup>3</sup> at 14.0 g CeO<sub>2</sub> loading. Furthermore, the reduction of tar concentration in the product gas could be attributed to the activity of kaolin/CeO<sub>2</sub> on cracking and partial oxidation reactions. The lowest tar yield was found to be 7.27 g/Nm<sup>3</sup> at 14 g CeO<sub>2</sub>. Another finding from this study showed that the addition of zirconia to the kaolin-ceria catalyst promotes tar cracking on the gasification product gas. Aromatic compounds showed a noticeable decrease while oxygenated compound decreased slightly. Furthermore, the addition of 14 g ZrO<sub>2</sub> in the kaolin-ceria containing 14 g CeO<sub>2</sub> increased the syngas heating value from 6.96 to 7.74 MJ/Nm<sup>3</sup>. Addition of zirconia also reduced tar yield from 7.27 g/Nm<sup>3</sup> to 3.55 g/Nm<sup>3</sup>.

The overall catalysis study has shown that ceria and copper doped pumice are potential catalysts for the catalytic processing of the gasification product gas. Their catalytic activity is demonstrated by a noticeable increase in cold gas efficiency. Other catalysts such as nickel doped pumice and kaolin-ceria/zirconia mixes also showed a noticeable improvement to syngas heating value and tar conversion.

Furthermore, all catalysts exhibited cracking, reduction and partial oxidation of gasification product gas.

## **9.2 Recommendations for Future Work**

Although the experimental investigation has shown viability in using a horizontal entrained-flow gasifier reactor, a number of possible future studies are obvious. The experimental work covered in this study was mostly conducted at a fixed gasifier reactor temperature and equivalence ratio to provide a strong basis for further investigations. Possible future studies may include experimentation at different operating conditions such as temperature, equivalence ratio and gasifying agent to explore their effect on the syngas and tar yield. In addition, the incorporation of the cyclone particle separator is important in the overall syngas cleaning process. Since CFD modeling has shown a clear difference between a horizontal and vertical configuration, a further experimental comparison is therefore proposed. Modeling gasification process using partially premixed combustion model has shown limitation on char combustion due to insufficient oxidising agent. Therefore, further work is required to improve char combustion and gasification process predictions.

In catalysis study, the current work has only examined the effect of doping pumice and kaolin with particular metal oxides on the gasification product gas. Thus, further investigation and experimentation into doping with various catalytic metals in form, either in metallic form or as oxide is proposed. Moreover, the study was limited with regard to the catalytic reactor temperature and gas hourly space velocity (GHSV). It would therefore be important to perform further tests on the performance of the catalysts by varying these parameters. Unlike treated pumice catalysts, all kaolin treated catalysts experienced a significant attrition. Further work need to be done to improve the resistance to attrition.

## REFERENCES

- [1] BP. (2009, *Statistical Review of World Energy*. Available: <http://www.bp.com>
- [2] COP15, "Decisions adopted by the Conference of the Parties," 2009.
- [3] C. S. Li and K. Suzuki, "Tar property, analysis, reforming mechanism and model for biomass gasification-An overview," *Renewable & Sustainable Energy Reviews*, vol. 13, 2009; pp. 594-604.
- [4] C. Higman and v. d. Burgt, Eds., *Gasification*. Elsevier Science (USA), 2003, p.^pp. Pages.
- [5] T. Hanaoka, Y. Y. Liu, K. Matsunaga, T. Miyazawa, S. Hirata, and K. Sakanishi, "Bench-scale production of liquid fuel from woody biomass via gasification," *Fuel Processing Technology*, vol. 91, 2010; pp. 859-65.
- [6] R. Marsh, A. J. Griffiths, and K. P. Williams, "Measurement of heat transfer and change in compressive strength of waste derived solid fuels due to devolatilisation," *Fuel*, vol. 87, 2008; pp. 1724-33.
- [7] S. Anis and Z. A. Zainal, "Tar reduction in biomass producer gas via mechanical, catalytic and thermal methods: A review," *Renewable & Sustainable Energy Reviews*, vol. 15, 2011; pp. 2355-77.
- [8] Y. Zhang, S. Kajitani, M. Ashizawa, and Y. Oki, "Tar destruction and coke formation during rapid pyrolysis and gasification of biomass in a drop-tube furnace," *Fuel*, vol. 89, 2010; pp. 302-09.
- [9] G. Del Angel, J. M. Padilla, I. Cuauhtemoc, and J. Navarrete, "Toluene combustion on gamma-Al<sub>2</sub>O<sub>3</sub>-CeO<sub>2</sub> catalysts prepared from boehmite and cerium nitrate," *Journal of Molecular Catalysis a-Chemical*, vol. 281, 2008; pp. 173-78.
- [10] K. Wilson, A. F. Lee, D. J. Macquarrie, and J. H. Clark, "Structure and reactivity of sol-gel sulphonic acid silicas," *Applied Catalysis a-General*, vol. 228, 2002; pp. 127-33.
- [11] F. E. Kiss, M. Jovanovic, and G. C. Boskovic, "Economic and ecological aspects of biodiesel production over homogeneous and heterogeneous catalysts," *Fuel Processing Technology*, vol. 91, 2010; pp. 1316-20.
- [12] NEP, "The National Energy Policy of Tanzania," 2003.
- [13] I. S. N. Mkilaha, M. M. Nyaruba, S. L. C. Mdoe, and J. B. Ngatunga, "Establishing a nuclear power programme in Tanzania," in *2nd International conference in Mechanical and industrial engineering*, Arusha-Tanzania, 2012.
- [14] M. F. Demirbas, M. Balat, and H. Balat, "Potential contribution of biomass to the sustainable energy development," *Energy Conversion and Management*, vol. 50, 2009; pp. 1746-60.
- [15] WEC. (2007, *Survey of Energy Resources*. Available: <http://www.worldenergy.org>
- [16] M. Parikka, "Global biomass fuel resources," *Biomass & Bioenergy*, vol. 27, 2004; pp. 613-20.
- [17] IEA. (2011, *International Energy Agency statistics*. Available: <http://www.iea.org>
- [18] W. R. Makundi and A. Okitingati, "Carbon flows and economic evaluation of mitigation options in Tanzania's forest sector," *Biomass & Bioenergy*, vol. 8, 1995; pp. 381-93.

- [19] M. Felix and S. H. Gheewala, "A Review of Biomass Energy Dependency in Tanzania," *9th Eco-Energy and Materials Science and Engineering Symposium*, vol. 9, 2011.
- [20] H. K. Sjolie, "Reducing greenhouse gas emissions from households and industry by the use of charcoal from sawmill residues in Tanzania," *Journal of Cleaner Production*, vol. 27, 2012; pp. 109-17.
- [21] A. K. Kivaisi and M. S. T. Rubindamayugi, "The potential of agro-industrial residues for production of biogas and electricity in Tanzania," *Renewable Energy*, vol. 9, 1996; pp. 917-21.
- [22] X. Gang, B. S. Jin, Z. P. Zhong, C. Yong, M. J. Ni, K. F. Cen, X. Rui, Y. J. Huang, and H. He, "Experimental study on MSW gasification and melting technology," *Journal of Environmental Sciences-China*, vol. 19, 2007; pp. 1398-403.
- [23] L. Tang and H. Huang, "Biomass gasification using capacitively coupled RF plasma technology," *Fuel*, vol. 84, 2005; pp. 2055-63.
- [24] J. Han and H. Kim, "The reduction and control technology of tar during biomass gasification/pyrolysis: An overview," *Renewable & Sustainable Energy Reviews*, vol. 12, 2008; pp. 397-416.
- [25] L. Devi, K. J. Ptasinski, and F. J. J. G. Janssen, "Pretreated olivine as tar removal catalyst for biomass gasifiers: investigation using naphthalene as model biomass tar," *Fuel Processing Technology*, vol. 86, 2005; pp. 707-30.
- [26] I. A. Legonda, "Analysis of energy balances in low and high temperature air gasification of pelleted biomass," Masters Dissertation, University of Dar es Salaam, Tanzania, 2008.
- [27] C. Syred, W. Fick, A. J. Griffiths, and N. Syred, "Cyclone gasifier and cyclone combustor for the use of biomass derived gas in the operation of a small gas turbine in cogeneration plants," *Fuel*, vol. 83, 2004; pp. 2381-92.
- [28] S. Z. Sun, Y. J. Zhao, F. M. Su, and F. Ling, "Gasification of rice husk in a cyclone gasifier," *Korean Journal of Chemical Engineering*, vol. 26, 2009; pp. 528-33.
- [29] C. P. Liao, C. Z. Wu, Yanyongjie, and H. T. Huang, "Chemical elemental characteristics of biomass fuels in China," *Biomass & Bioenergy*, vol. 27, 2004; pp. 119-30.
- [30] A. Nordin, "Chemical Elemental Characteristics of Biomass Fuels," *Biomass & Bioenergy*, vol. 6, 1994; pp. 339-47.
- [31] C. Syred, A. J. Griffiths, N. Syred, D. Beedie, and D. James, "A clean, efficient system for producing Charcoal, Heat and Power (CHaP)," *Fuel*, vol. 85, 2006; pp. 1566-78.
- [32] J. Corella, J. M. Toledo, and G. Molina, "Performance of CaO and MgO for the hot gas clean up in gasification of a chlorine-containing (RDF) feedstock," *Bioresource Technology*, vol. 99, 2008; pp. 7539-44.
- [33] D. Porbatzki, M. Stemmler, and M. Muller, "Release of inorganic trace elements during gasification of wood, straw, and miscanthus," *Biomass & Bioenergy*, vol. 35, 2011; pp. S79-S86.
- [34] F. V. Tinaut, A. Melgar, J. F. Perez, and A. Horrillo, "Effect of biomass particle size and air superficial velocity on the gasification process in a downdraft fixed bed gasifier. An experimental and modelling study," *Fuel Processing Technology*, vol. 89, 2008; pp. 1076-89.

- [35] P. M. Lv, Z. H. Xiong, J. Chang, C. Z. Wu, Y. Chen, and J. X. Zhu, "An experimental study on biomass air-steam gasification in a fluidized bed," *Bioresource Technology*, vol. 95, 2004; pp. 95-101.
- [36] L. G. Wei, S. P. Xu, L. Zhang, H. G. Zhang, C. H. Liu, H. Zhu, and S. Q. Liu, "Characteristics of fast pyrolysis of biomass in a free fall reactor," *Fuel Processing Technology*, vol. 87, 2006; pp. 863-71.
- [37] P. N. Sheth and B. V. Babu, "Production of hydrogen energy through biomass (waste wood) gasification," *International Journal of Hydrogen Energy*, vol. 35, 2010; pp. 10803-10.
- [38] Y. J. Zhao, S. Z. Sun, H. Zhou, R. Sun, H. M. Tian, J. Y. Luan, and J. A. Qian, "Experimental study on sawdust air gasification in an entrained-flow reactor," *Fuel Processing Technology*, vol. 91, 2010; pp. 910-14.
- [39] M. Gabra, E. Pettersson, R. Backman, and B. Kjellstrom, "Evaluation of cyclone gasifier performance for gasification of sugar cane residue - Part 1: gasification of bagasse," *Biomass & Bioenergy*, vol. 21, 2001; pp. 351-69.
- [40] T. Phuphuakrat, N. Nipattummakul, T. Namioka, S. Kerdsuwan, and K. Yoshikawa, "Characterization of tar content in the syngas produced in a downdraft type fixed bed gasification system from dried sewage sludge," *Fuel*, vol. 89, 2010; pp. 2278-84.
- [41] T. Garcia, B. Solsona, and S. H. Taylor, "Naphthalene total oxidation over metal oxide catalysts," *Applied Catalysis B-Environmental*, vol. 66, 2006; pp. 92-99.
- [42] A. Aranda, J. M. Lopez, R. Murillo, A. M. Mastral, A. Dejoz, I. Vazquez, B. Solsona, S. H. Taylor, and T. Garcia, "Total oxidation of naphthalene with high selectivity using a ceria catalyst prepared by a combustion method employing ethylene glycol," *Journal of Hazardous Materials*, vol. 171, 2009; pp. 393-99.
- [43] J. J. Hernandez, G. Aranda-Almansa, and A. Bula, "Gasification of biomass wastes in an entrained flow gasifier: Effect of the particle size and the residence time," *Fuel Processing Technology*, vol. 91, 2010; pp. 681-92.
- [44] M. Lapuerta, J. J. Hernandez, A. Pazo, and J. Lopez, "Gasification and co-gasification of biomass wastes: Effect of the biomass origin and the gasifier operating conditions," *Fuel Processing Technology*, vol. 89, 2008; pp. 828-37.
- [45] S. Rapagna and G. M. di Celso, "Devolatilization of wood particles in a hot fluidized bed: Product yields and conversion rates," *Biomass & Bioenergy*, vol. 32, 2008; pp. 1123-29.
- [46] J. S. Zhou, Q. Chen, H. Zhao, X. W. Cao, Q. F. Mei, Z. Y. Luo, and K. F. Cen, "Biomass-oxygen gasification in a high-temperature entrained-flow gasifier," *Biotechnology Advances*, vol. 27, 2009; pp. 606-11.
- [47] S. Kajitani, N. Suzuki, M. Ashizawa, and S. Hara, "CO<sub>2</sub> gasification rate analysis of coal char in entrained flow coal gasifier," *Fuel*, vol. 85, 2006; pp. 163-69.
- [48] Y. J. Zhao, S. Z. Sun, H. M. Tian, J. Qian, F. M. Su, and F. Ling, "Characteristics of rice husk gasification in an entrained flow reactor," *Bioresource Technology*, vol. 100, 2009; pp. 6040-44.
- [49] N. Kobayashi, M. Tanaka, G. Piao, J. Kobayashi, S. Hatano, Y. Itaya, and S. Mori, "High temperature air-blown woody biomass gasification model for the estimation of an entrained down-flow gasifier," *Waste Management*, vol. 29, 2009; pp. 245-51.

- [50] K. Qin, W. G. Lin, P. A. Jensen, and A. D. Jensen, "High-temperature entrained flow gasification of biomass," *Fuel*, vol. 93, 2012; pp. 589-600.
- [51] Y. C. Choi, X. Y. Li, T. J. Park, J. H. Kim, and J. G. Lee, "Numerical study on the coal gasification characteristics in an entrained flow coal gasifier," *Fuel*, vol. 80, 2001; pp. 2193-201.
- [52] A. Petrissans, M. Petrissans, and A. Zoulalian, "Modeling of a gas catalytic chemical reaction, taking into account the diffusion in the adsorbed phase," *Chemical Engineering Journal*, vol. 117, 2006; pp. 31-38.
- [53] J. Hagen, Ed., *Industrial catalysis: A practical approach*. Wiley-VCH, 2006, p. ^pp. Pages.
- [54] N. Kakuta, N. Morishima, M. Kotobuki, T. Iwase, T. Mizushima, Y. Sato, and S. Matsuura, "Oxygen storage capacity (OSC) of aged Pt/CeO<sub>2</sub>/Al<sub>2</sub>O<sub>3</sub> catalysts: roles of Pt and CeO<sub>2</sub> supported on Al<sub>2</sub>O<sub>3</sub>," *Applied Surface Science*, vol. 121, 1997; pp. 408-12.
- [55] J. Sun, D. F. Luo, P. Xiao, J. G. Li, and S. Yu, "High yield hydrogen production from low CO selectivity ethanol steam reforming over modified Ni/Y<sub>2</sub>O<sub>3</sub> catalysts at low temperature for fuel cell application," *Journal of Power Sources*, vol. 184, 2008; pp. 385-91.
- [56] R. J. Liu, P. A. Crozier, C. M. Smith, D. A. Hucul, J. Blackson, and G. Salaita, "Metal sintering mechanisms and regeneration of palladium/alumina hydrogenation catalysts," *Applied Catalysis a-General*, vol. 282, 2005; pp. 111-21.
- [57] U. Elghawi, K. Theinnoi, S. Sitshebo, A. Tsolakis, M. L. Wyszynski, H. M. Xu, R. F. Cracknell, R. H. Clark, and A. Mayouf, "GC-MS determination of low hydrocarbon species (C-1-C-6) from a diesel partial oxidation reformer," *International Journal of Hydrogen Energy*, vol. 33, 2008; pp. 7074-83.
- [58] G. B. Shul'pin, "Metal-catalysed hydrocarbon oxidations," *Comptes Rendus Chimie*, vol. 6, 2003; pp. 163-78.
- [59] P. Ferreira, E. Phillips, D. Rippon, and S. C. Tsang, "Catalytic oxidation of alcohols using molecular oxygen mediated by poly(ethylene glycol)-supported nitroxyl radicals," *Applied Catalysis B-Environmental*, vol. 61, 2005; pp. 206-11.
- [60] S. H. Yan, J. L. Wang, J. B. Zhong, Y. Q. Chen, Z. M. Liu, H. Y. Cao, and M. C. Gong, "Effect of metal doping into Ce<sub>0.5</sub>Zr<sub>0.5</sub>O<sub>2</sub> on catalytic activity of MnO<sub>x</sub>/Ce<sub>0.5-x</sub>Zr<sub>0.5-x</sub>M<sub>0.2x</sub>O<sub>y</sub>/Al<sub>2</sub>O<sub>3</sub> for benzene combustion," *Journal of Rare Earths*, vol. 26, 2008; pp. 841-45.
- [61] B. Puertolas, B. Solsona, S. Agouram, R. Murillo, A. M. Mastral, A. Aranda, S. H. Taylor, and T. Garcia, "The catalytic performance of mesoporous cerium oxides prepared through a nanocasting route for the total oxidation of naphthalene," *Applied Catalysis B-Environmental*, vol. 93, 2010; pp. 395-405.
- [62] I. P. Chen, S. S. Lin, C. H. Wang, L. Chang, and J. S. Chang, "Preparing and characterizing an optimal supported ceria catalyst for the catalytic wet air oxidation of phenol," *Applied Catalysis B-Environmental*, vol. 50, 2004; pp. 49-58.
- [63] T. Y. Li, S. J. Chiang, B. J. Liaw, and Y. Z. Chen, "Catalytic oxidation of benzene over CuO/Ce<sub>1-x</sub>Mn<sub>x</sub>O<sub>2</sub> catalysts," *Applied Catalysis B-Environmental*, vol. 103, 2011; pp. 143-48.
- [64] J. S. Yang, W. Y. Jung, G. D. Lee, S. S. Park, E. D. Jeong, H. G. Kim, and S. S. Hong, "Catalytic combustion of benzene over metal oxides supported on

- SBA-15," *Journal of Industrial and Engineering Chemistry*, vol. 14, 2008; pp. 779-84.
- [65] C. H. Wang, "Al<sub>2</sub>O<sub>3</sub>-supported transition-metal oxide catalysts for catalytic incineration of toluene," *Chemosphere*, vol. 55, 2004; pp. 11-17.
- [66] M. F. Luo, P. Fang, M. He, and Y. L. Xie, "In situ XRD, Raman, and TPR studies of CuO/Al<sub>2</sub>O<sub>3</sub> catalysts for CO oxidation," *Journal of Molecular Catalysis a-Chemical*, vol. 239, 2005; pp. 243-48.
- [67] J. Kaspar, P. Fornasiero, and N. Hickey, "Automotive catalytic converters: current status and some perspectives," *Catalysis Today*, vol. 77, 2003; pp. 419-49.
- [68] V. Snapkauskiene, V. Valincius, and P. Valatkevicius, "Experimental study of catalytic CO oxidation over CuO/Al<sub>2</sub>O<sub>3</sub> deposited on metal sheets," *Catalysis Today*, vol. 176, 2011; pp. 77-80.
- [69] E. G. Heckert, A. S. Karakoti, S. Seal, and W. T. Self, "The role of cerium redox state in the SOD mimetic activity of nanocerium," *Biomaterials*, vol. 29, 2008; pp. 2705-09.
- [70] A. A. Mirzaei, H. R. Shaterian, M. Habibi, G. J. Hutchings, and S. H. Taylor, "Characterisation of copper-manganese oxide catalysts: effect of precipitate ageing upon the structure and morphology of precursors and catalysts," *Applied Catalysis a-General*, vol. 253, 2003; pp. 499-508.
- [71] M. Ferrandon, J. Carno, S. Jaras, and E. Bjornbom, "Total oxidation catalysts based on manganese or copper oxides and platinum or palladium I: Characterisation," *Applied Catalysis a-General*, vol. 180, 1999; pp. 141-51.
- [72] T. P. Murphy and M. G. Hutchins, "Oxidation states in nickel oxide electrochromism," *Solar Energy Materials and Solar Cells*, vol. 39, 1995; pp. 377-89.
- [73] M. Siedlecki and W. de Jong, "Biomass gasification as the first hot step in clean syngas production process - gas quality optimization and primary tar reduction measures in a 100 kW thermal input steam-oxygen blown CFB gasifier," *Biomass & Bioenergy*, vol. 35, 2011; pp. S40-S62.
- [74] G. Neri, G. Rizzo, L. De Luca, F. Corigliano, I. Arrigo, and A. Donato, "Zeolitized-pumice as a new support for hydrogenation catalysts," *Catalysis Communications*, vol. 9, 2008; pp. 2085-89.
- [75] A. M. Venezia, L. F. Liotta, G. Deganello, Z. Schay, D. Horvath, and L. Guzzi, "Catalytic CO oxidation over pumice supported Pd-Ag catalysts," *Applied Catalysis a-General*, vol. 211, 2001; pp. 167-74.
- [76] B. Gunnarsson, B. D. Marsh, and H. P. Taylor, "Generation of Icelandic rhyolites: silicic lavas from the Torfajokull central volcano," *Journal of Volcanology and Geothermal Research*, vol. 83, 1998; pp. 1-45.
- [77] U. Mann, M. Marks, and G. Markl, "Influence of oxygen fugacity on mineral compositions in peralkaline melts: The Katzenbuckel volcano, Southwest Germany," *Lithos*, vol. 91, 2006; pp. 262-85.
- [78] B. Cordonnier, K. U. Hess, Y. Lavallee, and D. B. Dingwell, "Rheological properties of dome lavas: Case study of Unzen volcano," *Earth and Planetary Science Letters*, vol. 279, 2009; pp. 263-72.
- [79] M. W. Ackley, S. U. Rege, and H. Saxena, "Application of natural zeolites in the purification and separation of gases," *Microporous and Mesoporous Materials*, vol. 61, 2003; pp. 25-42.

- [80] O. J. Prado, M. C. Veiga, and C. Kennes, "Treatment of gas-phase methanol in conventional biofilters packed with lava rock," *Water Research*, vol. 39, 2005; pp. 2385-93.
- [81] G. Cruciani, "Zeolites upon heating: Factors governing their thermal stability and structural changes," *Journal of Physics and Chemistry of Solids*, vol. 67, 2006; pp. 1973-94.
- [82] MEM, "INDUSTRIAL MINERALS IN TANZANIA An Investor's Guide," 2008.
- [83] C. Perego and P. Villa, "Catalyst preparation methods," *Catalysis Today*, vol. 34, 1997; pp. 281-305.
- [84] M. O. Adebajo, M. A. Long, and R. L. Frost, "Spectroscopic and XRD characterisation of zeolite catalysts active for the oxidative methylation of benzene with methane," *Spectrochimica Acta Part a-Molecular and Biomolecular Spectroscopy*, vol. 60, 2004; pp. 791-99.
- [85] I. Czekaj, F. Loviat, F. Raimondi, J. Wambach, S. Biollaz, and A. Wokaun, "Characterization of surface processes at the Ni-based catalyst during the methanation of biomass-derived synthesis gas: X-ray photoelectron spectroscopy (XPS)," *Applied Catalysis a-General*, vol. 329, 2007; pp. 68-78.
- [86] H. Tanaka, N. Mizuno, and M. Misono, "Catalytic activity and structural stability of La<sub>0.9</sub>Ce<sub>0.1</sub>Co<sub>1-x</sub>Fe<sub>x</sub>O<sub>3</sub> perovskite catalysts for automotive emissions control," *Applied Catalysis a-General*, vol. 244, 2003; pp. 371-82.
- [87] M. M. Barroso-Quiroga and A. E. Castro-Luna, "Catalytic activity and effect of modifiers on Ni-based catalysts for the dry reforming of methane," *International Journal of Hydrogen Energy*, vol. 35, 2010; pp. 6052-56.
- [88] X. H. Meng, C. M. Xu, and J. S. Gao, "Coking behavior and catalyst deactivation for catalytic pyrolysis of heavy oil," *Fuel*, vol. 86, 2007; pp. 1720-26.
- [89] L. Bobrova, N. Vernikovskaya, and V. Sadykov, "Conversion of hydrocarbon fuels to syngas in a short contact time catalytic reactor," *Catalysis Today*, vol. 144, 2009; pp. 185-200.
- [90] Y. Q. Wu, J. J. Wang, S. Y. Wu, S. Huang, and J. S. Gao, "Potassium-catalyzed steam gasification of petroleum coke for H<sub>2</sub> production: Reactivity, selectivity and gas release," *Fuel Processing Technology*, vol. 92, 2011; pp. 523-30.
- [91] J. F. Akyurtlu and A. Akyurtlu, "Catalytic Gasification of Pittsburgh Coal Char by Potassium-Sulfate and Ferrous Sulfate Mixtures," *Fuel Processing Technology*, vol. 43, 1995; pp. 71-86.
- [92] Y. J. Lu, H. Jin, L. J. Guo, X. M. Zhang, C. Q. Cao, and X. Guo, "Hydrogen production by biomass gasification in supercritical water with a fluidized bed reactor," *International Journal of Hydrogen Energy*, vol. 33, 2008; pp. 6066-75.
- [93] I. Chorkendorff and J. Niemantsverdriet, *Concepts of modern catalysis and Kinetics*: Wiley-VCH, 2003.
- [94] K. Leistner, A. Nicolle, D. Berthout, and P. da Costa, "Kinetic modelling of the oxidation of a wide range of carbon materials," *Combustion and Flame*, vol. 159, 2012; pp. 64-76.
- [95] ANSY-FLUENT-12.0, "Manual," 2009.
- [96] C. Mayant, B. Grambow, A. Abdelouas, S. Ribet, and S. Lederqcq, "Surface site density, silicic acid retention and transport properties of compacted

- magnetite powder," *Physics and Chemistry of the Earth*, vol. 33, 2008; pp. 991-99.
- [97] B. Ersoy, A. Sariisik, S. Dikmen, and G. Sariisik, "Characterization of acidic pumice and determination of its electrokinetic properties in water," *Powder Technology*, vol. 197, 2010; pp. 129-35.
- [98] BS-EN:15413:2011, "Solid recovered fuels-Methods for the preparation of the test sample from the laboratory sample."
- [99] BS-EN:1477-3:2009, "Solid biofuels - Determination of moisture content - Oven dry method Part 3: Moisture in general analysis sample."
- [100] BS-EN:15403:2011, "Solid recovered fuels - Determination of ash content."
- [101] CEN/TS:15148:2009, "Solid biofuels - Determination of the content of volatile matter."
- [102] U. Arena, R. Chirone, and P. Salatino, "The fate of fixed carbon during the fluidized-bed combustion of a coal and two waste-derived fuels," *Twenty-Sixth Symposium (International) on Combustion, Vols 1 and 2*, 1996; pp. 3243-51.
- [103] BS-ISO:1928:2009, "Solid mineral fuels-Determination of gross calorific value by the bomb calorimetric method and calculation of net calorific value."
- [104] BS:1016:1996, "Analysis and testing of coal and coke - Part 106: Ultimate analysis of coal and Coke."
- [105] BS-EN-ISO:11358:1997, "Plastics - Thermogravimetry (TG) of polymers - General principles."
- [106] BS-EN:15149-2:2010, "Solid biofuels - Determination of particle size distribution Part 2: Horizontal screen method using sieve apertures of 3,15mm and below."
- [107] DD-CEN/TS:15410:2006, "Solid recovered fuels. Method for the determination of the content of major elements ".
- [108] W. J. You, H. J. Moon, S. P. Jang, J. K. Kim, and J. Koo, "Effects of porosity, pumping power, and L/D ratio on the thermal characteristics of an N<sub>2</sub>O catalytic igniter with packed bed geometry," *International Journal of Heat and Mass Transfer*, vol. 53, 2010; pp. 726-31.
- [109] BS-EN:1936:2006, "Natural stone test methods - Determination of real density and apparent density, and of total and open porosity."
- [110] BS-EN:15169:2007, "Characterization of waste - Determination of loss on ignition in waste, sludge and sediments."
- [111] preEN-1744-7:2010, "Tests for chemical properties of aggregates - Part 7: Determination of loss of ignition of Municipal Incinerator Bottom Ash (MIBA Aggregate)."
- [112] N. Kakuta, Y. Sugino, H. Rachi, H. Ohkita, and T. Mizushima, "Chemical Removal of CeO<sub>2</sub> Segregated on the Surface of CeO<sub>2</sub>-ZrO<sub>2</sub> Binary Oxides for Improvement of OSC," *Topics in Catalysis*, vol. 52, 2009; pp. 1888-92.
- [113] S. Abdollahzadeh-Ghom, C. Zamani, T. Andreu, M. Epifani, and J. R. Morante, "Improvement of oxygen storage capacity using mesoporous ceria-zirconia solid solutions," *Applied Catalysis B-Environmental*, vol. 108, 2011; pp. 32-38.
- [114] CEN/TS:15439, "Biomass gasification-Tar and particles in product gases-Sampling and analysis," 2006.

- [115] A. Moshfegh, M. Shams, G. Ahmadi, and R. Ebrahimi, "A new expression for spherical aerosol drag in slip flow regime," *Journal of Aerosol Science*, vol. 41, 2010; pp. 384-400.
- [116] T. Fraser, "Numerical Modeling of an Inverted Cyclone Gasifier," PhD, Cardiff University, 2004.
- [117] M. Issa, C. Petit, A. Brillard, and J. F. Brillhac, "Oxidation of carbon by CeO<sub>2</sub>: Effect of the contact between carbon and catalyst particles," *Fuel*, vol. 87, 2008; pp. 740-50.
- [118] A. Skreiberg, O. Skreiberg, J. Sandquist, and L. Sorum, "TGA and macro-TGA characterisation of biomass fuels and fuel mixtures," *Fuel*, vol. 90, 2011; pp. 2182-97.
- [119] Y. F. Huang, W. H. Kuan, P. T. Chiueh, and S. L. Lo, "A sequential method to analyze the kinetics of biomass pyrolysis," *Bioresource Technology*, vol. 102, 2011; pp. 9241-46.
- [120] B. Singh and R. J. Gilkes, "The Recognition of Amorphous Silica in Indurated Soil Profiles," *Clay Minerals*, vol. 28, 1993; pp. 461-74.
- [121] Y. M. Liew, H. Kamarudin, A. M. M. Al Bakri, M. Luqman, I. K. Nizar, C. M. Ruzaidi, and C. Y. Heah, "Processing and characterization of calcined kaolin cement powder," *Construction and Building Materials*, vol. 30, 2012; pp. 794-802.
- [122] M. E. Borges, L. Diaz, M. C. Alvarez-Galvan, and A. Brito, "High performance heterogeneous catalyst for biodiesel production from vegetal and waste oil at low temperature," *Applied Catalysis B-Environmental*, vol. 102, 2011; pp. 310-15.
- [123] N. M. Deraz, M. M. Selim, and M. Ramadan, "Processing and properties of nanocrystalline Ni and NiO catalysts," *Materials Chemistry and Physics*, vol. 113, 2009; pp. 269-75.
- [124] D. L. Trimm, "Catalysts for the control of coking during steam reforming," *Catalysis Today*, vol. 49, 1999; pp. 3-10.
- [125] B. M. Steenari and O. Lindqvist, "High-temperature reactions of straw ash and the anti-sintering additives kaolin and dolomite," *Biomass & Bioenergy*, vol. 14, 1998; pp. 67-76.
- [126] I. A. Legonda, R. Marsh, A. J. Griffiths, K. Wilson, and A. F. Lee, "The effect of Ceria doped pumice upon coking resistance during gasification of biomass," presented at the Proceedings of the 2nd MIE 2012 International Conference Arusha, Tanzania, 243-250, 2012.
- [127] D. Iranshahi, M. R. Rahimpour, and A. Asgari, "A novel dynamic radial-flow, spherical-bed reactor concept for naphtha reforming in the presence of catalyst deactivation," *International Journal of Hydrogen Energy*, vol. 35, 2010; pp. 6261-75.
- [128] G. Asgari, B. Roshani, and G. Ghanizadeh, "The investigation of kinetic and isotherm of fluoride adsorption onto functionalize pumice stone," *Journal of Hazardous Materials*, vol. 217, 2012; pp. 123-32.
- [129] C. C. E. Verenum, BGT, DTI, ECN, KTH, SenterNovem, Fraunhofer Institute and VTT. (2005, June 2010). Sampling and analysis of tar and particles in biomass producer gases-Technical Report.
- [130] G. Malhotra, "Effect of different process conditions on pyrolysis products," M.Sc, Cardiff University, 2009.

- [131] J. J. Hernandez, G. Aranda, J. Barba, and J. M. Mendoza, "Effect of steam content in the air-steam flow on biomass entrained flow gasification," *Fuel Processing Technology*, vol. 99, 2012; pp. 43-55.
- [132] K. Stanczyk, N. Howaniec, A. Smolinski, J. Swiadrowski, K. Kapusta, M. Wiatowski, J. Grabowski, and J. Rogut, "Gasification of lignite and hard coal with air and oxygen enriched air in a pilot scale ex situ reactor for underground gasification," *Fuel*, vol. 90, 2011; pp. 1953-62.
- [133] Y. Cao, Y. Wang, J. T. Riley, and W. P. Pan, "A novel biomass air gasification process for producing tar-free higher heating value fuel gas," *Fuel Processing Technology*, vol. 87, 2006; pp. 343-53.
- [134] J. D. Martinez, K. Mahkamov, R. V. Andrade, and E. E. S. Lora, "Syngas production in downdraft biomass gasifiers and its application using internal combustion engines," *Renewable Energy*, vol. 38, 2012; pp. 1-9.
- [135] M. Czaplicka, "Sources and transformations of chlorophenols in the natural environment," *Science of the Total Environment*, vol. 322, 2004; pp. 21-39.
- [136] A. O. Olaniran and E. O. Igbinsosa, "Chlorophenols and other related derivatives of environmental concern: Properties, distribution and microbial degradation processes," *Chemosphere*, vol. 83, 2011; pp. 1297-306.
- [137] A. Holmgren, B. Andersson, and D. Duprez, "Interactions of CO with Pt/ceria catalysts," *Applied Catalysis B-Environmental*, vol. 22, 1999; pp. 215-30.
- [138] J. DeCoster, A. Ergut, Y. A. Levendis, H. Richter, J. B. Howard, and J. B. Carlson, "PAH emissions from high-temperature oxidation of vaporized anthracene," *Proceedings of the Combustion Institute*, vol. 31, 2007; pp. 491-99.
- [139] D. Butt, "Formation of phenols from the low-temperature fast pyrolysis of Radiata pine (*Pinus radiata*) - Part II. Interaction of molecular oxygen and substrate water," *Journal of Analytical and Applied Pyrolysis*, vol. 76, 2006; pp. 48-54.
- [140] N. Laosiripojana and S. Assabumrungrat, "Catalytic dry reforming of methane over high surface area ceria," *Applied Catalysis B-Environmental*, vol. 60, 2005; pp. 107-16.
- [141] R. Trane, S. Dahl, M. S. Skjoth-Rasmussen, and A. D. Jensen, "Catalytic steam reforming of bio-oil," *International Journal of Hydrogen Energy*, vol. 37, 2012; pp. 6447-72.
- [142] K. Shimizu, H. Kawachi, S. Komai, K. Yoshida, Y. Sasaki, and A. Satsuma, "Carbon oxidation with Ag/ceria prepared by self-dispersion of Ag powder into nano-particles," *Catalysis Today*, vol. 175, 2011; pp. 93-99.
- [143] C. F. Wu and P. T. Williams, "Ni/CeO<sub>2</sub>/ZSM-5 catalysts for the production of hydrogen from the pyrolysis-gasification of polypropylene," *International Journal of Hydrogen Energy*, vol. 34, 2009; pp. 6242-52.
- [144] X. Y. Jiang, G. L. Lu, R. X. Zhou, J. X. Mao, Y. Chen, and X. M. Zheng, "Studies of pore structure, temperature-programmed reduction performance, and micro-structure of CuO/CeO<sub>2</sub> catalysts," *Applied Surface Science*, vol. 173, 2001; pp. 208-20.
- [145] X. An, Y. Z. Zuo, Q. Zhang, and J. F. Wang, "Methanol Synthesis from CO(2) Hydrogenation with a Cu/Zn/Al/Zr Fibrous Catalyst," *Chinese Journal of Chemical Engineering*, vol. 17, 2009; pp. 88-94.
- [146] Y. Tanaka, T. Utaka, R. Kikuchi, T. Takeguchi, K. Sasaki, and K. Eguchi, "Water gas shift reaction for the reformed fuels over Cu/MnO catalysts

- prepared via spinel-type oxide," *Journal of Catalysis*, vol. 215, 2003; pp. 271-78.
- [147] Y. F. Zhao, Y. Yang, C. Mims, C. H. F. Peden, J. Li, and D. H. Mei, "Insight into methanol synthesis from CO(2) hydrogenation on Cu(111): Complex reaction network and the effects of H(2)O," *Journal of Catalysis*, vol. 281, 2011; pp. 199-211.
- [148] M. S. Wainwright and D. L. Trimm, "Methanol Synthesis and Water-Gas Shift Reactions on Raney Copper-Catalysts," *Catalysis Today*, vol. 23, 1995; pp. 29-42.
- [149] A. Fullana and S. S. Sidhu, "Fate of PAHs in the post-combustion zone: Partial oxidation of PAHs to dibenzofuran over CuO," *Journal of Analytical and Applied Pyrolysis*, vol. 74, 2005; pp. 479-85.
- [150] K. M. Parida and D. Rath, "Structural properties and catalytic oxidation of benzene to phenol over CuO-impregnated mesoporous silica," *Applied Catalysis a-General*, vol. 321, 2007; pp. 101-08.
- [151] S. M. Grimes, H. Lateef, A. J. Jafari, and L. Mehta, "Studies of the effects of copper, copper(II) oxide and copper(II) chloride on the thermal degradation of poly(vinyl chloride)," *Polymer Degradation and Stability*, vol. 91, 2006; pp. 3274-80.
- [152] C. Y. Lee, K. H. Han, and B. H. Ha, "Characteristics and combustion/decomposition activities of CuO/mordenite," *Microporous Materials*, vol. 11, 1997; pp. 227-35.
- [153] H. Noichi, A. Uddin, and E. Sasaoka, "Steam reforming of naphthalene as model biomass tar over iron-aluminum and iron-zirconium oxide catalyst catalysts," *Fuel Processing Technology*, vol. 91, 2010; pp. 1609-16.
- [154] F. Patcas and F. C. Patcas, "Reaction pathways and kinetics of the gas-phase oxidation of cyclohexane on NiO/gamma-Al2O3 catalyst," *Catalysis Today*, vol. 117, 2006; pp. 253-58.
- [155] B. H. Yue, X. G. Wang, X. P. Ai, J. Yang, L. Li, X. G. Lu, and W. Z. Ding, "Catalytic reforming of model tar compounds from hot coke oven gas with low steam/carbon ratio over Ni/MgO-Al2O3 catalysts," *Fuel Processing Technology*, vol. 91, 2010; pp. 1098-104.
- [156] V. Gaur, A. Sharma, and N. Verma, "Catalytic oxidation of toluene and m-xylene by activated carbon fiber impregnated with transition metals," *Carbon*, vol. 43, 2005; pp. 3041-53.
- [157] S. J. Juutilainen, P. A. Simell, and A. O. I. Krause, "Zirconia: Selective oxidation catalyst for removal of tar and ammonia from biomass gasification gas," *Applied Catalysis B-Environmental*, vol. 62, 2006; pp. 86-92.
- [158] T. Viinikainen, H. Ronkkonen, H. Bradshaw, H. Stephenson, S. Airaksinen, M. Reinikainen, P. Simell, and O. Krause, "Acidic and basic surface sites of zirconia-based biomass gasification gas clean-up catalysts," *Applied Catalysis a-General*, vol. 362, 2009; pp. 169-77.
- [159] O. Demoulin, M. Navez, J. L. Mugabo, and P. Ruiz, "The oxidizing role of CO2 at mild temperature on ceria-based catalysts," *Applied Catalysis B-Environmental*, vol. 70, 2007; pp. 284-93.
- [160] J. Harker, H. and J. Backhurst, R., *Fuel and energy*: Academic Press (London and New York), 1981.
- [161] J. C. van Dyk, "Development of an alternative laboratory method to determine thermal fragmentation of coal sources during pyrolysis in the gasification process," *Fuel*, vol. 80, 2001; pp. 245-49.

- [162] T. Yamamoto, H. Momida, T. Hamada, T. Uda, and T. Ohno, "First-principles study of dielectric properties of cerium oxide," *Thin Solid Films*, vol. 486, 2005; pp. 136-40.
- [163] T. W. G. Solomons, *Organic chemistry*, 8th ed.: Johns Wiley & Sons Inc., 2004.

# APPENDICES

## Appendix A. Gas Chromatography-Mass Spectrometer calibration standards



110 Benner Circle  
 Bellefonte, PA 16823-8812  
 Tel: (800)356-1688  
 Fax: (814)353-1309

www.Restek.com

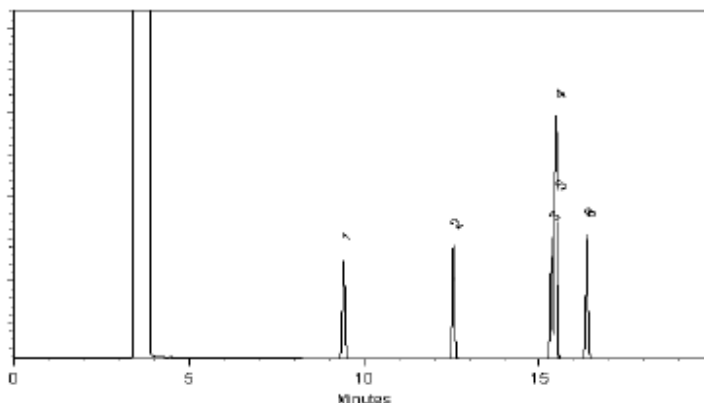
### Certificate of Analysis

FOR LABORATORY USE ONLY-READ MSDS PRIOR TO USE.

Catalog No. : 30051 Lot No.: A084972  
 Description : BTEX Standard  
VOA Mix, BTEX Std, 200µg/ml, P&T MeOH, 1ml/ampule  
 Container Size : <sup>5</sup> 2 mL Pkg Amt:<sup>5</sup> > 1 mL  
 Expiration Date : <sup>1</sup> December 2018 Storage: 0°C or colder

Elution Order	Compound	CAS #	Percent Purity <sup>2</sup>	Grav. Conc. (weight/volume) <sup>3</sup>	Grav.Uncert. (95% C.L.; K=2) <sup>4</sup>
1	Benzene	71-43-2	99%	200.0 ug/mL	+/- 1.4182 ug/mL
2	Toluene	108-88-3	99%	200.0 ug/mL	+/- 1.4182 ug/mL
3	Ethylbenzene	100-41-4	99%	200.0 ug/mL	+/- 1.4182 ug/mL
4	m-Xylene	108-38-3	99%	200.0 ug/mL	+/- 1.4182 ug/mL
5	p-Xylene	106-42-3	99%	200.0 ug/mL	+/- 1.4182 ug/mL
6	o-Xylene	95-47-6	99%	200.0 ug/mL	+/- 1.4182 ug/mL
Solvent:	P&T Methanol	67-56-1	99%		

Column:  
 105m x .53mm x 3.0µm  
 Itx-S02.2 (cat.#10910)  
 Carrier Gas:  
 hydrogen-constant pressure 11.0 psi.  
 Temp. Program:  
 40°C (hold 2 min.) to 240°C  
 @ 8°C/min. (hold 5 min.)  
 Inj. Temp:  
 200°C  
 Det. Temp:  
 250°C  
 Det. Type:  
 FID



*Christopher Zucco*  
 Christopher Zucco - QA Analyst

Date Passed: 07-Nov-2011 Balance: 1121472889

Manufactured under Restek's ISO 9001:2008  
 Registered Quality System  
 Certificate #FM 80387

- 1 Expiration date of the unopened ampule stored at the recommended storage condition is the last day of the month listed.
- 2A Purity and chemical identity are determined by one or more of the following techniques: GC/FID, HPLC, GC/ECD, GC/MS. Purity value is rounded to the nearest whole number. See data pack or contact Restek for further details.
- 2B Compounds with a listed purity of less than 99% have been weight corrected to compensate for impurities.
- 2C The following types of compounds will have a listed purity of less than 99%: Aldehyde/Ketone-DNPH compounds, Bromides, Chlorides, HCl salts, HBR salts, sulfates, hydrates, and other compounds as necessary. The listed purity is a correction factor that is equivalent to the percentage of parent compound in the molecule. This correction factor is used to calculate the amount of compound necessary to achieve the desired concentration of the parent compound in solution. The concentration listed on the certificate is the concentration of the parent compound in the solution.
- 2D Purity of isomeric compounds is reported as the sum of the isomers. Value is rounded to the nearest whole number after summation.
- 3 Based upon gravimetric preparation with balance calibration verified using NIST traceable weights (seven mass levels) and/or class A glassware used for dilutions.
- 4 Uncertainties determined using data for balances and glassware from measurement systems analysis methodology, raw material purity, and, when significant, equipment tolerances or calibration results.
- 5A Containers are overfilled to ensure the packaged amount, as a minimum.
- 5B Restek supplies deactivated vials along with most standards packed in 2 ml ampules, for the handling and storage of standards. Due to space constraints, Restek does not supply vials for larger volume ampules. Samples should be transferred into deactivated vials for handling and storage. Restek sells DMDCS for the purpose of glassware deactivation as catalog number 31840, which includes complete instructions. Restek will also deactivate larger volume vials from our inventory, as a custom ordered item. Contact your Restek sales or customer service representative for details.



# Certificate of Analysis

110 Benner Circle  
 Bellefonte, PA 16823-8812  
 Tel: (800)356-1688  
 Fax: (814)353-1309

**FOR LABORATORY USE ONLY-READ MSDS PRIOR TO USE.**

Catalog No.: 31455 Lot No.: A054272

Description: 610 PAH Calibration Mix B

Expiration Date<sup>1</sup>: September 2014 Storage: Room Temperature

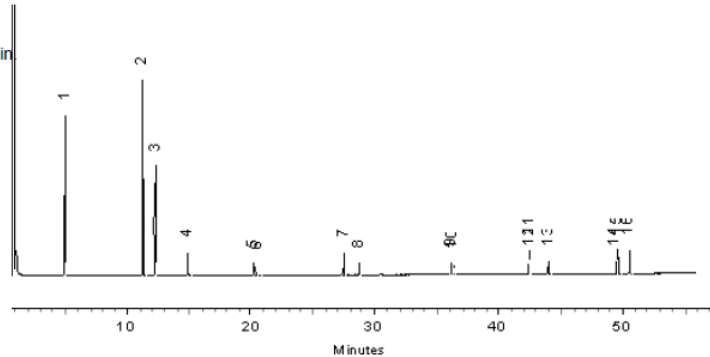
Handling: Warm & Sonicate prior to use

Elution Order	Compound	CAS #	Percent Purity <sup>2</sup>	Concentration <sup>3</sup> (weight/volume)	Percent Uncertainty <sup>4</sup>
1	Naphthalene	91-20-3	99%	1,000.000 ug/ml	+/-0.05 %
2	Acenaphthylene	208-96-8	99%	2,000.000 ug/ml	+/-0.05 %
3	Acenaphthene	83-32-9	99%	1,000.000 ug/ml	+/-0.05 %
4	Fluorene	86-73-7	99%	200.000 ug/ml	+/-0.05 %
5	Phenanthrene	85-01-8	99%	100.000 ug/ml	+/-0.05 %
6	Anthracene	120-12-7	97%	100.000 ug/ml	+/-0.05 %
7	Fluoranthene	206-44-0	98%	200.000 ug/ml	+/-0.05 %
8	Pyrene	129-00-0	98%	100.000 ug/ml	+/-0.05 %
9	Benz(a)anthracene	56-55-3	99%	100.000 ug/ml	+/-0.05 %
10	Chrysene	218-01-9	99%	100.000 ug/ml	+/-0.05 %
11	Benzo(b)fluoranthene	205-99-2	99%	200.000 ug/ml	+/-0.05 %
12	Benzo(k)fluoranthene	207-08-9	99%	100.000 ug/ml	+/-0.05 %
13	Benzo(a)pyrene	50-32-8	99%	100.000 ug/ml	+/-0.05 %
14	Indeno(1,2,3-cd)pyrene	193-39-5	99%	100.000 ug/ml	+/-0.05 %
15	Dibenz(a,h)anthracene	53-70-3	99%	200.000 ug/ml	+/-0.05 %
16	Benzo(g,h,i)perylene	191-24-2	99%	200.000 ug/ml	+/-0.05 %

Solvent: Methylene Chloride/Methanol (50:50) 75-09-2/67-56-1 99%

Column: 30m x .25mm x .5um  
 Rtx-5 (cat.#10238)  
 Carrier Gas: hydrogen @ 40 cm/sec  
 Temp. Program: 100°C to 330°C @ 4°C/min

Inj. Temp: 250°C  
 Det. Temp: 330°C  
 Det. Type: FID



*Diane Shaffer*  
 Diane Shaffer - QA Analyst

Balance 1113372841



Manufactured under Restek's ISO 9001 Registered Quality System Certificate #FMB0397

<sup>1</sup> Expiration date of the unopened ampul stored at recommended temperature.  
<sup>2</sup> Purity was determined by one or more of the following techniques: GC/FID, HPLC, GC/ECD, GC/MS. Value rounded to the nearest LOWER whole percentage. In addition to detectors listed above, chemical identity and purity are confirmed using 1 or more of the following: MS, DSC, solid probe MS, GC/FPD, GC/NPD, GC/TIC, FTIR, melting point, refractive index, and Karl Fisher. See data pack or contact Restek for further details.  
<sup>3</sup> Based upon gravimetric preparation with balance calibration verified using NIST traceable weights (seven mass levels).  
<sup>4</sup> Percent Uncertainty based upon balance AND ASTM Class A volumetric glassware accuracy.



110 Benner Circle  
 Bellefonte, PA 16823-8812  
 Tel: (800)356-1688  
 Fax: (814)353-1309

www.Restek.com

## Certificate of Analysis

FOR LABORATORY USE ONLY-READ MSDS PRIOR TO USE.

Catalog No. : 31088 Lot No.: A083734  
 Description : 8040 Phenols Mix #1  
 SV Mix, 8000 Series Method, 8040 Calibration Std #1, phenols mix,  
 2,000µg/ml, Isopropanol, 1ml/ampule  
 Container Size : <sup>5</sup> 2 mL Pkg Amt:<sup>5</sup> > 1 mL  
 Expiration Date : <sup>1</sup> September 2019 Storage: 10°C or colder

Elution Order	Compound	CAS #	Percent Purity <sup>2</sup>	Grav. Conc. (weight/volume) <sup>3</sup>	Grav.Uncert. (95% C.L.; K=2) <sup>4</sup>
1	Phenol	108-95-2	99%	2,000.0 ug/mL	+/- 11.8794 ug/mL
2	3-Methylphenol (m-cresol)	108-39-4	99%	2,000.0 ug/mL	+/- 11.8794 ug/mL
3	2-Nitrophenol	88-75-5	99%	2,000.0 ug/mL	+/- 11.8794 ug/mL
4	2,4-Dichlorophenol	120-83-2	99%	2,000.0 ug/mL	+/- 11.8794 ug/mL
5	4-Chloro-3-methylphenol	59-50-7	99%	2,000.0 ug/mL	+/- 11.8794 ug/mL
6	2,4,6-Trichlorophenol	88-06-2	99%	2,000.0 ug/mL	+/- 11.8794 ug/mL
7	4-Nitrophenol	100-02-7	99%	2,000.0 ug/mL	+/- 11.8794 ug/mL
8	4,6-Dinitro-2-methylphenol (Dinitro-o-cresol)	534-52-1	99%	2,000.0 ug/mL	+/- 11.8794 ug/mL
9	Pentachlorophenol	87-86-5	99%	2,000.0 ug/mL	+/- 11.8794 ug/mL
Solvent:		Isopropanol	67-63-0	99%	

Column:  
 30m x .25mm x .25um  
 Rtx-5 (cat.#10223)

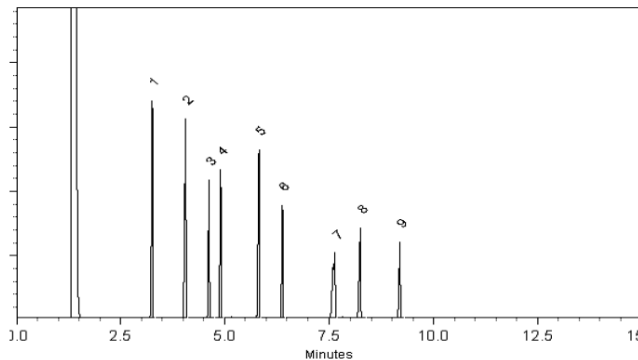
Carrier Gas:  
 hydrogen-constant pressure 10 psi.

Temp. Program:  
 75°C (hold 1 min.) to 330°C  
 @ 20°C/min. (hold 5 min.)

Inj. Temp:  
 250°C

Det. Temp:  
 330°C

Det. Type:  
 FID



*Diane Shaffer*  
 Diane Shaffer - QA Analyst

Date Passed: 31-Aug-2011 Balance: 1128353505

Manufactured under Restek's ISO 9001:2008  
 Registered Quality System  
 Certificate #FM 80397

- Expiration date of the unopened ampule stored at the recommended storage condition is the last day of the month listed.
- Purity and chemical identity are determined by one or more of the following techniques: GC/FID, HPLC, GC/ECD, GC/MS. Purity value is rounded to the nearest whole number. See data pack or contact Restek for further details.
- Compounds with a listed purity of less than 99% have been weight corrected to compensate for impurities.
- The following types of compounds will have a listed purity of less than 99%: Aldehyde/Ketone-DNPH compounds, Bromides, Chlorides, HCL salts, HBR salts, sulfates, hydrates, and other compounds as necessary. The listed purity is a correction factor that is equivalent to the percentage of parent compound in the molecule. This correction factor is used to calculate the amount of compound necessary to achieve the desired concentration of the parent compound in solution. The concentration listed on the certificate is the concentration of the parent compound in the solution.
- Purity of isomeric compounds is reported as the sum of the isomers. Value is rounded to the nearest whole number after summation.
- Based upon gravimetric preparation with balance calibration verified using NIST traceable weights (seven mass levels) and/or class A glassware used for dilutions.
- Uncertainties determined using data for balances and glassware from measurement systems analysis methodology, raw material purity, and, when significant, equipment tolerances or calibration results.
- Containers are overfilled to ensure the packaged amount, as a minimum.
- Restek supplies deactivated vials along with most standards packed in 2 mL ampules, for the handling and storage of standards. Due to space constraints, Restek does not supply vials for larger volume ampules. Samples should be transferred into deactivated vials for handling and storage. Restek sells DMDCS for the purpose of glassware deactivation as catalog number 31840, which includes complete instructions. Restek will also deactivate larger volume vials from our inventory, as a custom ordered item. Contact your Restek sales or customer service representative for details.



110 Benner Circle  
Bellefonte, PA 16823-8812  
Tel: (800)356-1688  
Fax: (814)353-1309

www.RESTEK.com

## Certificate of Analysis

FOR LABORATORY USE ONLY-READ MSDS PRIOR TO USE.

Catalog No. : 31900 Lot No.: A085199  
Description : OLM 01.1 Revised SV MegaMix  
SOM01.1 SVOA MegaMix® Revised, 1,000µg/ml, CH2Cl2, 1ml/ampule  
Container Size : <sup>5</sup> 2 mL Pkg Amt: <sup>5</sup> > 1 mL  
Expiration Date : <sup>1</sup> May 2013 Storage: 0°C or colder  
Handling: Sonication required. Mix is photosensitive.

Elution Order	Compound	CAS #	Percent Purity <sup>2</sup>	Grav. Conc. (weight/volume) <sup>3</sup>	Grav.Uncert. (95% C.L.; K=2) <sup>4</sup>
1	Phenol	108-95-2	99%	1,000.0 ug/mL	+/- 6.6846 ug/mL
2	Bis(2-chloroethyl)ether	111-44-4	99%	1,000.0 ug/mL	+/- 6.6846 ug/mL
3	2-Chlorophenol	95-57-8	99%	1,000.0 ug/mL	+/- 6.6846 ug/mL
4	Bis(2-chloroisopropyl)ether	108-60-1	99%	1,000.0 ug/mL	+/- 6.6846 ug/mL
5	2-Methylphenol (o-cresol)	95-48-7	99%	1,000.0 ug/mL	+/- 6.6846 ug/mL
6	Acetophenone	98-86-2	99%	1,000.0 ug/mL	+/- 5.9397 ug/mL
7	Hexachloroethane	67-72-1	99%	1,000.0 ug/mL	+/- 6.6846 ug/mL
8	N-Nitroso-di-n-propylamine	621-64-7	99%	1,000.0 ug/mL	+/- 6.732 ug/mL
9	4-Methylphenol (p-cresol)	106-44-5	99%	500.0 ug/mL	+/- 3.3481 ug/mL
10	3-Methylphenol (m-cresol)	108-39-4	99%	500.0 ug/mL	+/- 3.3481 ug/mL
11	Nitrobenzene	98-95-3	99%	1,000.0 ug/mL	+/- 6.6846 ug/mL
12	Isophorone	78-59-1	99%	1,000.0 ug/mL	+/- 6.6846 ug/mL
13	2-Nitrophenol	88-75-5	99%	1,000.0 ug/mL	+/- 6.6846 ug/mL
14	2,4-Dimethylphenol	105-67-9	99%	1,000.0 ug/mL	+/- 6.6846 ug/mL
15	Bis(2-chloroethoxy)methane	111-91-1	99%	1,000.0 ug/mL	+/- 6.6846 ug/mL
16	2,4-Dichlorophenol	120-83-2	99%	1,000.0 ug/mL	+/- 6.6846 ug/mL
17	Naphthalene	91-20-3	99%	1,000.0 ug/mL	+/- 6.6846 ug/mL
18	4-Chloroaniline	106-47-8	99%	1,000.0 ug/mL	+/- 6.732 ug/mL
19	Hexachlorobutadiene	87-68-3	98%	1,000.0 ug/mL	+/- 6.6848 ug/mL
20	2-Methylnaphthalene	91-57-6	97%	1,000.1 ug/mL	+/- 6.7325 ug/mL
21	4-Chloro-3-methylphenol	59-50-7	99%	1,000.0 ug/mL	+/- 6.6846 ug/mL
22	1,2,4,5-Tetrachlorobenzene	95-94-3	99%	1,000.0 ug/mL	+/- 6.732 ug/mL
23	Hexachlorocyclopentadiene	77-47-4	99%	1,000.0 ug/mL	+/- 6.6846 ug/mL
24	2,4,6-Trichlorophenol	88-06-2	99%	1,000.0 ug/mL	+/- 6.6846 ug/mL
25	2,4,5-Trichlorophenol	95-95-4	99%	1,000.0 ug/mL	+/- 6.6846 ug/mL
26	2-Chloronaphthalene	91-58-7	99%	1,000.0 ug/mL	+/- 6.6846 ug/mL
27	Biphenyl	92-52-4	99%	1,000.0 ug/mL	+/- 5.9397 ug/mL
28	2-Nitroaniline	88-74-4	99%	1,000.0 ug/mL	+/- 6.732 ug/mL
29	Acenaphthylene	208-96-8	99%	1,000.0 ug/mL	+/- 6.6846 ug/mL
30	Dimethylphthalate	131-11-3	99%	1,000.0 ug/mL	+/- 6.6846 ug/mL
31	2,6-Dinitrotoluene	606-20-2	99%	1,000.0 ug/mL	+/- 6.6846 ug/mL

32	Acenaphthene	83-32-9	99%	1,000.0 ug/mL	+/- 6.6846 ug/mL
33	3-Nitroaniline	99-09-2	97%	1,000.1 ug/mL	+/- 6.7325 ug/mL
34	2,4-Dinitrophenol	51-28-5	98%	1,000.0 ug/mL	+/- 6.6848 ug/mL
35	Dibenzofuran	132-64-9	99%	1,000.0 ug/mL	+/- 5.9397 ug/mL
36	2,4-Dinitrotoluene	121-14-2	99%	1,000.0 ug/mL	+/- 6.6846 ug/mL
37	4-Nitrophenol	100-02-7	99%	1,000.0 ug/mL	+/- 6.6846 ug/mL
38	2,3,4,6-Tetrachlorophenol	58-90-2	99%	1,000.0 ug/mL	+/- 6.732 ug/mL
39	Fluorene	86-73-7	99%	1,000.0 ug/mL	+/- 6.6846 ug/mL
40	4-Chlorophenyl phenyl ether	7005-72-3	99%	1,000.0 ug/mL	+/- 6.6846 ug/mL
41	Diethylphthalate	84-66-2	99%	1,000.0 ug/mL	+/- 6.6846 ug/mL
42	4-Nitroaniline	100-01-6	99%	1,000.0 ug/mL	+/- 6.732 ug/mL
43	4,6-Dinitro-2-methylphenol (Dinitro-o-cresol)	534-52-1	99%	1,000.0 ug/mL	+/- 6.6846 ug/mL
44	Diphenylamine	122-39-4	99%	1,000.0 ug/mL	+/- 6.732 ug/mL
45	4-Bromophenyl phenyl ether	101-55-3	99%	1,000.0 ug/mL	+/- 6.6846 ug/mL
46	Hexachlorobenzene	118-74-1	99%	1,000.0 ug/mL	+/- 6.6846 ug/mL
47	Pentachlorophenol	87-86-5	98%	1,000.0 ug/mL	+/- 6.6848 ug/mL
48	Phenanthrene	85-01-8	99%	1,000.0 ug/mL	+/- 6.6846 ug/mL
49	Anthracene	120-12-7	99%	1,000.0 ug/mL	+/- 6.6846 ug/mL
50	Carbazole	86-74-8	98%	999.6 ug/mL	+/- 6.7293 ug/mL
51	Di-n-butylphthalate	84-74-2	99%	1,000.0 ug/mL	+/- 6.6846 ug/mL
52	Fluoranthene	206-44-0	98%	1,000.0 ug/mL	+/- 6.6848 ug/mL
53	Pyrene	129-00-0	98%	1,000.0 ug/mL	+/- 6.6848 ug/mL
54	Benzyl butyl phthalate	85-68-7	99%	1,000.0 ug/mL	+/- 6.6846 ug/mL
55	Benz(a)anthracene	56-55-3	99%	1,000.0 ug/mL	+/- 6.6846 ug/mL
56	Chrysene	218-01-9	99%	1,000.0 ug/mL	+/- 6.6846 ug/mL
57	3,3'-Dichlorobenzidine	91-94-1	99%	1,000.0 ug/mL	+/- 6.732 ug/mL
58	Bis(2-ethylhexyl)phthalate	117-81-7	99%	1,000.0 ug/mL	+/- 6.6846 ug/mL
59	Di-n-octyl phthalate	117-84-0	99%	1,000.0 ug/mL	+/- 6.6846 ug/mL
60	Benzo(b)fluoranthene	205-99-2	99%	1,000.0 ug/mL	+/- 6.6846 ug/mL
61	Benzo(k)fluoranthene	207-08-9	99%	1,000.0 ug/mL	+/- 6.6846 ug/mL
62	Benzo(a)pyrene	50-32-8	99%	1,000.0 ug/mL	+/- 6.6846 ug/mL
63	Indeno(1,2,3-cd)pyrene	193-39-5	99%	1,000.0 ug/mL	+/- 6.6846 ug/mL
64	Dibenz(a,h)anthracene	53-70-3	99%	1,000.0 ug/mL	+/- 6.6846 ug/mL
65	Benzo(g,h,i)perylene	191-24-2	99%	1,000.0 ug/mL	+/- 6.6846 ug/mL
<b>Solvent:</b>		<b>Methylene Chloride</b>	<b>75-09-2</b>	<b>99%</b>	

**Column:**

30m x .25mm x .25um  
Rtx-5 (cat.#10223)

**Carrier Gas:**

hydrogen-constant pressure 10 psi

**Temp. Program:**

35°C (hold 3 min.) to 330°C  
@ 3°C/min. (hold 3 min.)

**Inj. Temp:**

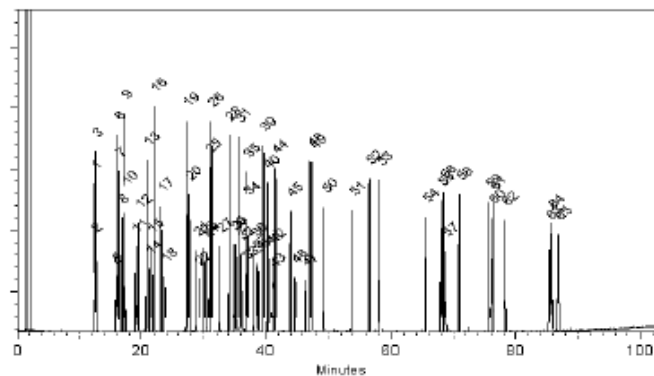
250°C

**Det. Temp:**

300°C

**Det. Type:**

FID



*Diane Shaffer*  
Diane Shaffer - QA Analyst

Date Passed: 29-Nov-2011 Balance: 1128342314

Manufactured under Restek's ISO 9001:2008  
Registered Quality System  
Certificate #PM 80397

- Expiration date of the unopened ampule stored at the recommended storage condition is the last day of the month listed.
- Purity and chemical identity are determined by one or more of the following techniques: GC/FID, HPLC, GC/ECD, GC/MS. Purity value is rounded to the nearest whole number. See data pack or contact Restek for further details.
- Compounds with a listed purity of less than 99% have been weight corrected to compensate for impurities.
- The following types of compounds will have a listed purity of less than 99%: Aldehydes/Nitroso-DNPH compounds, Bromides, Chlorides, HCl salts, HBr salts, sulfates, hydrates, and other compounds as necessary. The listed purity is a correction factor that is equivalent to the percentage of parent compound in the molecule. This correction factor is used to calculate the amount of compound necessary to achieve the desired concentration of the parent compound in solution. The concentration listed on the certificate is the concentration of the parent compound in the solution.
- Purity of isomeric compounds is reported as the sum of the isomers. Value is rounded to the nearest whole number after summation.
- Based upon gravimetric preparation with balance calibration verified using NIST traceable weights (seven mass levels) and/or class A glassware used for dilutions.
- Uncertainties determined using data for balances and glassware from measurement systems analysis methodology, raw material purity, and, when significant, equipment tolerances or calibration results.
- Containers are overfilled to ensure the packaged amount, as a minimum.
- Restek supplies deactivated vials along with most standards packed in 2 mL ampules, for the handling and storage of standards. Due to space constraints, Restek does not supply vials for larger volume ampules. Samples should be transferred into deactivated vials for handling and storage. Restek sells DMOCS for the purpose of glassware deactivation as catalog number 31840, which includes complete instructions. Restek will also deactivate larger volume vials from our inventory, as a custom ordered item. Contact your Restek sales or customer service representative for details.

**Tech Tip:**

N-Nitrosodiphenylamine is prone to breakdown in the injection port and will be converted to diphenylamine. N-Nitrosodiphenylamine is also a reactive species that can initiate premature decomposition of other compounds in the mix. For these reasons diphenylamine is used in the preparation of this mixture. When comparing the response of this compound to mixtures manufactured using N-nitrosodiphenylamine, a difference in response will be observed.

## Appendix B. Biomass Gasification Modeling

The following parameters and values were used in modeling of the biomass gasification process.

### A.1 Energy

- Energy Equation

### A.2 Viscous Model

1. Model: K-epsilon (2 eqn)
2. K-epsilon Model: Standard
3. Near-Wall Treatment: Standard Wall Functions

### A.3 Species Model

1. Model: Partially Premixed Combustion
2. PDF Option: Inlet Diffusion
3. Premixed Model: C Equation
4. PDF Table Creation
  - Chemistry:
    - State relation: Equilibrium
    - Energy treatment: Non-Adiabatic
    - Stream options: Secondary Stream and Empirical Secondary Stream
    - Model settings:
      - Operation Pressure (pascal): 101325
      - Empirical Secondary Lower Calorific Value (j/kg): 1.9e+07
      - Empirical Secondary Specific Heat (j/kg-k): 2400
      - Empirical Secondary Molecular Weight (kg/kgmol): 30
  - Boundary:
    - Species: C, H, O, N, S, CH<sub>4</sub>, H<sub>2</sub>, N<sub>2</sub>, O<sub>2</sub>, C(s), CO, CO<sub>2</sub>, H<sub>2</sub>O, OH, C<sub>2</sub>H<sub>6</sub>, C<sub>3</sub>H<sub>8</sub>
    - Temperature: For fuel, oxidiser and secondary streams
      - Fuel (k) : 300
      - Oxid (k) : 300

- Second (k) : 300
- Specify Species in: Mole Fraction
- Composition of the species
  - Fuel: C(s): 1, all other species were 0
  - Oxid: N2: 0.78992, O2: 0.21008
  - Second: C: 0.22618, H: 0.56045, O: 0.21217, N: 0.0012, S: 0

#### **A.4 Discrete Phase Model**

1. Interaction: Interaction with Continuous Phase
2. Number of Continuous Phase Iterations per DPM Iteration: 10
3. Tracking
  - Tracking parameters:
    - Max. Number of Steps: 50000
    - Specify Length Scale:
      - Length Scale (m): 0.01
  - Drag Parameters:
    - Drag Law: Nonspherical
    - Shape Factor: 0.7
4. Physical Models
  - Options:
    - Thermopheretic Force
    - Brownian Motion
    - Saffman Lift Force
    - Errosion/Accretion
  - Numerics:
    - Options:
      - Accuracy Control: 1e-05
      - Max. Refinement: 20
      - Coupled Heat-Mass Solution
  - Injection:

## A.5 Materials

1. Mixture: PDF mixture:
2. Solid:
  - Combusting Particle
  - Wood

## A6. Boundary Conditions

1. Inlet: Mass Flow Inlet
  - Momentum:
    - Mass Flow Specification Method: Mass Flow Rate
    - Mass Flow Rate (kg/s): 0.0003
    - Turbulence:
      - Specification Method: Intensity and Viscosity ratio
      - Turbulent Intensity (%): 10
      - Turbulent Viscosity Ratio: 10
  - Thermal:
    - Total Temperature (k): 300 Constant
  - Species:
    - Mean Mixture Fraction: 0.21, all others 0.
  - DPM:
    - Discrete Phase BC Type: Escape
2. Outlet:
  - Momentum:
    - Gauge Pressure (pascal): -50 , Constant
    - Backflow Direction Specification Method: Normal to Boundary
    - Turbulence:
      - Specification Method: K and Epsilon
      - Backflow Turbulent Kinetic Energy (m<sup>2</sup>/s<sup>2</sup>): 1
      - Backflow Turbulent Dissipation Rate (m<sup>2</sup>/s<sup>3</sup>): 1

- Thermal:
  - Backflow Total Temperature (k): 300 Constant

## **A7. Solution**

1. Solution Methods:
  - Pressure Velocity Coupling Scheme: SIMPLE
  - Spatial Discretisation:
    - Gradient: Least Squares Cell Based
    - Pressure: Standard
    - All other parameters were set to Second Order Upwind
2. Solution Control: Under-Relaxation Factors: Default
3. Solution Initialisation: Compute from inlet

## Appendix C. Catalytic Gasification Modeling

The following parameters and values were used in modeling of the catalytic gasification process.

### B.1 Energy

- Energy Equation

### B.2 Viscous Model

1. Model: Laminar

### B.3 Species Model

1. Model: Species Transport
2. Reactions:
  - Volumetric
  - Wall Surface
3. Wall Surface Reaction Options:
  - Mass Deposition Source Aggressiveness Factor: 0
4. Options:
  - Diffusion Energy Source
  - Full Multicomponent Diffusion
5. Turbulence-Chemistry Interactions:
  - Laminar Finite-Rate
6. Mixture Species:
  - Selected Species: CH<sub>4</sub>, H<sub>2</sub>, N<sub>2</sub>, O<sub>2</sub>, CO, CO<sub>2</sub>, H<sub>2</sub>O
  - Selected Site species: CeO<sub>2</sub>, Ce<sub>2</sub>O<sub>3</sub>
7. Reactions:
  - Total Number of Reactions: 4
  - Reaction ID: 1
    - Reaction Type: Wall Surface
    - Reactants: 2
      - Reactant Species: H<sub>2</sub>, CeO<sub>2</sub>  
Stoichiometric coefficient: H<sub>2</sub>=1, CeO<sub>2</sub>=2
      - Product Species: H<sub>2</sub>O, Ce<sub>2</sub>O<sub>3</sub>

- Stoichiometric coefficient: H<sub>2</sub>O=1, Ce<sub>2</sub>O<sub>3</sub>=1
    - Pre-Exponential Factor: 1.9e+19
    - Activation Energy (j/kgmol): 154
  - Reaction ID: 2
    - Reaction Type: Wall Surface
    - Reactants: 2
      - Reactant Species: CO<sub>2</sub>, Ce<sub>2</sub>O<sub>3</sub>  
Stoichiometric coefficient: CO<sub>2</sub>=1, Ce<sub>2</sub>O<sub>3</sub>=1
      - Product Species: CO, CeO<sub>2</sub>  
Stoichiometric coefficient: CO=1, CeO<sub>2</sub>=2
      - Pre-Exponential Factor: 1.9e+19
      - Activation Energy (j/kgmol): 154
  - Reaction ID: 3
    - Reaction Type: Wall Surface
    - Reactants: 2
      - Reactant Species: C<sub>7</sub>H<sub>8</sub>, CeO<sub>2</sub>  
Stoichiometric coefficient: C<sub>7</sub>H<sub>8</sub>=1, CeO<sub>2</sub>=2
      - Product Species: CO, H<sub>2</sub>, CH<sub>4</sub>, C, Ce<sub>2</sub>O<sub>3</sub>  
Stoichiometric coefficient: CO=1, H<sub>2</sub>=2, CH<sub>4</sub>=1, C=5,  
Ce<sub>2</sub>O<sub>3</sub>=1
      - Pre-Exponential Factor: 3.26e+17
      - Activation Energy (j/kgmol): 154
  - Reaction ID: 4
    - Reaction Type: Wall Surface
    - Reactants: 2
      - Reactant Species: C, CeO<sub>2</sub>  
Stoichiometric coefficient: C=1, CeO<sub>2</sub>=1
      - Product Species: CO, Ce<sub>2</sub>O<sub>3</sub>  
Stoichiometric coefficient: CO=1, Ce<sub>2</sub>O<sub>3</sub>=1
      - Pre-Exponential Factor: 2550
      - Activation Energy (j/kgmol): 134

**B.4 Cell Zone Conditions:**

- Catalyst part: Porous, Reaction

**B.5 Boundary Conditions:**

- Refer Table 5.3

**B6. Solution**

- Pressure Velocity Coupling Scheme: SIMPLE
- Spatial Discretisation:
  - Gradient: Least Squares Cell Based
  - Pressure: PRESTO!
  - All other parameters were set to Second Order Upwind
- Solution Control: Under-Relaxation Factors: Default
- Solution Initialisation: Compute from inlet

## Appendix D: Material and energy balances for all experimental tests

### (a) Non-catalytic

Stream	Mass balance (g)			Carbon balance (g)			Energy balance (MJ)		
	In	Out	% error	In	Out	% error	In	Out	% error
Wood powder	60.00			29.64			1.01		
Air	45.83								
Gas		94.00			20.04			0.63	
Tar		3.13			2.87			0.07	
Char		0.18			0.10			0.00	
Total	105.83	97.31	8.05	29.64	23.00	22.39	1.01	0.70	30.82

### (b) Ceria catalysts

#### 0.65 g CeO<sub>2</sub>

Stream	Mass balance (g)			Carbon balance (g)			Energy balance (MJ)		
	In	Out	% error	In	Out	% error	In	Out	% error
Wood powder	60.00			29.64			1.01		
Air	45.83								
Gas		101.07			22.71			0.74	
Tar		3.40			2.73			0.07	
Char		0.18			0.10			0.00	
Total	105.83	104.65	1.12	29.64	25.54	13.85	1.01	0.81	19.75

#### 1.44 g CeO<sub>2</sub>

Wood powder	60.00			29.64			1.01		
Air	45.83								
Gas		97.45			22.92			0.75	
Tar		3.21			2.55			0.07	
Char		0.18			0.10			0.00	
Total	105.83	100.84	4.72	29.64	25.56	13.76	1.01	0.82	18.84

#### 1.73 g CeO<sub>2</sub>

Wood powder	60.00			29.64			1.01		
Air	45.83								
Gas		100.99			25.16			0.85	
Tar		3.51			2.81			0.08	
Char		0.18			0.10			0.00	
Total	105.83	104.68	1.09	29.64	28.07	5.31	1.01	0.93	8.58

**(c) Copper catalysts****0.74 g CuO**

Stream	Mass balance (g)			Carbon balance (g)			Energy balance (MJ)		
	In	Out	% error	In	Out	% error	In	Out	% error
Wood powder	60.00			29.64			1.01		
Air	45.83								
Gas		97.20			23.15			0.72	
Tar		2.12			1.71			0.05	
Char		0.18			0.10			0.00	
Total	105.83	99.50	5.99	29.64	24.96	15.78	1.01	0.77	23.75

**1.79 g CuO**

Wood powder	60.00			29.64			1.01		
Air	45.83								
Gas		101.41			25.22			0.77	
Tar		1.82			1.42			0.04	
Char		0.18			0.10			0.00	
Total	105.83	103.41	2.29	29.64	26.74	9.80	1.01	0.82	19.47

**2.81 g CuO**

Wood powder	60.00			29.64			1.01		
Air	45.83								
Gas		101.90			24.99			0.82	
Tar		1.64			1.26			0.04	
Char		0.18			0.10			0.00	
Total	105.83	103.72	2.00	29.64	26.36	11.08	1.01	0.86	15.56

**(d) Kaolin-ceria catalysts****9.2 g CeO<sub>2</sub>**

Stream	Mass balance (g)			Carbon balance (g)			Energy balance (MJ)		
	In	Out	% error	In	Out	% error	In	Out	% error
Wood powder	60.00			29.64			1.01		
Air	45.83								
Gas		97.04			22.48			0.69	
Tar		2.18			1.75			0.05	
Char		0.18			0.10			0.00	
Total	105.83	99.40	6.08	29.64	24.33	17.90	1.01	0.74	26.66

**14 g CeO<sub>2</sub>**

Wood powder	60.00			29.64			1.01		
Air	45.83								
Gas		96.05			22.03			0.67	
Tar		1.81			1.44			0.04	
Char		0.18			0.18			0.00	
Total	105.83	98.04	7.36	29.64	23.65	20.21	1.01	0.72	29.40

**21 g CeO<sub>2</sub>**

Wood powder	60.00			29.64			1.01		
Air	45.83								
Gas		89.05			18.66			0.59	
Tar		1.81			1.44			0.04	
Char		0.18			0.10			0.00	
Total	105.83	91.04	13.98	29.64	20.20	31.85	1.01	0.63	37.69

**(e) Kaolin-ceria-Zirconia catalyst****14 g CeO<sub>2</sub>**

Stream	Mass balance (g)			Carbon balance (g)			Energy balance (MJ)		
	In	Out	% error	In	Out	% error	In	Out	% error
Wood powder	60.00			29.64			1.01		
Air	45.83								
Gas		95.96			22.81			0.73	
Tar		0.75			0.53			0.02	
Char		0.18			0.10			0.00	
Total	105.83	96.88	8.46	29.64	23.44	20.91	1.01	0.75	26.06

**(f) Nickel catalysts****1.07 g NiO**

Stream	Mass balance (g)			Carbon balance (g)			Energy balance (MJ)		
	In	Out	% error	In	Out	% error	In	Out	% error
Wood powder	60.00			29.64			1.01		
Air	45.83								
Gas		94.03			20.93			0.63	
Tar		1.90			1.53			0.04	
Char		0.18			0.10			0.00	
Total	105.83	96.12	9.18	29.64	22.55	23.90	1.01	0.68	33.11

**2.04 g NiO**

Wood powder	60.00			29.64			1.01		
Air	45.83								
Gas		95.76			21.96			0.69	
Tar		2.16			1.63			0.05	
Char		0.18			0.10			0.00	
Total	105.83	98.10	7.30	29.64	23.69	20.08	1.01	0.74	27.42